Investigations on ZnO Embedded Polymer Matrix Nanocomposite Coatings and Films for UV/IR Shielding Solar Thermal Control Surfaces

Thesis Submitted to the

UNIVERSITY OF KERALA

for the Award of the Degree of

DOCTOR OF PHILOSOPHY IN CHEMISTRY

Under the Faculty of Science

By

SOUMYA S.

Functional Materials Section
Materials Science and Technology Division
CSIR-National Institute for Interdisciplinary Science and Technology
Thiruvananthapuram - 695 019
Kerala, India

July 2017

Dedicated to My Family, Teachers

&

My Beloved Husband

Anesh Raj…

DECLARATION

I hereby declare that the Ph. D thesis entitled **"Investigations on ZnO Embedded Polymer Matrix Nanocomposite Coatings and Films for UV/IR Shielding Solar Thermal Control Surfaces"** is an independent work carried out by me at the **Materials Science and Technology Division of Council of Scientific and Industrial Research-National Institute for Interdisciplinary Science and Technology (CSIR-NIIST), Thiruvananthapuram** under the supervision of **Dr. S. Ananthakumar** and it has not been submitted anywhere else for any other degree, diploma, or title.

Soumya S.

Thiruvananthapuram

July, 2017

CSIR-National Institute for Interdisciplinary Science and Technology
Council of Scientific & Industrial Research
Industrial Estate P.O., Thiruvananthapuram-695 019

Dr. S. Ananthakumar
Senior Principal Scientist, Materials Science and Technology Division
Tel: 0471-2515289 (O); +91-9497271547 (M)
E-mail: ananthakumar70@gmail.com

CERTIFICATE

This is to certify that the work embodied in the thesis entitled **"Investigations on ZnO Embedded Polymer Matrix Nanocomposite Coatings and Films for UV/IR Shielding Solar Thermal Control Surfaces"** has been carried out by Ms. SOUMYA S. under my supervision and guidance at the Material Science and Technology Division of CSIR-National Institute for Interdisciplinary Science and Technology (CSIR-NIIST), Thiruvananthapuram and the same has not been submitted elsewhere for any degree.

Dr. S. Ananthakumar
(Thesis Supervisor)

Thiruvananthapuram
July, 2017

ACKNOWLEDGEMENTS

*First and foremost, I humbly bow before **'The Almighty God'** for his immense blessings which showered on me the strength and wisdom to reach this milestone in my life.*

It calls for the support and assistance of a whole lot of people without whom the work cannot be materialized. Hence, I owe an enormous share of appreciation to each one of them who have directly or indirectly helped me in my endeavor.

Words fall short in expressing my profound gratitude to my Research Supervisor, Dr. S. Ananthakumar, Senior Principal Scientist, CSIR-NIIST, Thiruvananthapuram, for his adroit guidance, motivation, constant encouragement, intellectual support, constructive criticism and above all the freedom he gave me during my doctoral studies. I am greatly indebted to him for all the efforts he has put in for the achievement of this thesis.

I express my immense gratefulness to Dr. A. Ajayaghosh, Director and former Directors Dr. Suresh Das and Dr. G. Prathap of CSIR-NIIST, Trivandrum, for providing me the necessary facilities and infrastructure of the institute for carrying out my Ph. D. work. Let me express my true thanks to Dr. P. Prabhaker Rao, Head and Dr. M.T. Sebastian, Dr. M.L.P. Reddy former Heads of MSTD, for his support during this study.

My sincere thanks are due to Dr. T.P.D. Rajan, Dr. K.G.K. Warrier, Dr. S. K. Ghosh, Dr. S. Shukla, Dr. U. S. Hareesh, Dr. N. N. Balagopal, Dr. K. P. Surendran, Dr. K. G. Nishanth, Dr. G. Bhoje and all other scientists in MSTD for their help and advice during my work.

I would like to say a particular word of thanks to Mr. Peer Mohamed for helping me with the instruments. I exuberantly acknowledge the contributions of XRD, SEM and TEM groups to this work, Mr. P. Guruswami, Mr. M. R. Chandran, Ms. V. Soumya, Ms. P. Lucy, Mr. M. Kiran and Mr. P. Robert. I am gratefully thanks to Dr. M.L.P. Reddy and Dr. J. Sheethu for NIR analysis. My special thanks to Dr. K. Nishanth for anti-fungal study. At this moment, I wish to acknowledge all scientists and technical staffs of NIIST for their kind co-operation.

I always cherish the real support and warm friendship of my former colleagues Dr. P. S. Suchithra, Ms. V. Linsha, Dr. S. Rahul, Dr. S. Anas, Mr. S. Sujith, Mr. S. Balanand, Mr. Raymond, Ms. Susheela, Mr. Gautam and Mr. Shinto. I would like to acknowledge the contributions of Mr. E. Adrein, Ms. P. Amba, Mr. V. Ajesh and Ms. N. Nayana for providing valuable inputs to this thesis.

I wish to thank whole-heartedly my present colleagues Ms. V. N. Sheemol, Mr. Mahesh., Ms. K. B. Babitha, Mr. S. S. Vaisakh, Ms. M. M. Jeen, Ms. N. Minju, Ms. K. A. Suhailath, Mr. D. Akhil, and Mr. Y. Dhaneesh which made my days at NIIST memorable. I am grateful to Ms. Sheemol for her invaluable contributions regarding fruitful discussions.

Other group members who deserve thanks are Dr. T. S. Sreeremya, Dr. K. B. Jaimy, Dr. K. Asha, Dr. N. Harsha, Dr. J. Manu, Dr. V. S. Smitha, Dr. K. A. Manjumol, Dr. S. Sanker, Ms. P. V. Subha, Ms. Suyana, Ms. J. Mega, Ms. T. Minju, Ms. S. Swetha, Ms. Sumina, Ms. N. Shijina, Mr. K. Firoz, Ms. P. Gayatri, Ms. R. Remya, and Ms. Neethu.

I would also like to extend my honest thanks to all my teachers for their encouragement and blessing.

I acknowledge the University Grants Commission for awarding the Junior and Senior Research Fellowship.

At this juncture, I owe my deep sense of gratitude to my Parents, Sugathan (Late) and Jaya Sudha, for their whole-hearted support and prayers to achieve this goal. I am incredibly grateful to my elder brothers, Sujith and Sreejith, for their motivation and help. I also extend thanks to my in-laws and family for their tremendous support. Words fall short in expressing my heartfelt appreciation and forever satisfying to Anesh Raj, my beloved husband, who was always a source of constant support and stimulation. Without his love, care, appreciation, affection, and inspiration this thesis would never be realized. With the great sense of gratitude, I dedicated this thesis to him.

Soumya S.

PREFACE

The Sun blessed the Universe by showering it's bright sunlight for a meaningful life on the Earth. As the sunlight passes through the atmosphere, it is partly absorbed by gases. However the solar light continuously releases it's energy to the Earth's surface in the forms of Ultraviolet radiation (below 400 nm, 5%), Visible (400-700 nm, 43%) and Near-Infrared Radiations (700-2500 nm, 52%). Among these solar radiations, the IR energy is termed as, 'heat carriers' and when an object is directly impinged by the solar radiations on the Earth; the IR energy is either absorbed or reflected depends upon its' emissivity character. In high absorbing surfaces a temperature gradient builds-up naturally across the object. It obviously needs a kind of IR shielding top-coats to prevent the heating which is otherwise demands external cooling mechanism such as use of air-conditioning equipments. Unfortunately, the energy demand for the climate control air-conditioning equipment is excessively high that has to be controlled for meeting energy requirements in the future.

It is proved that by means of IR reflective coatings a substrate can surely prevent the heat build-up. Learned from the Nature, scientists have discovered and developed innovative advanced functional materials and created protective surface coatings to effectively shield the harmful UV and IR energies. As one of the most versatile II-VI semiconductors, Zinc oxide (ZnO) is a promising candidate for solar reflectance. It is nontoxic and chemically stable towards air and moisture and is less expensive. In this background, this thesis is devoted to investigate the ZnO based UV/IR shielding surface coatings, mainly on glass substrates and textiles. Today, IR shielding coatings are popular and mostly it is achieved by TiO_2/ZnO inorganic pigments.

The main objectives of the thesis are;

- Design and development of doped and surface modified ZnO and its hybrid nanomaterials.
- Study the role of particle size/particle morphology on the Near- IR energy reflectance properties.

- Develop nano ZnO embedded PMMA polymer coatings and study the UV shielding, transparency and IR reflectance qualities.
- Synthesize nano ZnO/PMMA hybrid coatings via in situ sol-gel technique.
- Application of reflective nano ZnO/PMMA composites coatings on glass and textile surfaces.

The present thesis is embodied in five chapters.

The **first chapter** encompasses an introduction about functional nanomaterials, composite architectures, and inorganic-organic nanocomposte coatings for UV/IR shielding surface coatings. The scope, statement of the research problem and objectives of the thesis is also presented in the first chapter.

Second chapter of the thesis describes the effect of morphology on the IR reflectance properties of nano ZnO. In this chapter synthesis of nano ZnO with varied morphologies, fabrication of nano ZnO embedded in poly(methyl methacrylate) [PMMA] and polyurethane (PU) polymer matrix composite films and their UV shielding/NIR reflectance efficiency are documented. The effective morphology is identified to enhance the IR reflectance property of PMMA and PU top coats [*Solar Energy Materials and Solar Cells*, 125, **2014**, 102-112].

The **third working chapter** of the thesis deals with the effect of doping strategy to achieve optically transparent top coats on glass substrates. In this chapter aluminium doped nano ZnO (AZO) is synthesized and dispersed in PMMA precursor sol. Subsequently Layer-by-Layer coatings are developed on glass substrates and studied for the UV/Near-infrared (NIR) radiation shielding efficiency, ice/fog formation resistance and optical transparency to be used in green- building constructions. Functional properties such as UV absorption, NIR shielding, self-cleaning, surface hardness and scratch resistance were assessed for AZO/PMMA coatings. Finally it is concluded that the AZO/PMMA coatings can be an inexpensive interface/interphase layers for multifunctional glass-windows [*Solar Energy Materials and Solar Cells*, 143, **2015**, 335-346].

The **fourth chapter** emphasizes the effect of Sn and Ag doped ZnO quantum dots (ZQDs) on IR reflectance and UV shielding properties. The ZQDs were synthesized via microwave-reflux assisted sol-gel synthesis. An *in situ* polymerization reaction was conducted with ZQDs dispersed acrylic monomer to obtain ZQDs/PMMA transparent coatings. A facile ZQDs/PMMA hybrid coating was developed for multifunctional applications such as UV shielding, NIR reflective, photochromic top coats on glass substrates **[**Manuscript Communicated, **2017]**.

In the **fifth chapter,** an investigation is made on the multifunctional coatings prepared using silane capped nano ZnO hybrids. The silane modified ZnO is directly blended with PMMA medium and ZnO/PMMA colloidal suspension was obtained. It was further applied over a dark color cotton textile. This surface engineered black cotton was subjected to phase analysis, chemical interaction, morphological features, NIR reflectance, UV shielding efficiency and antifungal properties. The textile surfaces engineered with infrared/ultraviolet energy shielding coatings is an emerging technology in the processing of solar heat protective cool-textiles [*New Journal of Chemistry*, 40, **2016**, 7210].

Finally, in the conclusion, salient features of the various research components and the notable outcome made in the each working chapter are clearly summarized. The present investigation engaged in this thesis drawn a conclusion that the morphologically tuned nano ZnO doped with suitable dopants and chemically modified with appropriate silane molecules can result in optically transparent, IR reflective and UV shielding multifunctional coatings on glass/textile surfaces that can further act as UV/IR shielding solar thermal control interface layers for any polymer composites, window glass panels and even on textile surfaces.

CONTENTS

LIST OF TABLES

LIST OF FIGURES

ABBREVIATIONS

a.u.	arbitrary units
AFM	Atomic Force Microscopy
Ag@ZQDs	Ag doped ZnO Quantum Dots
AIBN	α, α′-Azobisisobutyronitrile
APS	3-Aminopropyltrimethoxy silane
APZO	APS modified ZnO
ASTM	American Society for Testing and Materials
ATR	Attenuated Total Reflectance
AZO	Aluminium doped ZnO
CIE	Commission Internationale de 1' Eclairage
CTAB	N-Cetyl-N,N,N-trimethylammonium bromide
DCM	Dichloromethane
DLS	Dynamic Light Scattering
DTA	Differential Thermal Analysis
EDX	Energy-Dispersive X-ray Spectroscopy
E_g	Energy band gap
et al.	et alli (and others)
FTIR	Fourier Transform Infrared Spectroscopy
FWHM	Full Width of Half Maximum
HRTEM	High Resolution Transmission Electron Microscopy
ICDD	International Centre for Diffraction Data
IEP	Isoelectric Point
IR	Infrared
JCPDS	Joint Committee on Powder Diffraction Standards
$LaPO_4$	Lanthanum Phosphate
LbL	Layer-by-Layer
MEA	Monoethanolamine
Min.	Minute
MMA	Methyl Methacrylate

mol.%	Mole percent
MW	Microwave
MW_CTAB	CTAB capped ZnO via Microwave method
MW_PEG	PEG capped ZnO via Microwave method
MW_PVP	PVP capped ZnO via Microwave method
MW_Uncapped	Uncapped ZnO via Microwave method
NHs	Nanohybrids
NIR	Near-Infrared
nm	nanometer
NPs	Nanoparticles
PCS	Photon Correlation Spectroscopy
PEG	Polyethylene glycol
PEG300	Polyethylene glycol 300
PL	Photoluminescence
PMMA	Poly(methyl methacrylate)
PTFE	Poly(tetraflouroethylene)
PU	Polyurethane
PVP	Polyvinylpyrrolidone
QDs	Quantum dots
R*	NIR Solar Reflectance
Ref_CTAB	CTAB capped ZnO via Reflux method
Ref_PEG	PEG capped ZnO via Reflux method
Ref_PVP	PVP capped ZnO via Reflux method
Ref_Uncapped	Uncapped ZnO via Reflux method
RI	Refractive index
SAED	Selected Area Electron Diffraction
SEM	Scanning Electron Microscopy
Sn@ZQDs	Sn doped ZnO Quantum Dots
SP	Spiropyran
TEM	Transmission Electron Microscopy
TGA	Thermogravimetric Analysis

Un_ZQDs	Undoped ZnO quantum dots
UV	Ultraviolet
UV/Vis/NIR	Ultraviolet/Visible/Near infrared
wt%	weight percent
XRD	X-ray Diffraction
Z_{ave}	Average hydrodynamic diameter
ZnO	Zinc Oxide

CHAPTER 1

Nanomaterials and Functional Coatings:

A Way to Shut the Sun-Heat

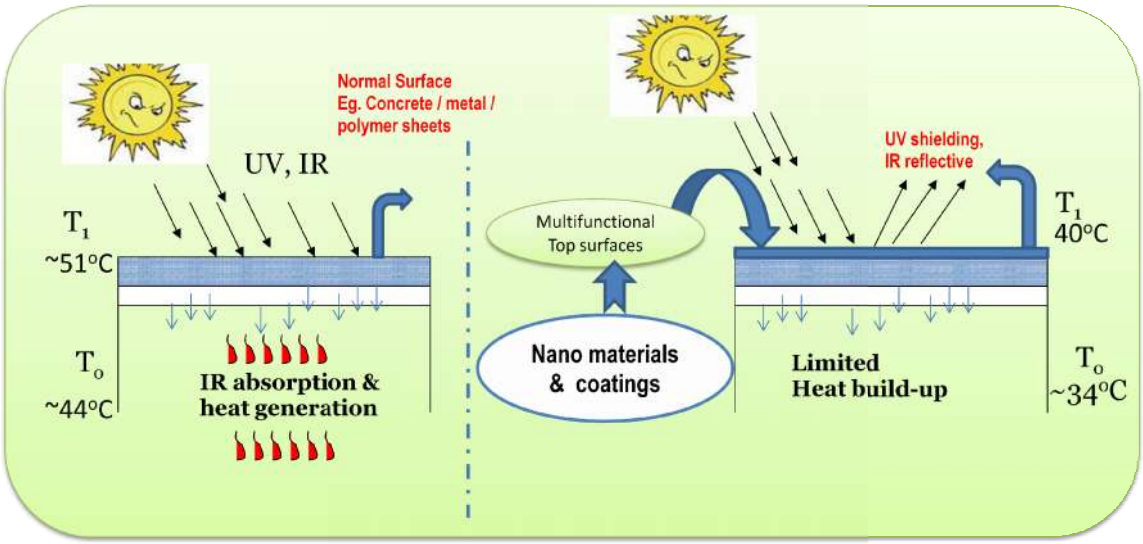

1.1. NANOMATERIALS

Nanoscale materials are defined as a set of substances where at least one dimension is less than approximately 100 nm [Figure 1.1]. Nanomaterials have received significant attention because at this scale unique optical, magnetic, electrical, and thermo-chemical properties emerge. Moreover, nanoparticles possess high surface areas making them useful for a variety of functional coatings.

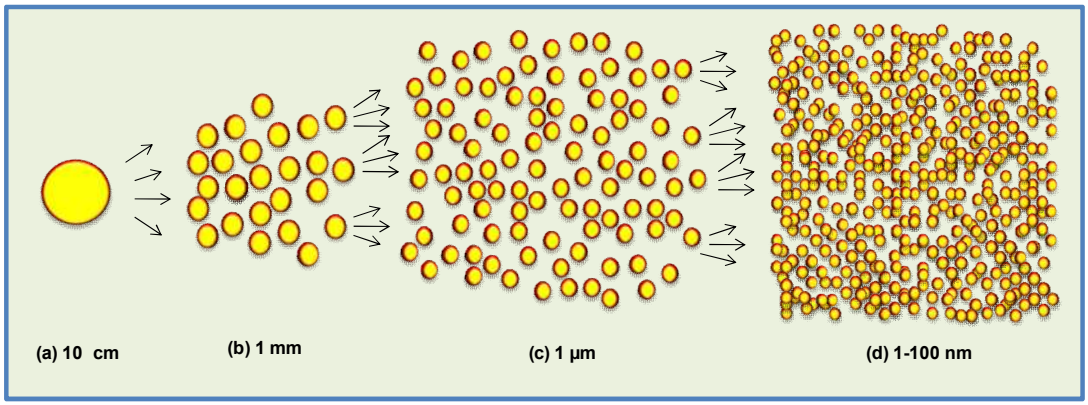

Figure 1.1: Schematic representation of micro to nano size particles

At the beginning of this introductory chapter, the overwhelming opportunities of nanomaterials *(limited to inorganic/semiconducting nanoscale materials)* as polymer matrix functional coatings are described. The later part of the chapter focused more on IR reflective nanocoatings for solar thermal control surfaces which are the main theme of this thesis work.

1.2. Nanomaterials: Opportunities for Functional Nanocomposites and Coatings

Dispersion of nanoscale inorganic particles into polymer coatings offered improved mechanical as well as thermal properties of industrial polymer coatings. Many nanoparticle dispersed polymer matrix nanocomposites have been reported over the past few decades. For example, design of nanocomposite functional coatings out of ZnO/PMMA [Hayashida *et al*., 2016], ZnO/poly(hydroxyethyl methacrylate) [Hung *et al*., 2005], CeO_2/PMMA [Parlak *et al*., 2011], TiO_2/poly(vinyl alcohol) [Nussbaumer *et al*., 2003], CdS/PS [Du *et al*., 2002], CdS/PMMA [Khanna *et al*., 2007], ZrO_2/PMMA [Fangqiang *et al.,* 2013], ZnO/PDMS [Chakradhar *et al*., 2011] are seen in the literature.

Such inorganically treated polymer nanocomposites are recommended to develop coatings for functional applications like UV protection, NIR shielding, anti-icing, photocatalytic, self-cleaning, photochromic surface coatings, *etc.* [Wu *et al.*, 2015; Demir *et al.*, 2006].The dispersion of inorganic semiconducting nanoscale materials into polymeric coatings was found to offer properties like antireflection, fluorescence, luminescence, high refractive index, enhanced mechanical (stiffness and toughness), thermal insulation, EMI shielding, antiglare and also scratch resistant [Wu *et al.*, 2015] top coats. The following section presents brief account on nanomaterials incorporated polymer matrix nanocomposites and functional coatings. The technical limitation in such polymer nanocomposite coatings are also mentioned at the end.

1.2.1. Ultraviolet Radiation Shielding Coatings: Inorganic/polymer nanocomposite coatings and films play a critical role in controlling the effects of UV on polymeric surface coatings processed over glass and other soft materials like textiles/papers. Nanoscale TiO_2 and CeO_2 are the most common candidate materials for UV shielding coatings. Researchers have earlier reported UV absorbing ZnO/polymer nanocomposite coatings [Mu *et al*., 2011; Eita *et al*., 2012b]. For example PMMA/ZnO nanocomposite [Zhang *et al*., 2012; Li *et al*., 2007], Polystyrene/ZnO thin films [Tu *et al*., 2010], and poly(butyl methacrylate) (PBMA)/ZnO [Liu *et al*., 2012a], and ZnO/ polydimethylsiloxane (PDMS) thin films [Eita *et al*., 2012a], etc., have been reported in this category. ZnO quantum dots are also employed to produce highly transparent UV shielding coatings. Due to its quantum size effect, it retains the excellent UV absorption capability and making them suitable UV absorbers.

1.2.2. Infrared Shielding Coatings: Controlling the effects of IR waves is another highly preferred characteristic of inorganic/polymer nanocomposite coatings in applications such as thermally insulative window glasses. IR control surface coatings are also reported for camouflaging the military vehicles. IR shielding films are also seen in display technologies. Due to low cost and easy *in situ* application to glass /polycarbonate polymer substrates, NIR-shielding organic/inorganic nanocomposite coatings are developed via embedding of NIR shielding functional inorganic nanoparticles into the polymer/hybrid matrix systems. ITO nanoparticle is often used as the functional nanofiller to make transparent NIR-shielding nanocomposite coatings. Zhao *et al.*

reported mechanically blended ITO nanoparticles into polyethylene glycol terephthalate prepare IR blocking films [Zhao *et al.,* 2009]. One of the other typical IR absorbing fillers is LaB_6. Highly conducting metals and black inorganic compounds like silver, gold, ruthenium dioxides, rhenium trioxides, and lanthanum hexaborides (LaB_6) [Stefan *et al.,* 2003] are also reported as fillers for IR control films and coatings.

1.2.3. Photoluminescent Coatings: If semiconducting nano particles like ZnO, CeO_2 are dispersed into monomers with an appropriate initiator, the polymerization subsequently produced bulk nanocomposite materials that show photoluminescent property. Hung and Whang [Hung *et al*., 2005] modified ZnO with 3-(trimethoxysilyl) propyl methacrylate (TPM) and then polymerized hydroxyethyl methacrylate (HEMA) monomers. The resulting TPM modified ZnO/PHEMA nanocomposites had better dispersibility and controllable luminescence. They have demonstrated that the PHEMA containing unmodified ZnO nanoparticles showed weaker red-shifted luminescence while the TPM modified ZnO/PHEMA composites exhibited stronger luminescence [Figure 1.2].

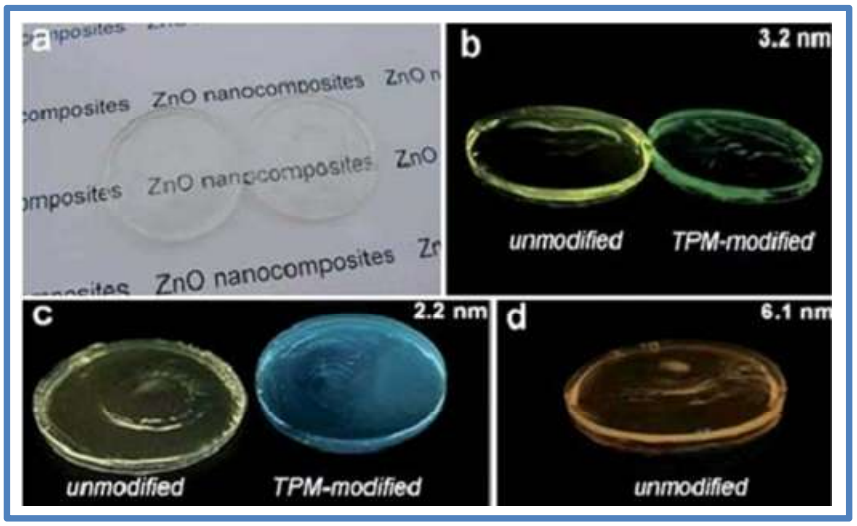

Figure 1.2: Photographs of transparent, luminescent ZnO/PHEMA nanocomposites. (a) under daylight and (b)-(d) under a UV lamp. These luminescent nanocomposites were fabricated with ZnO particles with an average diameter of (b) 3.2 nm, (c) 2.2 nm and (d) 6.1 nm, respectively [Hung *et al*., 2005].

Li *et al.* [Li *et al.,* 2007] hydrolyzed zinc acetate with monoethanolamine in ethanol and then added MMA monomer for polymerization. The products were bulk transparent PMMA/ZnO hybrid materials (PZHM). In this study, the authors have achieved *in situ* growth of ZnO quantum dots [QDs]. When the nanoscale ZnO is reduced into the sub nanometer size ZnO QDs, even a very small amount of ZnO QD could make the bulk materials to exhibit strong blue fluorescence, while the pure PMMA had no fluorescence [Figure 1.3].

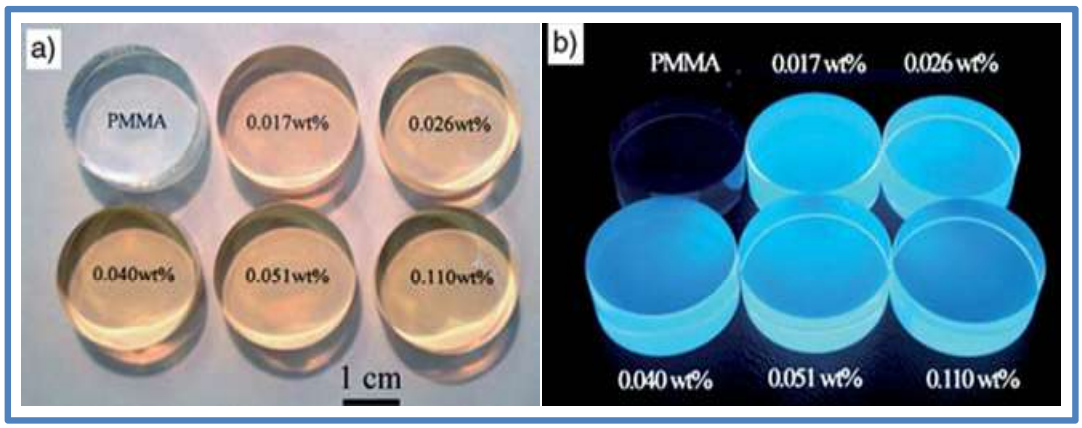

Figure 1.3: Photographs of the ZnO dispersed PZHMs under visible light. (b) PZHMs containing various concentrations of ZnO QDs under a low intensity UV light (362 nm) show significant blue emission from the ZnO QDs in the PMMA matrix [Li *et al*., 2007].

1.2.4. Photochromic Coatings: Photochromism is the reversible photocoloration of a single chemical species between two states having distinguishably different absorption spectra, which results from the effects of electromagnetic radiation in at least one particular direction [Minkin, 2004; Abdel, 2006]. Consequently, a photochromic material is one which undergoes a reversible color change in response to light [Ohko *et al*., 2003]. There are many different types of chromogenic materials, with the most extensively studied being photochromic glass and polymers [Granqvist, 1990]. Thin films based on TiO_2 [Naoi *et al*., 2004] and WO_3 [Avendaño *et al*., 2003] have been studied for photochromic properties. Each of these transition metal oxides mentioned above have been recently discovered as having multicolour photochromic properties. Andersson and co-workers reported the synthesis of photochromic pigments that can be added to various matrices including polymers like PMMA, and also in hybrid organic–inorganic

composites like O*rmosils* and surfactant templated mesostructured materials [Andersson *et al*., 2005]. The photochromic nanomaterials are usually incorporated into a matrix in two ways, either by covalent bonding or by doping [Pardo *et al*., 2011; Mennig *et al*., 1999].

1.2.5. Scratch Resistant Nanocomposite Coatings: Nanoparticles such as SiO_2, ZrO_2, Al_2O_3 and TiO_2 have been embedded in the polymer matrix, to have improved scratch and abrasion resistance of the polymer coatings. Such mechanically reliable nanocomposite coatings find vast applications as automotive top-coats, floor wear layers, acrylic eye-glass lenses, and scratch resistant polycarbonate sheets [Sangermano *et al.,* 2010]. Sol-gel derived inorganic/organic hybrid coatings for scratch resistance improvements often employ a combination of UV and thermal cure. Linking the inorganic nano-phase with the organic matrix through covalent bonds is important in achieving improved scratch resistance [Amerio *et al.,* 2008]. Protection coatings against scratch are critical for transparent plastics such as PC and PMMA [Hwang *et al*., 2003; Chakraborty *et al*., 2014].

1.2.6. Photocatalytic, Self-Cleaning Coatings: Photocatalytic activity of ZnO and TiO_2 nanomaterials is well exploited in polymer nanocomposite coatings to make them self-cleaning functional coatings [Mauro *et al*., 2017; Textor *et al*., 2007]. Pure as well as doped TiO_2 embedded polymer surfaces can catalyze the degradation of organic compounds in the presence of UV radiation and even in Sunlight. The recent introduction of self-cleaning technology is even found an application on metal panels where the photoactive nano ZnO is dispersed in the polymer which is further sprayed as coatings over metal panels [Stieberova *et al.,* 2017].

1.2.7. Antifogging Coatings: Antifogging surfaces are needed to maintain visibility through transparent surfaces in high-humidity environments. Antifogging coatings impact diverse applications such as automobile windshields, optical devices, windows, eyeglasses, or any other transparent glass or plastic surface. Recently, a new antifogging coating has been developed for plastic substrates; the surface consists of a hydrophilic/hydrophobic bilayer structure [Chang *et al*., 2012].

1.2.8. Anti-icing Coatings: Ice formation on material surfaces has significantly impacted on safety and energy consumption. The superhydrophobic inorganic/polymer composite coatings such as SiO_2/PDMS, TiO_2/PDMS, Al_2O_3/PDMS, ZnO/PMMA (polymethyl methacrylate) and $CaCO_3$/PS (polystyrene) were explored to develop icephobic/anti-icing coatings in engineering materials, such as aircraft's and power lines [Yang *et al*., 2016].

1.2.9. Antibacterial Coatings: The antibacterial activity of ZnO is well known. Antibacterial Polymer/ZnO nanocomposites find wide applications in building interior surface mainly in health care coatings in toilets and hospitals. Applications into textiles are also attempted to develop bio-safe textile. Droval *et al*., reported ZnO nanoparticles incorporated into polyamide 6 and low-density polyethylene nanocomposites which show great antimicrobial activity with low content of ZnO, which increases with increasing the concentration of ZnO [Droval *et al*., 2008].

Technical limitation*:* Control over particle size and the uniform dispersion of the nanometer scale inorganic phases within the organic polymer matrix is a critical issue often realized in inorganic/polymer nanocomposite functional coatings. Growth of nanoparticles *insitu* at low temperatures during the curing reaction of polymer coatings is another scientific challenge noticed in inorganic/polymer nanocomposite coatings. Another technical limitation realized in nano-dispersed polymer coatings is the optical transparency of the coatings. Usually nano-dispersoids enhance the optical transparency. However, it is critical to have un-agglomerated nanoparticles.

For this reason, the dispersion is homogenously achieved via suitable surface treatment. Many times the surface of the nanoparticles is capped (modified) with some organic functional moiety. Capped nanoparticles are always preferred owing to the excellent interfacial interaction between the surface of the nanoparticles and polymers [Kango *et al*., 2013]. Capped nanoparticles that have been embedded into polymer matrices result from superior hybrid nanocomposites, which possess light weight and high strength. The capped nanoparticles enhance the mechanical, rheological, optical, electrical, thermal, and flame retardant properties of the polymer matrices [Briener *et al*., 1998; Rong *et al*., 2001].

1.3. IR Reflective Nanomaterials and Solar Heat Control Coatings

The solar radiation that reaches the Earth's surface encompasses the wavelengths from 280 to 2500 nm. The spectral energy distribution of solar radiations at Sea level is presented in Figure 1.4. This range is divided into three different regions, namely: **Ultraviolet (UV) region** (280-400 nm), **Visible (Vis) region** (400-700 nm) and **Near-Infrared (NIR) region** (ca. 700 nm-2500 nm) [Brady *et al*., 1992; Levinson *et al*., 2005a; Bendiganavale *et al*., 2008; Xing *et al*., 2015].

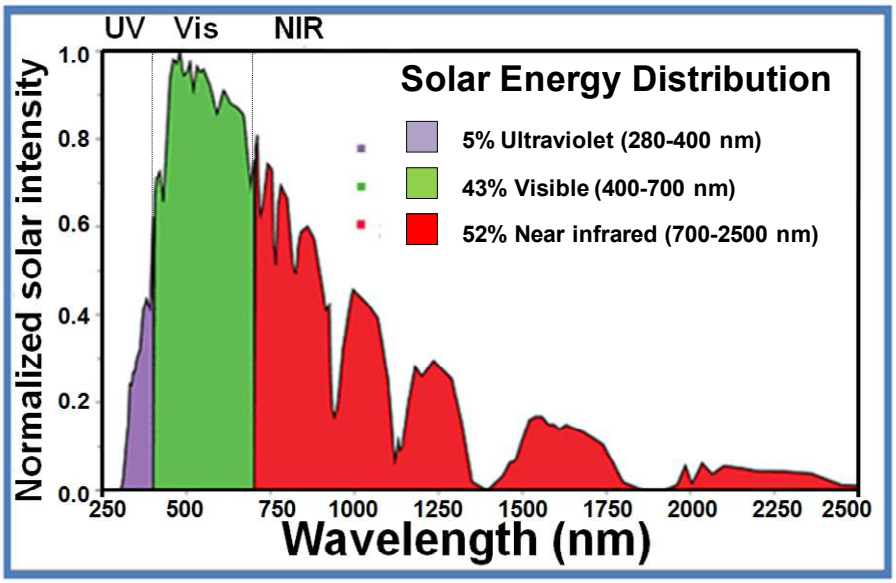

Figure 1.4: Spectral solar energy distribution [Levinson *et al*., 2005a]

Ultraviolet Region (280-400 nm): UV radiation accounts for about 5% of the solar energy; has the wavelength ranging from 280 to 400 nm [Figure 1.4]. The spectral UV-range is divided into three components: UV-A (λ = 315-400 nm), UV-B (λ = 280-315 nm) and UV-C (λ < 280 nm) [Levinson *et al*., 2005a]. During the past decades, the dosage of both UV-B and UV-A radiation has increased profoundly due to the adverse climate and continuous ozone depletion. Therefore, for the protection against UV radiation, to develop a material which can block UV rays is truly important.

Visible Region (400-700 nm): Around 43% of the solar energy occurs in the visible region of the electromagnetic spectrum. Different colors are detected by the human optical system in the wavelength range from 400 to 700 mm. Colored materials

selectively absorb the visible light and reflect the remaining. Thus the visible region consists of wavelengths that give us the perception of color [Bendiganavale *et al*., 2008].

Infrared Region (>700 nm): The near-infrared (Near-IR or NIR) radiation lies within a wavelength ranging from ~700 to 2500 nm. IR irradiation accounts for 52% of the solar irradiance energy reaching the earth, most of which is transferred to thermal energy. The heat producing region of the infrared radiation ranges from 700 to 1100 nm. The infrared (IR) waves at this wavelength region have harmful effects. Absorption of infrared radiations is primarily responsible for heating the objects [Omer, 2008]. Buildings, metallic roofs, glass windows/panels and synthetic polymer composite building materials which are exposed to Sun energy absorb the IR radiation, and as a result these objects are developing heat and radiate the same as per their thermal and emissivity characteristics. The significant amount of heat is absorbed into the building materials using conduction [Bendiganavale *et al*., 2008; Levinson *et al*., 2005a; Rezaei *et al*., 2017]. In the present context, this issue needs scientific intervention because heat build-up over the building structures, especially in industrial buildings and large size civil buildings must be controlled to save the electrical energy. It is a fact that about 60% electric power is consumed for either cooling or heating to maintain the indoor climate comfortable. Research is strongly motivated to develop affordable inorganic materials and coatings that can shield both UV and IR energy and protect the objects from the heat build-up effect. This is the main theme of this thesis.

1.3.1. Mechanism of Solar Heat Control Coatings

Solar thermal control is a term describing the property of regulating the amount of solar heat energy which is allowed to pass through a material/object. When Sunlight strikes the surface of the material, the light beam is refracted, reflected and scattered, leading to the diffuse reflection of near infrared light. Energy conservation yields, at each wavelength, that $A(\lambda) + R(\lambda) + T(\lambda) = 1$ where *A, R*, and *T* denote absorbance, reflectance, and transmittance, respectively. The ratio of the radiant energy reflected by a body to that incident upon it is defined as the 'reflectance' and may vary from 0 to 100% [Figure 1.5].

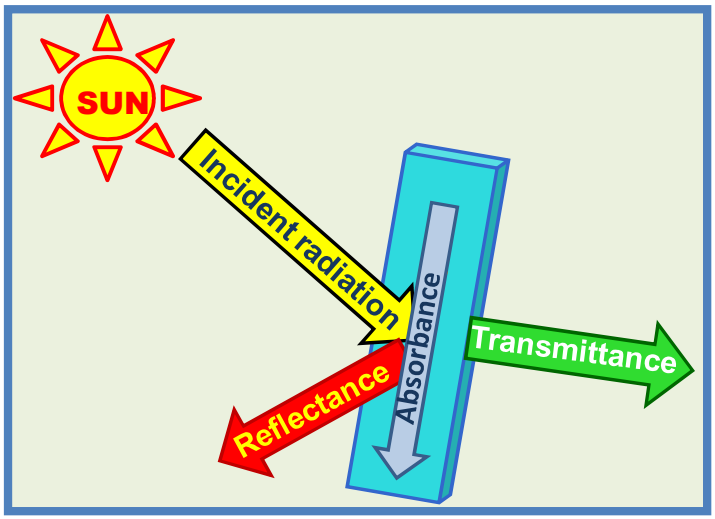

Figure 1.5: Schematic representation of Sun radiation when it hits on a glass surface being transmitted, reflected and absorbed.

Mie theory and Kubelka-Munk (KM) theory describe the interactions of light with matter. Mie theory is useful for describing the interaction of light with spherical particles that are isolated and homogeneous. KM theory is widely accepted for explaining the optical properties of complex systems such as powders and inhomogeneous system. According to KM theory, when the particle size (d) decreases, the scattering coefficient increases (for $d \geq 1$ μm) resulting in a reflectance increase. Otherwise, when the particle size increases, the depth of penetration increases and absorption increases, leading to a decrease in the reflectance [Brady *et al*., 1992; Fang *et al.,* 2013]. Reflectance is again dependent on the optical properties of the material (powders, particles, films, and coatings) and is both specular and diffuse. Specular reflection is necessary for optically smooth surfaces and highly absorbing samples. Diffuse reflection takes place when the incident radiation penetrates into the powder and gets reflected by grain boundaries of the particles. Diffusion reflection is also highly influenced by the size of particles [Demir *et al*., 2012]. When the particle size of the particles decreases, the number of reflections at the grain boundaries also increases. Thus, the depth of penetration of incident light decreases leading to a decrease in absorption and increase in reflectance. The net effect will be a decrease in the absorbed portion of light and an increase in the reflected portion of light [Fang *et al.,* 2013]. Reflecting the solar radiation minimizes the amount of energy absorbed by the objects [Figure 1.6]. Therefore, near infrared reflective functional

coatings are extremely important to ultimately control the solar energy and protect the objects from heating.

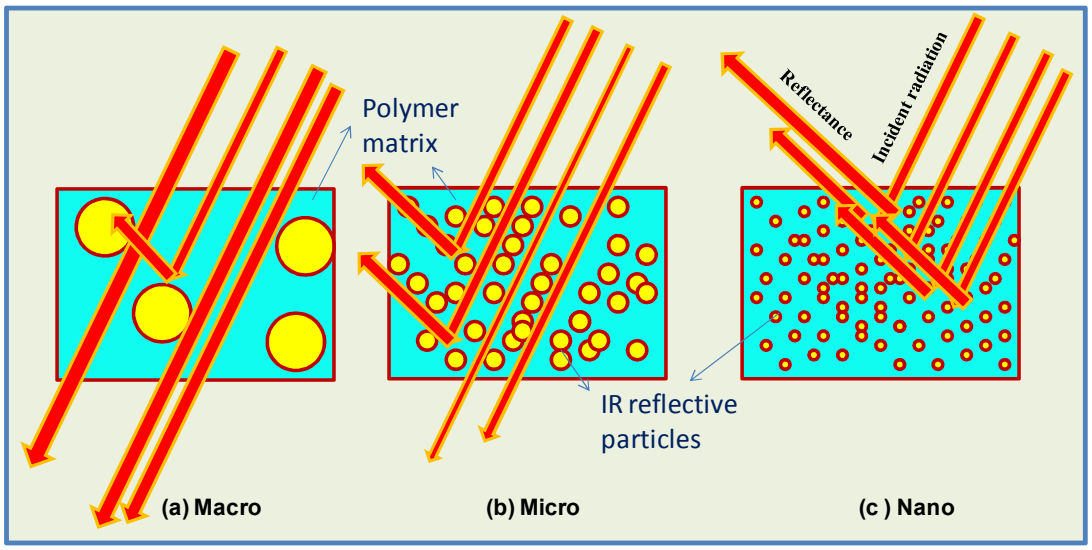

Figure 1.6: Schematic mechanism of solar radiation when incident on (a) macro, (b) micro and (c) nanosized particles embedded in the polymer matrix.

1.3. 2. Factors Affecting IR Reflectivity

The IR reflectivity depends on the relative refractive index of the particles and that of their surrounding medium, distribution of particles in the coating, loading of particles, matrix concentration and wavelength of the incident light. A significant physical data for inorganic materials consist of optical constants and geometric data such as mean particle size, particle size distribution, and particle shape. For the highest reflectivity, the particle size should be more than half the wavelength of the light to be reflected. Thus for reflecting infrared light of 800 to 1200 nm wavelength, particle size may be in the range 0.4 to 0.6 microns [Fang *et al.,* 2013].

Effect of Nanoparticles: Nanosized materials possess interesting optical properties such as increased band gap and optical transparency. Metal oxide nanoparticles prepared in unique morphologies exhibit remarkably different optical properties compared to their macro size counterparts. Among the nanosized materials, metal oxide nanoparticles such as TiO_2, ZnO, SiO_2, Al_2O_3, MgO, and CeO_2 find potential applications as functional

coatings. The controlled size and shape of these oxidic nanoparticles offer significant infrared radiation reflectance properties.

Doping Effect: Doping with elements like Al, Li, and K is another method to improve the reflectance of metal oxide particles. It creates defects in the metal oxide crystal lattice and introduced traps for electrons and holes. Doping will prevent migration of electrons and holes towards the surface of the metal oxide. Kumar *et al.* have investigated the effect of Al doping on the reflective properties of TiO_2 nanoparticles. The coating made with Al doped TiO_2 nanoparticles on a plastic substrate with different coating thicknesses was found to yield diffuse reflectance of more than 98% for 0.25 mm thick coatings [Kumar *et al.,* 2013]. Ranade *et al.* reported the enhancement of reflectance in the NIR range for Niobium (Nb)-doped TiO_2 [Ranade *et al.*, 2011].

Matrix Effect: Matrix weight ratio affects the final reflectance of the coating. With the increase in the matrix weight ratio, there is an increase in the diffuse reflectance of the coating. With higher matrix weight ratio, there is a strong capillary action between the matrix particles, causing them to fuse together and bind reflective particles into a continuous film. It has been found that coating materials, with less than certain weight ratios are unable to form a stable coating layer and are easily detached from the plastic sheet. However, coatings with more than a certain weight ratio develop cracks which might be from the large surface tension of the coating [Fang *et al.,* 2013].

***Effect of Refractive Indices of Particles and Matrix*:** The scattering of visible and infrared radiation by a particle is a function of the difference between the refractive indices of the particle and the binder in which it is dispersed. The refractive index of the commercial particle varies between 1.4 and 2.8 [Brady *et al*., 1992]. Substantial changes in scattering power cannot be achieved by choice of binder, for conventional binders in coatings do not show a significant variation in refractive index. Standard organic binders have refractive indices between 1.45 and 1.50.

***Coating Thickness*:** Thickness of the coating is another factor which affects IR reflectance. Higher layer thickness leads to better reflectance because of the larger number of reflective materials particles on the substrate for reflecting [Fang *et al.,* 2013].

1.3.3. Materials Scenario for IR Reflective Functional Coatings

IR reflective materials are divided into four categories: transition metals, inorganic or organic compounds, and natural substances. The transitional metals such as gold, silver, copper, aluminum, titanium, and rhodium are the most NIR reflective materials [Mohelnikova, 2009]. Silver claims the highest reflectivity and aluminum reflects a broad range from UV to NIR. Aluminum and silver are also used as IR reflective material in the form of thin films or flakes in NIR reflective coating. Although gold possesses high reflectivity and is anti-oxidizing, it is not utilized due to the cost [Bendiganavale *et al*., 2008]. NIR reflective organic materials are rare. Chlorophyll is the only known NIR reflective natural material to date.

Developments in solar control glass windows have led to coatings where a large part of visible light is transmitted while near-IR radiation is reflected or absorbed. These surfaces are made up of multiple layers, where the active component in the coating usually is silver [Gorgolis *et al.*, 2016]. These sheets are soft and must be protected by using a laminated glazing. Solar control glass was initially made by adding a metal oxide such as iron, cobalt or selenium oxide to the glass melt. These metal oxides created a tinted glass, which would be set as the outside pane in a window, where it would absorb more radiation than normal glass. More of the absorbed radiation is re-emitted and transported by convection to the outside of the window.

The NIR reflective inorganic materials are mainly metal oxides and sulfides. In recent years, developers have mostly used as pigments in NIR reflective coating for residential and commercial buildings. Semiconducting metal oxides preferably SnO_2, indium tin oxide (ITO), antimony tin oxide (ATO), aluminum oxide (Al_2O_3), zinc oxide (ZnO), titanium dioxide (TiO_2), cerium dioxide (CeO_2), and or a mixture thereof is earlier reported in the literature for obtaining IR reflecting materials [Hwang *et al.,* 2013; Mastai *et al.,* 2001; Park *et al.,* 2010]. Jeevanandam *et al*. studied the NIR reflectance of metal oxides nanoparticles (CeO_2, TiO_2, MgO, Al_2O_3, and ZnO) in the wavelength region 750 - 2500 nm [Jeevanandam *et al*., 2007]. It was found that the nanosized metal oxides possess ~15-20% higher NIR reflectance. The increase in reflectance is due to smaller crystallite sizes coupled with smaller mean aggregate sizes. It is believed that the band gap of these materials is large (approximately 3 eV) enough to make them transparent to visible light. Such nanosized metal oxides also intrinsically possess high refractive index (n = 2.2 to 2.7) and contribute light-scattering at all wavelengths. They have a unique

property of high solar reflectance in the near-infrared region and solar energy absorbance in ultraviolet region which makes them ideal for multifunctional, optically transparent surface coatings.

1.3.4. Review of IR Reflective Materials

Table 1.1: % IR reflectance (R%) of recently reported ceramic colors

Materials	**Color**	**R (%)**	**References**
$(LiLaZn)_{1/3}MoO_4$−$BiVO_4$	Brilliant yellow	95%	[Tara *et al.*, 2017]
$NiTiO_3$ and $NiTiO_3/TiO_2$	Dark yellow	89.7%	[Tong *et al*., 2016]
Nano $YIn_{0.9}Mn_{0.1}O_3$-ZnO	Intense blue	79%	[Jose *et al*., 2016]
Rare earth double molybdate $BiVO_4$	Brilliant yellow	90%	[Sameera *et al*., 2015]
Terbium-doped yttrium cerate	Intense red color	80%	[Raj *et al*., 2015]
Y_2BaCuO_5	Brilliant green	61%	[Jose *et al*., 2014]
Cr_2O_3-$3TiO_2$	Orange	53%	[Li *et al*., 2014]
Lanthanum–strontium copper silicates	Blue	67%	[Jose *et al.*, 2013]
La- and Pr- doped chromium (III) oxide	Green	85%	[Sangeetha *et al.*, 2012]
Si-doped yttrium molybdate, Pr-doped yttrium molybdate	Dark yellow, Dark brown	98%, 92%	[George *et al*., 2011]

The reported colored inorganic materials and its NIR reflectance were tabulated in Table 1.1. Many of the colored inorganic particles (chromium green, cobalt blue, cadmium yellow, nickel titanate yellow and lead chromate) encompass toxic metal ions, and hence their consumption is being restricted [Sangeetha *et al*., 2012; Smith *et al*., 2003]. Recently reported colored, NIR reflecting inorganic materials are less hazardous

to health and environment. Figure 1.7 represents the images of similar published colored inorganic materials.

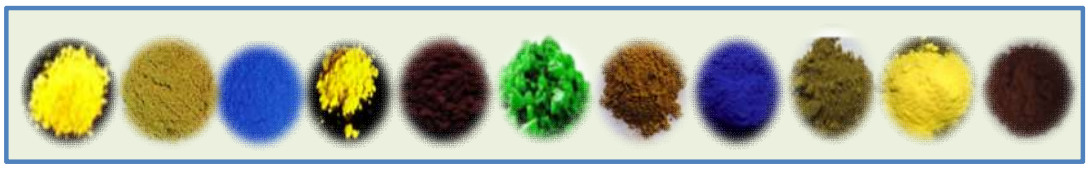

Figure 1.7: Reported colored IR reflective materials [References are shown in Table 1.1 from top to bottom].

Table 1.2: Recently published white inorganic materials for IR reflectance performance

Materials	**Reflectance Performance**	**References**
Nano $Gd_2Ti_2O_7$	NIR reflective and cool material	[Balamurugan *et al.,* 2016]
Rutile and Anatase	Anatase:Rutile coated on cotton fabrics (35:65% reflectance)	[Wong *et al*., 2015]
Nano ZnO	UV absorption and NIR reflectance	[Kiomarsipourn *et al.,* 2014]
Zn-MCM-41	Thermal control coatings for spacecraft	[Kiomarsipourn *et al*., 2013a]
Macro ZnO	NIR reflectance with morphology	[Kiomarsipourn *et al*., 2013b]
Nano and micro TiO_2	NIR reflectance of Cotton/Nylon fabrics	[Mehrizi *et al*., 2012]
Nano SnO_2	Tuning the shape with NIR reflectance	[Liu *et al*., 2010]
Co doped TiO_2	Effect of Co doping for optical properties	[Subramanian *et al*., 2008]
Nano and micro CeO_2, TiO_2, MgO, Al_2O_3, ZnO	Nano metal oxide shows 15-20% higher reflectance than micro	[Jeevanandam *et al.,* 2007]
Micro ZnO	Spacecraft thermal control coatings	[Johnson *et al.,* 2003]

In the category of white color materials, inorganic semiconducting metal oxides such as TiO_2 and ZnO are the two most dominated IR reflective materials. These two semiconducting materials show > 90% NIR reflectance. A few millimeter thick spraying of acrylic and polyurethane paints containing TiO_2 and ZnO white pigments are widely recommended as NIR shielding roof coatings. Replication of such coatings on glass surfaces would result in cool-windows, provided a high optical transparency to the level of at least 95% is retained. Table 1.2 presents the list of some of the IR reflective white color nanomaterials.

1.3.5. Multifunctional Nature and Applications of IR Reflective Materials

The IR reflective nanomaterials have impressive multifunctional properties. Apart from the high IR reflectance and UV shielding, they offer antimicrobial, antifungal and self-cleaning properties. Table 1.3 shows the versatile multifunctional properties of some of the IR reflective nanomaterials.

Table 1.3: IR reflective nanoparticles and their functional properties [Bendiganavale, 2008; Mauro *et al*., 2017; Fang *et al.,* 2013]

Nanomaterials	**Coating property**
CuO, TiO_2, ZnO	Anti microbial
TiO_2, ZnO, $BaSO_4$, CeO_2	UV stability
ZnO, ITO, ATO, TiO_2, In_2O_3	IR absorption/reflection
TiO_2, ZnO	Photocatalysis, self-cleaning
Al_2O_3, SiO_2, ZrO_2	Mechanical, scratch resistance
Nanoclays, boehmite	Corrosion
Nanoclays	Fire retardant
Fe_2O_3	Magnetic

Since near-infrared radiation in the wavelength region 810 to 1100 nm is said to be the prime reason for the heat build-up, NIR reflecting inorganic materials have become necessary for designing thermal control surface coatings. NIR control surface coatings can curtail solar heat transfer through the glass and building surfaces [Libbra *et al*.,

2011]. Coatings made with nanoparticles offer high optical transparency combined with light reflectance quality. Brady and Wake [Brady *et al*., 1992] first formulated the approaches for achieving solar heat reflecting coatings. Patent documents cover most of the literature on IR reflective materials because of ample scope for business [Hwang *et al*., 2013; Viasnoff *et al.,* 2012; Condo *et al.,* 2010; Huang *et al.,* 2012]. IR reflective materials find primary use in the construction fields, plastics, paint and ink industries and functional paints [Coser *et al*., 2015]. IR reflective materials have been widely used in roof coatings (like the concrete terrace, ceramic tiles, metal roofing structures, red clay tiles, wood and asbestos sheets), vinyl window and sliding, cement bonded pavement blocks. [Levinson *et al.*, 2005a; Levinson *et al.*, 2005b; Shiao *et al.*, 2005; Bendiganavale *et al*., 2008]. Their applications are expanded to other fields such as spacecraft thermal control coatings [Johnson *et al.,* 2003], military camouflage [Gupta *et al*., 2001], and cool-textiles [Wong *et al*., 2015]. Viasnoff *et al.* [Viasnoff *et al.,* 2012] proposed ZnO based thin films for the high near infrared reflecting building windows. Huang *et al.* [Huang *et al.,* 2012] demonstrated infrared reflective coating composition composed of polymeric materials with inorganic materials. IR reflective screens are also proposed for 'greenhouses' [Verscharen *et al.,* 1996].

1.4. Research Problem and Outline of the Thesis

Global energy consumption has been increasing, and this creates a substantial demand for energy saving materials to be developed. According to the report of "World Energy Outlook 2016" by the U.S Energy Information Administration (EIA), world energy demand could grow 30% by 2040. Earth's 2016 surface temperatures were the warmest since modern record-keeping began in the year 1880, according to independent analyses by NASA and the National Oceanic and Atmospheric Administration (NOAA). In countries like India, due to the El Nino effect and greenhouse gas emission, the overall atmospheric temperature is dangerously high, and in fact, the temperature is rising as high as 40 °C in most of India. These greenhouse gases are also typically taken into account for the carbon footprint. A way in which this can be reduced is to use thin film coatings by which one can limit the amount of solar radiation entering a building. Large buildings situated in hot regions of the Globe need to be agreeable to their residents. Air conditioning is extensively used to make these buildings comfortable, with consequent energy consumption. Absorption of solar visible and infrared radiations is responsible for

heating the objects on the surface of the Earth, including houses and buildings [Omer, 2008]. It is possible to use coatings formulated with energy saving materials, which are capable of reflecting the radiation in the infrared spectrum, to avoid excessive energy consumption [Rezaei *et al*., 2017]. The exposure to infrared (IR) radiation is the primary source of heat radiation. Transparent near-IR shielding coatings are strongly required for solar control windows in architectural and automotive applications to provide interior comfort as well as to reduce energy consumption. Optically transparent NIR-shielding coatings are indeed very much important for solar thermal control coatings. This thesis lies in this aspect and research problem is selected based on nano ZnO based IR reflective functional coatings and films. In the early part of this chapter, the use of ZnO as UV as well as IR shielding coatings was briefly described. Two important issues are very critical.

Issue 1: For any practical applications, and to develop effective solar thermal control surfaces and coatings, the IR reflective multifunctional nano ZnO need to be embedded in a polymer based matrix material. In general, the refractive indices of polymers and inorganic particles are different. Inorganic pigment particles have a refractive index (RI) in between 2.0 to 3.5; on the other hand, the RI of polymers lies in the range of 1.5-2.0 [Parlak *et al.*, 2011]. Unfortunately, most of the industrial polymers have very weak IR reflectance. They also destroy the IR reflectance of nano ZnO if they are incorporated into the polymer without proper doping and surface modification. The present thesis addresses this issue first. The first research aspect was based on the question, How to have IR reflective polymer based coatings and films with nano ZnO? For this, the research elements such as the role of ZnO morphology, the effect of doping and role of layer thickness or number of polymer layers are investigated.

Issue 2: Apart from the coatings on glass surfaces, the research was also devoted to making IR reflective textiles, mainly the dark color textiles. Usually, the light shade textiles offer about 40% IR reflectance. However, the dark ones mainly brown and black cotton textiles offer much less IR reflectance. Hence an attempt was made to enhance the IR reflective quality of dark color cotton textiles using ZnO embedded polymer coatings. The effects of coatings on IR reflectance, UV absorbance, flexibility as well as on the natural porosity of the cotton textile were investigated. PMMA polymer is used as a coating material and ZnO is exploited as IR reflective active component. The following

sections briefly describe the different fundamental properties of ZnO and PMMA polymer.

1.5. Zinc Oxide: A Multifunctional IR Reflective Material

ZnO reflect more than 90% incident near-infrared radiation while transmitting high-level solar light in the visible spectra. Compared to TiO_2, the white pigment ZnO has slightly better advantages. First of all, the nanoscale ZnO can be synthesized using inexpensive chemical methods. Nanocrystalline ZnO synthesis is very much possible at relatively low synthesis temperatures. Well, crystalline phase pure ZnO is accomplished even at less than 100 ^{o}C. Most importantly the ZnO can be grown at various nano-morphologies. Direct fabrication of individual structures with controlled crystalline morphology can provide unique electronic and optical properties due to size confinement and dimensionality. ZnO is the second most significant white pigment shielding both UV/IR regions. Therefore nano ZnO was selected in this study for developing UV/IR shielding functional coatings. Effect of nano ZnO particles due to its optical transparency and UV/IR shielding property in the different polymer based coatings materials received significant interest worldwide for developing mechano-chemically reliable solar thermal control surface coatings.

1.5.1. A Brief Account on Nano ZnO

As one of the most versatile II-VI semiconductors, ‘zinc white’ is a promising candidate for solar reflectance. It is nontoxic and chemically stable towards air and moisture and is less expensive. Zinc oxide (ZnO) possess wide band gap of 3.37 eV and high excitation binding energy (60 meV) which gained the interest of scientific community since 1935 [Özgür *et al.,* 2005; Janotti *et al*., 2009]. The native doping of ZnO due to oxygen vacancies or zinc interstitials is n-type [Özgür *et al*., 2005]. ZnO has high refractive index [Takahashi *et al*., 2007], high thermal conductivity [Wu *et al*., 2016], antibacterial/antifungal [Kumar *et al*., 2014; Lakshmeesha *et al*., 2014] and UV/NIR protection properties [Kiomarsipourn *et al*., 2014]. Compared to macro sized ZnO, nanosized ZnO shows excellent optical transparency in coatings. Nano ZnO is one of the most promising materials for energy-saving or heat-protecting windows and a wide range of technological applications due to its optical transparency.

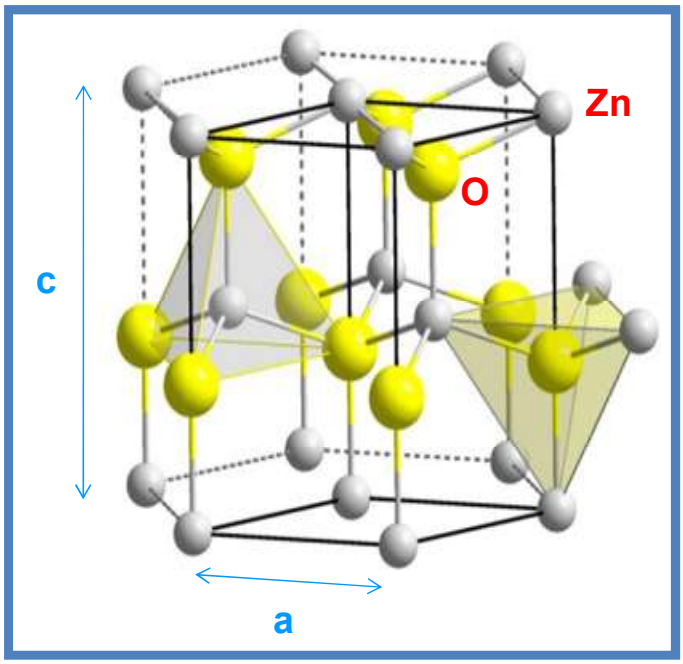

Figure 1.8: Wurtzite crystal structure of ZnO. Zinc atoms are shown in gray and oxygen atoms are shown in yellow [http://en.wikipedia.org/wiki/Zinc_oxide].

ZnO has hexagonal wurtzite crystal structure [Figure 1.8] which is a thermodynamically stable phase under ambient conditions. ZnO wurtzite crystal with lattice parameters a, b = 3.25 Å and c = 5.12 Å, their ratio *c/a* ~ 1.60 is close to the ideal value for a hexagonal cell. The density of ZnO is 5.605 g·cm^{-3} [Lide, 1992]. In the wurtzite structure, each Zn^{2+} is surrounded tetrahedrally by four O^{2-} and vice versa. This tetrahedral coordination characterizes covalent bonds with sp^3 hybridization. The tetrahedral coordination gives a polar symmetry along the *c*-axis. This polarity is responsible for its anisotropic crystal growth habit, etching behavior, and defect generation. The wurtzite structure of ZnO has 13 different growth facets directions. Therefore, together with a pair of polar surfaces and its highly ionic character, ZnO can produce a rich family of various nanostructures [Shahroosvand *et al*., 2013]. Table 1.4 summarizes the basic crystallographic parameters, thermal, optical and electrical properties of ZnO.

Table 1.4: Bulk ZnO physical properties [Takahashi *et al*., 2007]

Property	**Parameter**
Molecular formula	ZnO
Molecular weight	81.37
Stable phases at 300 K	Wurtzite
Energy band gap	3.37 eV (direct)
Exciton binding energy	60 meV
Lattice parameters at 300 K:	
a	0.32495 nm
c	0.52069 nm
c/a	1.602 (1.633 for ideal hexagonal structure)
u	0.345
Refractive index	2.029, 2.008
Density	5.606 g/cm^3
Thermal conductivity	0.6, 1-1.2
Melting point	1975 °C
Linear expansion coefficient, α (/°C)	α_a: 6.5 x 10^{-6}, α_c: 3.0 x 10^{-6}
Static dielectric constant	8.656
Intrinsic carrier concentration	<10^6 /cm^3
Electron effective mass	0.24
Hole effective mass	0.59
Electron Hall mobility at 300 K for low n-type conductivity	200 cm^2/V•s
Hole Hall mobility at 300 K for low p-type conductivity	5-50 m^2/V•s

1.5.2. ZnO Nanostructures: Synthesis Strategies

The French and American process is used most commonly for the commercial synthesis of bulk ZnO [Moezzi *et al*., 2012]. Several synthetic methods have been proposed for ZnO nanoparticles and their surface functionalization. A variety of precursors such as zinc hydroxide, chloride, nitrate, carbonate or acetate can be converted

into ZnO in a wide range of temperatures, pressures and a selection of solvents or atmospheres. ZnO forms variety of zero (0D), one (1D), two (2D), and three-dimensional (3D) nanostructures with unique physicochemical properties. ZnO Quantum Dots (QDs) represent a class of zero-dimensional nanostructures. 1D nanostructures of ZnO have the richest variety of structures, which include wires, combs, needles, ribbons, rings, tubes, rods, belts, *etc.* The 2D nanostructures of ZnO include nanosheet and nanoplate. Examples of ZnO 3D nanostructures include flowers, snowflakes, dandelion, coniferous urchin-like, *etc.* [Radzimska *et al.,* 2014; Wang, 2004; Sirelkhatim *et al*., 2015; Yoffe, 2001; Xu *et al.,* 2011; Ahmad *et al*., 2011; Djurisic *et al*., 2012].

Various physical and chemical synthesis methods such as spray pyrolysis, thermal decomposition, combustion synthesis, microwave thermal evaporation deposition, chemical vapor deposition, evaporation techniques, sonochemical, hydrothermal method, etc. [Sirelkhatim *et al.,* 2015] are attempted and reported in the literature to make these differently shaped nano ZnO. Table 1.5 illustrates the different ZnO morphology obtained from various synthesis methods.

Table 1.5: Nano ZnO: Chemical synthesis and resultant morphologies [Sirelkhatim *et al.,* 2015; Radzimska *et al.,* 2014]

Synthetic Approaches	ZnO Morphology
Microwave Decomposition	Sphere
Simple Wet Chemical route	Nano and micro flowers, dumbbell shaped, rice flakes, and rings
Simple Precipitation Method	Nano-flakes
Hydrothermal Synthesis	Hexagonal prismatic rods
Solvothermal Method	Nano-flowers, nanorods, nanospheres
Microwave Hydrothermal Method	Mulberry-like
Hydrothermal Technique	Nanorods

1.5.3. Nano ZnO: Proposed Growth Mechanism for Diverse Morphologies

The growth of a ZnO nanostructure is due to two processes namely Ostwald ripening and oriented attachment. According to Ostwald ripening, the increase in the particle size is due to the merging of the smaller particles into larger ones [Spanhel *et al*.,

1991; Meulenkamp, 1998] and is a result of the potential energy difference between small and large particles and can occur through solid-state diffusion. Oriented attachment mechanism comprises of the direct self-organization of two particles into a single crystal by sharing a common crystallographic orientation. This process is dominant at the nanometer level. It is reported that the capping agents, as they directly modify the nanoparticle surface can largely influence the oriented attachment procedures [Wu *et al*., 2007]. Exploiting these mechanisms using suitable capping agents is an exciting and challenging aspect of the synthesis of ZnO nanostructure.

1.5.4. Influence of Capping Agents

The effect of capping agents on the growth of ZnO nanocrystals has been extensively examined [Kango *et al.,* 2013; Wu *et al*., 2007]. The capping agent plays a critical role in controlling the physical size of the nanoparticle as well as its morphology. It also prevents aggregation of the nanoparticles. A sort of repulsive force among the particles is generated due to capping agent. The repulsive force can in principle be due to electrostatic repulsion, steric exclusion or a hydration layer on the surface. Depending on the particle system, i.e. the core material, and the solvent in which the particles are dispersed, the choice of the right capping agent might yield to stable particles. First, the capping agent has to be bound to the particle surface by some attractive interaction, either chemisorption, electrostatic attraction or hydrophobic interaction, most commonly provided by a head group of the capping agent. To control the growth of the nanoparticles, most of the researchers used organic stabilizers (or polymers) during the wet-chemical synthesis [Guo *et al*., 2000; Xiong, 2010; Costenaro *et al*., 2013]. Commonly used capping agents are polyethylene glycol (PEG), polyvinyl pyrrolidone (PVP), polyvinyl butyral (PVB), cetyl trimethylammonium bromide (CTAB) and 3-aminopropyl trimethoxy silane (APS). Cao *et al.* developed surface modified ZnO using silica and trimethyl siloxane (TMS) [Cao *et al*., 2009]. Modification of the surface of ZnO particles using 3-methacryloxy propyl trimethoxy silane was also performed by Kotecha *et al.* [Kotecha *et al.,* 2006]. The introduction of silane into the ZnO structure caused a decrease in the particle size (40–100 nm) and an increase in the diameters of the aggregates, even to the order of micrometers. Organosilanes are highly attractive candidates for surface modification and stabilization of ZnO nanocrystals to inhibit decomposition in aqueous media. To the ability of silane molecules to form covalent

siloxane bonds with the metal oxide surface, these molecules are found to create a shielding barrier of cross-linked silanes (polysiloxanes) that protect the nanocrystal at the core. ZnO quantum dots were modified with 3-aminopropyltrimethoxysilane, where the amine groups at the periphery contribute to the stability of these quantum dots [Shi *et al.* 2011]. In turn, Kang and Park [Kang *et al*., 1999] modified ZnO using silver ions and obtained a ZnO-Ag composite with particles size measuring approximately 120–250 nm. Shim *et al.* carried out modification of ZnO using poly(methyl methacrylate) (PMMA) via *in situ* polymerization [Shim *et al*., 2002]. The schematic presentation in Figure 1.9 summarizes the ways of surface modification of ZnO [Radzimska *et al.,* 2014]. Surface modification or functionalization is indeed very essential to tune the optical properties of ZnO nanostructures.

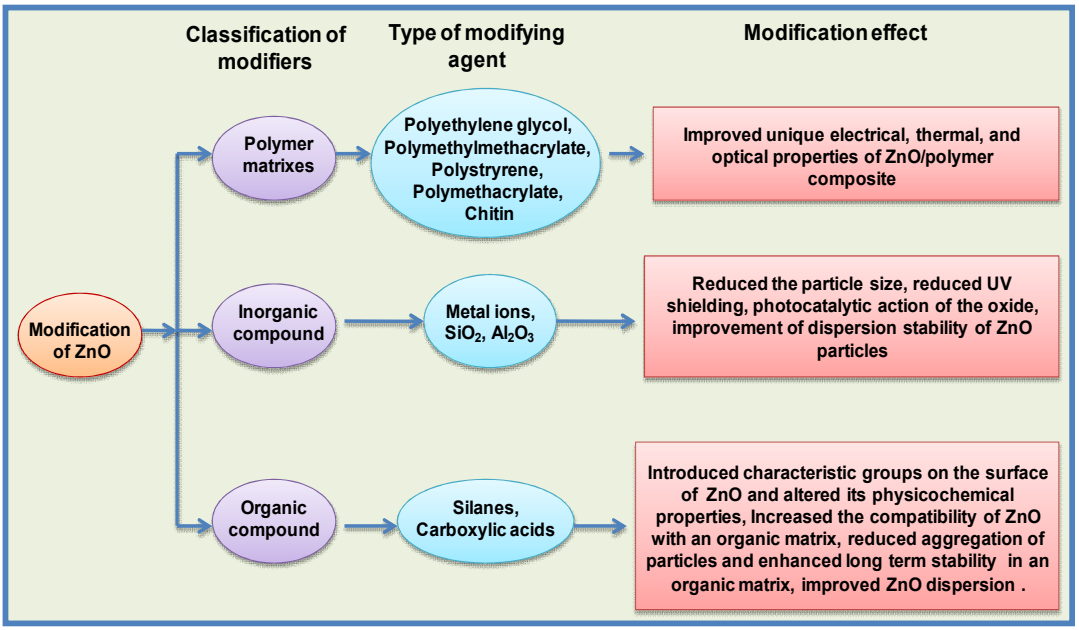

Figure 1.9: Classification of modifiers, types of modifying agent and its modification effect of ZnO.

1.6. PMMA as a Polymer Matrix

In the current study, PMMA is selected as a supporting matrix for inorganic/polymer composites because it has superior intrinsic physio-chemical properties, such as, optical clarity, higher tensile strength, biocompatibility, and dimensional stability. In this context, PMMA has been a favorite choice for the preparation of inorganic/polymer nanocomposites. However, low level of thermal

stability coupled with an inability to block UV rays limits high-temperature application of PMMA. Some researchers have studied the strategies to develop UV absorbing TiO_2/PMMA or ZnO/PMMA nanocomposites [Meng *et al*., 2011; Li *et al*., 2007; Zhang *et al.*, 2013].

PMMA is a thermoplastic, optically transparent amorphous versatile glassy polymer material. It is widely used as a substitute for inorganic glass because it shows higher impact strength and undergoes ductile rather than brittle fracture. PMMA polymer has an RI of 1.49 at 633 nm, high mechanical stability and very low thermal conductivity (~0.19 $W.m^{-1}.K^{-1}$) [Demir *et al*., 2006]. It also has poor UV and NIR shielding capability. PMMA is also widely used as a housing material or surface coating material of machinery because of its excellent weather resistance. It is widely utilized to make windows, eye contact lenses, camera lenses for mobile phones, and other optical devices because it has good transparency [Wang *et al*., 2010b; Zhang *et al.,* 2013]. Moreover, inorganic or organically modified inorganic particles embedding PMMA has been cast into films to yield enhanced functional properties such as electrical conductivity, photoconductivity, photo-induced charge-transfer, nonlinear optical properties, photoluminescence, mechanical and magnetic properties [Gibelli *et al.*, 2013]. The best known UV-blocking nanocomposite is that consisting of PMMA for its high transparency and ZnO nanoparticles for their UV absorption efficiency. The combination of ZnO and PMMA leads to a full absorption of the UV radiation in the range of 290-340 nm, PMMA absorbs the radiation in the range of 200-280 nm, but the whole composite shows a reasonable transparency in the visible region.

In this thesis, incorporation of UV/IR shielding nano ZnO in PMMA polymer matrix produces functional nanocomposites which can be a better way to make efficient solar thermal control interface structures. ZnO/PMMA exhibits an ensemble of properties of its constituents, and ultimately offer thermo-mechanically stable, UV/IR shielding multifunctional hybrid materials. Such UV/IR shielding nanocomposite films and layers find applications in fabricating plastics, sandwich glass panels, and textiles. In this thesis focused on the UV/IR shielding application of ZnO embedded PMMA nanocomposite coatings and films for solar thermal control surfaces such as plastics, glass, and textiles.

DEFINITION OF THE PRESENT RESEARCH PROBLEM

IR-reflective functional nanomaterials are in high demand for the development of solar thermal control surface coatings *[usually termed as 'cool coatings']* on surfaces such as roof, textiles, and windows. IR reflective solar control coatings can save energy by reflecting the sun's heat. Similarly UV protecting coatings are also essential for outdoor applications and over the years TiO_2/Silver based UV protective functional coatings are developed. UV/IR shielding nanocoatings primarily protect the objects from the damage of IR/UV rays coming from the Natural Sun Energy.

A possible research questions that arises when functional nanoparticles are employed to fabricate UV/IR control functional coatings is: What is the effect of the particle morphology? How to enhance the IR reflectance and UV shielding? Is there a need to introduce any dopant ions to maximize the IR/UV shielding qualities? Apart from the UV/IR shielding properties, can the nanoparticles offer any additional functionality such as anti icing, anti bacterial and also photochromic property? In this thesis, attempt is made to answer some of these research questions.

ZnO has multifunctional properties including transparency, wide band gap, and strong room-temperature luminescence. Nano ZnO has better IR reflectance compared to macro ZnO. Therefore, ZnO is a versatile material for energy saving solar heat-protecting functional coatings. If nano ZnO is embedded in polymer matrix, to what extend the polymer attains benefits with respect to IR reflectance and UV shielding properties. This is the research aspect studied and reported in this thesis.

Objectives:

Investigate the UV/IR reflectance of nano ZnO embedded PMMA coatings and films is the prime objective of this thesis. Design and Fabrication of nano ZnO embedded PMMA coatings and films are focused to obtain UV shielding and IR reflective functional coatings that can be applied on polymer, glass, and textile surfaces.

The various research elements and research components carried out in this thesis are:

- Synthesis of morphologically varied nano ZnO via microwave and reflux techniques and investigate the effect of morphology on the IR reflectance quality. Fabricate the PMMA and PMMA/PU matrix nanocomposite thick films by incorporating the nano ZnO as 'functional dispersoids', and study the morphologies to obtain effective IR reflectance and UV shielding properties for any practical use.

- Investigate the effect of Al doping on nano ZnO and study the IR reflectance and UV shielding properties of doped nano ZnO. Incorporate the doped ZnO in PMMA polymer matrix and fabricate nanocomposite coatings on glass substrates. Record the IR reflectance with respect of numbers of coating layers. Study the ZnO embedded multilayer PMMA coatings for anti-icing, as well as a few selected mechanical properties.

- Synthesis of Sn and Ag doped ZnO quantum dots (ZQDs) via microwave-reflux assisted sol-gel techniques. Study the effect of ZnO QDs on IR reflectance an UV shielding properties when they are incorporated into the polymer matrix. What kinds of photochromic and photoluminescence properties are possible in such ZnO QDs modified PMMA top coats if any organic *chromophore* is introduced?

- Design of silane modified ZnO nanohybrids (APZO NHs) and studying the effect of such hybrid nanomaterial in PMMA matrix to have IR reflective coatings. Fabricate the IR reflective APZO NHs/PMMA coatings, on cotton fabrics mainly on dark color fabrics and study the IR reflectance, UV-shielding, and antifungal properties of textiles finally to obtain cool textiles.

With these objectives, research was conducted systematically and the results are summarized in the Ph.D report. The outcome of this research is well documented in the form of international scientific publications. About 3 international publications were produced and one is submitted for possible publication.

CHAPTER 2

Effect of Morphologically Varied Nano ZnO for UV and IR Shielding PMMA Polymer Films

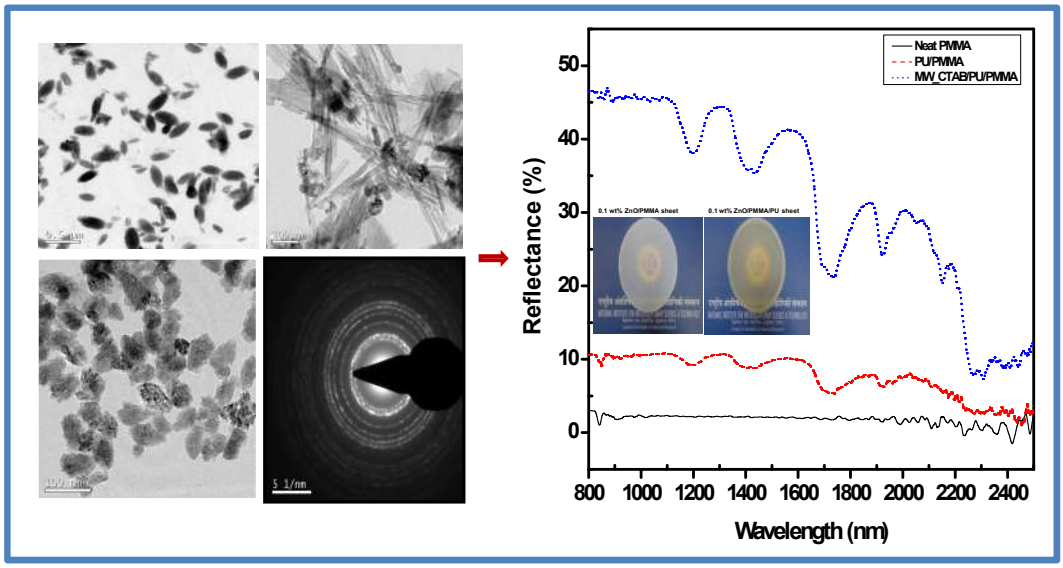

PREAMBLE

IR reflectance is an optical property that largely varies with respect to the physical dimension of the nano crystalline particle. In earlier works, research attempts were made to understand the particle size effect as well as to determine the appropriate physical size of the particle required to reflect the maximum amount of IR energy. However, the aspect of morphology is often not considered and hence not well covered in the earlier research. This chapter devotes to study the effect of morphology on the IR reflectance property of nano ZnO and its composite coatings. The IR reflectance quality of morphologically varied nano ZnO is studied in PMMA as well as PU polymer matrices.

2.1. INTRODUCTION

Nanodimensional TiO_2, SiO_2, Al_2O_3, ZrO_2, CNT, graphene, *etc*., embedded in industrial polymer matrices has been steadily increasing for developing functional composites and interface structures [Cano *et al.,* 2013; Pandey *et al.,* 2010; Chen *et al.,* 2010]. Such nanocomposites offer attractive properties like resistance against UV radiation, thermal insulation, EMI shielding, antiglare,, and also scratch resistant. Energy saving, eco-friendly building design, and constructions demand these kinds of advanced functional materials to cut the cost towards maintenance and electricity usages. Optically transparent, inter-phase films that can control the heat and light are particularly important in recent years because of the drastic rise in overall atmospheric air temperature due to CO_2 emissions [Fang *et al.,* 2012]. Near IR rays in solar radiation are generally termed as 'heat rays' because they carry heat energy to generates radiant heat in buildings when it is transferred through conventional glass windows and transparent polymer roofing structures. Polyurethane, polypropylene and polycarbonate polymer sheets are used as roofs and partition walls in buildings. Unfortunately, normal glass and most of these polymers have very poor NIR reflectance quality. Against this backdrop, development of an interface capable of superior NIR shielding for heat control is highly demanding [Shiao *et al.,* 2005]. Semiconducting metal oxides preferably antimony tin oxide, tin oxide, indium tin oxide, aluminium oxide, zinc oxide, titanium dioxide, or a mixture thereof is earlier reported in literature for obtaining NIR reflecting transparent coatings [Hwang *et al.,* 2013; Mastai *et al.,* 2001; Park *et al.,* 2010]. Such nanosized metal oxides have regular structure whose equal intermolecular spaces block a large portion of light in the infrared region due to the presence of metal bonds. Composite structures made out of a material with high solar reflectance (ability to reflect sunlight) and high thermal emittance (ability to radiate heat) stay cool in the sun, which in turn reduces the demand for usage of air-conditioners and thereby lower the emission of CO_2 and use of electrical energy.

Nano ZnO has been well known for its multifunctional properties like solar reflectance, UV absorbance, antibacterial/antifungal, and hydrophobic functional properties [Raghupathi *et al*., 2011]. Incorporation of NIR shielding nano ZnO in PMMA polymer matrix produces functional nanocomposites which can be a better way to make effective solar thermal control interface structures. ZnO/PMMA exhibits an ensemble of

properties of its constituents, and ultimately offer thermo-mechanically stable, UV/NIR shielding multifunctional hybrid materials. Such UV/NIR shielding nanocomposite films and layers find applications in fabricating sandwich glass panels, glazed roofs, and active functional fillers in high-performance paints as described in the previous Chapter.

In this chapter, bulk nano ZnO was synthesized first by reflux and microwave methods using polyethylene glycol 300 (PEG 300), polyvinylpyrrolidone (PVP), N-cetyl-N,N,N-trimethylammonium bromide (CTAB) as capping agents. The end products were characterized for phase purity, particle size, morphology and UV/NIR optical properties. Morphologically varied nano ZnO was subsequently employed for fabricating ZnO/PMMA and ZnO/PMMA/polyurethane (PU) nanocomposite films. The NIR reflectance properties of these films were studied and correlated with ZnO morphological features.

2.2. EXPERIMENTAL SECTION

2.2.1. Materials

Zinc acetate dihydrate ($Zn(CH_3COO)_2.2H_2O$, Merck, India, 99%) and sodium hydroxide (NaOH, Merck, India, 99%) were used as chemicals. Polyvinylpyrrolidone (PVP, SD fine chem.), polyethylene glycol 300 (PEG 300, Merck), N-cetyl-N,N,N-trimethylammonium bromide (CTAB, Analytical Rasayan) were selected as capping agents. Poly(methyl methacrylate) (PMMA, Sigma- Aldrich, India) and polyurethane (PU, commercial paint Sleek) were employed as polymers. Dichloromethane (DCM, Analytical Rasayan) and ethanol were utilized as solvents. All chemicals were used without any further purification. Double distilled water was used as the medium for particle synthesis.

2.2.2. Synthesis of ZnO Nanoparticles

Zinc oxide nanostructures were synthesized by two different methods; reflux and microwave-assisted nucleation and growth process. The typical procedures followed in these are described below:

2.2.2.1. ZnO Nanoparticles *via* Conventional Reflux Method

In reflux method, 0.1 M zinc acetate dihydrate [$Zn(CH_3COO)_2.2H_2O$] solution was prepared in 200 mL distilled water. To this solution, 15 mL of PEG 300 was added dropwise under constant stirring. The reactant mixture was stirred well until it became chemically homogeneous solution. It was then refluxed at 80 $^{\circ}$C for 2 h. After 2 h the reaction flask was cooled to ice cold temperature. 1 M NaOH solution was then added dropwise under vigorous stirring until a milky white precipitate was formed (pH~10). The molar ratio of $Zn(CH_3COO)_2.2H_2O$ to NaOH was fixed as 1:10. The final white product was separated by centrifugation, subsequently washed several times with distilled water and finally with ethanol, and then dried at 60 $^{\circ}$C in the electrical oven for 24 h. By changing PEG 300 with PVP and CTAB, the nano ZnO was prepared under the same experimental conditions. In PVP and CTAB capping, 20 mL and 2 g were added respectively to the 0.1 M Zn^{2+} precursor solutions.

2.2.2.2. ZnO Nanoparticles *via* Microwave Method

The preparative conditions were maintained similar to reflux technique. Instead of reflux, in microwave method 0.1 M zinc acetate dihydrate [$Zn(CH_3COO)_2.2H_2O$] solution containing 15 mL PEG was subjected to microwave energy at a power level of 300 W for 30 min. Once the microwave irradiation was complete, the $Zn(OH)_2$ precipitate was cooled to ice cold temperature in an ice bath. The white product thus obtained was separated by centrifugation, washed with distilled water and ethanol, finally dried at 60 $^{\circ}$C in an oven to collect ZnO nanoparticles. The experiment was repeated with 20 mL PVP and 2 g CTAB to obtain ZnO particles with different morphologies.

2.2.3. Mechanism of Nano ZnO Synthesis

The possible chemical reactions involved in the nucleation and growth of nano ZnO particles in reflux and microwave heating is represented as follows:

$$Zn(OAc)_2 + 2NaOH = Zn(OH)_2 + 2NaOAc$$

$$Zn(OH)_2 + 2OH^- \rightarrow Zn(OH)_4^{2-} \text{ (Intermediate step)}$$

$$Zn(OH)_2 \rightarrow ZnO + H_2O \text{ (Reflux or Microwave)} \quad (2.1)$$

The ZnO prepared under microwave and reflux techniques using PEG, PVP and CTAB capping agents were designated as MW_Uncapped, MW_PVP, MW_PEG and MW_CTAB and Ref_Uncapped, Ref_PVP, Ref_PEG and Ref_CTAB respectively.

2.2.4. Fabrication of ZnO/PMMA Nanocomposite Films

Nano ZnO/PMMA composite films were prepared by solution casting technique [Eita *et al.,* 2012b]. 10% PMMA solution was prepared in dichloromethane solvent. 0.1 wt% nano ZnO was also separately dispersed in dichloromethane. Both solutions were mixed mechanically at room temperature until a viscous and homogeneous ZnO/PMMA solution was formed. The solution was transferred to glass mould and allowed to dry at normal room temperature. After a particular period of time, a free-standing ZnO/PMMA sheets were formed. Finally, they were removed from the glass mould and used for further characterizations. Using polyurethane, one set of ZnO/PMMA/PU films was also prepared for any comparison.

2.2.5. Characterizations

In this Chapter, ZnO nanoparticles were characterized by X-Ray Diffraction, Dynamic Light Scattering, Fourier Transform Infrared, Scanning Electron Microscopy, Transmission Electron Microscopy, and UV/Vis absorption analysis was carried out. The optical properties of ZnO/PMMA films were characterized by UV/Vis absorption and UV/Vis/NIR spectroscopic analysis. The brief procedures were explained given below:

The crystalline nature and phase purity of the as-prepared nano ZnO particles and films were structurally characterized by X-ray diffractometer using X'Pert Pro, Philips X-ray diffractometer equipped with CuK_{α} radiation (λ= 1.5406 A°) in the 2θ range 10° to 80° with 0.02 scan increment. Surface functional groups in ZnO nanoparticles were performed by IR Prestige-21, Shimadzu FTIR spectrophotometer in the scanning range of 4000-400 cm^{-1} using standard KBr (Sigma-Aldrich, 99%) pellet as the reference. The particle size distribution was measured using Dynamic Light Scattering (DLS) technique, a Zetasizer 3000H (Malvern Instruments, Worcestershire, UK) using a 60 mW He-Ne laser. For these measurements, ZnO nanoparticle (0.01 wt%) dispersion was prepared ultrasonically in the suitable solvent and subsequently de-agglomerated using Ultrasonic Processor P2 (Vibronics Pvt. Ltd., Bombay, India) and then size analysis was carried out.

The microstructure and morphological features of ZnO nanoparticles were examined using ZEISS EVO 18 Special Edition scanning electron microscope (SEM) operated at 20 kV. Nano morphology, chemical composition, and microstructure of the ZnO nanoparticle were further ascertained by Transmission Electron Microscopy (TEM) and selected area electron diffraction (SAED) analysis using the instrument FEI Tecnai 30G2S-TWIN transmission electron microscope operated at an accelerating voltage of 300 kV. A drop of colloidal nanoparticles was dispersed ultrasonically in acetone medium. It was carefully deposited by drop-casting on the TEM grid. After evaporation of the solvent, the surface was examined using TEM analysis.

UV/Vis absorption analysis of the ZnO nanoparticle dispersion and ZnO/PMMA nanocomposite films were monitored by Shimadzu UV/Vis Spectrophotometer (UV 240 IPC) in the wavelength region 200 to 800 nm. The near-infrared reflectance of the ZnO reinforced PMMA and also PMMA/PU/ZnO nanocomposite films were measured by a UV/Vis/NIR spectrophotometer (Shimadzu, UV-3600 with an integrating sphere attachment) using poly(tetraflouroethylene) (PTFE) as the reference. The typical experimental procedure as described in reference [Vishnu *et al.,* 2011] was followed for the diffuse reflectance measurements in UV/Vis/NIR regions. Firstly, a set of powder sample holders filled with PTFE was mounted on both the sample and reference sides of the exits port of the integrating sphere to set the baseline measurements. Secondly, the sample holder was filled with nano ZnO prepared in this work and the optical measurements were performed in the 700 nm to 2500 nm range for determining the reflectance property.

2.3. RESULTS AND DISCUSSION

2.3.1. Characterizations of Synthesized ZnO Nanoparticles

2.3.1.1. XRD Analysis of ZnO Nanoparticles

In Figure 2.1, the powder X-ray diffraction results for different nano ZnO are given. In both reflux and microwave heating techniques, the ZnO samples show excellent crystallinity. All the diffraction peaks are very sharp indicating the high degree of crystallinity. The diffraction lines are consistent with the standard values reported for the polycrystalline ZnO [JCPDS card No: 36-1451] providing clear evidence of the presence

of hexagonal wurtzite-type ZnO with space group of $P6_3mc$ [Espi *et al.,* 2007]. The X-ray diffraction pattern shows all the standard ZnO peaks correspond to (100), (002), (101), (102), (110) and (103) crystal planes. No diffraction peaks for any un-reactive $ZnAc_2.2H_2O$, $Zn(OH)_2$ and any other products were noticed, providing an idea of the purity of the ZnO products.

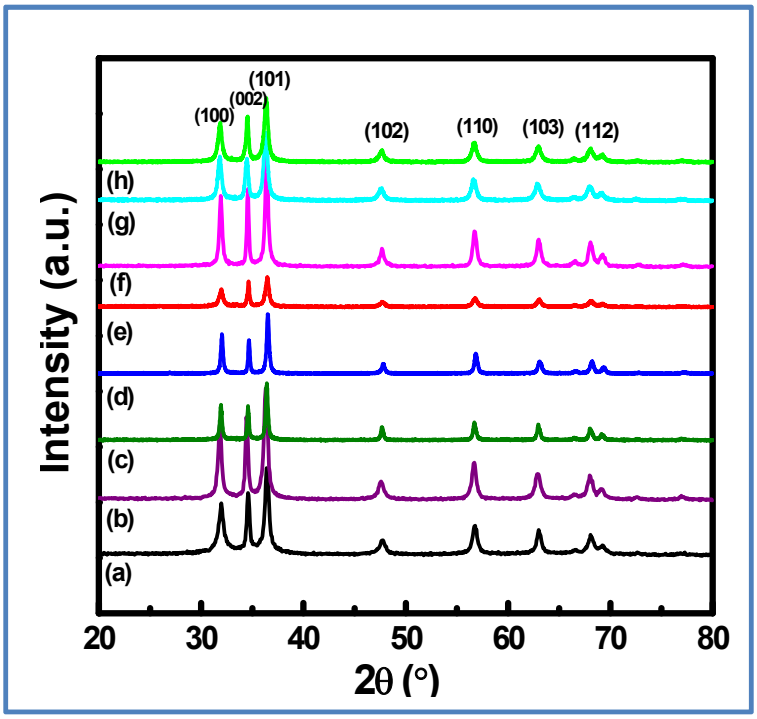

Figure 2.1: XRD patterns of ZnO nanocrystals at different synthesis conditions (a) MW_ PEG, (b) MW_ PVP, (c) MW_CTAB, (d) MW_Uncapped, (e) Ref_PEG, (f) Ref_PVP, (g) Ref_CTAB, and (h) Ref_Uncapped.

The average crystallite size of the as-prepared ZnO was determined using Debye-Scherrer's formula (Equation 2.2) [Wu *et al.,* 2011]. To determine the crystallite size, highly intense and sharp diffraction peak at $2\theta = 36.3^{\circ}$ corresponds to (101) diffraction of the ZnO hexagonal wurtzite phase was considered.

$$\text{Crystalline size } \langle D \rangle = 0.89\lambda/\beta\text{Cos}\theta \qquad (2.2)$$

where $\langle D \rangle$ is the average crystallite size, 0.89 is the Debye-Scherrer constant, λ is the CuK_α radiation wavelength (1.5406 A°), β is the full-width at half maximum in radians and θ is the scattering angle in degree. From the XRD data, the crystallite size was calculated as 21.3, 24.4, 28.4, 20.0, 34.2, 20.9, 23.2 and 35.9 nm for the ZnO samples

Ref_Uncap, Ref_PEG, Ref_PVP, Ref_CTAB, MW_Uncap, MW_PEG, MW_PVP and MW_CTAB, respectively.

2.3.1.2. Particle Size Analysis

The particle size distribution of the ZnO prepared *via* microwave and reflux methods are shown in Figure 2.2. The microwave technique resulted in a very wide size distribution for various capping agents compared to its counterpart, reflux method. The cluster size varied between 50 and 400 nm. The peak maximum represents the mean particle diameter of nano ZnO. The capping effect was distinctly noticed in microwave synthesis. ZnO prepared without capping produced particles with an average size 250 nm, whereas the particles obtained with PVP and PEG capping agents had shown size less than 180 nm. Although the PEG capping showed size controlled ZnO particles, the size distribution was not very narrow. However, in these cases, better control over crystal growth was seen compared to CTAB. In conventional heating, heat transport by conduction was the driving force that controls the mass transfer and deciding the ZnO crystal growth. In microwave, the bulk dielectric heating caused by the reversible dipole movements that happen at molecular level act as driving force [Cho *et al.,* 2008]. Water is a highly polar medium and microwaves readily interact with water molecules. As a result of kinetically strong reversible dipole interactions, the molecular heating takes place. The rate of thermal gradient in the reaction vessel depends on the microwave power. The thermal gradients occurred due to dipolar interactions vary with dielectric nature of the capping molecules. It strongly influenced the particle growth and the extent of ZnO clustering, finally resulting in wide size variations. In microwave synthesis, the samples MW_PVP and MW_PEG showed less particle size because of their stable complexation with Zn-precursor, and differential rate of nucleation [Anumol *et al.,* 2011]. In the reflux method, a narrow size distribution was successfully obtained. In this case, only a mild reflux temperature condition was employed. However, the reflux time given for the complete conversion of Zn-precursor to ZnO was longer. Unlike microwave heating, the mild heating highly controls the abnormal ZnO growth. However, as a result of prolonged time, the crystals had grown excessively to the size between 200-250 nm for various capping agents.

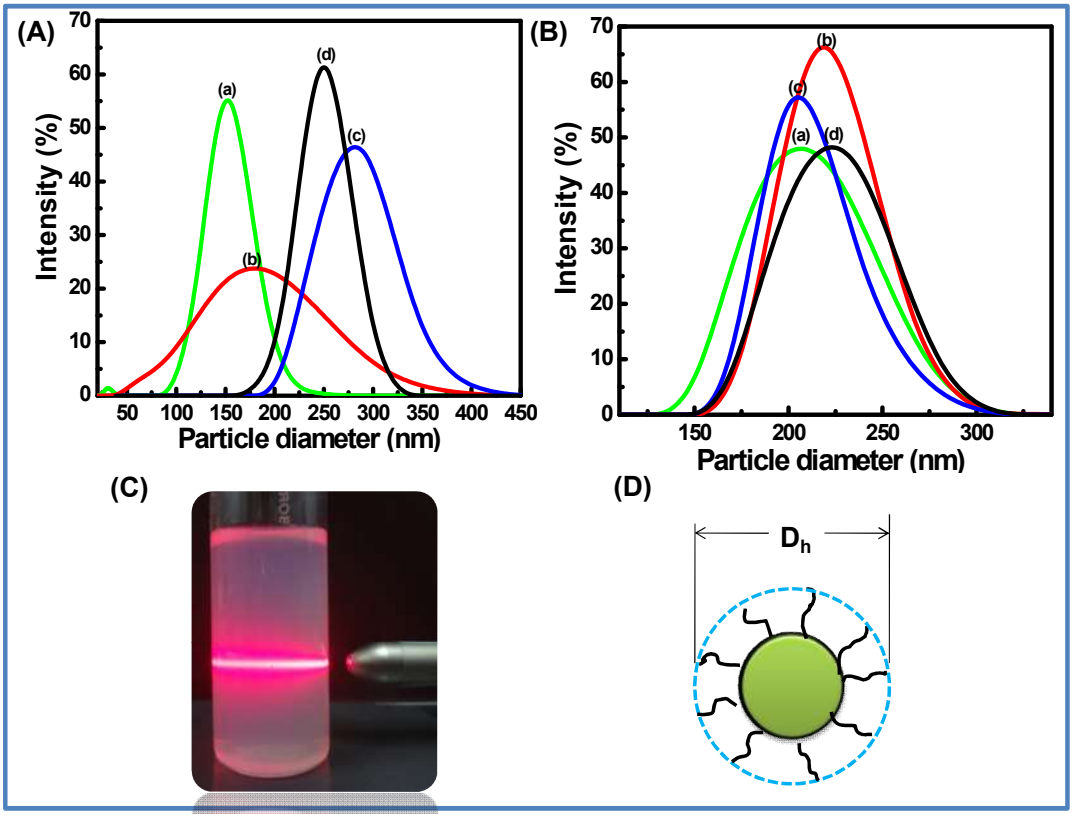

Figure 2.2: Particle size distribution analyses of (A) microwave synthesis: (a) MW_PVP, (b) MW_PEG, (c) MW_CTAB, and (d) MW_Uncapped; (B) reflux synthesis: (a) Ref_PVP, (b) Ref_PEG, (c) Ref_CTAB, and (d) Ref_Uncapped; (C) photographic image of capped ZnO NPs shows Tyndall effect; (D) schematic representation of surface capped ZnO NPs (where D_h is the hydrodynamic diameter).

2.3.1.3. Functional Group Analysis

The uncapped and capped ZnO nanoparticles synthesized using microwave and reflux methods were validated by the vibrational spectroscopy for understanding the nature of the chemical bonding in the metal oxide. The FTIR spectra of the PEG 300, PVP and CTAB capped nano ZnO and uncapped counterpart is shown in Figure 2.3 for the microwave and reflux methods.

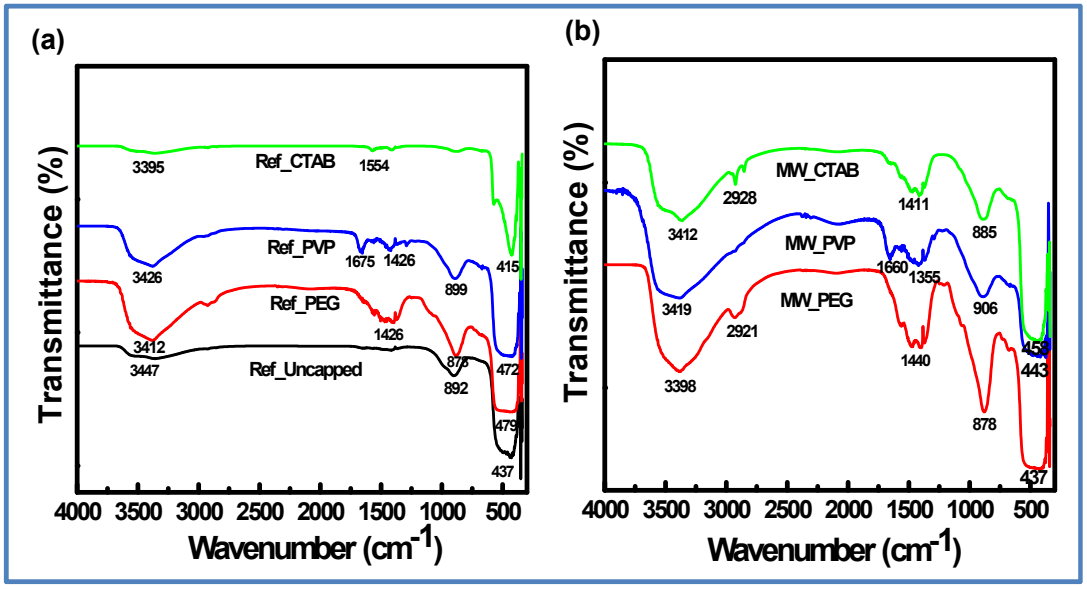

Figure 2.3: FTIR spectra of microwave and reflux techniques of as-prepared Ref_Uncapped, Ref_PEG, Ref_PVP, Ref_CTAB, MW_PEG, MW_PVP, and MW_CTAB samples dried at 60 °C/24 h.

In FTIR, the broad vibrational bands in the range 3342 to 3389 cm^{-1} represent the O-H stretching which was expected because of aqueous synthesis and mild drying conditions. In PVP and PEG capped samples, the O-H stretching was more prominent because of their more hydrophilic nature. The peaks at ~1400-1600 cm^{-1} indicate the C=O and O-H stretching vibrations of the capping molecules adsorbed on the ZnO surface. In the case of pure PVP [Kang *et al.,* 2009], the strong peak at 1654 cm^{-1} is assigned to the stretching vibration of carbonyl group and the peak at 1292 cm^{-1} is attributed to –C-N vibrations. But in PVP capped ZnO, the C=O stretching is shifted to ~1675 cm^{-1} confirming the capping effect. The alkyl C-H stretching vibration of PVP is seen at 2914-2919 cm^{-1} whereas the pyrrolidone ring related bands exist at ~1426 cm^{-1}. The characteristic stretching mode of Zn-O vibration bands normally seen at low absorption peaks in the range 415 to 448 cm^{-1} [Yang *et al.,* 2011]. In this study, the IR vibrational bands show significant differences in the peak values with respect to the given processing conditions of capping, microwave and reflux synthesis. The characteristic stretching bands of ZnO appear at 415, 437, 472, and 479 cm^{-1} depending upon the synthesis and capping agents. It provided further insight that even though a highly crystalline ZnO was formed at all the given synthesis conditions; they may have crystallographically different growth patterns and orientations leading to morphologically tuned ZnO particles with various

surface features [Raula *et al.,* 2010]. Figure 2.4 shows the chemical bindings of different capping agents on ZnO surface.

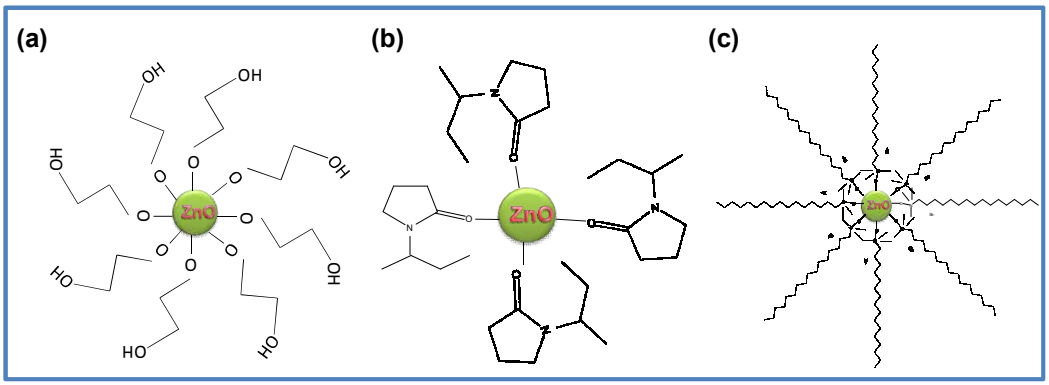

Figure 2.4: Chemical bindings of capping agents on ZnO (a) PEG-ZnO, (b) PVP-ZnO, and (c) CTAB-ZnO bindings.

2.3.1.4. Morphological Analysis of Capped ZnO Nanoparticles

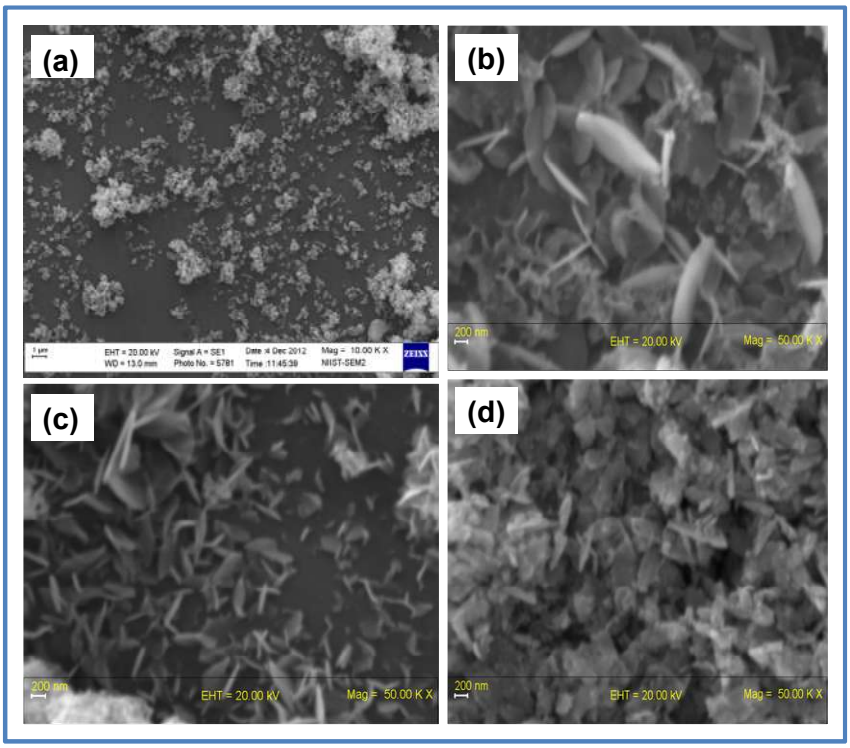

Figure 2.5: SEM images of ZnO nanoparticles by MW method: (a) Uncapped, (b) PEG 300, (c) PVP, and (d) CTAB (Scale bar: (a) 1 µm, (b) 200 nm, (c) 200 nm, (d) 200 nm).

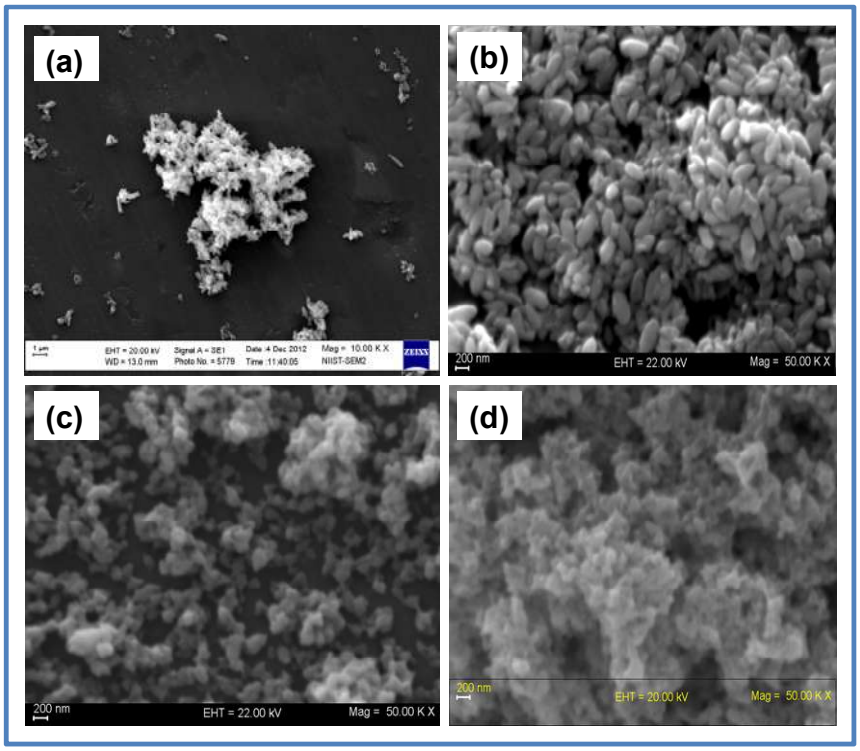

Figure 2.6: SEM images of ZnO nanoparticles by reflux method: (a) Uncapped, (b) PEG 300, (c) PVP, and (d) CTAB (Scale bar: (a) 1 μm, (b) 200 nm, (c) 200 nm, (d) 200 nm).

This had been further verified with SEM microstructures. The SEM morphologies correspond to various ZnO products are shown in Figure 2.5 and Figure 2.6. The morphology changed entirely with reflux and microwave techniques for the same capping agents. In general, the different crystal growth can be attributed to the change in the surface tension of the reactants solution, length of the molecular chains in the polymeric capping agents, and the strong nature of the complex formation. The uncapped ZnO nanoparticles in reflux method have weakly agglomerated ZnO whiskers morphology and the same in microwave method were spherical clusters. The capping agents completely altered the directional growth of the ZnO crystals and their orientations. Capping with PVP observed semi-spherical shaped ZnO nanoparticles in reflux method and nanoflake structures in microwave technique. The capping agent PEG 300 resulted in rice shaped ZnO in reflux method and the same attained nano-sheet like structure in microwave. ZnO morphology was quite different when CTAB was used. In this case, ZnO nanoneedles and nanoplatelets were obtained in reflux and microwave methods respectively. The effect of capping agents on the growth of ZnO nanocrystals has been examined by numerous researchers [Biswas *et al.,* 2008; Viswanatha *et al.,* 2006]. The dispersed Zn^{2+} ions in

water quickly reacted with the OH^- ions to form the insoluble $Zn(OH)_2$, which tends to be a cloudy milky solution. It reacted with capping molecules to form respective primary parent oxy-hydroxide [$ZnO\text{-}Zn(OH)_2$] complex species. The size and shape of the complex moiety determine the crystal growth directions and orientations and hence the final shapes formed. With PVP addition, the viscosity of water in the solution increased and in result caused a slow diffusion of ions and hence the rate of reaction of Zn^{2+} ion with the hydroxide ion decreased [de Dood *et al.,* 2003], which resulted in the suppressed growth of the ZnO nuclei resulting in semi-spherical and flaky particles.

2.3.1.5. TEM Analysis of ZnO Nanoparticles

The TEM analysis further revealed clearly the extent of the crystallinity, actual size, shape, and growth patterns of the ZnO particles at nano-regime with high degree of accuracy. Figure 2.7 shows respective TEM images of the uncapped, PEG 300, PVP, and CTAB capped ZnO particles obtained through microwave and reflux methods. In microwave technique; spherical, sheet, flake and platelets shaped morphologies were confirmed, whereas in reflux technique; whiskers, rice-like grains, semi-spherica,l and nanoneedles morphologies obtained. The TEM images confirm structurally uniform, nano dimensional ZnO particles having size ranges 50-100 nm. The SAED patterns of the representative ZnO samples revealed the single crystalline nature.

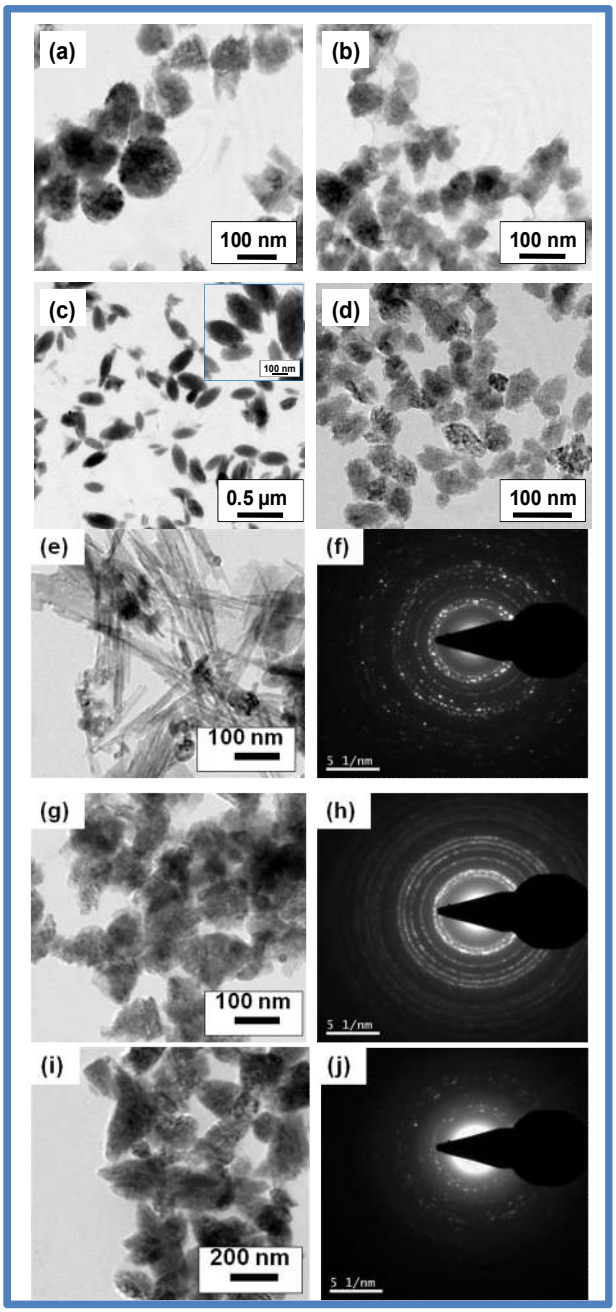

Figure 2.7: TEM images of (a) Ref_PVP, (b) MW_PVP, (c) Ref_PEG (inset 100 nm scale bar), (d) MW_PEG, (e) Ref_CTAB, (g) MW_CTAB, and (i) Ref_Uncapped. SAED patterns of (f) Ref_CTAB, (h) MW_CTAB, and (j) Ref_Uncapped.

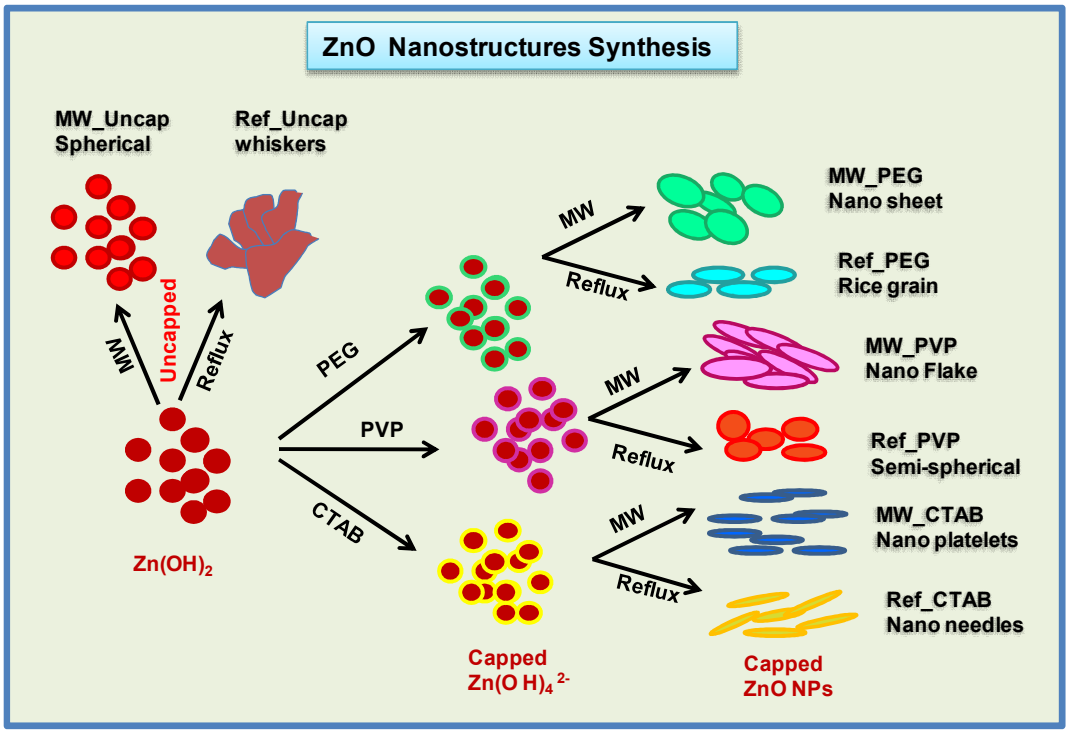

Figure 2.8: Schematic representation of growth mechanism of ZnO nanoparticles using different capping agents and synthetic methods.

Figure 2.8 shows the schematic representation of growth mechanism of ZnO nanoparticles using different capping agents and synthetic methods. The role of PEG in controlling the shape and size of nano ZnO was also studied and reported earlier [Shi *et al.,* 2009]. Water soluble PEG 300 with molecular structure HO-(CH_2-CH_2-O-)$_n$-H is mostly preferred for capping. The -OH group is at the chain ends, and the chain is formed by the repetition of the ethylene oxide group. Such type of capping molecules will bind to the growth units of ZnO nuclei. In presence of PEG 300, the Zn^{2+} ion is easily adsorbed on the oxygen site of the C-O-C chain. When Zn^{2+} interacts with PEG 300 polymer matrix, the polymer chains containing Zn^{2+} neutralize with hydroxide ions to produce the PEG-$Zn(OH)_2$ complex [Feng *et al.,* 2010]. Upon microwave irradiation and reflux heating, the PEG-$Zn(OH)_2$ complex dehydrates to form ZnO nuclei and the C-O-C chains decide the growth directions. Although both PEG 300 and PVP are non-ionic capping agents, they would be partially-charged. Especially oxygen in PVP is more partially charged than oxygen in PEG because of positively-charged nitrogen in PVP [Panigrahy *et al.,* 2009]. Therefore PVP would electrostatically adhere to the surface of ZnO nuclei stronger than

PEG 300 resulting in different shapes. Using CTAB as cationic capping agent, nanoneedle and nanoplatelets shaped ZnO were obtained in reflux and microwave methods. Since CTAB is a kind of strong-acid-weak-base salt, it can accelerate the ionization of $[Zn(OH)_4]^{2-}$ [Zhang *et al.,* 2004]. The $[Zn(OH)_4]^{2-}$ anion and cationic CTAB form CTA^+-$[Zn(OH)_4]^{2-}$ ion pairs. Due to the coulomb force action, $[Zn(OH)_4]^{2-}$ anions and CTA^+ cations electrostatically interact to form CTA^+-$[Zn(OH)_4]^{2-}$ complexing agents which get adsorbed on the environs of the ZnO nuclei. As a result of this, the surface tension of the reactants as well as the surface energy of ZnO nuclei is decreased. At these favorable conditions, ZnO nuclei transform to ZnO crystals at lower saturation temperatures resulting in the formation of long and uniform ZnO nanoneedles and nanoplatelets [Sun *et al.,* 2002].

2.3.1.6. UV/Vis Absorption Analysis

The UV/Vis absorption properties of all the nano ZnO products prepared *via* microwave and reflux techniques with different capping agents are shown in Figure 2.9.

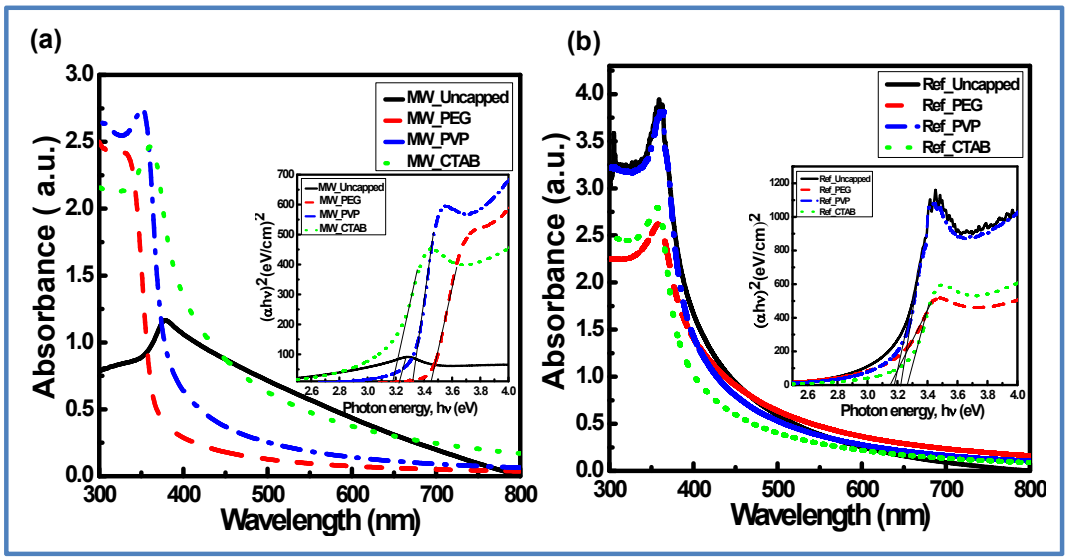

Figure 2.9: UV/Vis spectra of ZnO nanoparticles (inset shows the optical absorption spectra for photon energy in terms of eV) synthesized under reflux and microwave route using uncapped and different capping agents PEG 300, PVP and CTAB.

The as-prepared nanoparticles were ultrasonically dispersed in water medium and the colloids were examined for the UV-absorption using water as the reference. The absorption was corrected for the solvent distribution. The excitonic absorption spectrum

of ZnO nanoparticles showed well-defined excitation band between 334-364 nm depending upon the size and shape of ZnO crystals formed with various capping agents in both microwave and reflux methods. This absorption curves showed blue-shift by the quantum confinement effect compared to the bulk ZnO excitation absorption at 380 nm (band gap energy E_g = 3.26 eV). In both cases, the UV absorption was very sharp, which indicated the monodispersed nature of the ZnO nanoparticles [Pueyo *et al.,* 2008]. This is, in fact, supportive to the TEM images where a high degree of monodispersity of nanoparticle distribution was seen. The size of the ZnO nanoparticle and its concentration in the solution were also calculated from the absorption studies. L.E. Brus proposed the relationship between the band gap of nanoparticle E and particle radius r which is given by:

$$E \cong E^{bulk} + \hbar^2\pi^2/2er^2(1/m_em_o+1/m_hm_o)\text{-}1.8e/4\pi\varepsilon\varepsilon_0r \quad (2.3)$$

where E^{bulk} is bulk band gap, $\hbar$ is Planck's constant divided by 2π, e is elementary electric charge, m_e is the electron effective mass, m_h is hole effective mass, m_0 is electron mass, ε is relative permittivity, and ε_0 is the permittivity of vacuum. The following equation was used to calculate the particle size (radius) [Brus, 1968; Hu *et al.,* 2003].

$$r\ (\text{nm}) = -0.3049+\sqrt{(-26.23012+10240.72/\lambda_p)}/(-6.3829+2483.2/\lambda_p) \quad (2.4)$$

The above equation is derived using the effective mass model which described the particle size (r, radius) as a function of peak absorbance wavelength (λ_p) in nm for ZnO nanoparticles. The data extracted from the UV/Vis absorbance spectra was used to calculate the average size (D) of ZnO nanoparticles according to the expression proposed by Meulenkamp [Meulenkamp, 1998] as follows:

$$1240/\lambda_{1/2} = 3.301 + 294.07/D^2 + 1.09/D \quad (2.5)$$

where $\lambda_{1/2}$ (nm) is the wavelength corresponding to the absorption profile at the half-height of the intensity and D is the particle diameter (nm) [Huang *et al.,* 2010]. The inset of the Figure 2.9 showed its photon energy in terms of electron volt which was used to find out the band gap energy with respect to absorption measurement. The wurtzite ZnO structure possessed a direct band gap and the absorption edge for a direct interband transition is given by Serpone *et al.* [Serpone *et al.,* 1995].

$$(\alpha h\nu)^2 = E_D\,(h\nu - E_g) \quad (2.6)$$

where α is the optical absorption coefficient, h is the Planck's constant, ν is the frequency of incident photon, E_D is a constant and E_g is the direct band gap energy. In this study, the absorption coefficient (α) could be evaluated by the following equation [Zhao *et al.,* 1991]

$$\alpha = A/d_s' \quad (2.7)$$

where A is the measured absorbance and d_s' is the thickness of the sample in UV/Vis cell (0.4 cm).

The plot of $(\alpha h\nu)^2$ versus photon energy ($h\nu$) for the morphologically varied ZnO nanoparticles was obtained in both microwave and reflux syntheses. The linear dependence of $(\alpha h\nu)^2$ on $h\nu$ at higher photon energies indicated that the capped ZnO nanoparticles are essentially a direct transition type semiconductor. The linear portion of the curve when extrapolated to zero gave the value of the direct band gap (E_g) corresponding to the morphologically varied ZnO nanoparticles depending upon the capping molecules. According to the results from this figure**,** the E_g values of the uncapped ZnO nanoparticles are about 3.22 and 3.40 eV for microwave and reflux methods respectively. The E_g values of the MW_PEG, MW_PVP and MW_CTAB obtained are 3.71, 3.32 and 3.45 eV respectively. Similarly, the E_g value of the Ref_PEG, Ref_PVP and Ref_CTAB resulted as 3.46, 3.41 and 3.48 eV respectively. The blueshift behaviour or broadening in the band gap is mainly due to the Moss-Burstein band filling effect [Shan *et al.,* 2004]. Based on the Moss-Burstein theory, for the samples MW_PEG, MW_PVP, the donor electrons occupied states at the bottom of the conduction band. The average crystalline size of nano-sized ZnO powders can be figured out by using the following equation [He *et al.,* 2008]:

$$S_{BET} = 6000/\rho d_{BET} \quad (2.8)$$

where S_{BET} is the BET specific surface area (in m^2/g), ρ is the density of nanosized ZnO powder (in g/cm^3) and d_{BET} is the crystalline size (in nm). In this study, S_{BET} was obtained by using the 5.605 g/cm^3 power density. The agglomeration coefficient can be calculated using the following formula:

$$C_F = d_{BET}/\langle D \rangle \quad (2.9)$$

Here, C_F is agglomeration coefficient and <D> is the crystallite size from the XRD Scherrer formula. From the aforementioned mathematical equations, the particle diameter ($2r$), agglomeration coefficient (C_F), and surface area (S_{BET}) were determined for the different ZnO samples and summarized in Table 2.1.

Table 2.1: Morphologies, dimensional size and band gap of nano ZnO obtained for different capping agents.

ZnO Samples	Morphology	DLS $2r$ (nm)	<D> (nm)	$2r$ from Eq.(2.4) (nm)	C_F	S_{BET} (m^2/g)	UV λ (nm)	E_g (eV)
Ref_Uncap	Whiskers	223	21.29	4.8958	0.11499	219	364	3.40
Ref_PEG	Rice grain	218	24.41	4.4679	0.18300	240	358	3.46
Ref_PVP	Semi spherical	206	28.39	4.8165	0.16968	222	363	3.41
Ref_CTAB	Nano needles	205	20.04	4.2830	0.21370	250	355	3.48
MW_Uncap	Spherical clusters	250	34.23	4.7357	0.13835	226	362	3.22
MW_PEG	Nano sheets	178	20.98	3.4228	0.16315	313	334	3.71
MW_PVP	Nano flakes	153	23.24	4.1816	0.17995	256	353	3.32
MW_CTAB	Nano platelets	281	35.92	4.8161	0.13406	222	363	3.45

2.3.2. Fabrication of ZnO/PMMA Nanocomposite Films

Nano ZnO/PMMA composite films were characterized by XRD analysis, UV/Vis absorption spectra and near-IR reflectance spectra.

2.3.2.1. Phase Analysis of ZnO/PMMA Nanocomposite Films

Figure 2.10 shows XRD patterns of the ZnO/PMMA nanocomposite films. A broad peak in the range of 15–25° confirms the amorphous nature of the PMMA matrix [Kos *et*

al., 2013]. In the case of the nanocomposite films, the trends are almost the same regarding the PMMA peaks, while subsequent peaks of the ZnO NPs also appear at their respective locations. The intensity of the ZnO NPs peaks is quite less in PMMA matrix, as the concentration of the nanoparticles is very low (0.1 wt%) in the PMMA films.

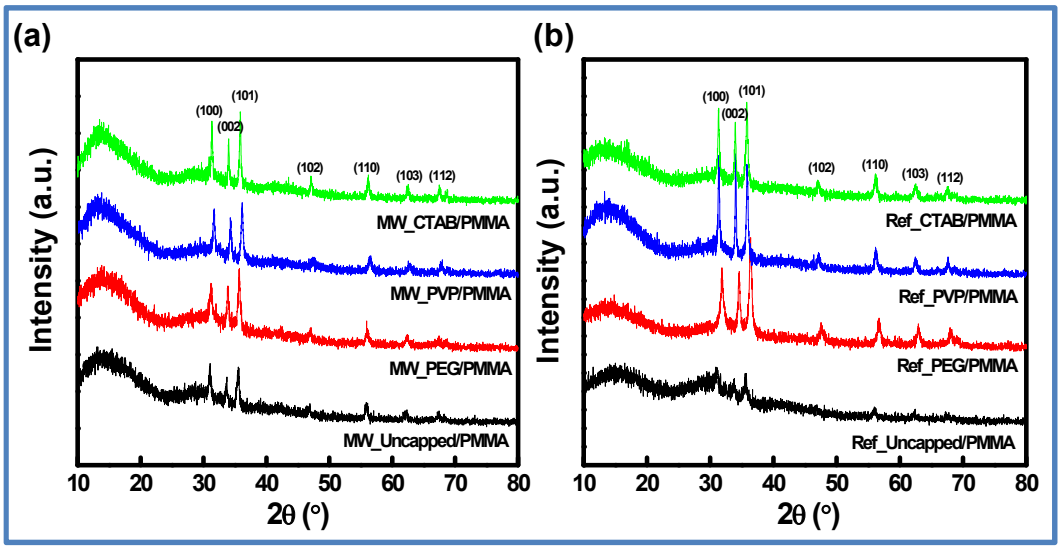

Figure 2.10: XRD patterns for ZnO/PMMA nanocomposite films using (a) microwave and (b) reflux methods.

2.3.2.2. UV/Vis Spectra Analysis of ZnO/PMMA Nanocomposites

The UV absorption properties of nano ZnO cover both UVB and UVA ranges. For this reason, the prepared PMMA/ZnO nanocomposites were also tested for the UV-shielding efficiency. Figure 2.11 shows the effect of ZnO addition in PMMA polymer film on the UV absorbance. The absorption range of pure PMMA was seen at the wavelength of 300 nm which was close to the window glass and also commercially available and purchased bulk ZnO (Sigma-Aldrich, India), denoted as Ald_ZnO; dispersed in PMMA at 380 nm. When as-prepared, using microwave method, ZnO nanoparticles were dispersed well and the absorption shifts to wavelengths in ranges 350, 375 and 379 nm for the PEG 300, PVP and CTAB as capping agents, respectively. The absorption ranges 350 to 380 nm indicate the UV shielding efficiency of microwave and reflux derived ZnO in both UVA and UVB ranges [Liu *et al.,* 2012a]. In PMMA nano composite fabricated with PEG capped ZnO nanoparticle, a slight blue-shifting was seen in the absorption that was due to relatively small size of the ZnO particles. In this work, fabrication of thin film PMMA sheets with thickness 0.04 mm is engineered with capped

nano ZnO and polyurethane additive for normal solar light transmittance but capability to shield NIR and UV radiations.

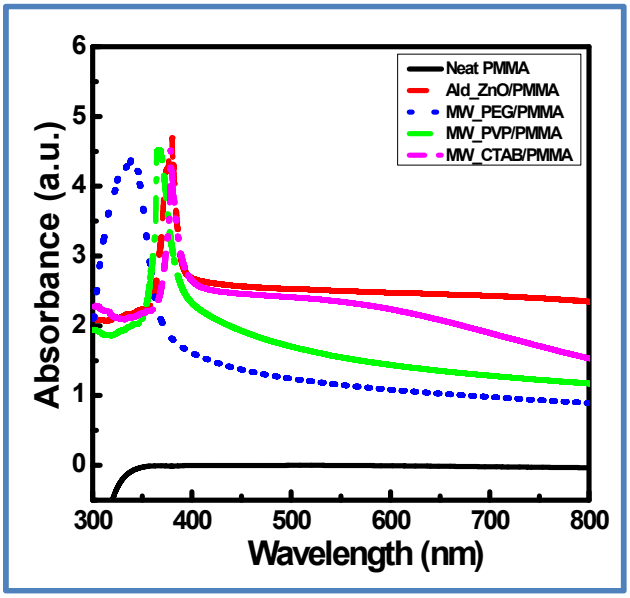

Figure 2.11: UV/Vis absorbance spectra of ZnO nanoparticles embedded in PMMA matrix.

2.3.2.3. Near-Infrared (NIR) Reflectance Analysis of ZnO/PMMA Nanocomposites

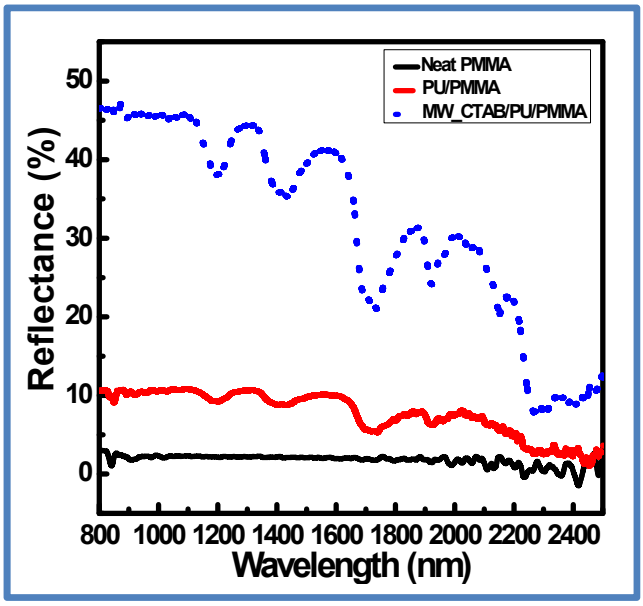

Figure 2.12: NIR reflectance of neat PMMA, PU/PMMA and ZnO/PMMA/PU films.

A comparison of the NIR reflectance properties between PMMA and PMMA/PU nanocomposite sheets dispersed with ZnO nanoparticles prepared with various capping agents is given in Figure 2.12 and Figure 2.13. In general, 100% Incident Light = Total Reflectance (%) + Absorbance (%) + Total Transmittance (%), where Total Reflectance (%) = Diffuse Reflectance (%) + Specular Reflectance (%), and Total Transmittance (%) = Diffuse Transmittance (%) + Specular Transmittance (%).

The diffuse reflectance data, without including the specular reflectance, given by the instrument SHIMADZU UV/Vis/NIR spectrophotometer [UV-3600] in the wavelength region 800 to 2500 nm is directly plotted for the PMMA films which were prepared with only 0.1 wt% ZnO particles. Figure 2.12 depicts NIR reflectance of neat PMMA and PMMA having Polyurethane additive. In both these cases, the NIR reflectance is very poor, and only <10% is observed. Upon 0.1 wt% dispersion of ZnO [sample prepared with CTAB surfactant under microwave], the PMMA/PU films attain NIR reflectivity above 40%.

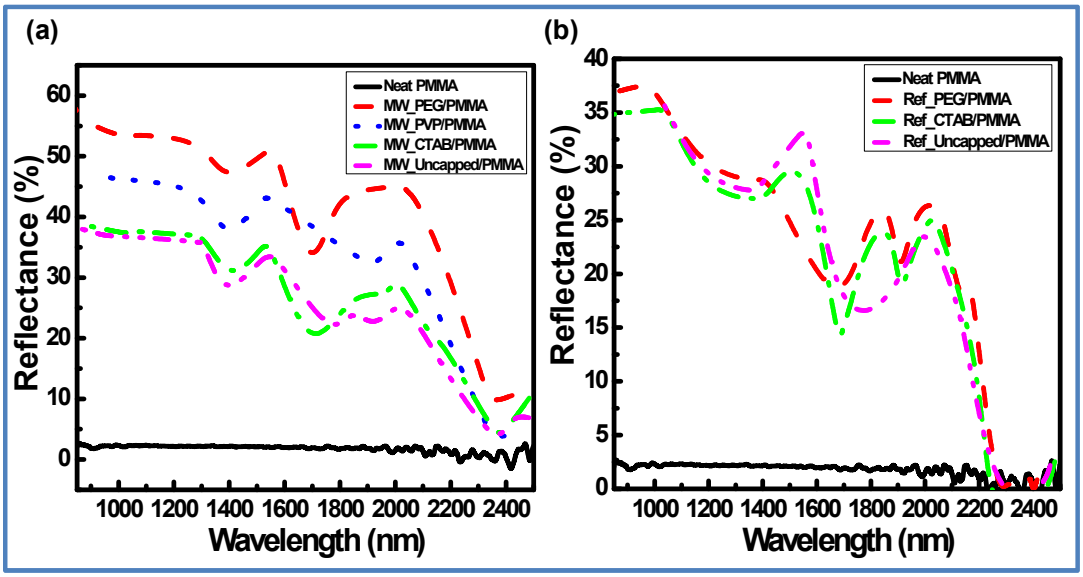

Figure 2.13: NIR reflectance of (a) microwave method synthesis of ZnO/PMMA films with and without different capping agent and (b) reflux method synthesis of ZnO/PMMA films with and without different capping agent.

Figure 2.13(a) and Figure 2.13(b) is only the comparison of PMMA films dispersed with various ZnO particles obtained *via* microwave and reflux techniques. The

microwave derived ZnO shows better NIR reflectivity than the reflux counter parts. In the NIR reflectance spectra, low reflectance means high absorption in that wavelength region. In general we have noticed very strong absorptions in the wavelength regions 1300-2500 nm. These strong absorptions arise from the combination and overtones of fundamental processes that occur in the mid-IR region ($\lambda > 2500$ nm) [Du *et al.,* 1999]. The composites prepared with microwave derived ZnO showed better NIR reflectance compared to its reflux counterpart at NIR wavelengths 810 and 1100 nm. PMMA film prepared without any ZnO was optically transparent but it showed only 2% reflectivity in the entire NIR region indicating the highest absorption of NIR by the PMMA matrix. Similarly in case of PU/PMMA polymer composites, the control sample prepared without any ZnO, provided only below 10% NIR reflectance. When the PMMA and PMMA/PU films were prepared with only 0.1 wt% nano ZnO, a high degree of NIR reflectivity was observed. The PMMA/ZnO nanocomposites showed the bulk NIR reflectivity in the range 40 to 60% depending upon the ZnO size and shape. The same was increased to 45% in PU/PMMA/ZnO nanocomposites. The % NIR reflectance was taken directly at the wavelengths 810 and 1100 nm on the 0.04 mm thick PMMA films and is summarized in Table 2.2 for various ZnO. The physical appearance of ZnO/PMMA and ZnO/PU/PMMA was also given for showing the optical transparency [Figure 2.14].

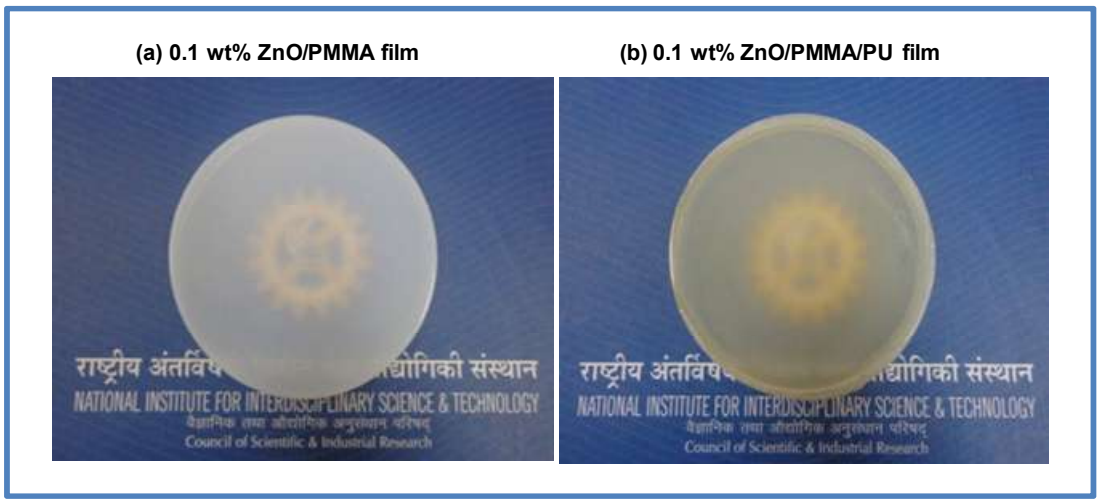

Figure 2.14: Photographic images of (a) ZnO/PMMA and (b) ZnO/PU/PMMA films.

Table 2.2: The (%) NIR reflectance of ZnO/Polymer sheets @ 810 and 1100 nm NIR wavelengths.

ZnO/Polymer Nanocomposite	**(%) NIR Reflectance @ 1100 nm**	**(%) NIR Reflectance @ 810 nm**
Neat PMMA	2	2
MW_PEG/PMMA	53	55
MW_PVP/PMMA	46	48
MW_CTAB/PMMA	37	38
MW_Un capped/PMMA	37	38
Ref_PEG/PMMA	32	38
Ref_CTAB/PMMA	31	35
Ref_Uncapped/PMMA	32	38
PU/PMMA	11	11
MW_CTAB/PU/PMMA	45	48

The extent of NIR reflectivity strongly varied with the given processing and capping conditions. For example, the PMMA nanocomposite films have highest reflectivity to NIR when it was reinforced with PEG 300 capped ZnO. In microwave technique, it is determined as 55%. It is known that the NIR reflectance property highly depends upon the color of the inorganic fillers, their refractive index and crystalline qualities [Keefe, 2008]. TiO_2 and ZnO are the most preferred NIR reflecting pigments due to their attractive bright white and the wide optical refractive index values. The refractive index values for TiO_2 and ZnO were reported in the range 2.02 to 2.6. Depending upon the refractive index values, the light beam is refracted, reflected and scattered leading to diffuse reflection of NIR light. For an effective reflection of NIR-radiation, particle size was reported as essential parameter. For highest reflectivity, the particle size should be more than half the wavelength of the light to be reflected. Thus for reflecting infrared light of 700-1100 nm wavelength, particle size should be at least 0.35 to 0.55 microns [Bendiganavale *et al.,* 2008]. In this study, we obtained ZnO particles with varying physical dimensions and crystalline morphologies ranging from spherical to

flake and sheet. The overall physical size of the ZnO particles was found to be within 150 to 400 nm and 200 to 250 nm for microwave and reflux techniques respectively. Figure 2.13(a) shows the % NIR reflectance of PMMA/ZnO nanocomposites with respect to the ZnO particle size. The NIR reflectance at the wavelength 810 nm was taken for the comparison. From the figure, it is clear that the NIR reflectance increased with decreasing particle size. The ZnO samples prepared with PEG and PVP capping have mean size of 177 and 153 nm respectively in microwaves. These samples have shown high reflectance compared to other ZnO particles where the particle size was above 200 nm.

We have seen that such particle size range, say 150 to 170 nm, and were favorable for effectively reflecting the NIR rays. However, it appeared that, in addition to the particle size, a fine control of morphology is also important to shift the reflectance to a maximum value with minimum amounts of ZnO dispersion. The plot in Figure 2.15(a) confirms that among the obtained ZnO morphologies, nano sheets and flakes have better IR reflectance. The NIR reflectance @ 810 nm and 1100 nm were plotted against the ZnO morphologies and shown in Figure 2.15(b). All the morphologies showed high NIR reflectivity at 810 nm compared to the wavelength of 1100 nm. The ZnO nanosheets obtained for MW_PEG show 55% reflectance at 810 nm and about 53% at 1100 nm. Similarly, the nanoflake structure derived for the sample MW_PVP shows 48% reflectivity at 810 nm and 46% at 1100 nm. The NIR reflectivity was comparatively high for the nano ZnO having relatively large surface features. In sheet, flake and platelets, the surface area was high compared to its thickness which was only a few nanometers. The active surface available for the IR to interact with other ZnO morphologies such as semispherical, rice grain and whisker was comparatively less and therefore they exhibit poor reflectivity. Nanosheets showed the highest NIR reflectance followed by nanoflakes, nanoplatelets, spherical, rice grains, whiskers and nanoneedles. Moreover, these kinds of particle morphologies also vary in their degree of agglomeration. It also significantly influences the NIR reflectivity. In this work, the (%) NIR reflectance at the wavelengths 810 nm and 1100 nm was also plotted against the agglomeration coefficient of the various ZnO and is shown in Figure 2.15(c). Since the morphologies nano sheets and flakes had less tendency for agglomeration and clustering, these samples had higher NIR reflectance at both 810 nm and 1100 nm wavelengths. As evident from the SEM, the

other ZnO morphologies like nanoneedles and semispherical particles have higher agglomeration and exhibit poor NIR reflectance.

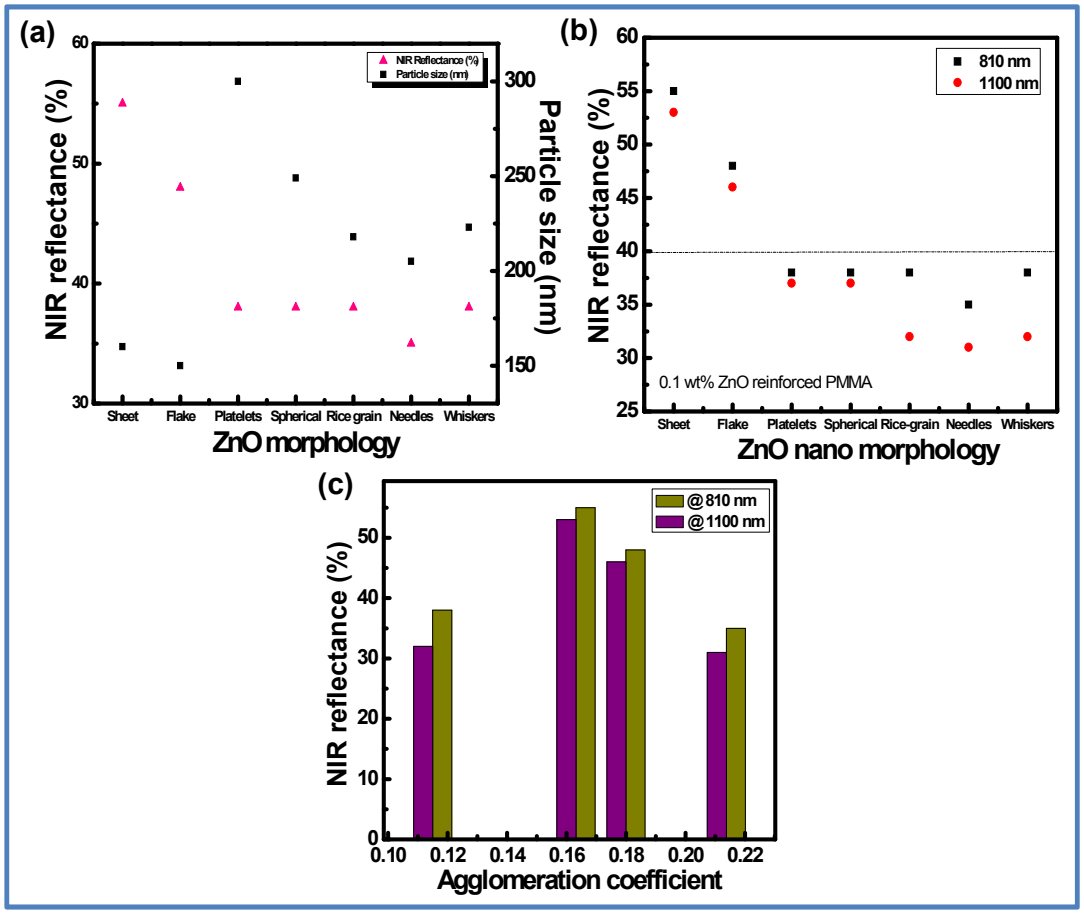

Figure 2.15: (a) NIR reflectance @ 810 nm *vs.* Particle size with respect to the ZnO morphology, (b) NIR reflectance @ 810 & 1100 nm *vs.* ZnO nano morphology, and (c) NIR reflectance *vs.* Agglomeration coefficient @ 810 & 1100 nm.

2.4. CONCLUSIONS

In summary, we report the NIR reflectance property of ZnO dispersed PMMA polymer nanocomposite films. The UV/NIR shielding property of PMMA polymer was correlated with various ZnO morphologies that differ in the average physical size and surface features. Highly crystalline, hexagonal wurtzite ZnO particles were successfully prepared *via* microwave and reflux techniques with various capping agents. These techniques produced ZnO with mean particle size in the range 150-400 nm. Morphologically varied nano ZnO having physical shapes such as spherical clusters, rice grains, needle and whiskers as well as one dimensional nano needles and sheets were obtained. This study revealed that in addition to the particle size of ZnO, the morphology and the crystalline quality also played equally an important role in obtaining better NIR/UV shielding quality. The microwave technique resulted in nano-thick one-dimensional sheet shape ZnO morphologies. Such nano thick sheet like particles had high surface sites that help to reflect the NIR effectively. The PMMA film without any ZnO had only 2% NIR reflectivity whereas the same was increased to 55% where 0.1 wt% ZnO was dispersed in the PMMA matrix. The high particle size of ZnO affected the optical transmittance strongly and resulted in highly opaque PMMA/ZnO nanocomposite films. The additions of small amount of polyurethane produced visibly clear PMMA/PU/ZnO sheets compared to PMMA/ZnO film. The NIR reflectance followed the order nanosheet > nanoflake > nanoplatelets > spherical > rice grain > whiskers > nanoneedles morphologies. The PEG 300 capped ZnO reinforced PMMA polymer film showed comparatively higher reflectance to NIR wavelength than the other capping agents. On comparing the results, the PMMA/ZnO and PU/PMMA/ZnO nanocomposites showed better UV/NIR shielding properties that can be explored as interface layers/films and membranes in glass and polymer type sandwich panels for the effective solar thermal controlled indoors of buildings.

The investigations of this Chapter have been published.

Soumya, S.; Mohamed, A. P.; Paul, L.; Mohan, K.; Ananthakumar, S., Near IR reflectance characteristics of PMMA/ZnO nanocomposites for solar thermal control interface films, *Solar Energy Materials & Solar Cells*, 125, **2014**, 102-112.

CHAPTER 3

Effect of Al-Doped ZnO Nanoparticles for UV/IR Shielding PMMA Polymer Coatings

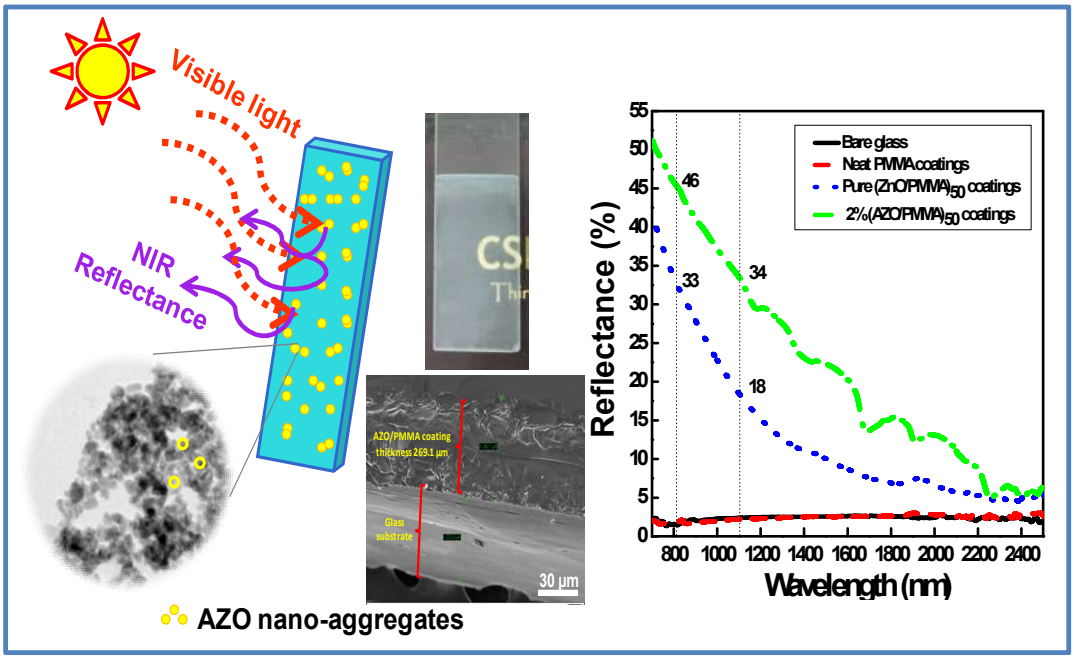

PREAMBLE

This chapter deals with the doping strategy to achieve optically transparent IR reflective top-coats on glass substrates. Aluminium doped nano ZnO (AZO) was synthesized and dispersed in PMMA precursor sol. Subsequently Layer-by-Layer coatings were developed on glass substrates. Functional properties such as UV absorption, and NIR shielding efficiency of the AZO/PMMA coatings were monitored with respect to number of layers. In addition to that the heat build-up control under infrared radiation was also recorded. The AZO/PMMA coating was also validated for the ice/fog formation resistance, self-cleaning, surface hardness and scratch resistance properties.

3.1. INTRODUCTION

NIR control surface coatings can curtail solar heat transfer through the glass and building surfaces [Viasnoff, 2014; Levinson *et al.,* 2007; Levinson *et al.,* 2010; Levinson *et al.,* 2005a; Viasnoff *et al.,* 2012]. Infrared radiation in the wavelength region 810 to 1100 nm is said to be the prime reason for the heat build-up, hence NIR reflecting white pigments are necessary for designing thermal control surface coatings and functional paints [Viasnoff, 2014; Zou *et al.,* 2014; Levinson *et al.,* 2005b; Guo *et al.,* 2011; Jiang *et al.,* 2013]. A few millimeter thick spraying of acrylic and polyurethane paints containing TiO_2 and ZnO white pigments shows NIR shielding which is in the form of coatings on concrete roofs found effective in decreasing the overall temperatures. Replication of such coatings on glass surfaces would result in cool-windows, provided a high optical transparency to the level of at least 95% is retained. Coatings made with nanoparticles offer high optical transparency combined with light reflectance quality [Viasnoff, 2014; Viasnoff, *et al.,* 2012; Mahlitig *et al.,* 2005].

Nanoscale inorganic white pigments such as rutile TiO_2, ZnO, CeO_2, and SnO_2, intrinsically have the high refractive index (n = 2.2 to 2.7) and contribute light-scattering at all wavelengths. They have a unique property of high solar reflectance in the NIR region and solar energy absorbance in UV region, which makes them ideal for multifunctional, optically transparent surface coatings. Among many metal oxides, nanostructured ZnO coatings offer multifunctional properties; they reflect more than 90% incident light near-infrared radiation while transmitting high-level solar light in the visible spectra. However, it is critical to have nanoparticles in size range ~350 nm for effective NIR shielding [Hwang *et al.,* 2013] where transparency is considerably decreased. ZnO is a well known semiconductor having a band gap of 3.37 eV, which makes it as a photoactive in the UV region for any self-cleaning functions [Fateh *et al.,* 2014; Minhao *et al.,* 2009; Kumar *et al.,* 2014; Giusti *et al.,* 2014; Qiu *et al.,* 2011]. ZnO coatings are also characterized for hydrophobic functionality [Gao *et al.,* 2014]. Recently published reports strongly indicate ZnO nanostructures can be tailored to have anti-icing or anti-frosting, and anti-fogging surfaces [Wang *et al.,* 2013b; Wen *et al.,* 2014]. Above all, ZnO is non-toxic and can easily be processed in different nanostructures which draw more attention to develop transparent window-glass coatings using nano ZnO [Kittler *et al.,* 2009].

In this context, we are investigating the role of particle size, particle morphology and dispersibility of ZnO nanoparticles to produce inorganic/polymer functional coatings that can offer high visible brightness and thermal control effect for green buildings [Jiang *et al.,* 2013; Li *et al.,* 2007]. In fact, low-emitting surfaces decrease radiative heat transfer by reflecting the incident infrared radiation which reduces the radiative heat emission in the near-infrared spectral region. In the previous Chapter, we reported the influence of nano ZnO morphologies upon near-IR reflectance in both ZnO nanoparticles as well as ZnO nanoparticles embedded PMMA polymer sheets. Here, we fabricated multilayered coatings of Al-doped ZnO nanoparticles embedded in a PMMA matrix on glass surfaces for multifunctional applications.

PMMA has high optical transparency throughout the visible range in addition to high mechanical stability. It has very low thermal conductivity [λ = 0.2 W/m.K] that generates heat build-up upon exposure to solar radiations. It also has poor UV and NIR shielding capability [Viasnoff, 2014; Viasnoff *et al.,* 2012; Sun *et al.,* 2007; Kulyk *et al.,* 2010]. PMMA thin films are reported with ZnO to have UV stable, transparent coatings [Li *et al.,* 2010; Eita *et al.,* 2012b]. However, it is understood that the past research attempts dedicated to investigating the enhanced mechanical and UV shielding advantages of PMMA polymer with nano ZnO inclusions. NIR control characteristics as well as optical transparency for window coatings have not been studied and yet reported.

Compared to pure ZnO, nanocoatings made by Al-doped ZnO (AZO) are found very effective due to improved spectral selectivity, optical band gap tunability for transmitting almost complete solar radiation and low-emitting surface properties. AZO is already studied as anti-reflection coatings for solar cells [Kluth *et al.,* 2003; Verma *et al.,* 2010]. Further, Al-doped ZnO shows metallic properties and hence reflect near-IR radiation. It is already demonstrated with bulk AZO/epoxy composites [Yuan *et al.,* 2011; Yong *et al.,* 2009].

In this chapter, AZO/PMMA nanocomposite multilayered coatings were built *via* Layer-by-Layer technique [LbL]. UV absorption, NIR shielding efficiency, mechanical hardness, and surface roughness were analyzed and reported. Al-doped ZnO/PMMA coating was also tested for the anti-freezing property with liquid nitrogen.

3.2. EXPERIMENTAL SECTION

3.2.1. Materials

Zinc acetate dihydrate ($Zn(CH_3COO)_2.2H_2O$, Merck Ltd., India, purity; >99%), Sodium hydroxide (NaOH, Merck Ltd.), Aluminium nitrate nonahydrate ($Al(NO_3)_3.9H_2O$, Merck Ltd., purity; 99%), Polyethylene glycol with an average M_w 300 (PEG 300, Merck Ltd) and Poly(methyl methacrylate) (PMMA, Sigma-Aldrich Chemical Company, India) with an average M_w ~996,000 by GPC were used in as received condition.

3.2.2. Synthesis of Al-Doped ZnO (AZO) Nanoparticles

Zinc acetate dihydrate precursor solution containing different mol% aluminium ion, *viz*, 0.25, 0.5, 1, 2, 3, 5, and 10 mol% was prepared by dissolving required quantity of aluminium nitrate nonahydrate ($Al(NO_3)_3.9H_2O$) precursor in 200 mL distilled water. To this solution, 10 mL PEG 300 was added and continuously stirred for 4 h to form a homogeneous reactant mixture. The total number of moles of zinc acetate dihydrate and aluminium nitrate nonahydrate was 0.1 M. An aqueous solution of 1 M NaOH was added dropwise with continuous stirring till the pH value reached 10. A white precipitate was collected at the end and centrifuged several times at 3000 rpm using distilled water and final centrifugation was carried out with ethanol. The as-precipitated AZO nanoparticles were dried at 80 °C for 24 h and subsequently calcined at 500 $^{\circ}$C for better crystallization. The obtained powder was ball milled for 24 h in toluene medium for de-agglomeration and subsequently dried to obtain AZO nanoparticles for fabricating coatings. The AZO nanoparticles were represented as 0.25, 0.5, 1, 2, 3, 5, and 10% AZO with respect to mol% of Al content. For comparison, nano ZnO without any Al-doping was also processed at identical conditions and was represented as 0% nano AZO.

3.2.3. Fabrication of AZO/PMMA Nanocomposite Coatings via LbL Technique

Blue star® micro slides (PIC-1, Polar industrial corporation, Mumbai, India) with a size of 75 mm long × 25 mm in width and thickness of 1.35 mm were selected for coatings. The as-received glass slides were boiled in concentrated HNO_3 and washed with soap solution, acetone and ethanol, finally cleaned glass surface was dried at 80 $^{\circ}$C in a hot air oven.

For the preparation of AZO/PMMA coating solution, 3.33 wt% of PMMA granule was dissolved in 60 mL toluene. The amount of 0.1, 0.3 and 0.7 wt% AZO nanoparticles was ultrasonically dispersed to form a stable AZO/PMMA viscous sol. The viscosity was measured using stress-controlled Anton Paar Viscometer (Rheolab MC-1) at varying shear rates and the sol stability was observed for 1 month without any disturbance.

The cleaned glass plates were immersed into the AZO/PMMA colloid using a computer program with an advancing and receding rate of 85.5 mm min^{-1}. One minute residence time produced a thin coating on both sides and prior to any successive dip-coatings, the coated glass substrate was cured. Likewise, different layers were built by Layer-by-Layer coating technique and samples were made with 1, 3, 7, 12, 20, and 50 layers and represented as $(AZO/PMMA)_1$, $(AZO/PMMA)_3$, $(AZO/PMMA)_7$, $(AZO/PMMA)_{12}$, $(AZO/PMMA)_{20}$ and $(AZO/PMMA)_{50}$. The procedure was repeated with 2 and 10 mol% AZO nanoparticles to have PMMA layer coatings with different contents of AZO.

3.2.4. Characterizations

In this Chapter, AZO nanoparticles were characterized by XRD, DLS, SEM, TEM, SAED, EDX, UV/Vis absorption and UV/Vis/NIR spectroscopic analysis were carried out. In coatings, the surface morphologies, mechanical and optical properties of AZO/PMMA coatings were characterized.

The crystalline nature and phase purity of the AZO nanoparticles were characterized by powder X-ray diffractometer using X'Pert Pro, Philips X-ray diffractometer equipped with Cu K_α radiation (λ = 1.5406 A°) in the 2θ range 10 to 80° with 0.02 scan increment. Particle size was measured using dynamic light scattering (DLS) technique [Zetasizer 3000H, Malvern Instruments, Worcestershire, UK]. Particle dispersion was prepared ultrasonically in the aqueous medium using Ultrasonic Processor P2 (Vibronics Pvt. Ltd., Bombay, India) and then size analysis was carried out. Particle morphology and thickness of AZO/PMMA films were examined using the scanning electron microscope (SEM) [Model: ZEISS EVO 18], operated at 20 kV. The chemical composition and mapping of samples were ascertained using energy-dispersive X-ray (EDX) analysis.

Nano morphology, chemical composition, and microstructure of the AZO particles were further ascertained by transmission electron microscopy (TEM) and

selected area electron diffraction (SAED) analysis using the instrument FEI Tecnai 30G2S-TWIN transmission electron microscope operated at an accelerating voltage of 300 kV. A drop of AZO colloid prepared ultrasonically in acetone medium was carefully deposited by drop-casting on the TEM grid. After evaporation of the solvent, the surface was examined for the morphology. The presence of elemental aluminium in AZO nanoparticles was further detected by energy-dispersive X-ray (EDX) spectroscopy. The glass coating surface was also scanned in tapping mode using atomic force microscope (AFM) [Nanovea] in area 84 × 84 μm for determining the surface profile. The viscosity was measured using stress-controlled Anton Paar Viscometer (Rheolab MC-1) at varying shear rates, and the sol stability was observed for 1 month without any disturbance. The rheology studies ZnO/PMMA sol samples were evaluated by shear stress and viscosity along the shear rate from 0 to 1000 s^{-1}.

The coating was performed using a computer control dip-coater KSV Instruments, Netherlands [Figure 3.1].

Figure 3.1: Dip-coating set-up used for coating in this study

Programmable dip-coater is used to coat a substrate with any liquid or sol. There is a substrate holder at the bottom end of a moving rod can move up and down within a limited zone. The speed of substrate holder can be controlled using a program. The main advantage of using this instrument is that we can avoid discontinuity of the film due to jerking at the time of drawing the substrate and speed of drawing the substrate can be controlled perfectly.

The mechanical stability of AZO nanoparticles dispersed PMMA coatings was assessed by microhardness measurement at a load of 0.5 N using Shimadzu

microhardness tester. First of all, microhardness indentation mark was made on the bare glass substrate to check the deformation resistance. The development of unambiguous indentation impression mark at the given load was carefully examined for selecting the optimum loading condition. After seeing hardness and load effect on the glass substrate, the indentation was made on the coatings to know the bulk hardness. The change in indentation area with the number of coatings was checked and plotted. Hardness was measured in Vicker's scale and indentation velocity was fixed at 10 s. Nanoscratch testing was done on coated surface using Nanovea scratch testing equipment using diamond sphero conical indenter within the loads ranges from 0.1 to 30 mN. The delamination during the scratch test and the respective penetration were measured and compared for the different number of layered coatings.

UV/Vis absorption analysis of the AZO nanoparticles and coatings were monitored by Shimadzu UV/Vis spectrophotometer (UV 240 IPC) in the wavelength region 200 to 800 nm. UV-absorption was also measured for AZO dispersion prepared ultrasonically in ethanol medium. For baseline correction, ethanol was used as the reference.

Near-infrared diffuse reflectance of the AZO nanoparticles and AZO/PMMA nanocomposite coatings on the glass substrate was measured using UV/Vis/NIR spectrophotometer (Shimadzu, UV-3600) with an integrating sphere attachment, ISR-3100 using PTFE reference as reported in the previous Chapter [Vishnu *et al.,* 2011; Soumya *et al.,* 2014; Jose *et al.,* 2014; Sangeetha *et al.,* 2012]. The NIR reflectance measurements of the samples were performed in the wavelength 700 to 2500 nm range.

Solar Heat Control Efficiency

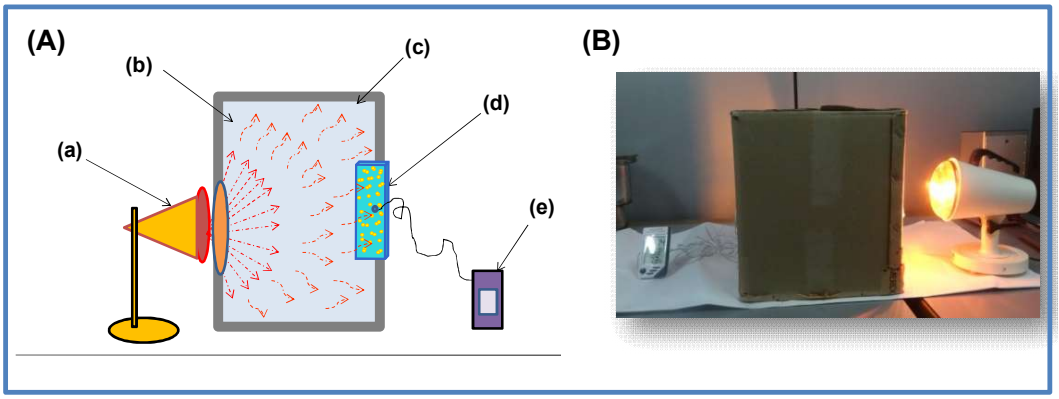

Figure 3.2: (A) Schematic of indigenously made IR temperature measurement set-up for AZO/PMMA coatings (a) IR lamp, (b) wooden box, (c) aluminium foil covered with the wooden box, (d) AZO/PMMA layer coated the substrate, and (e) digital thermocouple. (B) Photographic image of the corresponding set-up.

Solar heat control efficiency of AZO/PMMA NIR reflective multi-layer coatings were examined using indigenously designed experimental set-up. A schematic and its photographic image of the set-up were shown in Figure 3.2. It consists of a wooden box, digital thermocouple and a Nisco® Infrared lamp (National Industrial Corporation, Delhi, India). The inner side of the box was covered with aluminium foil on all the four sides to have maximum IR reflectivity and heat build-up through radiation. A rectangular hole with the dimension of length and width is 50 mm and 15 mm respectively, was made to place the AZO/PMMA coated glass. One side of the test specimen was exposed to IR radiation, and the other side was provided with the flat thermocouple to measure the heat transfer across the glass plate. The distance between the IR lamp and the coated glass plate can able to vary to obtained the different rate of heat radiation. The temperature build-up on the outer surface of coated glass was monitored with time.

3.3. RESULTS AND DISCUSSION

3.3.1. Characterizations of AZO Nanoparticles

3.3.1.1. Structural and Dimensional Analysis of AZO NPs

Figure 3.3 shows the powder X-ray diffraction patterns of AZO prepared nanoparticles. The X-ray diffraction peaks are consistent with the standard polycrystalline ZnO reported in the JCPDS card No: 36-1451, providing clear evidence on the formation of hexagonal wurtzite-type ZnO with space group of $P6_3mc$. The diffraction peaks show good agreement with the standard ZnO peaks correspond to (100), (002), (101), (102), (110), and (103) crystal planes. Even though the main peaks in AZO particles prepared with Al-doping are in accordance with the pure ZnO, the peaks slightly shift in its 2θ values indicating the doping effect in the ZnO crystal structure. The samples prepared with high Al-doping of 5 and 10 mol% showed additional peaks at 2θ values = 23.5 and 39.2°. The intensity of these peaks also increased with the level of Al-doping indicating the formation of reactive chemical species from the Al-dopant element.

The X'Pert Pro analysis of these peaks matches with the hydrated hydroxide moiety of zinc/aluminum precursors [ICDD data PDF No. 48-1021]. Since the peak intensity is considerably stronger, it is concluded that at a high % of Al-doping, co-precipitation resulted in nucleation of reactive double hydroxides that transform to mixed oxides upon calcination.

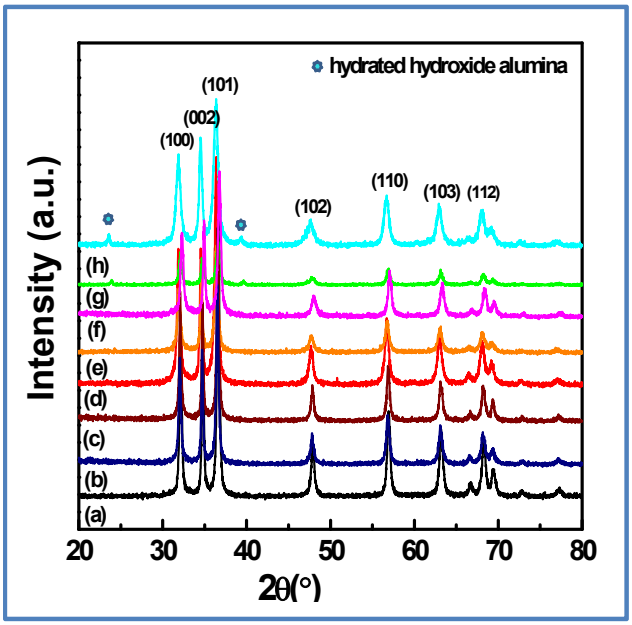

Figure 3.3: XRD patterns of AZO nanoparticles calcined at 500 °C/3h (a) 0, (b) 0.25, (c) 0.5, (d) 1, (e) 2, (f) 3, (g) 5, and (h) 10% AZO.

The average crystallite size of the AZO nanoparticles was determined using Debye-Scherrer's formula (Equation 2.2) [Wu *et al.,* 2014]. For the crystallite size analysis, highly intense and sharp diffraction peak at 2θ = 36.3° corresponds to the (101) plane of the ZnO hexagonal wurtzite phase was considered. It gives the crystallite size in the range between 24-29 nm for 0, 0.25, 0.5, 1, 2, 3, 5 mol% Al and 19 nm for 10% Al-doped AZO nanoparticles, respectively. A comparatively smaller crystallite size in 10% Al-doped AZO samples indirectly indicates the crystal growth is substantially inhibited by the co-existence of hydrated Al_2O_3. Unfortunately, small crystals have a strong tendency for aggregation. This results were also supported by Particle size analysis. Figure 3.4 gives the DLS size distribution curves correspond to AZO nanoparticles prepared with 2 and 10 mol% Al doping. For comparison, ZnO without any dopants was also displayed. It shows undoped nano ZnO has a mean particle size as 215 nm. It is slightly increased to 256 nm for 2 mol% Al doping, that decreases to 242 nm for 10 mol% Al doping. Overall, AZO nanoparticles have an average particle size in the range

200-350 nm indicating they are agglomerated nanoclusters. The particle diameter ($2r$), and the agglomeration coefficient (C_F) were calculated and summarized in Table 3.1.

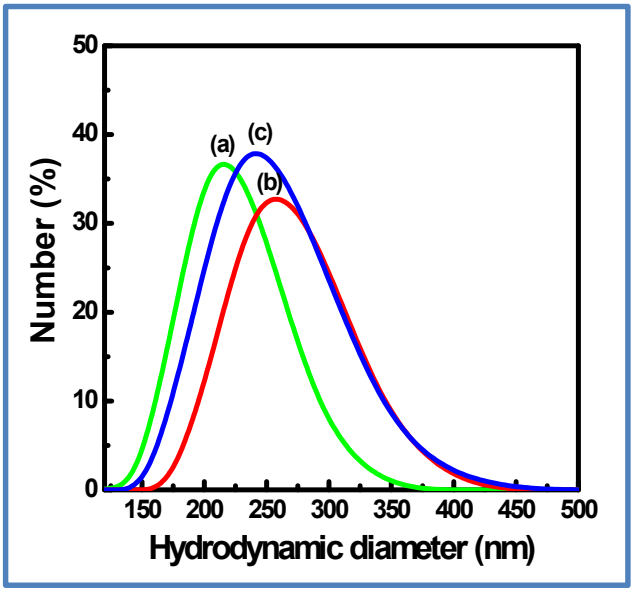

Figure 3.4: DLS particle size distribution by number of ZnO with different mol% of Al doping (a) 0, (b) 2, and (c) 10% AZO nanoparticles dispersed in aqueous medium.

Table 3.1: Illustration of morphologies, dimensional size and agglomeration coefficient of AZO nanoparticles obtained with different mol% of aluminum doping.

ZnO Samples	**Morphology**	**<*D*> (nm)**	**DLS *2r* (nm)**	***2r*** **(nm)**	***C_F***	**UV *λ* (nm)**	***E_g*** **(eV)**
0% AZO	Nano-spherical	28	215	4.9826	0.17798	365	3.40
1% AZO	Semi-spherical	27	261	4.3490	0.16107	356	3.48
2% AZO	Semi-spherical	25	257	4.2902	0.17161	355	3.49
5% AZO	Agglomerate spherical	29	330	4.2284	0.14581	358	3.46
10% AZO	Micro-spherical	19	242	4.2902	0.22580	355	3.49

From Table 3.1, the crystallite size <D> determined from Debye-Scherrer's formula (Equation 2.2), DLS ($2r$) is the particle size distribution analysis, $2r$ calculated

from Equation 2.4, C_F is the agglomeration coefficient obtained from Equation 2.9. It clearly shows that undoped ZnO has higher particle radius and size decreases with Al-doping. The extent of decrease particle size is increasing with the amount of Al-doping. Accordingly, the agglomeration coefficient is also increased as a result of the higher surface area.

3.3.1.2. Morphological Analysis of AZO Nanoparticles

The extent of inter-particle agglomeration is further clear from the SEM morphology. SEM images of AZO nanoparticles containing a different Al mol% were displayed in Figure 3.5. In undoped ZnO nanoparticles, finely grown nano-spherical particles were loosely bonded to each other is seen. In doped counterpart, strong agglomeration is evidenced. ZnO particles having 2 and 5 mol% Al-doping have the particles contain large size aggregates. In every agglomerate, assembly of many primary ZnO nanocrystallites is apparently seen. The morphology was completely changed when 10 mol% Al doped ZnO was employed. In this category, SEM microstructure indicates the formation of highly reactive particles, possibly with coverage of partially dehydrated nano Al_2O_3. Effect of Al-doping on the morphological features of AZO nanoparticles is once again verified under TEM and also with SAED. Figure 3.6(a) to (c) show the TEM images of AZO nanoparticles correspond to 0, 5, and 10% Al-doping. Figure 3.6(d) to (f) represents corresponding SAED patterns. Undoped ZnO [Figure 3.6(a)] has highly crystalline, hexagonal nanocrystal morphology with an average size of 50 nm. The SAED pattern can be indexed to the reflection of the nanocrystalline wurtzite ZnO. The crystallite size and crystalline nature appear to decrease with Al-doping. At 10% Al-doping, the TEM image confirms the growth of mixed oxide particles and its SAED pattern further ascertains amorphous nature, indicating the ZnO nanocrystals are covered with partially transformed hydrated Al_2O_3 species. The Al concentration in AZO nanoparticles was further detected by energy-dispersive X-ray (EDX) spectroscopy. The EDX spectrum of AZO nanoparticles without any Al-doping [Figure 3.6(g)] contains only phase pure ZnO. In 10% AZO nanoparticles [Figure 3.6(h)], the EDX analysis reveals the presence of elemental aluminium. In this sample, EDX confirms that presence of 10.0 at.% Al. TEM, SAED and EDX results clearly show that the 10 mol% AZO nanoparticles are composed of the mixture of elemental oxygen, aluminium, and zinc.

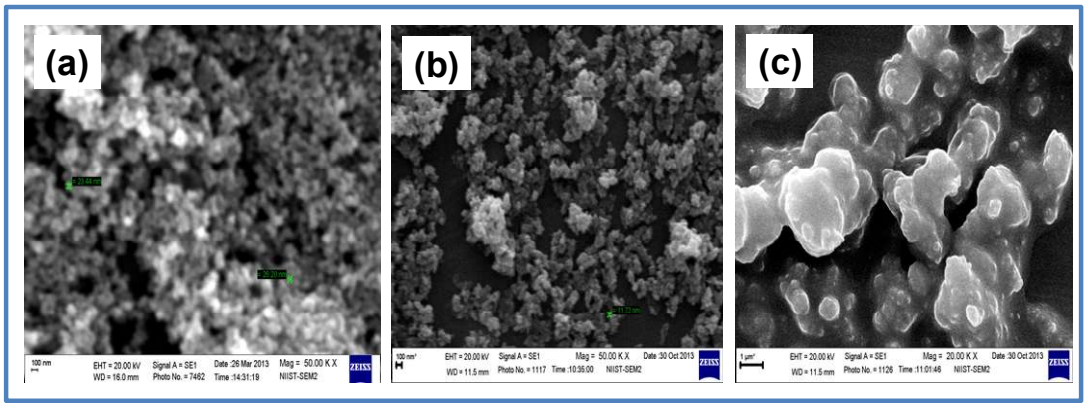

Figure 3.5: SEM morphologies of ZnO nanoparticles with different mol% of aluminium: (a) 0, (b) 5, and (c) 10% AZO nanoparticles (Scale bar: (a) 100 nm, (b) 100 nm, (c) 1 µm).

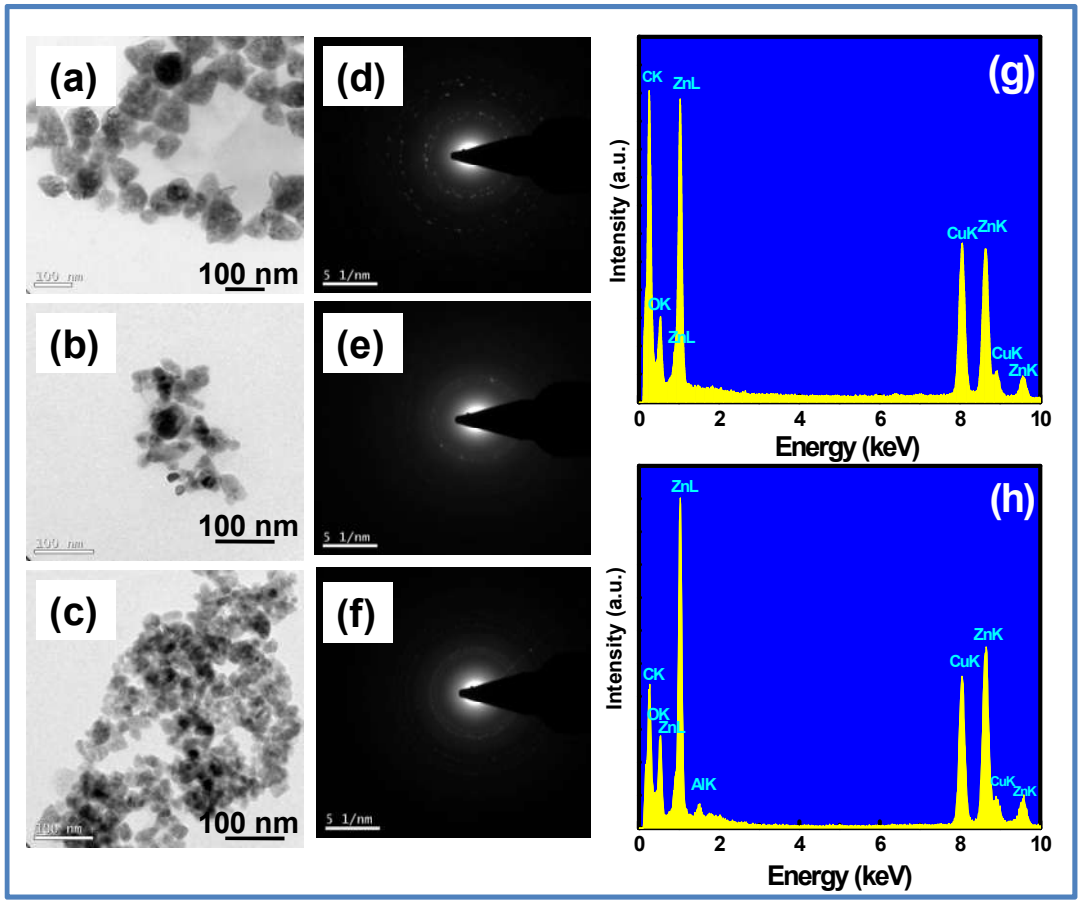

Figure 3.6: TEM images of (a) 0, (b) 5, and (c) 10% AZO nanoparticles and its selected area electron diffraction (SAED) pattern (d), (e), and (f) respectively. EDX patterns of (g) 0% AZO and (h) 10% AZO nanoparticles.

3.3.1.3. UV/Vis Absorption of AZO Nanoparticles

Figure 3.7 depicts the UV/Vis absorption spectra of AZO nanoparticles in the wavelength 300-800 nm. The results clearly show that irrespective of Al-doping, the AZO nanoparticles have strong UV absorption below 400 nm (3.10 eV). In pure nano ZnO, the well-defined absorption band is obtained at 366 nm. The absorption efficiency was enhanced with the increase in mol% of Al doping. The UV absorption wavelength (λ) corresponds to 1, 2, 5, and 10 mol% Al doping varies between 355 to 358 nm. It is observed that by increasing the mol% of Al doping correspondingly decreases the UV absorption. It is also supported by powder X-ray analysis results where we find the evolution of hydrated Al_2O_3 mixed phases in the particles at a higher amount of Al doping. In all AZO nanoparticles two kinds of optical-effects are clear; a strong UV-shielding effect in both UVA (400-315 nm) and UVB region (315-300 nm) and also UV photoactivity for any self-cleaning property.

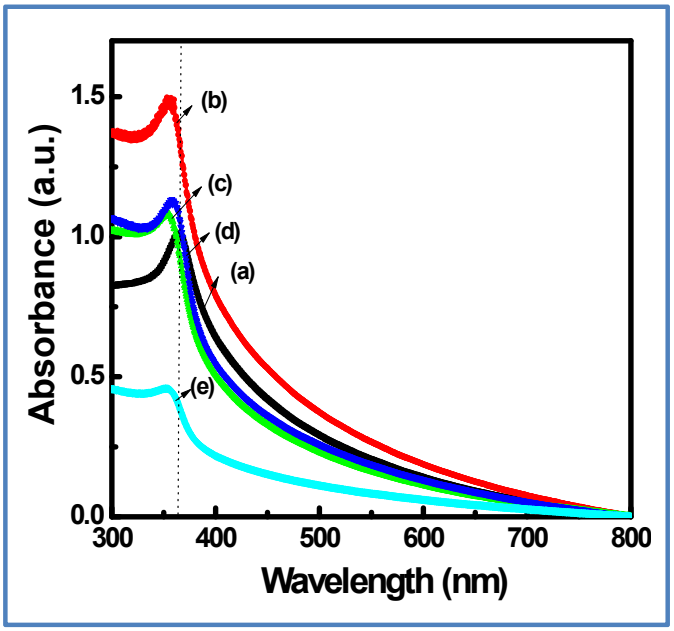

Figure 3.7: UV/Vis absorption spectra of (a) 0, (b) 1, (c) 2, (d) 5, and (e) 10% AZO nanoparticles were dispersed in ethanol medium.

3.3.1.4. NIR Diffuse Reflectance of AZO Nanoparticles

Bulk ZnO particles are said to have high NIR reflection by virtue of its high refractive index [Kortum, 1969]. Upon doping with viz., Al, Sn and Mg elemental ions, the pigment has more chance to gain better optical reflectance. The diffuse reflectance

results obtained for all the AZO nanoparticles in the wavelength region 200-2500 nm is given in Figure 3.8(a). It indicates that all nanoparticles have appreciably high NIR reflectance in the near-IR region, i.e., 810 to 1100 nm. The curves also confirm more than 90% reflectance in the visible wavelengths. In the case of Al-doped ZnO, a reflectance of about 80% was observed. From the NIR reflectance curves, the % decrease in NIR reflectance was determined and correlated with Al doping [Figure 3.8(b)]. The AZO nanoparticles attained better NIR reflectance with Al doping at both 810 and 1100 nm. These two wavelengths in NIR region are usually reported to determine the IR shielding efficiency of particles [Jeevanandam *et al.,* 2007]. At 810 nm, NIR reflectance was found to be 93, 87, 94, and 93% for the AZO nanoparticles prepared with 0, 1, 2, and 10 mol% Al-doping, respectively. The reflectance results indicate that the NIR reflectance quality in ZnO particles is not much affected neither due to Al doping nor by the presence of Al_2O_3. Both Al_2O_3 and ZnO are optically white. The size distribution curve also exhibited wide particle sizes varies from few nm to few hundred nm. Optical reflectivity is predominantly a surface phenomenon. In inorganic nanoparticles, surface atoms, surface texture, preferably the roughness influences the light-matter interaction. A highly ordered atomic surface is said to trap light in multiple reflections. In this case, Al-doping causes varied surface roughness as evident from the SEM morphology in addition to the advantages of crystallite size and particle size control. Al doping was in fact found favorable to increase the brightness and thereby IR reflectance. The CIE 1976 L*a*b* colorimetric method as recommended by the Commission Internationale del'Eclairage (CIE) was used to know the brightness of AZO nanoparticles. The color coordinates obtained from analytical software (UVPC Color Analysis Personal Spectroscopy Software V3, Shimadzu) attached with UV-3600 spectrophotometer clearly show high brightness. L*, a*, and b* values of color coordinates correspond to AZO nanoparticles were found to be 100, -0.49, and 1.20. Almost all the AZO nanoparticles have L* value close to 100 indicating their good optical reflectivity. The analysis of high NIR solar reflectance (~90%) combined with better optical brightness at all the Al-doping levels; confirm AZO nanoparticles are interesting candidate for cool pigments.

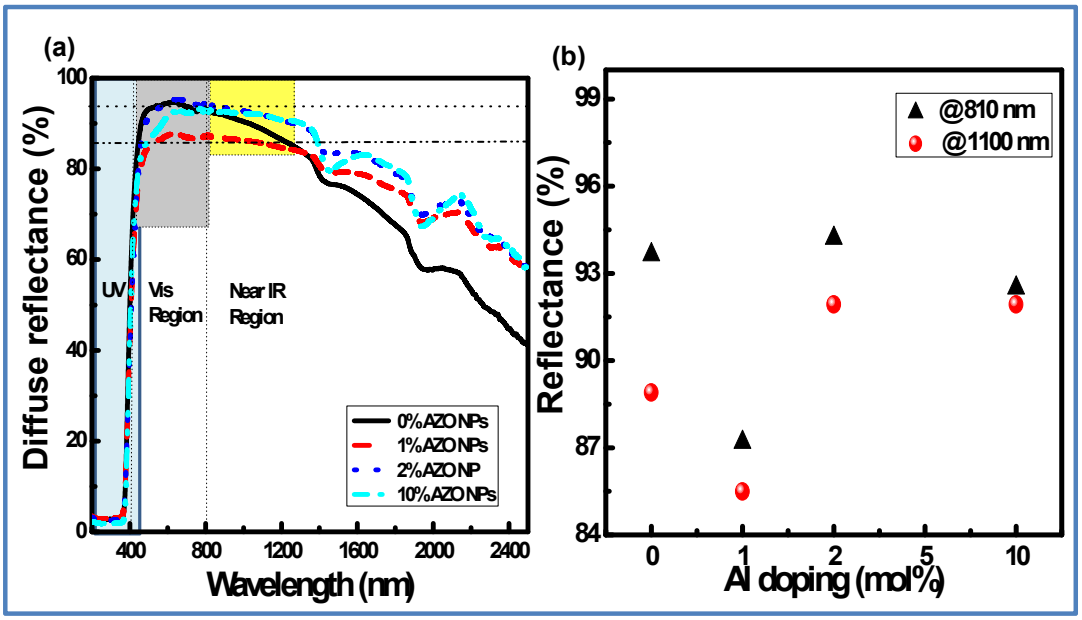

Figure 3.8: (a) NIR reflectance with different mol% of AZO nanoparticles in the range 700-2500 nm and (b) The plot of reflectance *vs*. mol% of Al doping at 810 and 1100 nm.

3.3.2. Characterizations of AZO/PMMA Coatings

3.3.2.1. Rheology of AZO/PMMA Colloid

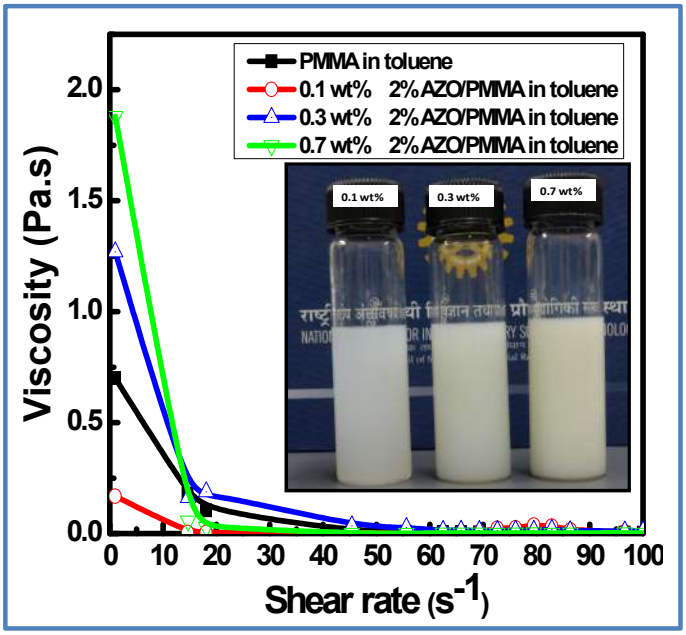

Figure 3.9: Viscosity measurement of 2% AZO/PMMA sol with respect to different wt% of AZO nanoparticles dispersed in toluene solution. Inset in the figure shows digital photographic images of corresponding AZO/PMMA stable colloidal sol with 0.1, 0.3, and 0.7 wt% AZO nanoparticles.

Figure 3.9 gives the viscosity and colloidal stability of AZO nanoparticles. It is noticed that AZO nanoparticles are highly stable in PMMA dispersed toluene medium and this sol has shear dependent flow-behavior. At low shear, the viscosity of PMMA solution marginally increased with the addition of AZO particles. In all the cases, the viscosity was constant at high shear rates. High colloidal stability and faster rate of toluene evaporation at elevated temperature give highly uniform AZO/PMMA coatings.

3.3.2.2. Structural Analysis of AZO/PMMA Coatings

Figure 3.10 depicts the X-ray diffraction analysis of fabricated neat PMMA, $(ZnO/PMMA)_{50}$ and $(2\%\ AZO/PMMA)_{50}$ coatings on the glass substrate. The neat PMMA coating shows amorphous nature. The nanocomposite coatings showed evidence of nano ZnO in the X-ray pattern. Highly intense and sharp diffraction peak corresponds to (101) plane of the ZnO hexagonal wurtzite phase is confirmed at $2\theta = 36.3^{\circ}$ for AZO/PMMA nanocomposite coatings.

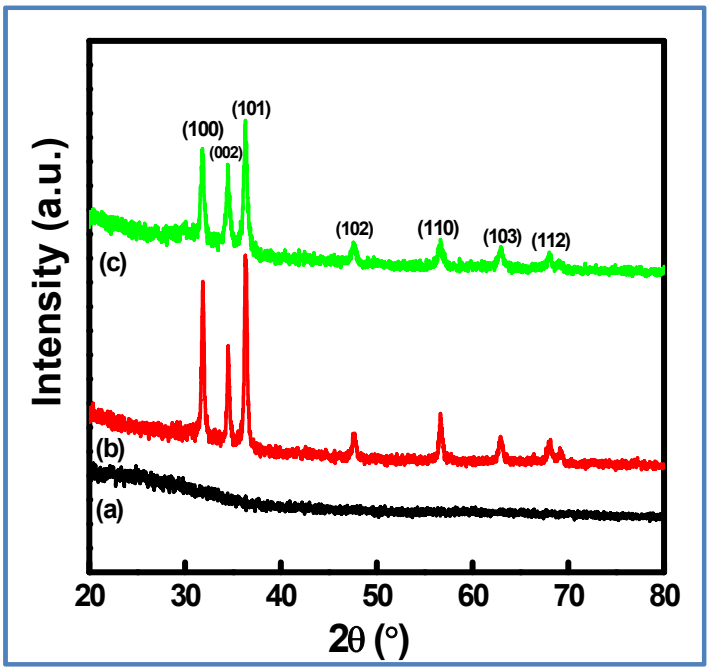

Figure 3.10: XRD patterns of (a) neat PMMA, (b) 0% $(AZO/PMMA)_{50}$ coating, and (c) 2% $(AZO/PMMA)_{50}$ coating on glass substrate.

3.3.2.3. Morphological Analysis of AZO/PMMA Coatings

The surface texture of pure $(ZnO/PMMA)_1$ and 2% $(AZO/PMMA)_1$ coatings is also shown in Figure 3.11(a) & (b). The top surface of a single-layer shows relatively clear coat, indicating the colloidal nature and homogeneous dispersion of ZnO nanoparticles in PMMA matrix. The surface texture of 2% Al doped $(AZO/PMMA)_1$ nanocomposite coatings shows comparatively aggregated particles dispersoids in PMMA matrix [Figure 3.11(b)]. The cross-sectional view of 2% $(AZO/PMMA)_1$ coatings [Figure 3.11(c)] confirmed the film thickness as ~269 µm.

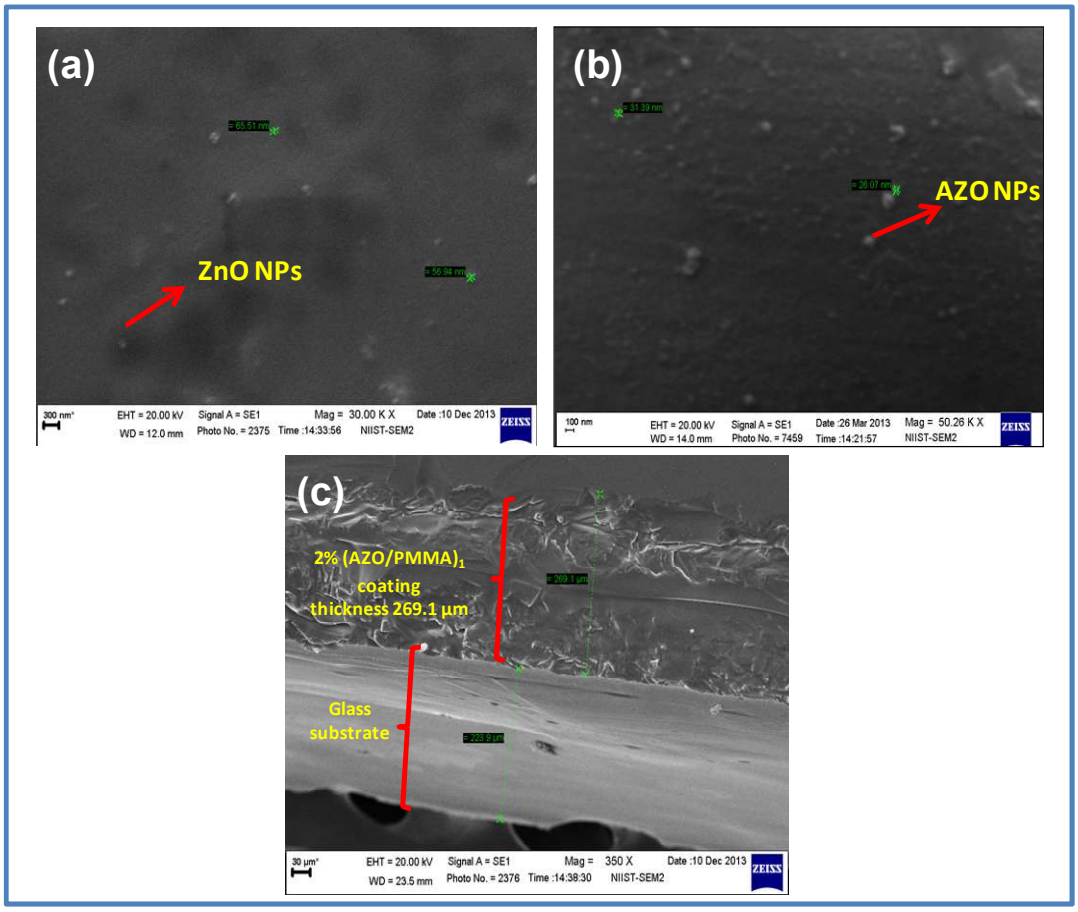

Figure 3.11: SEM images of the pure AZO/PMMA and 2% AZO/PMMA coatings on a glass substrate using dip-coating method: (a) top view of pure $(ZnO/PMMA)_1$ coating (scale bar 300 nm), (b) top view of 2% $(AZO/PMMA)_1$ coating (scale bar 100 nm), and (c) cross-section image of 2% $(AZO/PMMA)_1$ coatings, the scale bar corresponds to 30 µm and thickness 269.1 µm.

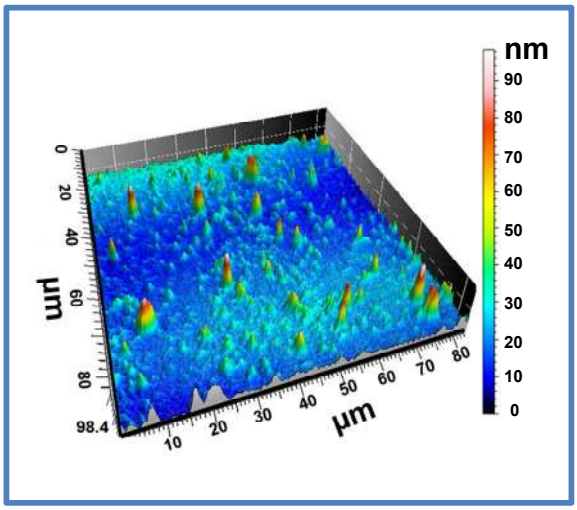

Figure 3.12: 3D AFM images of 2% $(AZO/PMMA)_1$ coatings in area 84 × 84 μm.

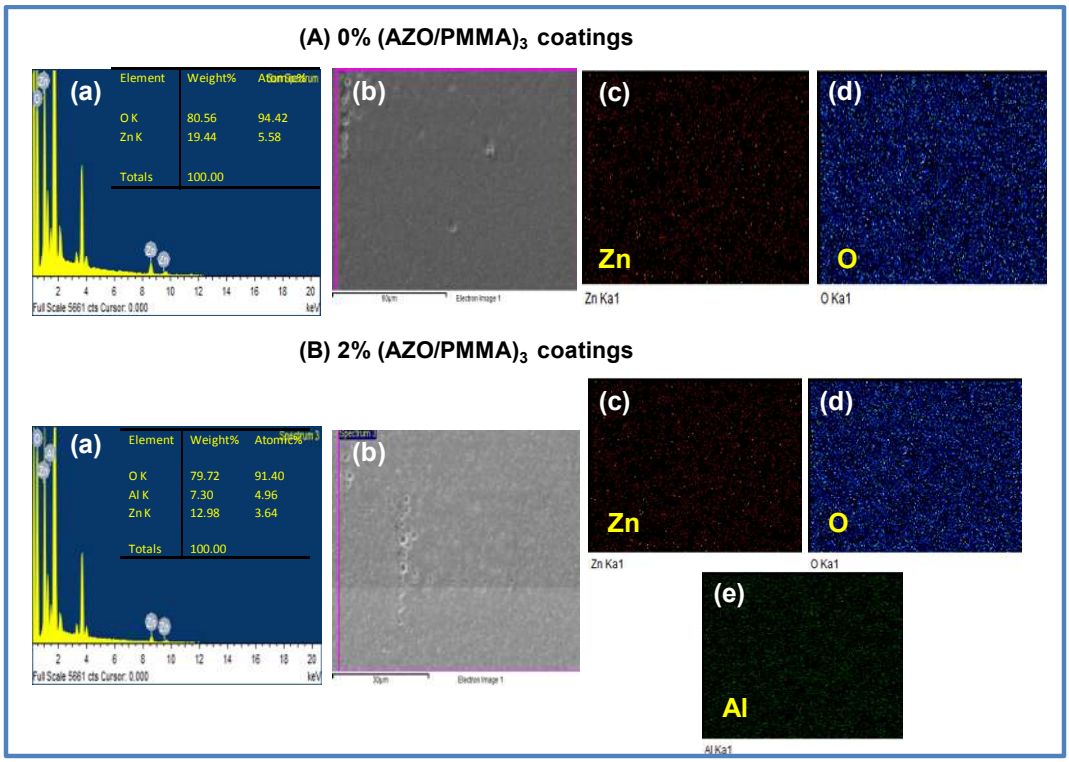

Figure 3.13: (A) 0% $(AZO/PMMA)_3$ coatings: (a) EDX, (b) SEM, and (c, d) its mapping analysis of 0% $(AZO/PMMA)_3$ coatings; (B) 2% $(AZO/PMMA)_3$ coatings: (a) EDX, (b) SEM, and (c-e) its mapping analysis of 2% $(AZO/PMMA)_3$ coatings.

Figure 3.12 gives the 3D AFM image of 2% Al doped AZO/PMMA monolayers where structural homogeneity can be clearly seen. AFM image gives the maximum surface roughness approximately 100 nm.

EDX analyses in Figure 3.13A show that the surface of the 0% $(AZO/PMMA)_3$ coatings were composed of elements Zn and O and its nanostructure could be further distinguished by SEM and mapping analysis [Figure 3.13A(b-d)]. The presence of Al doping in 2% $(AZO/PMMA)_3$ coatings on the glass surface is confirmed by EDX analyses and also the elements Zn, O and Al are distributed were analyzed by SEM and mapping [Figure 3.13B(b-e)].

The SEM/AFM images confirm that even though the single coat is transparent, by multilayer AZO/PMMA coatings on glass surface make it multifunctional as follows:

3.3.3. Functional Properties of AZO/PMMA Coatings

3.3.3.1. Mechanical Stability of AZO/PMMA Nanocomposite Coatings

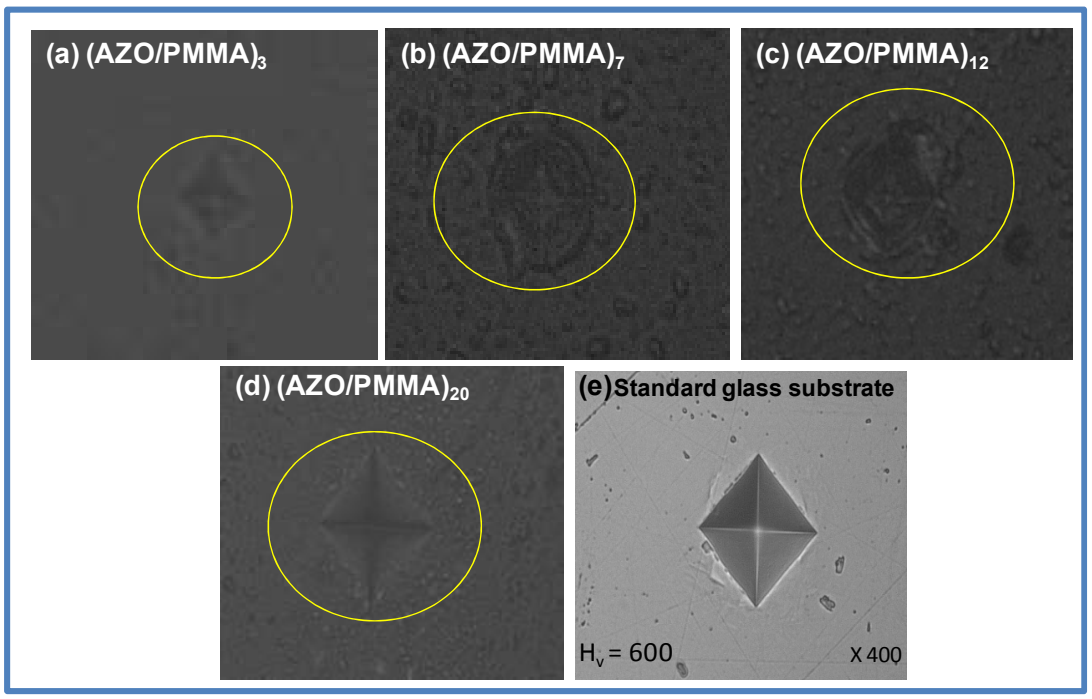

Figure 3.14: Microhardness of 2% AZO/PMMA coatings (a) $(AZO/PMMA)_3$, (b) $(AZO/PMMA)_7$, (c) $(AZO/PMMA)_{12}$, (d) $(AZO/PMMA)_{20}$, and (e) Standard glass substrate.

Bulk microhardness and scratch resistance qualities of AZO/PMMA coatings are given in Figure 3.14 and 3.15 that shows the mechanical stability of these coatings. A clear indentation impression was obtained at a load of 0.5 N. At this loading, the bare glass surface exerted the bulk hardness of H_v= 600. In nanocomposite coatings, the load caused deformation as envisaged, and the extent of surface damage was understood from the enlargement of the indented area. For example, the coatings having 3 layers do not deform much indicating that the stress is absorbed by the glass surface due to very thin coatings. When the substrate coated with 7 and 12 layers, the deformation damage on the surface is more cleared. In these samples, images have clearly shown delaminated edges of the layers. When the number of layers is increased, the indentation mark is sharp, showing better structural stability due to nano-reinforcement. In AZO/PMMA coatings, the bulk hardness, H_v is noticed as 181, 133, and 117 for 7, 12, and 20 layers respectively. Earlier works reported the Vickers hardness of bulk PMMA with and without reinforcements. Bare PMMA without any second phase was reported to have surface hardness approximately H_v= 85 [Fu *et al.,* 2009]. Interestingly, the bulk hardness is increased significantly with ZnO nanoparticles due to the high surface energy of the nano-dispersoids and its interaction with PMMA chains via physical bonding.

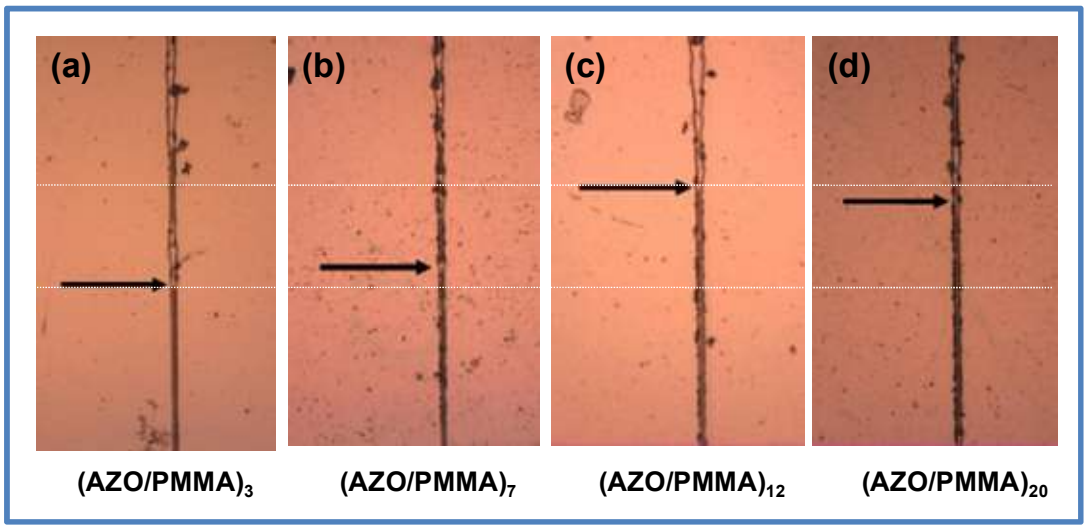

Figure 3.15: Delamination of 2% AZO/PMMA coatings with respect to the applied force (a) $(AZO/PMMA)_3$, (b) $(AZO/PMMA)_7$, (c) $(AZO/PMMA)_{12}$, and (d) $(AZO/PMMA)_{20}$.

The nano effect was also confirmed *via* macro-scratch tests conducted on the coatings at different layers. The optical images of the scratch marks and their penetration depths at specifically applied force were given in Figure 3.15(a) to (d). The force required to start the delamination of the coating layer during scratching and the penetration depth caused by the indenter is indirectly giving the mechanical resistance against scratching failure. For 7 numbers of layers, the delamination starts at 3.14 mN that gives the penetration depth of 292 nm. This was increased to 3.79 mN in order to cause delamination when the coating is made to 20 numbers of layers. The progressive increase in the loading with an increase in the number of layers indicated the coating attained more resistance against scratch due to increased loading of the particles phase.

3.3.3.2. UV-Shielding Efficiency

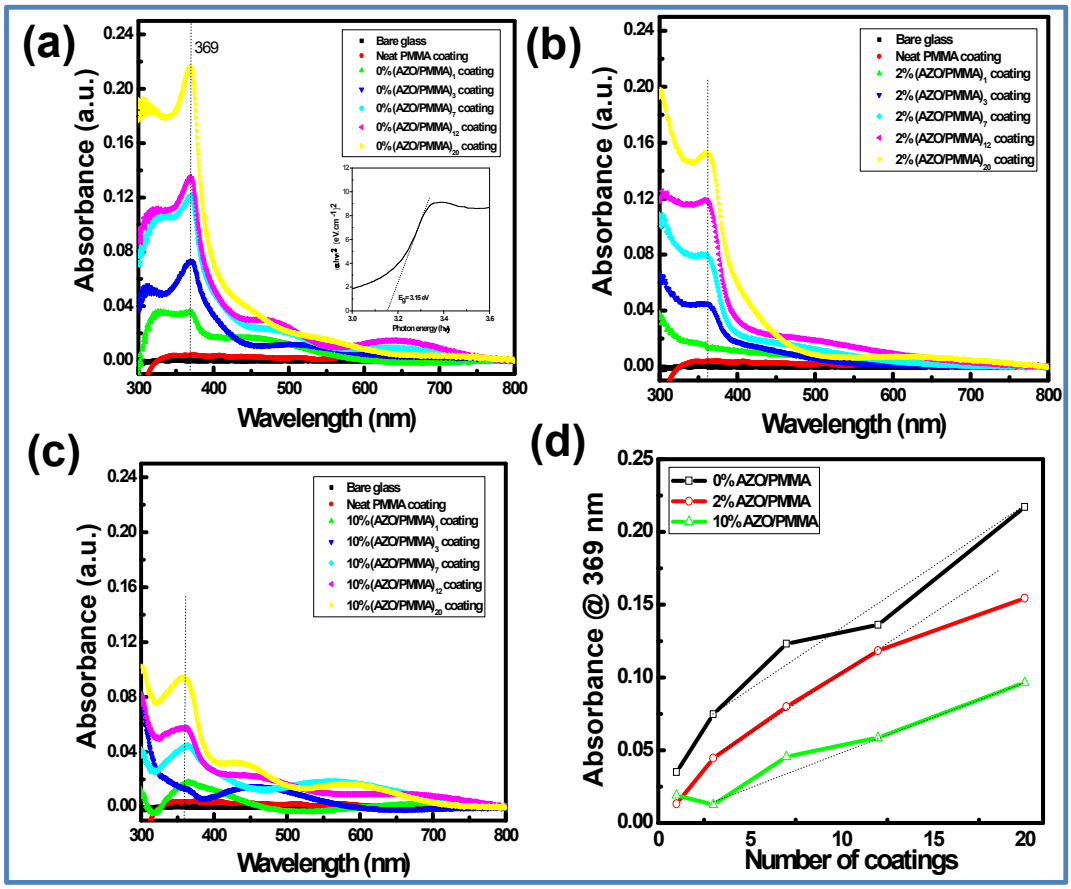

Figure 3.16: UV/Vis absorption spectra with LbL assembly of (a) 0, (b) 2, and (c) 10% AZO/PMMA coatings; (d) absorbance *vs.* number of layers of 0, 2, & 10% AZO/PMMA coatings @ 369 nm.

Characteristically, PMMA has UV absorption at the wavelength of 300 nm which is close to the bare glass substrate. Its refractive index is approximately 1.2 between the wavelength ranges 200 to 800 nm [Ogata *et al.,* 2012]. Increase in its bulk refractive index by any reinforcements can offer better light scattering control. Unfortunately, incorporation of any second phase particles hampers the transparency. It is envisioned that nano size dispersoids retain the optical quality in addition to functionality [Jiang *et al.,* 2013]. Figure 3.16(a) to (c) shows the UV/Vis absorption of ZnO/PMMA nanocomposite coatings. Invariably, all the ZnO/PMMA nanocomposite coatings have good UV radiation absorption at 369 nm. The absorption increases linearly with increasing number of coatings, indicating the coatings have steady pick-up of ZnO each time. UV absorption of the coatings at 369 nm was exactly matched with the absorption band seen in colloidal ZnO, further indicating the ZnO preserve their molecular state even after dispersed in PMMA matrix. The inset in Figure 3.16(a) presents the plot $(\alpha hv)^2$ vs. hv for determining the composite effect on the band gap energy. From the UV absorption measurements, the coatings up to 20 layer exhibit band gap energy as 3.15 eV. In the case of Al-doping, when the amount of Al-doping is increased from 2 to 10 mol%, the coatings apparently show a reduction in UV absorbance with respect to increasing number of layers [Figure 3.16(d)]. It gives an indication that the desired level of UV shielding for any specific application, can adjust by the number of coatings. In any case, it was confirmed that these coatings effectively block the UV radiation in the wavelengths 320 to 369 nm.

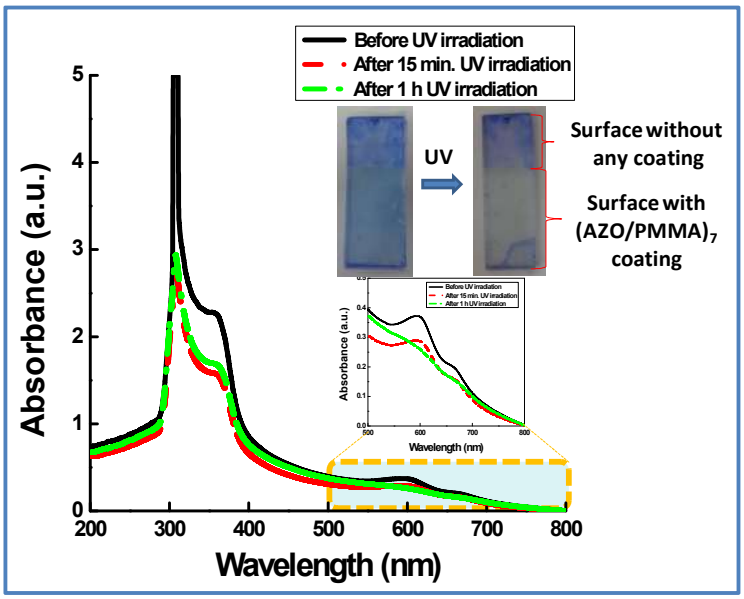

Figure 3.17: Before and after UV irradiation of 2% $(AZO/PMMA)_7$ treated with MB. Inset in the figure shows the enlarged portion of wavelength between 500 to 800 nm and the photographic images of before (left) and after 1 h (right) UV irradiated 2% $(AZO/PMMA)_7$ sample.

UV absorption efficiency of AZO/PMMA layers is well understood from the decomposition of standard methylene blue (MB) dye under UV irradiation at room temperature. Dipping of representative AZO/PMMA nanocomposite coated glass substrate in ~3.33 mM concentration of MB dye was subjected to UV exposure and the decomposition was measured by UV/Vis spectrophotometer. Figure 3.17 gives the dye decomposition efficiency by AZO/PMMA coated glass substrate. Within 15 min. exposure to UV, the dye starts decolorizing and in 1h time the dye was completely decomposed which indicates that the UV-bleaching functionality of the AZO embedded PMMA coatings.

3.3.3.3. NIR Reflectance and Solar Thermal Control Efficiency of AZO/PMMA Coatings

The NIR reflectance performance of AZO/PMMA coated glass substrate is compared with the bare glass substrate, glass coated with neat PMMA and ZnO/PMMA in the wavelength region of 700–2500 nm and the results are shown in Figure 3.18(a). When bare glass and PMMA coated substrates showed identical optical behavior, the AZO/PMMA pigmented composite coatings exhibit 46 and 33% NIR reflectance in the wavelengths 810 and 1100 nm respectively [Figure 3.18(b)]. The undoped ZnO/PMMA coatings have 34 and 18% NIR reflectance in the same wavelengths. The aforementioned results confirmed that the Al-doped ZnO nanoparticles are relatively better because they offered 12 and 15% enhancement in NIR reflectance even with 0.1 wt% nanoparticles loading.

The physical appearance of neat PMMA, $(AZO/PMMA)_3$, $(AZO/PMMA)_7$, $(AZO/PMMA)_{12}$, $(AZO/PMMA)_{20}$, and $(AZO/PMMA)_{50}$ coated glass was also compared in Figure 3.19 to understand the change in optical transparency due to ZnO pick-up in the multilayered coatings. It shows the loss in optical transparency even though the pigment is in nano size. However, these coatings have shown benefits in curtailing the heat transfer across the glass matrix.

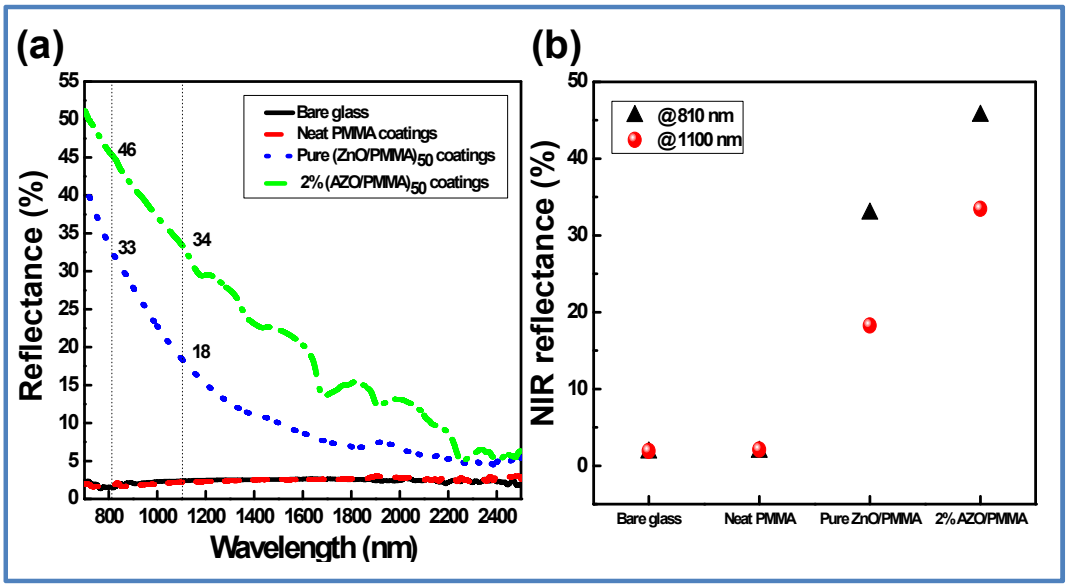

Figure 3.18: (a) Diffuse reflectance of the bare glass substrate, neat PMMA coating, pure $(ZnO/PMMA)_{50}$ coatings, 2% $(AZO/PMMA)_{50}$ coatings and (b) effect of Al-doping on NIR reflectance of nanocomposite coatings.

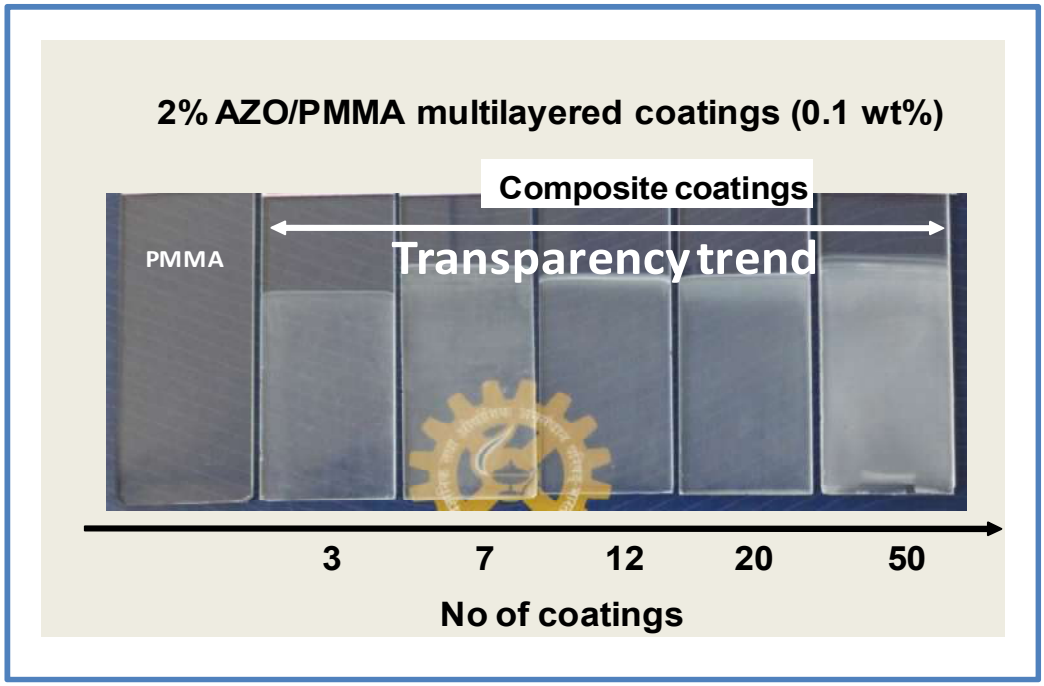

Figure 3.19: Photograph of neat PMMA and 2% AZO/PMMA coatings with 3, 7, 12, 20, and 50 layers.

The temperature cut-off result given by the glass substrate prepared with and without IR reflective AZO/PMMA nanocomposite coatings were shown in Figure 3.20(a) and (b). The distance between the IR lamp and the coated glass plate was positioned at different distances, such as 15, 30, and 45 cm to generate various temperature gradient profiles inside the chamber. When the IR source was placed close to the substrate, bare glass developed a surface temperature of ~52.6 ^{o}C [Figure 3.20(a)]. This heat built up is decreased when the IR source is kept away from the glass panel. At 30 and 45 cm, the surface temperature was estimated as ~38.09 and ~34.84 ^{o}C respectively. Under identical conditions, the glass substrate fabricated with 7 layers of AZO/PMMA nanocomposite coatings found to reduce the radiative heat transfer across the glass substrate to the temperature of 43.37 ^{o}C [Figure 3.20(b)]. Here, the nanoparticles loading in PMMA was only 0.7 wt%. Also, the ZnO nanoparticles contained 2 mol% of Al-doping. In fact, a consistent reduction in surface temperature was seen when the IR source was kept at 30 and 45 cm distances. It strongly indicated the AZO nanoparticles embedded PMMA coatings effectively block NIR radiation due to its inherent reflectance and optical brightness of the particles phase.

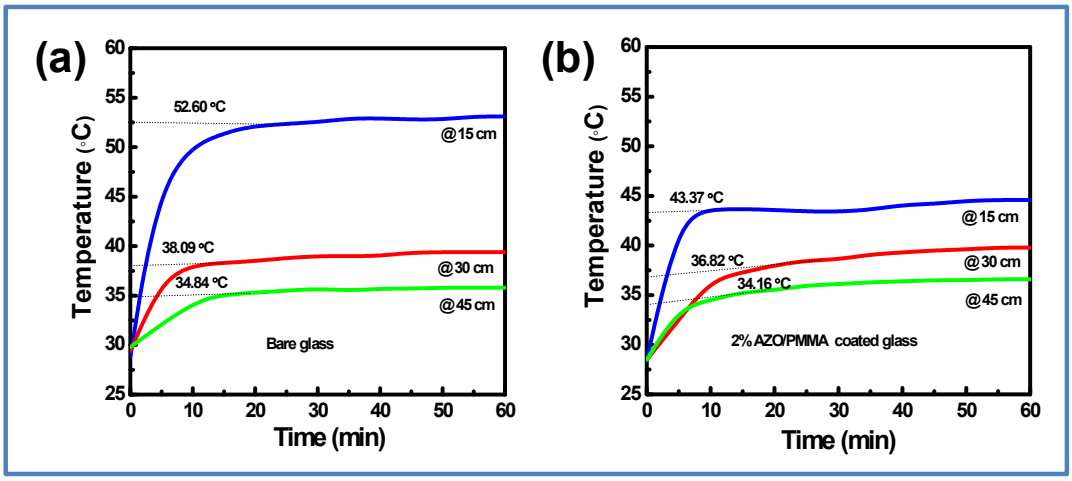

Figure 3.20: The plot of temperature *vs.* time obtained from IR lamp test positioned @ 15, 30 and 45 cm distance: (a) bare glass substrate and (b) 2% $(AZO/PMMA)_7$ coated glass substrate.

3.3.3.4. Anti-Freezing Quality of AZO/PMMA Coatings

Materials used to design the UV/IR reflective functional coating, PMMA and nano ZnO, are well known for the hydrophobic surface properties, which are also recommended for anti-icing surfaces. Since the AFM and SEM images confirmed the dispersion of Al-doped ZnO nanoparticles in the AZO/PMMA layer coatings and also they create the roughness on the surface, an anti-freezing property was tested using liquid nitrogen. The glass substrate coated with 7 numbers of AZO/PMMA layers were immersed in liquid nitrogen for 30 sec and then removed. The freezing of the surface was photographed and compared with uncoated glass substrates. A clear difference was noticed in AZO/PMMA coated glass substrates. Figure 3.21 shows the photographs of liquid nitrogen treated glass substrates. The AZO/PMMA coated surface became optically clear within few seconds without holding much water drops which formed due to condensation. Whereas, the uncoated glass surface not only took more time for drying but also exhibit affinity for retaining the droplets.

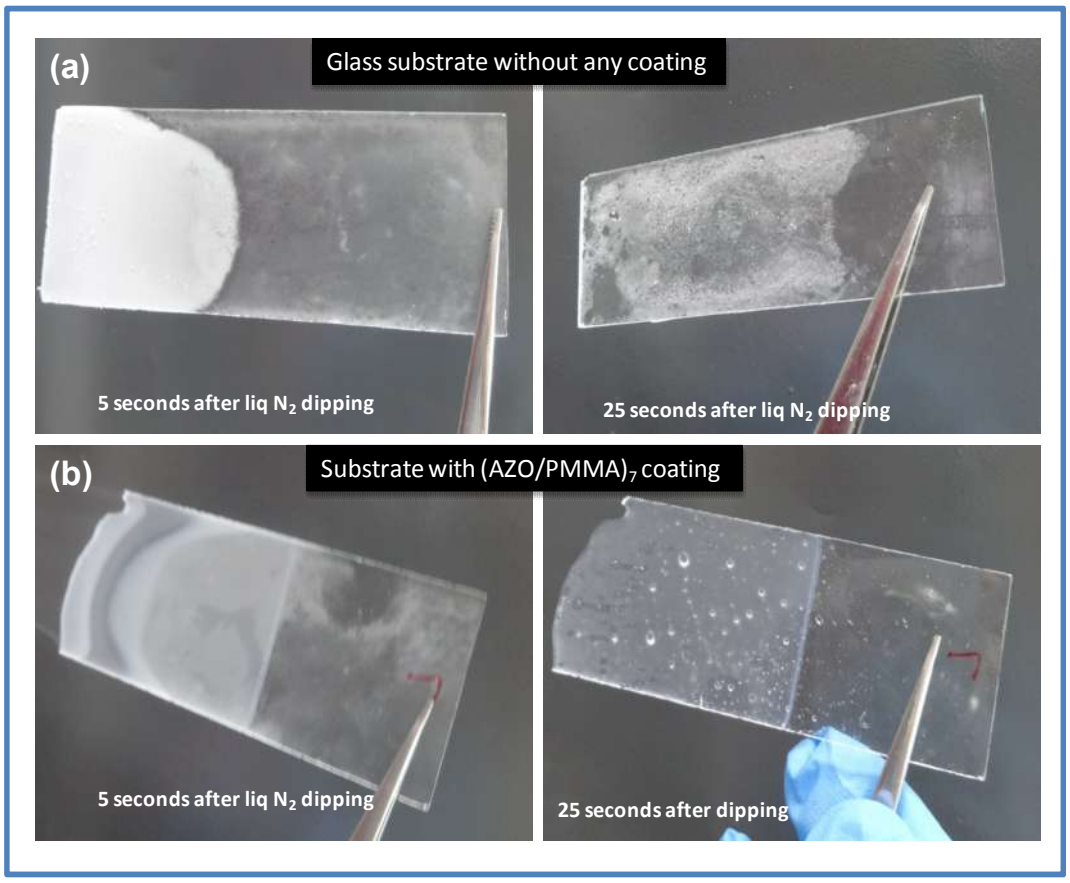

Figure 3.21: Photographic images of liquid nitrogen treated (a) bare glass and (b) 2% $(AZO/PMMA)_7$ layer coated glass substrates after 5 and 25 seconds.

3.4. CONCLUSIONS

Al-doped ZnO nanoparticles with an average particle size of 261 nm were prepared and dispersed in PMMA matrix for fabricating multifunctional nanocomposite coatings. A single layer of AZO embedded PMMA coatings having 269 μm thickness was obtained. This coating architecture was found to display potential physico-chemical functionalities depending upon the number of coating layers. It was found that the coatings deliver excellent UV absorption in the most harmful region of UV radiation (290-360 nm) and enhanced NIR reflectance at wavelengths of 810 and 1100 nm respectively. Overall, the Al-doping was favored in enhancing the NIR reflectance. The UV active photo-degradation of MB dye confirmed the self-cleaning activity of the nanoparticles in coatings. The AZO/PMMA coatings were prepared with 0.7 wt% of 2% Al-doped ZnO nanoparticles found to reduce the IR radiative heat generation built-up on the glass surface. A reduction of surface temperature from 52.6 to 43.37 ^{o}C was observed. However, the multilayer above 20 coatings, lost its optical transparency. In addition to heat reduction benefit, AZO dispersoids are also contributing to enhancing the mechanical hardness as well as scratch resistant of PMMA films. The AZO/PMMA coating was also attempted for its anti-freezing property with liquid nitrogen and found to be promising.

The studies of this Chapter have been published.

Soumya, S.; Mohamed, A. P.; Mohan, K.; Ananthakumar, S., Enhanced near-infrared reflectance and functional characteristics of Al-doped ZnO nano-pigments embedded PMMA coatings, *Solar Energy Materials & Solar Cells*, 143, **2015**, 335-346.

CHAPTER 4

ZnO Quantum Dots Dispersed PMMA Hybrid Coatings

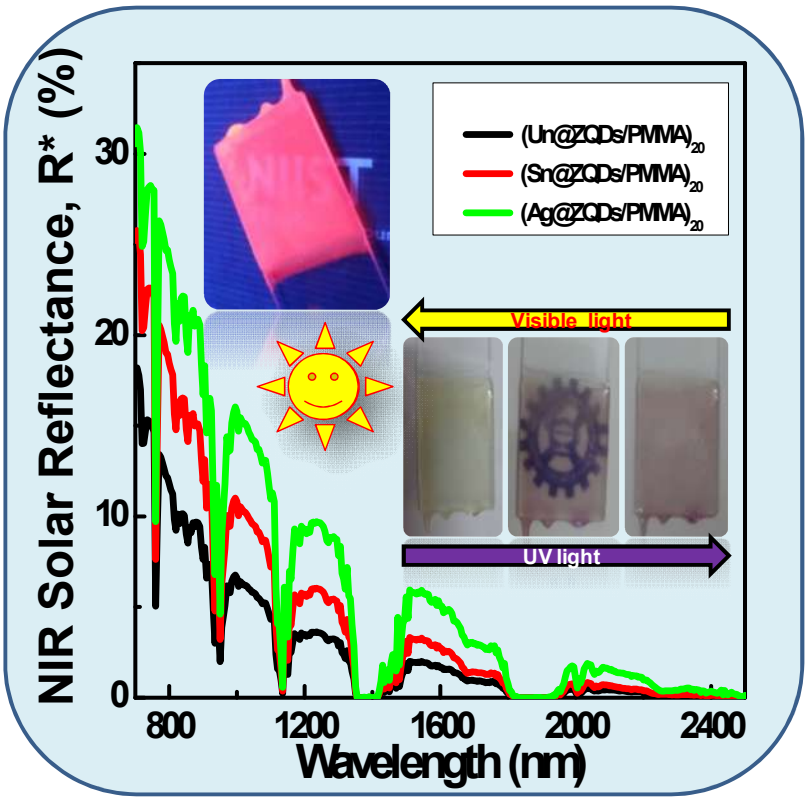

PREAMBLE

This part of the work emphasizes the effect of Sn and Ag doped ZnO quantum dots (ZQDs) on IR reflectance and UV shielding properties of PMMA coatings. The ZQDs were synthesized via microwave-reflux assisted sol-gel synthesis. An *in situ* polymerization reaction was conducted with ZQDs dispersed acrylic monomer to obtain ZQDs/PMMA hybrid coatings. In addition to the UV shielding and NIR reflective properties, the influence of organic chromophore (spiropyran) was also studied to obtain photochromic top coats on glass substrates.

4.1. INTRODUCTION

The solar radiation control coatings designed with doped semiconductor materials, which are further revamped and offers desirable multiple functions like UV shielding, photoluminescence, visible light transmission and significant IR reflectance [Gorgolis *et al*., 2016; Fang *et al*., 2013]. The aforesaid nanoscale semiconducting metal oxides out of Sn, In and Zn are recommended to develop spectrally selective thin films on glass and polymer substrates [Granqvist 2007; Jeevanandam *et al*., 2007; Sriramulu *et al*., 2016; Gorgolis *et al*., 2016]. Earlier reports show that low emissivity coatings are possible with indium tin oxide, antimony tin oxide and lanthanum hexaboride [Smith, 2004; Gorgolis *et al*., 2016]. However, in these kinds of semiconducting nanostructured coatings, only a limited success is realized since the doping level could not be made as high as to provide large reflectance in the IR part of the solar spectrum. One of the widely accepted coating designs is fabricated by the sequential deposition of appropriate metal/dielectric/metal oxide multilayers on the substrate, where the thickness of the individual films is carefully controlled to have maximum IR reflective quality [Zhou *et al*., 2014].

Studies of direct deposition of semiconducting metal oxides and high refractive index materials on the substrates were also reported earlier [Choi *et al*., 2014]. Sol-gel [Subramanian *et al*., 2008], sputtering [Kitano *et al*., 2006] and physical vapor deposition [Jung, 2008] techniques were widely employed for such thin film depositions. In fact, silver has been extensively considered as the best choice for the metal layer assembly because of its high infrared reflectivity and comparatively low absorption capability in the visible region [Glenn *et al*., 2013; Bartek *et al*., 1999; Fang *et al*., 2013; Gorgolis *et al*., 2016].

In recent days, application of active interface layers capable of shielding UV/IR waves effectively is preferred from polymer based low-temperature coatings. For the assembly of such active-interface layers, the polymer is modified with nanostructured metal oxides. However, uniform dispersion of nanometric metal oxides in polymer hybrids that too with high refractive index is still very critical and technologically challenging. In situ sol-gel polymerization is a dominant approach for making metal oxide/polymer hybrid coatings [Matsuyama *et al*., 2012]. A high IR reflectance is within reach with polymer hybrid coatings when nanolevel, high refractive index materials such as TiO_2, ZnO, CeO_2 and ZrO_2 are chemically reinforced [Smith *et al*., 2002; Soumya *et*

al., 2016; Acosta *et al*., 2015]. Poly(methyl)methacrylate [PMMA] is a model system widely reported for hybrid coatings [Soumya *et al*., 2016; Acosta *et al*., 2015; Li *et al*., 2007]. In our earlier work, we have shown morphologically varied nano ZnO can improve the IR reflectance quality of PMMA [Soumya *et al*., 2014]. In this work, we proposed a hybrid coating with Sn and Ag doped ZnO quantum dots in *in situ* polymerized PMMA films. A rare earth phosphate and an organic dye molecule were also employed as co-activators to make the coating multifunctional. The characteristics such as UV shielding, NIR reflectance, photochromic and photoluminescence behaviors of the ZQDs/PMMA hybrid have been studied with respect to the dopants and co-activators.

4.2. EXPERIMENTAL SECTION

4.2.1. Materials and Reagents

Tin (II) acetate [Sn $(CH_3COO)_2$, Sigma-Aldrich], Silver nitrate GR [$AgNO_3$, Extra pure-Merck Specialities Private Limited, Mumbai, India], Zinc acetate dihydrate, $Zn(CH_3COO)_2.2H_2O$, [Extra pure-Merck Specialities Private Limited, Mumbai, India, assay 99%], 3-Aminopropyltrimethoxy silane [APS, $H_2N(CH_2)_3Si(OCH_3)_3$, Sigma-Aldrich, 97%], Methyl methacrylate [MMA, $CH_2=C(CH_3)COOCH_3$, Merck], α, α'-Azobisisobutyronitrile [AIBN, $[(CH_3)_2C(CN)]_2N_2$, Spectrochem. Pvt. Ltd. Mumbai, India], 2-Methoxyethanol AR [$HOCH_2CH_2OCH_3$, SDFCL, 99.5%], Monoethanolamine (for synthesis) [$CH_3CH_2ONH_2$, Merck, ≥99.0%], Zinc oxide nanoparticle [ZnO, <100 nm, Sigma-Aldrich], Spiropyran [SP, CSIR-NIIST, Trivandrum, India], and Lanthanum Phosphate [$LaPO_4$, Indian Rare Earth Ltd., India] were used to fabricate inorganic-organic hybrids. Monoethanolamine and 2-methoxyethanol were used as a stabilizer and solvent, respectively. Blue stars® micro slides [PIC-1, Polar industrial corporation, Mumbai, India] was used as substrates. Toluene and double distilled water were also employed as solvents wherever necessary.

4.2.2. Microwave-reflux Assisted Sol-gel Synthesis

Doped and undoped ZnO quantum dots were processed by microwave-reflux assisted sol-gel synthesis. In a typical synthesis, zinc precursor of 2.7 g zinc acetate dihydrate and 30 mL of 2-methoxy ethanol ($CH_3OCH_2CH_2OH$) were homogeneously mixed under constant stirring. To this solution the dopant precursor $Sn(CH_3COO)_2$ (2 mol%) was then added followed by the addition of 0.25 mL 3-aminopropyltrimethoxy

silane (APS). A white colloidal dispersion was obtained at this stage. It became a transparent, clear sol upon the addition of monoethanolamine (MEA). The reaction mixture was maintained at pH 10. The prepared homogeneous, transparent sol was refluxed at 70 °C in a microwave reactor [Sineo Microwave Chemistry Technology (Shanghai) Co., Ltd., MAS-II Plus microwave synthesis/extraction reaction workstation] with the microwave power of 300 W. The reaction was continued for 30 min and then removed and aged for 24 h at room temperature. At the end, a pale yellow colored transparent Sn doped ZnO quantum dots sol was obtained. The same procedure was repeated for obtaining Ag doped ZnO quantum dots sol using $AgNO_3$ (2 mol%) as dopant precursor. For a comparative study, the typical synthesis undoped ZnO quantum dots procedure was repeated without any dopants.

The above three sols received from Sn doped, Ag doped and undoped ZnO quantum dots were stored at 4 °C in order to prevent any further particle growth and aggregation. The Sn doped, Ag doped and undoped ZnO quantum dots sols were represented by Sn@ZQDs, Ag@ZQDs and Un@ZQDs, respectively.

4.2.3. Synthesis of ZQDs/PMMA Hybrids Sol for Coatings

The doped and undoped sol was further treated with 1:1 ethanol-water mixture and to harvest the ZQDs by centrifugal filtration. The product was washed several times with ethanol and then used for making the hybrids.

0.25 g of AIBN initiator was first ultrasonically dissolved in 20 mL of MMA monomer and 30 mL of 2-methoxyethanol was further added and stirred well. To this reaction mixture, 0.5 wt% of Sn doped ZQDs was added and sonicated for 15 min. A stable, translucent colloidal dispersion was finally obtained. It was *in situ* polymerized by the conventional refluxing technique for 4 h at 70 ^{o}C. The polymerization reaction produced metal doped ZQDs dispersed PMMA hybrid precursor. The precursor was further diluted with the adequate amount of toluene that resulted in the semi-transparent hybrid colloid. The procedure was repeated for obtaining the Ag doped ZQDs/PMMA hybrid colloids and the undoped hybrid colloid was obtained with the same procedure without the inclusion of any dopants. They were further used for fabricating hybrids coatings on glass substrates.

4.2.4. Fabrication of ZQDs/PMMA Hybrid Coatings

Blue stars® glass slides with a size of 75 mm long; 25 mm width, and thickness of 1.35 mm was boiled in concentrated HNO_3, cleaned and washed thoroughly with ethanol. The slides were dried at 80 °C in a vacuum oven and then used for making coatings. The coating was fabricated using a computer controlled dip-coater [KSV Instruments, Netherlands]. The cleaned glass substrate was dipped into the doped (Sn or Ag) and undoped ZQDs/PMMA hybrid colloids with an advancing and receding rate of 85.5 mm min^{-1}. A neat thin coating on both sides of the glass slide was obtained by giving a residence time for about a minute. The glass substrate once coated was cured prior to any successive dip-coatings. The coating process was repeated for obtaining 3, 5, 7, 12 and 20 layers of coatings. We have summarized the experimental steps schematically and shown in Figure 4.1.

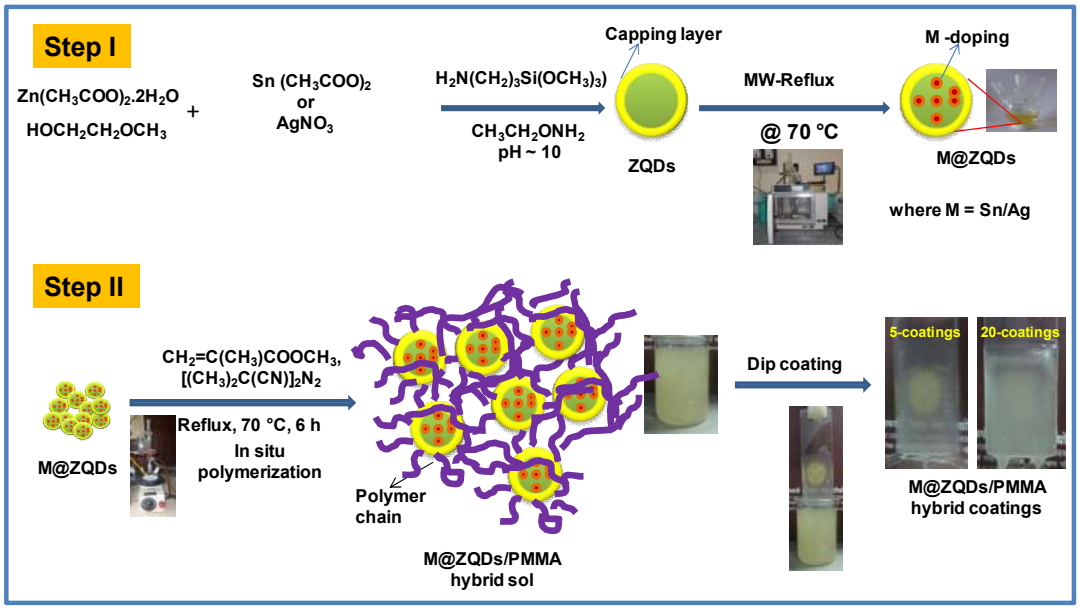

Figure 4.1: Schematic representation indicates (Step I) the synthesis of Sn and Ag doped ZQDs sol (Step II) *via in situ* polymerization process of metal ion doped ZQDs/PMMA hybrid coatings.

4.2.5. $LaPO_4$ Modified ZQDs/PMMA Hybrid Coatings

The doped ZQDs/PMMA colloid was ultrasonically blended with $LaPO_4$/PMMA sol prepared separately. 1 wt% $LaPO_4$ was used for obtaining the $LaPO_4$/PMMA precursor sol. The ZQDs/PMMA hybrid coated glass (20 times coatings) was further

employed for a top-coat with $LaPO_4$/PMMA sol in which the coating was developed for 3 times.

4.2.6. Preparation of Photochromic ZQDs/PMMA Hybrid Coatings

ZQDs dispersed PMMA precursor sol was treated with the organic dye molecule, *spiropyran* to obtain light sensitive hybrid coatings. 0.005 g of spiropyran (SP) was added to the doped ZQDs/PMMA hybrid colloid and stirred homogeneously for 30 min under dark condition. It was carefully coated on the glass substrate, in the absence of light, via a similar dip coating technique, under identical coating conditions.

4.2.7. Characterizations

In this Chapter, doped ZnO quantum dots were first confirmed by XRD, Raman, DLS, TEM, SAED, EDX, UV/Vis absorption and PL spectra. The surface analysis, coating thickness and optical properties of doped ZQDs/PMMA hybrid coatings were characterized using SEM, UV/Vis absorption, PL and UV/Vis/NIR spectroscopic analysis.

The crystalline nature and phase purity of the doped (Sn and Ag) and undoped ZQDs was first characterized by powder X-ray diffractometer using X'Pert Pro, Philips X-ray diffractometer equipped with Cu K_α radiation (λ = 1.5406 A°) in the 2θ range 10 to 80° with 0.02 scan increment. In order to ensure the doping, the as prepared Sn and Ag doped ZnO quantum dots were first examined using Confocal Raman, UV/Vis and PL spectroscopic techniques in addition to the powder X-ray diffraction (XRD) and TEM/EDAX analysis. Raman spectra were measured using WI-Tec Raman microscope (Confocal Raman Microscope (alpha300R, WITec Inc. Germany) with a wavelength of 633 nm laser excitation. Prior to every measurement, a calibration with a silicon standard (Raman peak centered at 520 cm^{-1}) was performed. WI-Tec Project plus (v 4.1) software package was used for the data evaluation. The confocal micro-Raman spectra of undoped and doped ZQDs were recorded in the range of 200-1500 cm^{-1}. The spectra of Aldrich ZnO (bulk ZnO) was also obtained to compare the nature and the structural modifications in ZnO quantum dot with the bulk ZnO. Raman scattering is a powerful technique for studying the doping characteristics and lattice disorders about the host lattice. Further, it could also reveal the existence of secondary phases due to the substitution of dopants as these secondary phases could not be detected by XRD [Georgekutty *et al*., 2008].

Shimadzu UV/Vis spectrophotometer (UV 240 IPC) was employed for recording the UV absorbance of doped and undoped ZQDs colloid in the wavelength region 200 to 800 nm. The UV/Vis absorption measurements were corrected initially using 2-methoxy ethanol as the reference. The PL spectra of the doped and undoped ZQDs in 2-methoxyethanol were taken at room temperature using a Cary Eclipse spectrofluorometer (Varian, Australia) with an excitation wavelength of 360 nm. The Dynamic Light Scattering (DLS) measurement was conducted to measure the particle size at 25 °C using the equipment Zetasizer 3000 HSA, Malvern Instruments, UK. The morphology and chemical composition of the doped and undoped ZQDs were further ascertained by Transmission Electron Microscopy (TEM) and Selected Area Electron Diffraction (SAED) analysis using the instrument FEI Tecnai 30G2S-TWIN transmission electron microscopy operated at an accelerating voltage of 300 kV. The presence of different elemental composition was further detected by Energy-Dispersive X-ray (EDX) spectroscopy. Surface functional groups of ZQDs were analyzed by IR Prestige-21, Shimadzu FTIR spectrophotometer in the scanning range 4000-400 cm^{-1} using the standard KBr (Sigma-Aldrich, 99%) pellet as the reference. The coating morphology and thickness were examined using Scanning Electron Microscope (SEM) [Model: ZEISS EVO 18]. The coating surface texture was scanned in tapping mode using Atomic Force Microscope (AFM) (Bruker Multimode, Germany) in the area 3 × 3 μm and 1 × 1 μm.

The Near-Infrared (NIR) diffuse reflectance (700-2500 nm) spectra of the doped and undoped ZQDs/PMMA hybrid coatings were analyzed by Shimadzu UV/Vis/NIR spectrophotometer (UV-3600) with an integrating sphere attachment (ISR-3100). The instrument was calibrated using poly(tetraflouroethylene) (PTFE) as reference. The NIR solar reflectance (R^*) in the wavelength range from 700 to 2500 nm was calculated in accordance with the ASTM standard number E891-87 [Jose *et al.* 2014; Sangeetha *et al.,* 2012]. The NIR solar reflectance at wavelengths between 700 and 2500 nm that is reflected by a surface is the irradiance-weighted average of its spectral reflectance, $r(\lambda)$ in Wm^{-2}, can be determined from the Equation 4.1:

$$R^* = \frac{\int_{700}^{2500} r(\lambda) i(\lambda) d(\lambda)}{\int_{700}^{2500} i(\lambda) d(\lambda)} \tag{4.1}$$

where $r(\lambda)$ is obtained from the experiment and $i(\lambda)$ is the solar spectral irradiance (Wm^{-2} nm^{-1}) obtained from ASTM standard E891-87. The optical studies were also conducted for the hybrid coatings using the aforementioned Shimadzu UV/Vis spectrophotometer (UV 240 IPC) and Cary Eclipse spectrofluorometer.

4.3. RESULTS AND DISCUSSION

4.3.1. Characterizations of Doped and Undoped ZnO Qunatum Dots

4.3.1.1. XRD Analysis of Doped and Undoped ZQDs

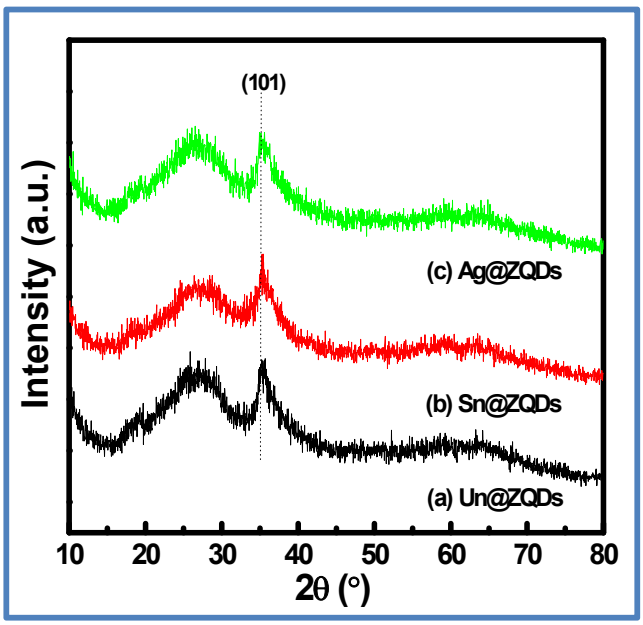

Figure 4.2: XRD patterns of (a) Un@ZQDs, (b) Sn@ZQDs and (c) Ag@ZQDs powder dried at 60 °C.

The powder X-ray crystallinity of ZQDs appearance of doped and undoped ZQDs was shown in Figure 4.2. The X-ray patterns in Figure 4.2(a) clearly reveal the evolution of single peak correspond to nucleation of ZnO crystallites in all three undoped, Sn doped and Ag doped ZQDs under the given mild reaction conditions of microwave-reflux synthesis. A slight shift in the 2θ value of ZnO peak from 35.56 to 34.86° in the doped ZQDs counterparts was observed indicating the influence of dopants in the crystal nature. Broadening of diffraction peaks is the evidence for the growth of sub-nano size ZQDs, which can be ascertained from the Debye-Scherrer formula: $(D) = 0.9\lambda/B \cos \theta$ [Zhang *et*

al., 2010a]. The calculated crystallite sizes in the cases of Un@ZQDs, Sn@ZQDs and Ag@ZQDs were in the range of 5.41, 3.16 and 4.56 nm respectively. It is well documented that the microwaves interact with the matters depending upon the dielectric nature of reaction medium. In addition to the low reaction temperature of 70 ^{o}C employed for the microwave-refluxing, the highly polar organic medium readily interact with the microwaves and provide actual driving force for the nucleation and growth of sub-nanometer sized Sn and Ag doped ZQDs crystallites within 30 min of reaction time. The dimensional control of the ZQDs is further taken care by the presence of capping agent, 3-aminopropyl trimethoxy silane [Zhang *et al*., 2010b]. From the XRD results, it is understood that there are no separate crystalline phases formed out of the doping ions. The doped impurity ions created only a random strain in the unit cell that resulted in the shifting of diffraction peaks to lower 2θ values [Lupan *et al*., 2010].

4.3.1.2. DLS Particle Size Analysis and Colloidal Nature of ZQDs

The average particle size of undoped and doped ZQDs was measured by DLS method is shown in Figure 4.3. The values obtained from DLS measurement were 3.27, 2.69, and 2.89 nm, for the monodispersed Un@ZQDs, Sn@ZQDs, and Ag@ZQDs respectively. In many studies, the exciton Bohr radius of ZnO has been reported as ~2.5 nm [Senger *et al.,* 2003; Sun *et al*., 2007]. In the present work, the dimension of the as-grown ZnO crystallites is close to the reported Bohr radius value. Since the microwave-refluxed sol-gel derived ZnO satisfy the Bohr radius dimensional limit, they can be defined as ZnO quantum dots. Moreover, the undoped and doped ZQDs crystallites were completely dispersed in 2-methoxy ethanol producing a transparent yellowish colloidal sol, which was stable over a period of 6 months under 4 °C. Figure 4.4 shows the colloidal nature of Tyndall effect observed in Un@ZQDs, Sn@ZQDs, and Ag@ZQDs, which is very typical to the nanometric dispersions.

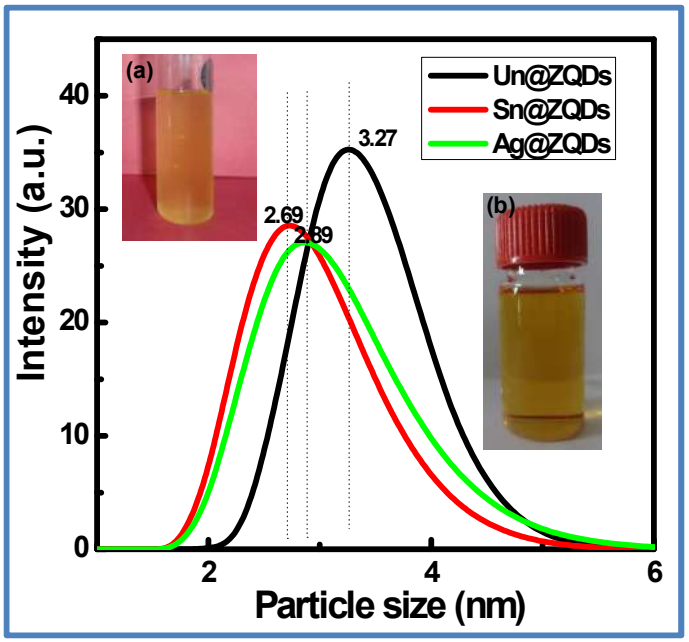

Figure 4.3: DLS shows the particle size of Un@ZQDs, Sn@ZQDs and Ag@ZQDs sol in 2-methoxy ethanol medium (inset photographic images of (a) Un@ZQDs and (b) Sn@ZQDs).

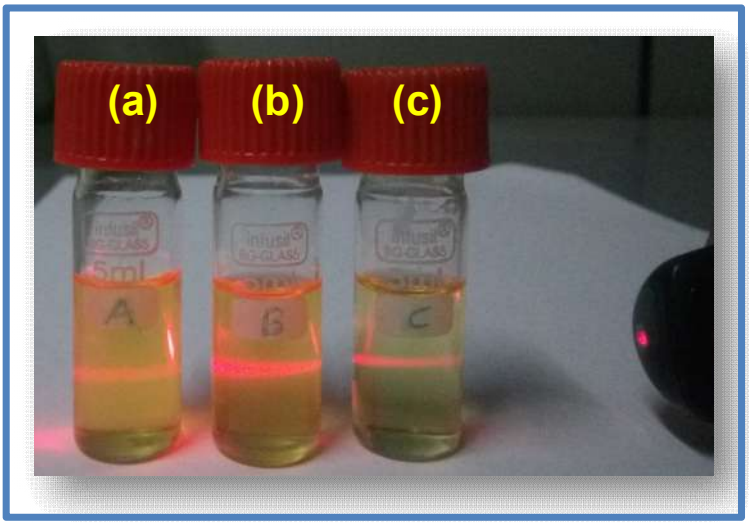

Figure 4.4: Photographic image shows the Tyndall effect observed in (a) Un@ZQDs, (b) Sn@ZQDs and (c) Ag@ZQDs.

4.3.1.3. Raman Spectral Analysis of Doped and Undoped ZQDs

The presence of Sn and Ag doping ions within ZnO is confirmed *via* Raman analysis. The doping ion impurities preferentially occupy the positions in the crystal lattice according to their ionic radius. The Ag^{+} and Sn^{2+} possess larger ionic radii compared to Zn^{2+} [Zn^{2+} (0.074 nm), Sn^{2+} (0.118 nm) and Ag^{+} (0.126 nm)]. As a result, the doping impurities occupy the site in the vicinity of grain boundaries of ZnO [Lupan *et al*., 2010]. Hence more defects were created in the host lattice. Figure 4.5 shows the fingerprint of Raman for the samples undoped and doped ZQDs. In the Raman spectra of standard bulk ZnO [Figure 4.5(a)], a sharp peak was obtained at 437 cm^{-1}. It can be assigned as the high frequency branch of E_2 mode of ZnO, which is the strongest and characteristic mode of wurtzite structure usually associated with the crystalline quality of ZnO [Mahmood *et al*., 2013]. The Raman shift at 393 and 570 cm^{-1} correspond to oxygen deficiencies present in the host lattice which was confirmed in the spectra of undoped ZQDs obtained in this work [Figure 4.5(b)].

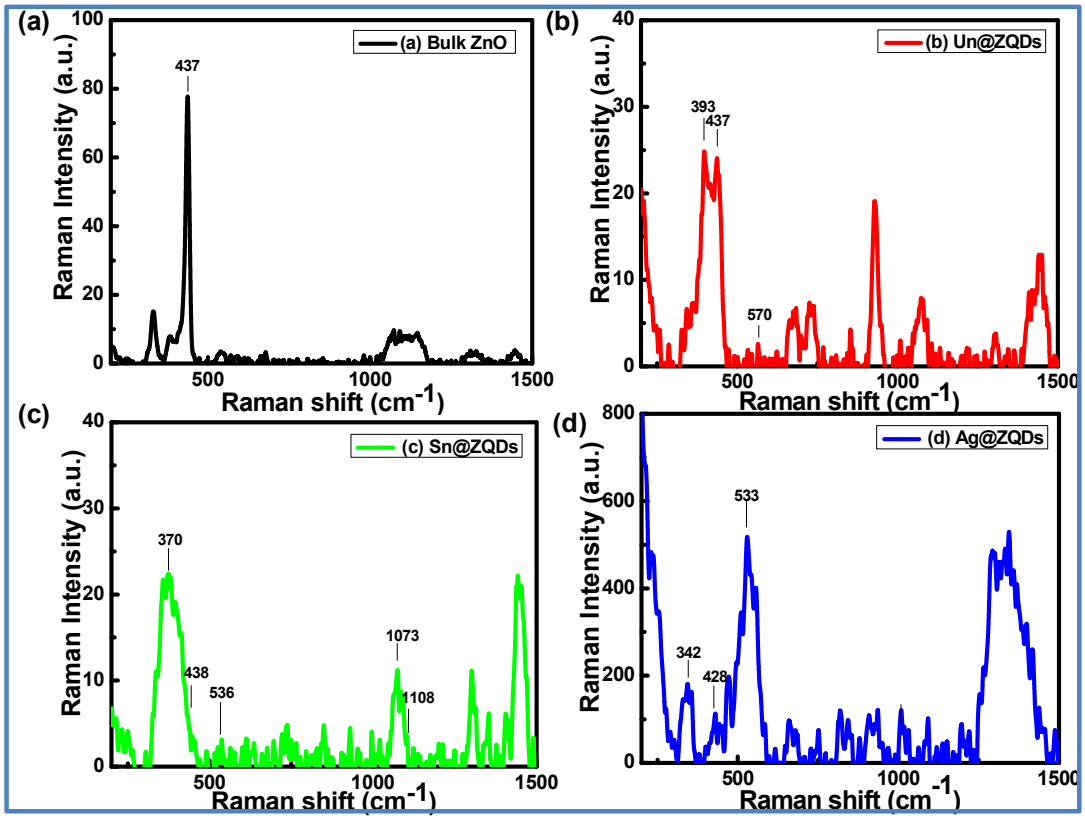

Figure 4.5: Raman spectral analysis of (a) Bulk ZnO, (b) Un@ZQDs, (c) Sn@ZQDs and (d) Ag@ZQDs.

All prominent peaks belonging to ZnO Raman spectra are confirmed in Sn and Ag doped ZQDs also. But slight shift in the peak positions with an intensity change and broadening of peaks indicate the incorporation of impurity at the Zn^{2+} lattice site. These changes are occurred due to the influence doping by Sn^{2+}/Ag^{+} and Zn^{2+}. The increase in the emission intensities at 370, 438, 536, 1073-1108 cm^{-1} for Sn-doped ZnO compared with that of pure and undoped ZQDs could be attributed to doped Sn in the ZnO host matrix [Figure 4.5(c)] [Bai *et al*., 2011]. Raman shifts occurred at these frequencies strongly indicate the diffusion of impurity dopant ions within the host lattice and generated intrinsic defects in the crystal lattice. In the case of Ag@ZQDs, the high intensity Raman shifts at 428 and 533 cm^{-1} strongly suggest the Ag impurity phase at the defective sites of ZnO [Figure 4.5(d)]. The downward shifting of peaks in the doped structure may be due to the phonon confinement effect in the quantum dots [Kuriakose *et al*., 2014]. The strong mode at 342 cm^{-1} confirming about the quantum dot modification of Ag obtained with ZnO [Serrano *et al*., 2007]. From Raman and XRD data, it is confirmed that the microwave assisted sol-gel refluxing resulted in doped ZQDs with controlled dimensions. The optical property of ZQDs is further ensured by UV/Vis absorbance and Photoluminescence studies.

4.3.1.4. UV/Vis Absorbance Spectra of Doped ZQDs

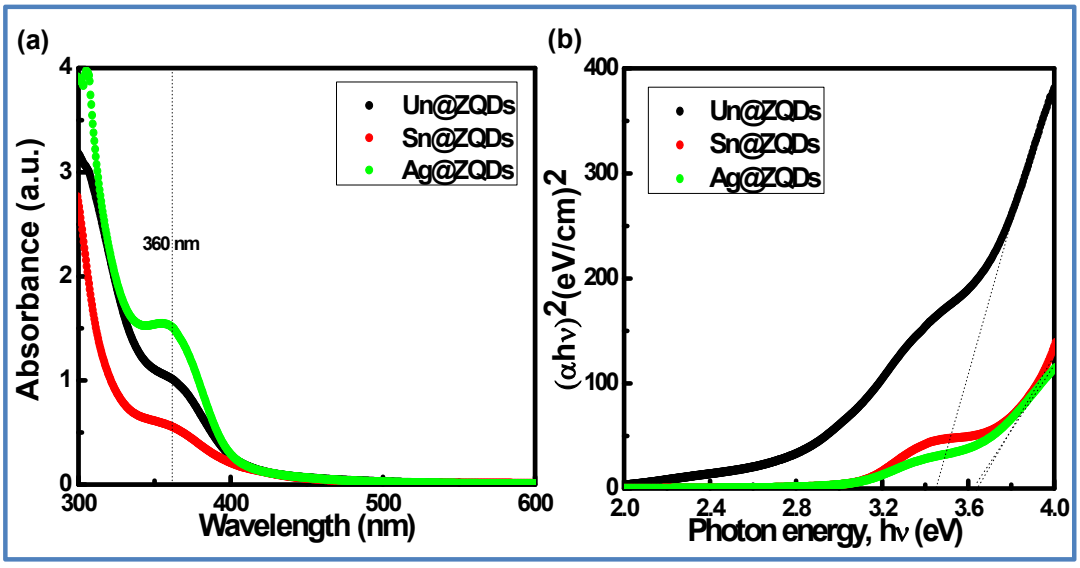

Figure 4.6: (a) UV/Vis absorbance spectra of Un@ZQDs, Sn@ZQDs and Ag@ZQDs sol, (b) The plot of $(\alpha h\nu)^2$ versus photon energy for corresponding ZQDs sol.

The optical absorbance/luminescence is also an evidence for understanding the doping and its associated crystal defects. We have studied the band gap of undoped and doped ZQDs by UV/Vis absorption spectra. Figure 4.6(a) shows the representative UV/Vis absorption spectra of undoped and doped ZQDs prepared *via* sol-gel microwave-reflux method. The results clearly indicate a strong UV absorption peak at 360 nm. This distinct λ_{max} at this absorption range reveals the as prepared ZQDs show quantum confinement. The absorption edge of ZQDs is comparatively broader than the bulk ZnO. In the case of doped ZQDs, rather than a sharp absorption maximum at 360 nm, a slight broadening only seen. The absorption intensity was higher in the case of Ag doped ZQDs compared to Sn doped counterpart. It is known that when the crystallite size is smaller than the excitation radius, quantum confinement leads to size-dependent enlargement of the band gap, which in turn results in a blue shift in the absorbance onset. The Figure 4.6(b) shows the photon energy of the synthesized ZQDs. From the plot between $(\alpha h\nu)^2$ *vs* photon energy ($h\nu$), the linear dependence of $(\alpha h\nu)^2$ on $h\nu$ at higher photon energies indicate the direct band gap transition of the respective ZQDs. The extrapolation of the linear portion of the curve to zero gave the value of the direct band gap (E_g) corresponding to the ZQDs. The E_g values of the Un@ZQDs, Sn@ZQDs, and Ag@ZQDs were determined as 3.45, 3.64 and 3.63 eV respectively. The optical band gap increased in the case of doped ZQDs explains the quantum size of the particles thus enhanced the blue shift in the absorption spectra [Fu *et al*., 2007].

4.3.1.5. Photoluminescence Spectra of Doped and Undoped ZQDs

Photoluminescence results further confirm the ZQDs crystal quality and doping effect. In PL spectrum, UV emission is attributed to the direct exciton recombination and could be termed as band gap emission. The origin of visible broadband is usually related to structural defects and/or impurities. Photoluminescence spectra of doped ZQDs sol reveal information about the intrinsic and extrinsic defects exist in the ZQDs. The defects could affect the position of band edge emission as well as the shape of the luminescence spectrum [Asok *et al*., 2012]. Figure 4.7 shows the PL spectra of undoped, Sn and Ag doped ZQDs synthesized *via* microwave-reflux method.

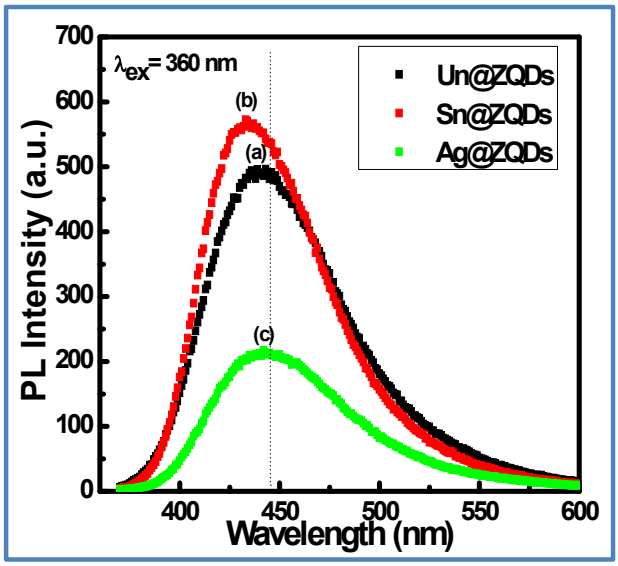

Figure 4.7: PL spectra of synthesized ZQDs sol in 2-methoxy ethanol *via* microwave-reflux method: (a) Un@ZQDs, (b) Sn@ZQDs, and (c) Ag@ZQDs.

Since nano dimensional semiconducting crystals have the large surface to volume ratio, the large number of surface defects is generated. It has a profound role in deciding the optical luminescence. In the present study, the appearance of blue luminescence at the wavelength region 430 to 450 nm is attributed to the dimensionally controlled small ZQDs particles. The PL intensity of Sn and Ag doped ZQDs sol shows excellent stability similar to the undoped ZQDs. In the PL spectra, the excitation at 360 nm emissions of Un@ZQDs, Sn@ZQDs and Ag@ZQDs sol are 434, 445, and 430 nm wavelengths respectively. In the spectra, it is obvious that the emissions of Sn@ZQDs sol are centered at 445 nm and the intensity of the maximum emission is enhanced remarkably in Sn doping, which may be attributed to the defective structure due to impurity [Xiong *et al*., 2009]. The present study is well supported by the literature reported on the synthesis of lanthanum-doped ZnO quantum dots by a modified sol-gel method under atmospheric conditions, which greatly shows the enhanced photoluminescence [Sun *et al*., 2012]. In the case of Ag@ZQDs, the substituted Ag^{+} for Zn^{2+} ions in the crystal may induce hybridization and charge transfer from a donar-derived impurity band to unoccupied 3d states at the ZnO Fermi level. The dopants create more oxygen vacancies in the host lattice, while doping and this internal defective structure offer the effective luminescence. The intensity of this band gap emission in Ag@ZQDs is considerably reduced compared to undoped ZQDs emission. The atomic level deposition of silver clusters must have

preferably formed a shielding layer on the surface of the doped ZQDs which may lower further concentration of surface defects thus resulted from the reduction of fluorescence intensity. The doping of silver into zinc oxide does not lead to a new emission band in the room temperature PL spectra, similar to earlier observations [Hosseini *et al*., 2015]. The emission nature of ZQDs dispersed in the 2-methoxyethanol medium is also photographed and is shown in Figure 4.8 under visible light (a-c) as well as under UV lamp at 365 nm (d-f).

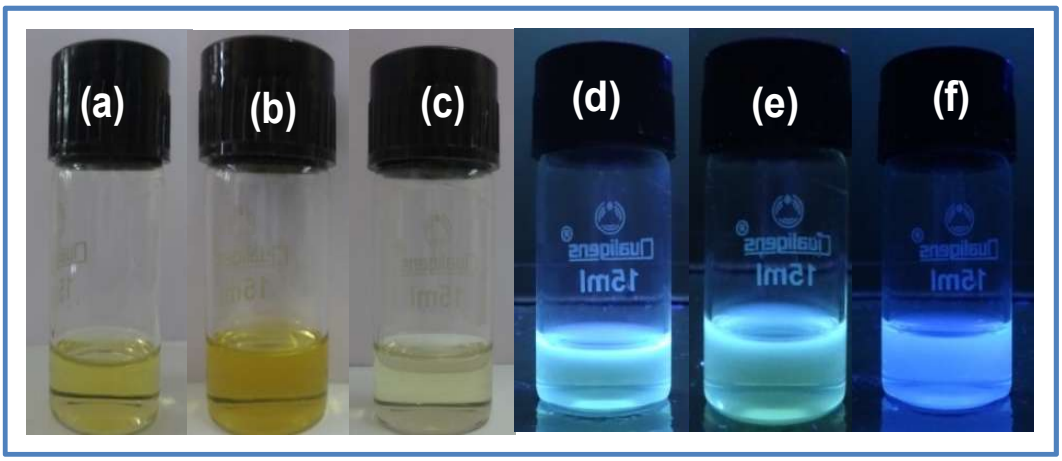

Figure 4.8: The photographic images of corresponding samples under visible light (a-c) and UV lamp @ 365 nm (d-f) respectively.

4.3.1.6. TEM analysis of ZQDs

Figure 4.9 depicts the TEM images of the doped and undoped ZQDs. In the microscopic images, the as-grown ZnO has actually appeared as nanoclusters in which the assembly of quantum size ZnO crystallites are seen [Figure 4.9A-C]. The size of a nanocluster is about 20 nm and contains ZnO quantum dots with the average size in the range of ~2-5 nm. The SAED analysis of synthesized ZQDs has shown the pattern of diffracted rings. The clarity of the SAED pattern diminished in the doped ZQDs. This indicates the doped ZQDs have weak crystalline nature; probably the impurity ions, as well as silane capping, prevented the excessive crystal growth. The TEM analysis further supports the particles are in quantum size range and the doping has also occurred effectively under the given mild synthesis conditions.

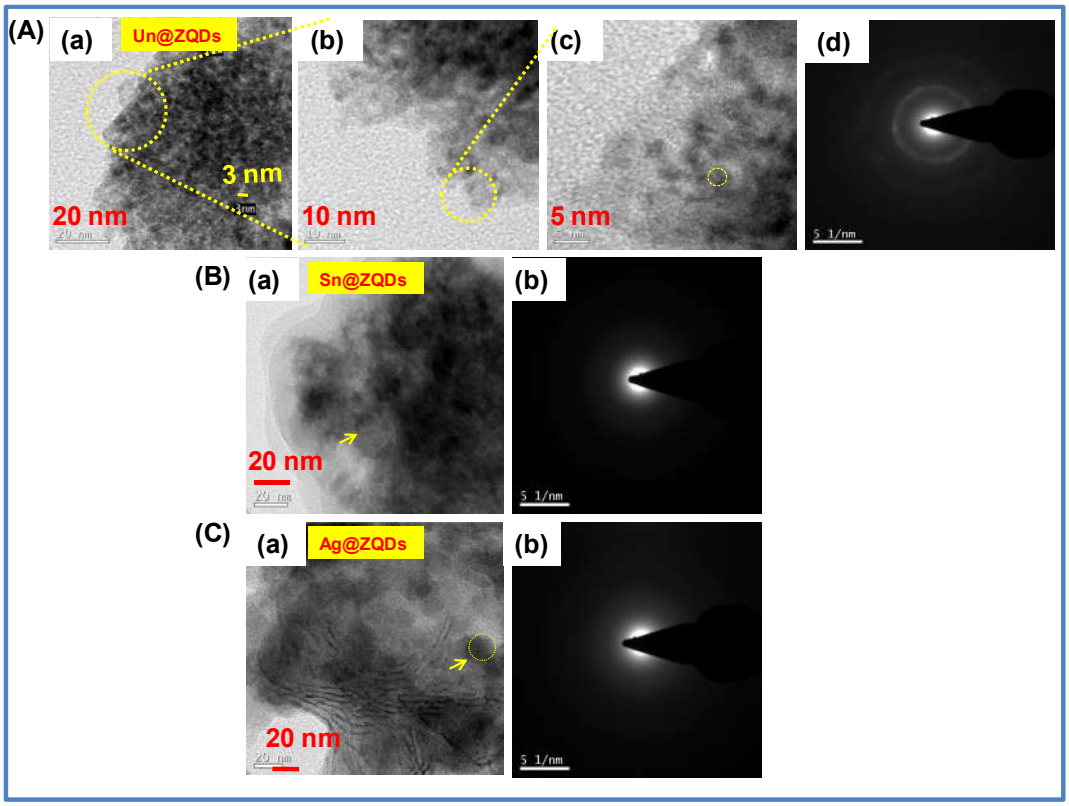

Figure 4.9: TEM, HRTEM images and its corresponding SAED patterns of microwave synthesized (A) (a) Un@ZQDs, (b, c) its higher magnifications and (d) its SAED pattern. (B) (a) Sn@ZQDs and (b) its SAED pattern. (C) (a) Ag@ZQDs and (b) its SAED pattern.

4.3.1.7. FTIR Analysis of the ZQDs

Figure 4.10 describes the FTIR spectra of undoped and doped ZQDs, obtained under vacuum conditions. The IR analysis provides a supporting proof for the metal ion doping on ZQDs lattice to form amorphous M^{n+}/ZQDs species. The most important information in the IR spectrum is found in the region below 1000 cm^{-1}, which illustrates the presence of internal metal–oxygen interactions. There stretching vibration for Zn-O nanoparticle was obtained between 420-550 cm^{-1} in the doped and undoped ZQDs having an absorption center at 548 cm^{-1} [Hosseini *et al.*, 2015; Shah *et al.*, 2013]. While doping with metal ions the bond deterioration takes place in Zn-O leading to a slight shift in the IR frequency. In the doped ZQDs a small band near at 764 and 718 cm^{-1} was observed due to the stretching of Sn-O and Ag-O respectively. The Zn-O-Si stretch was obtained at 1005 cm^{-1} in the undoped ZQDs and in doping it is reduced to the lower frequency of

1067 and 1020 cm^{-1} respectively in Sn@ZQDs and Ag@ZQDs. The organic capping is responsible for the shifting of M-O band (Ag-O/Sn-O) to the lower frequency region.

The bands at 1214, 1199, 1191 cm^{-1} are attributed to the vibrational modes of Si–O–Si groups in Sn@ZQDs, Ag@ZQDs and Un@ZQDs respectively. Zn–O–Si symmetrical stretching vibration at 889 cm^{-1} indicates the presence of silane capped ZQDs. As expected, the stretching frequency for C-H vibration was obtained in the range of 2885 – 2951 cm^{-1} in all cases which originate from the propyl chain of silane moiety attached on the ZnO surface. Meanwhile, the bending mode of H-C-H was reflected at 1586 cm^{-1}. The presence of aminopropyl fragment of APS is confirmed from a vibrational mode observed at 1338 cm^{-1} and ascribed to the wagging modes of methylene units. The above results confirm the successful formation of silane functionalized metal doped ZQDs hybrids.

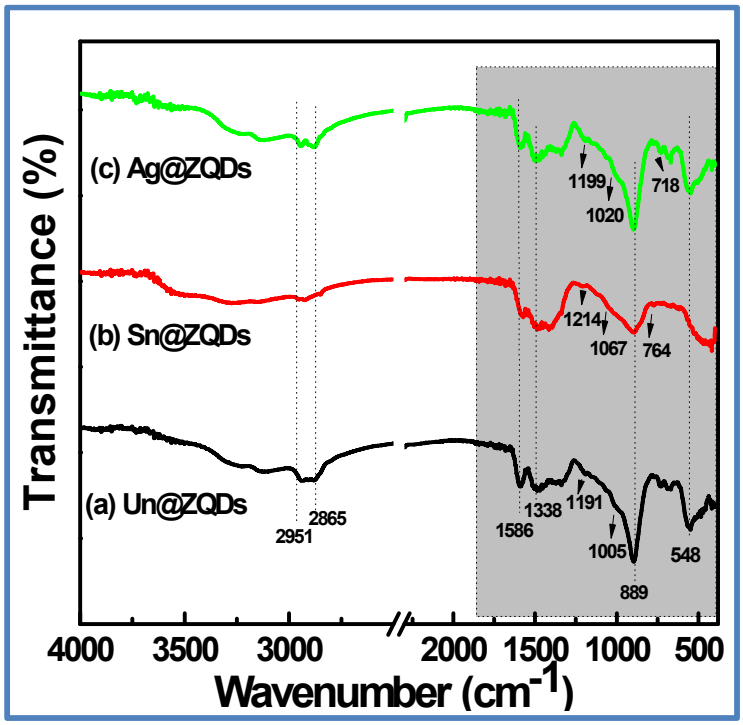

Figure 4.10: FTIR spectra of Undoped, Sn and Ag doped ZQDs dried powder at 60 °C.

4.3.2. Characterizations of ZQDs/PMMA Hybrids Coatings

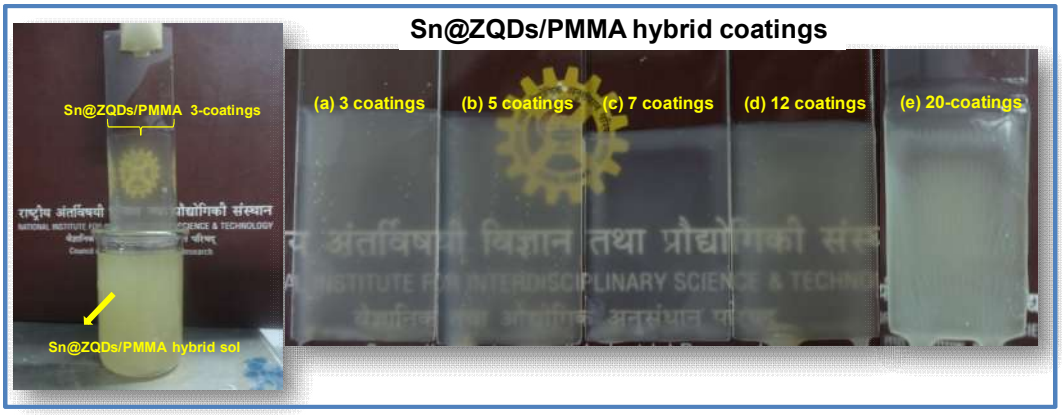

Figure 4.11: Photographic images of Sn@ZQDs/PMMA hybrid sol and its (a) 3, (b) 5, (c) 7, (d) 12, and (e) 20 coatings.

Multilayer assembly of ZQDs/PMMA coatings were characterized for studing the crystallinity and surface profile using SEM and AFM techniques. Figure 4.11 shows the photographic images of ZQDs/PMMA sol and the coatings developed on glass substrates. The coatings are transparent initially but as the number of coatings increases the transparency gradually decreases. The layer-by-layer hybrid coatings show appreciable transparency and homogeneity in the visible region up to 12 numbers of coatings.

4.3.2.1. Microstructure Analysis of ZQDs/PMMA Hybrid Coatings

In Figure 4.12 shows the SEM images of Ag and Sn doped ZQDs/PMMA hybrid coatings on the glass substrate. Figure 4.12A (a) and (b) depicts the top-surface view at different magnifications for the sample Ag@ZQDs/PMMA hybrids. This SEM image is observed on the 3 times coated layer assembly. The SEM shows ZQDs are well dispersed and forms a smooth topcoat. However, the coating has the distribution of pores with the average pore diameter of 4 µm. The pores nearly uniform and it is formed due to evaporation of solvent molecules. The cross-section image of the corresponding sample indicates the coating thickness is ~ 79 µm [Figure 4.12A(c)]. In Sn@ZQDs/PMMA hybrid coating, the formation of pores is visible. In this case, the 3-times coating layers produced thickness ~ 24 µm [Figure 4.12B(c)]. In this case, the clustering of ZQDs and its segregation is also noticed. In both cases, the SEM morphology confirms the

multilayer coatings obtained with ZQDs/PMMA hybrids are smooth, tightly bonded with the surface and wrinkle free. The coatings lost its transparency beyond 20 coatings.

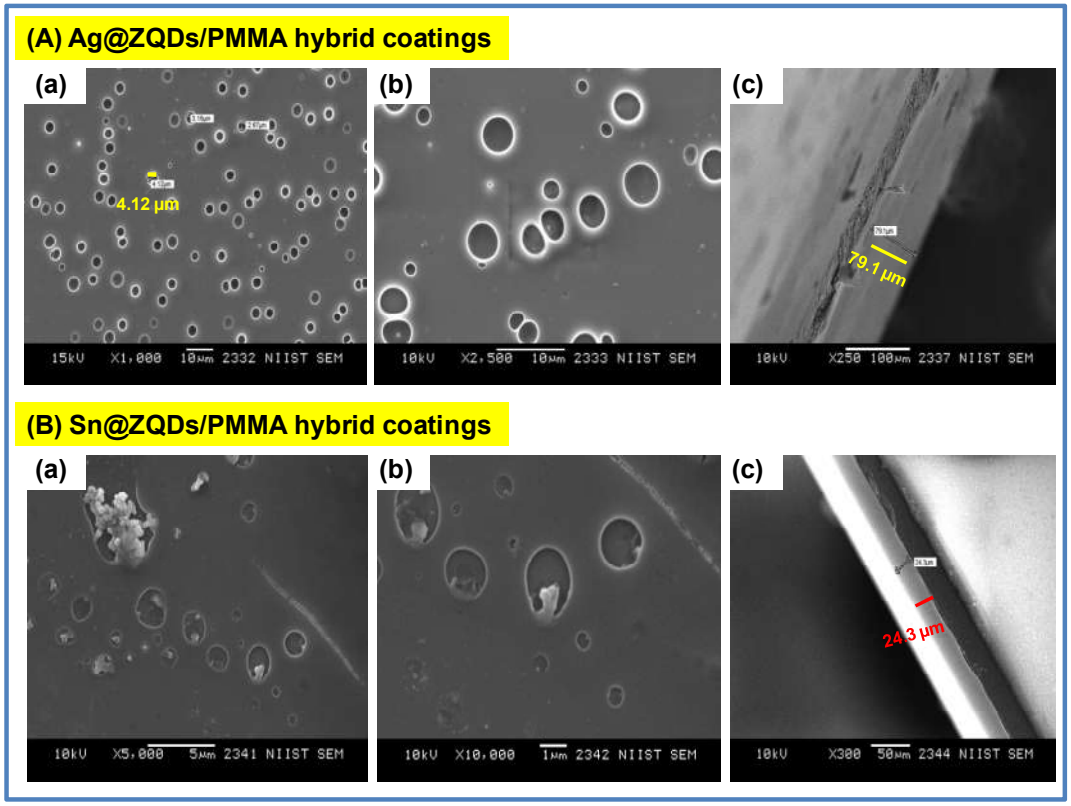

Figure 4.12: SEM images of doped ZQDs/PMMA nanohybrid coatings on the glass substrate (A) $(Ag@ZQDs/PMMA)_3$ coatings (a) top surface of the coating, (b) its magnified image and (c) cross-section image of the coating (coating thickness ~79 µm). (B) $(Sn@ZQDs/PMMA)_3$ coatings (a) its top surface view, (b) magnified image of the coating and (c) its cross-section with a coating thickness of 24 µm.

4.3.2.2. AFM Analysis of Doped ZQDs/PMMA Hybrid Coatings

AFM images in Figure 4.13 revealed the surface roughness and nano morphology of the doped ZQDs/PMMA hybrid coatings. The surface topography explains the structural uniformity of the coating with a crack free surface and confirms the ZQDs are embedded in PMMA matrix.

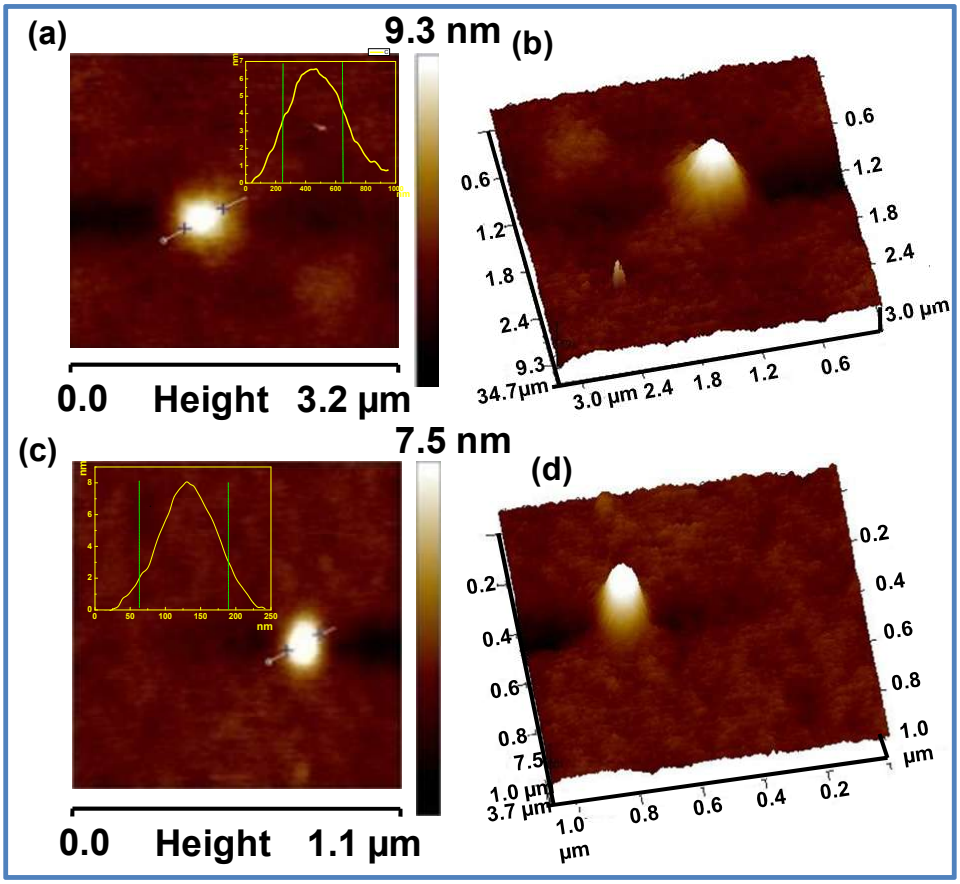

Figure 4.13: 2D and 3D AFM topography images of doped ZQDs/PMMA hybrid coatings: (a) & (b) $(Sn@ZQDs/PMMA)_1$ coating and (c) & (d) $(Ag@ZQDs/PMMA)_1$ coating. The inset shows the height profile diagram of the quantum dot.

4.3.2.3. UV/Vis Absorbance and PL analysis of ZQDs/PMMA Hybrids Coatings

Figure 4.14(a) shows the UV/Vis absorbance spectra of 20 times coated doped and undoped ZQDs/PMMA multilayer hybrid coatings. The absorption due to PMMA is 300 nm which is almost equivalent to amorphous glass [Soumya *et al*., 2015]. The absorption wavelength for Un@ZQDs/PMMA, Sn@ZQDs/PMMA, and Ag@ZQDs/PMMA are obtained at 343, 346 and 338 nm, respectively. The PMMA provides a hybrid binding to the quantum dots, due to this the absorption wavelength is greatly shifted to lower values in comparison with the absorption characteristics of the doped and undoped ZQDs. In Figure 4.14(b) depicts the photoluminescence emission spectrum of Sn@ZQDs/PMMA hybrid coatings with blue emission (inset in Figure 4.14(b) under UV lamp) exhibits a peak at 421 nm, which demonstrates the ZnO particles shows quantum size effect in PMMA matrix [Li *et al*., 2007].

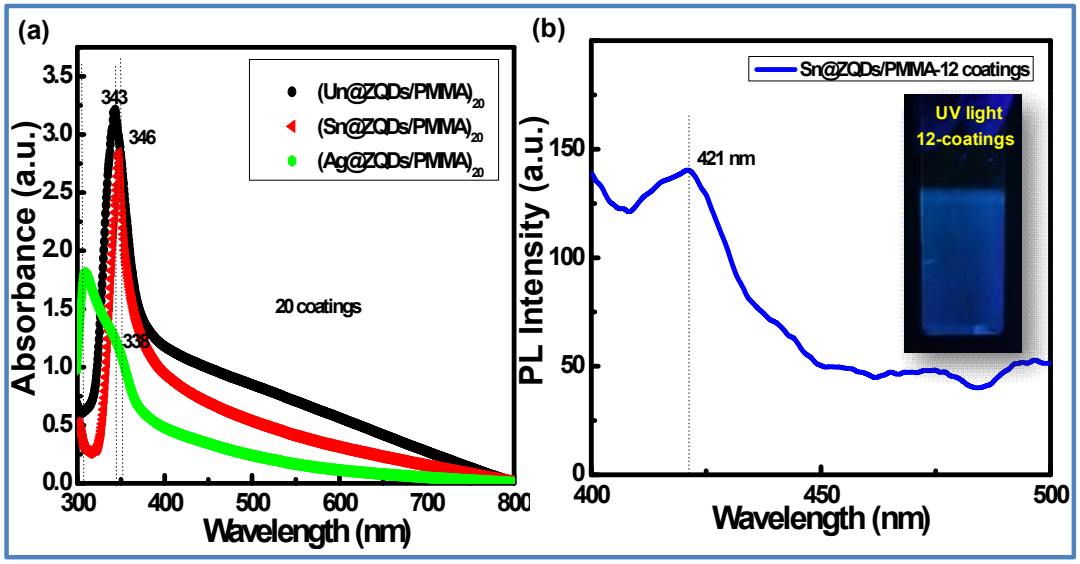

Figure 4.14: (a) UV/Vis absorbance spectra of Undoped, Sn and Ag doped ZQDs/PMMA hybrid 20-coatings on the glass substrate, (b) PL spectra of Sn@ZQDs/PMMA hybrid-12 coatings with excitation light of 330 nm (Inset shows the photographic image of its coatings under UV lamp @ 365 nm).

4.3.2.4. IR Reflectance Characteristics of Sn and Ag Doped ZQDs/PMMA Hybrid Coatings

It is reported that the doping of TiO_2 with elements like Al, Li, and K is one of the methods to improve the reflectance of TiO_2 particles [Kumar *et al*., 2013]. It is also proposed that the presence of impurities creates defects in the TiO_2 crystal lattice and introduces traps for electrons and holes. This will prevent the migration of electrons and holes towards the TiO_2 surface. In our previous study, we have observed the NIR reflectance of ZnO embedded PMMA enhances when Al is employed as the impurity to the matrix [Soumya *et al*., 2015]. Liu *et al.* investigated the near infrared reflectance of SnO_2 nanoparticles by tuning its shape via a sol–gel method [Liu et al., 2010]. In various reports, it is proved that the factors include mean particle size, particle size distribution, shape, porosity, packing density, surface texture, chemical composition, and refractive index are deciding the factors for the solar absorbance and optical reflection of a material in the NIR region [Fang *et al*., 2013]. The influence of doped quantum dots embedded PMMA hybrid coatings is seldom studied. The most appropriate particle size for reflecting the NIR waves in the wavelength region 800-1100 nm is reported as < 350 nm.

However, the quantum dots are much lower than the prescribed particle size range *i.e.* half the wavelength of the NIR waves. Interestingly quantum dots can result in highly transparent coatings and offer low thermal conductivity for good solar heat insulation. Moreover, in such hybrid quantum dots, the number of interparticle boundaries increases due to the reduction of physical dimension. It enables effective light reflection. The diffuse reflection usually takes place at the particle boundaries when a light irradiates onto the surfaces, and the intensity of the reflection depends on the number of particle boundaries. Apart from this, the coating thickness is another factor controls the NIR reflection. Higher coating thickness leads to a better reflectance of NIR waves because the number of reflective particles on the substrate is more.

In the present work, multiple layer coatings with doped quantum dots in PMMA is made up to 20 layers and the NIR reflectance is assessed. In the coatings, the undoped, and Sn and Ag doped ZQDs were well dispersed with a small degree of agglomeration.

The NIR reflectance and Total Solar Reflectance (R*) of Undoped, Sn and Ag doped ZQDs/PMMA hybrids coated 20 times on a glass substrate were presented in Figure 4.15 (a) & (b), respectively. The NIR diffuse reflectance of 14% was observed in the case of Un@ZQDs/PMMA. In the hottest NIR range of 700- 1100 nm, an enhanced reflectance of 23, and 30% was resulted with the Sn and Ag doped ZQDs/PMMA hybrids respectively. The reflectance was better when the impurity incorporated to the hybrid system of ZQDs/PMMA. The respective total solar reflectance values computed for the Un@ZQDs/PMMA, Sn@ZQDs/PMMA and Ag@ZQDs/PMMA coatings are 7, 19 and 29%, respectively. Compared to the undoped ZQD/PMMA hybrids, the TSR value is enhanced two times in Ag doped hybrids.

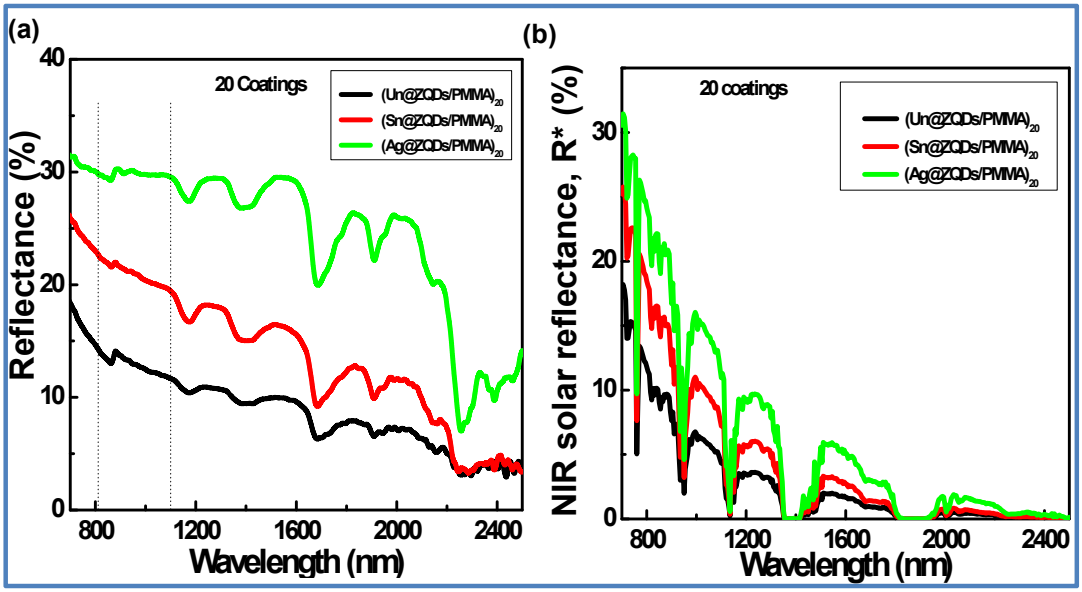

Figure 4.15: (a) & (b) depicts NIR reflectance and NIR solar reflectance of Undoped, Sn, and Ag doped ZQDs/PMMA coatings, respectively.

4.3.2.5. Effect of $LaPO_4$ Dispersoids in ZQDs/PMMA Hybrids

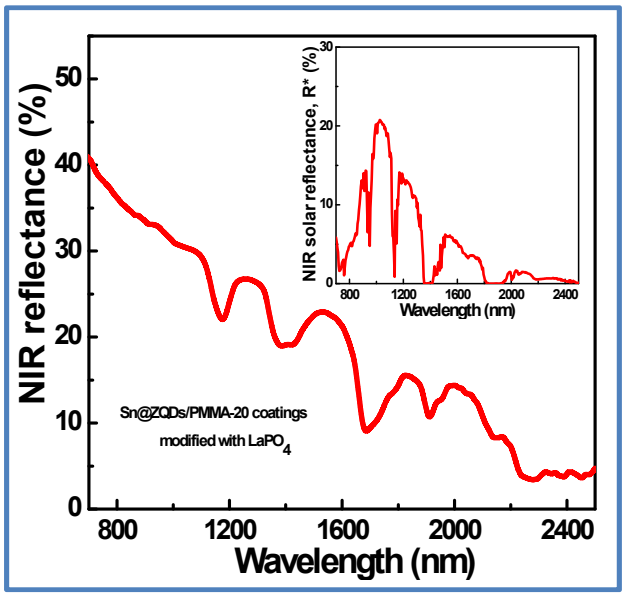

Figure 4.16: NIR reflectance and NIR solar reflectance of Sn@ZQDs/PMMA-20 coatings modified with $LaPO_4$/PMMA coatings.

In order to improve the NIR reflectance of Sn doped samples equal to that of Ag@ZQDs/PMMA hybrid, a novel top-coat was further incorporated using nano size $LaPO_4$ dispersed PMMA sol. PMMA/$LaPO_4$ sol was prepared by taking 3 wt% PMMA and 1 wt% $LaPO_4$ and applied over the Sn@ZQDs/PMMA hybrid coatings. When the modified coating is subjected to NIR reflectance characterization, we have seen the top-coat exhibits 36% of reflectance in the NIR range 700-1100 nm [Figure 4.16] and offered 23% of total solar reflectance [inset of Figure 4.16]. We have selected nano $LaPO_4$ for top-coat based on its IR reflectance, where we found the material covers more than 85% NIR reflectance in the entire IR region. It is observed that the additional coating provided with $LaPO_4$ improved the reflective behavior of the material by enhancing the brightness of the layer.

4.3.2.6. Photochromic Behaviour of Doped ZQDs/PMMA Hybrid Coatings

In addition to UV and IR shielding quality obtained in ZQDs/PMMA coatings, where a kind of solar heat control has arrived, a light sensitive organic dye is also introduced in the hybrid to make the coatings more functional. Thin films coatings made with TiO_2, MoO_3 and WO_3 have been earlier studied for photochromic properties by incorporating organic dye molecules [Kanu *et al*., 2010; Kafizas *et al*., 2013]. In this work, spiropyran (SP) was introduced into ZQDs/PMMA sol and coatings were developed. The photochromic behavior of ZQDs/PMMA/SP coated glass substrate was tested under UV and visible light and the results are presented in Figure 4.17.

A red luminescence was obtained for the coating under UV light, which is due to the conversion of spiropyran into merocyanine. The colorless spiropyran changes into red colored merocyanine on UV irradiation, which was confirmed by the absorption band obtained at 560 nm in the visible range [Yoon *et al*., 2013]. Later the red luminescence coating was turned to violet outside the UV chamber because the merocyanine is violet in the visible light. In the absence of UV irradiation, the merocyaninine (violet) shifts back to colorless spiropyran in the room temperature [Photographic image of coatings shown in Figure 4.18]. The UV-vis absorbance of the hybrid during the gradual reduction of its colorful violet to colorless was recorded in every 2 min. It is noticed that the absorption intensity reduces gradually and no absorption has resulted after 10 min. After 15 min, complete decolourization was taken place for the hybrid. This indicates the merocyanine dye has changed its isomeric state to spiropyran in the dye added ZQDs/PMMA hybrid

coating. The results confirm the photochromic behavior of the spiropyran added Ag@ZQDs/PMMA hybrid coated on a glass substrate.

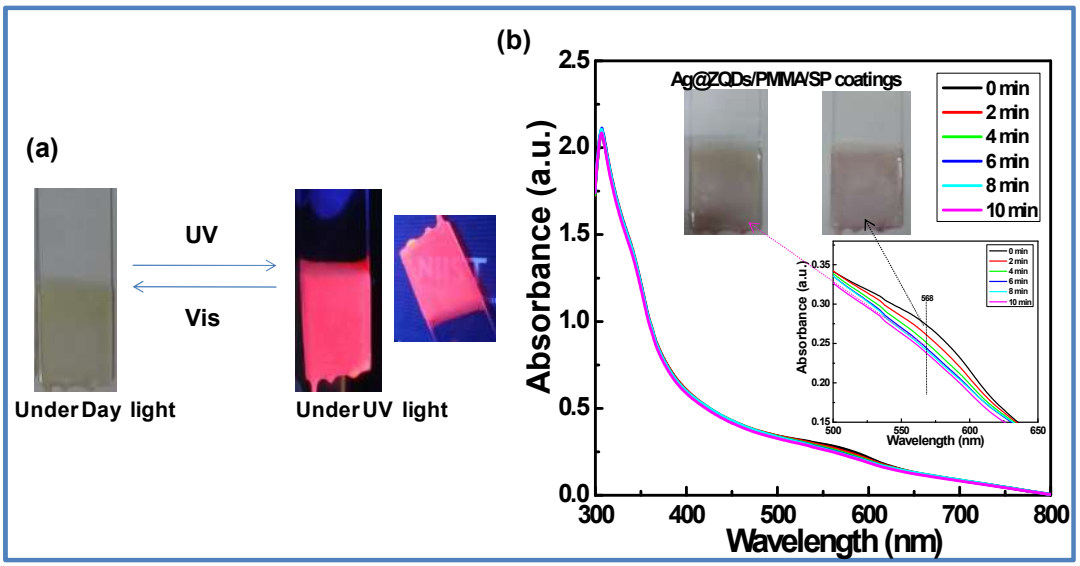

Figure 4.17: Photochromic behavior of spiropyran coated glass substrate. (a) Photographic images of Ag@ZQDs/PMMA/SP coated glass substrate under visible light and at long wave UV light, (b) UV-vis absorbance spectra of Ag@ZQDs/PMMA/SP coated glass substrate (inset shows the enlarged portion of the wavelength region from 500 to 650 nm).

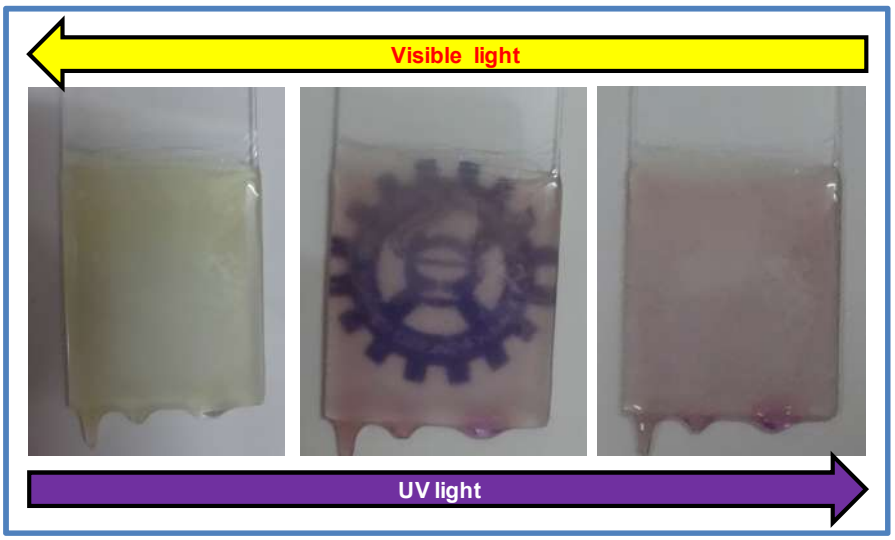

Figure 4.18: Photographic images show the photochromism of Ag@ZQDs/PMMA hybrid coatings.

4.4. CONCLUSIONS

In summary, we have successfully demonstrated a facile, low-temperature synthetic strategy for obtaining Sn and Ag doped ZQDs/PMMA hybrids and fabrication of multifunctional hybrid coatings. *In situ* sol-gel synthesis *via* microwave-reflux process is produced highly stable ZnO quantum dots with physical dimension close to the Bohr radius defined for the quantum dots. In this study, ZQDs size was noticed in the range 2.5 to 3.5 nm. The UV, PL, and Raman confirmed the photo-physical quality of ZnO quantum dots. The Sn and Ag doped quantum dots in *in situ* polymerized PMMA hybrid coatings showed excellent transparent layers up to 12 coatings. The AFM and SEM morphologies confirmed the surface homogeneity and coating thickness below 100 microns even after 3 coatings. The doped ZQDs/PMMA coatings offered better UV shielding, photoluminescence, and NIR reflectance properties. When the undoped ZQDs/PMMA coatings show only 7% total solar reflectance and the Sn and Ag doped hybrid coatings showed 19 and 29% TSR. A unique dispersoid, $LaPO_4$ is employed as top-coat for the enhanced NIR reflectance. The incorporation of a light sensitive organic photochromic dye makes the hybrids photochromic that shows excellent luminescence and reversible color changing property. The Sn and Ag doped, organically modified ZQDs/PMMA hybrid coating is a promising interface for obtaining solar light and solar heat control interface coatings. The present work is reported for the first time.

The present works of this Chapter have been communicated.

Soumya, S.; Sheemol, V. N.; Amba, P.; Mohamed, A. P.; Ananthakumar, S., Sn and Ag doped ZnO quantum dots with PMMA by in situ polymerization for UV/IR protective, photochromic multifunctional hybrid coatings.

CHAPTER 5

Silanated Nano ZnO Hybrids Embedded PMMA Polymer Coatings on Cotton Fabrics for Near-IR Reflective, Antifungal Cool-Textiles

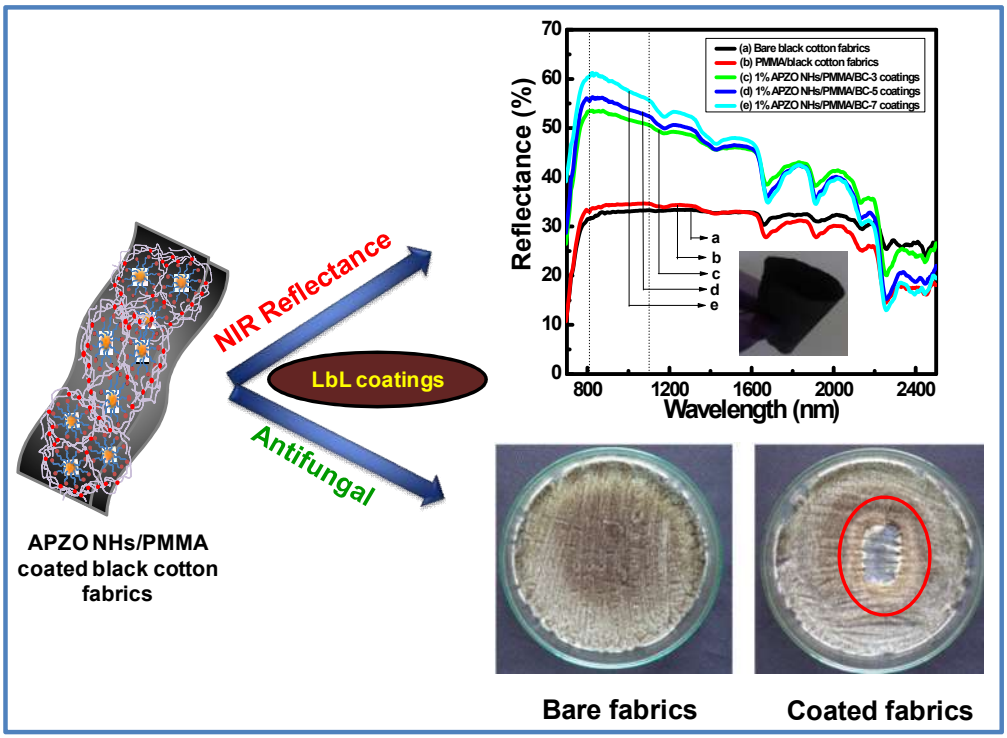

PREAMBLE

An investigation is made on the multifunctional coatings prepared using silane capped nano ZnO hybrids. The silane modified ZnO is directly blended with PMMA matrix to obtained ZnO/PMMA colloidal suspension. It was further applied over a dark color cotton textile. This surface engineered black cotton was subjected to phase analysis, chemical interaction, morphological features, NIR reflectance, UV shielding efficiency and antifungal properties. The textile surfaces engineered with infrared/ultraviolet energy shielding coatings is an emerging technology in the processing of solar heat protective cool-textiles.

5.1. INTRODUCTION

Textiles engineered with functional surface coatings using inorganic as well as metalized nanostructures successfully offer shielding effects of electromagnetic and infrared radiation energy. These kinds of engineered textiles find applications in military as well as strategic fields [Wong *et al.,* 2015; Wendel, 2015; Jang, 2014; Miao *et al.,* 2015]. In continuation of this research, attempts are being made to develop functional textiles that possess the UV protection capability, sunlight active photocatalytic self-cleaning property, solar heat absorption as well as solar-heat reflection qualities [Abidi *et al.,* 2009; Yu *et al.,* 2013; Wang *et al.,* 2010a; Li *et al.,* 2015; Wang *et al.,* 2005; Mehrizi *et al.,* 2012; Duan *et al.,* 2011]. Recently, textile industries have also shown great interest in surface engineering of textile products that can efficiently repel oil substance, organic dirt and even mosquitoes. Research is further extended to develop textiles with biomimetic camouflage coatings; as well as smart coatings with water and detergent free cleaning technology [Wendel, 2015; Manna *et al.,* 2015; Liu *et al.,* 2015; Xiong *et al.,* 2012].

Near-IR reflective coatings to minimize the solar heat penetration are an essential requirement for human beings. Textiles with such coatings can protect a large number of casual workers engaged in building constructions and exposed to sunlight in countries like India and Gulf regions. Surface functional coatings processed using inorganic metal oxides such as TiO_2, ZnO, and CeO_2 that are well recognized white pigments, have been largely studied on ceramic tiles and metal roofing sheets to prove their cool-functional properties [Johnson *et al.,* 2003; Li *et al.,* 2014; Balanand *et al.,* 2016; Levinson *et al.,* 2007; Levinson *et al.,* 2010]. Recently, they have also been tested over the textile and leather surfaces to incorporate antibacterial/ antifungal, and anti-wrinkle properties [Manna *et al.,* 2015; Petkova *et al.,* 2014; Perelshtein *et al.,* 2009]. Since conventional white pigments reflect >80% of the incident sunlight radiation, they are recognized as ideal active-pigment components for developing cool-coatings on textiles.

As described in previous Chapters, ZnO is a known pigment, which has been extensively patented for cool-paint products for building articles, mainly the metal/polymer roofing surfaces [Shiao *et al.,* 2013; Viasnoff *et al.,* 2012; Viasnoff, 2014; Hwang *et al.,* 2013]. ZnO is a non-corrosive, non-toxic, ingestion and inhalation material. It is also known for its UV absorption, hydrophobic qualities and high near-infrared

reflectivity [Miao *et al.,* 2015; Shi *et al.,* 2012; Gao *et al.,* 2014; Wu *et al.,* 2013; Wang *et al.,* 2013a; Soumya *et al.,* 2015; Soumya *et al.,* 2014; Kiomarsipour *et al.,* 2013b]. Chemically cross-linked nanohybrids offering near-infrared radiation reflectance in the critical wavelength region 700-2500 nm in the solar spectrum is the best way to imbibe cool-coatings on textiles. In situ growth of nano ZnO on the cotton fabric is a previously reported strategy [Perelshtein *et al.,* 2009]. However, poor mechanical adhesion is realized in such coatings. One of the most interesting ways to overcome this issue is perhaps the concept of using functional hybrid coatings processed from chemically capped hybrid nano dispersoids embedded within any polymer matrix. Organic capping molecules can chemically react with cellulosic units and promote better chemical bonding with textile surfaces.

PMMA is a bio-inert polymer with high optical transparency throughout the visible range in addition to high mechanical stability. Bulk PMMA/ZnO nanocomposites have previously been explored to understand the beneficial properties like UV blocking, optical transparency, tunable refractive index, wear resistance, and thermal stability [Zhang *et al.,* 2012; Matsuyama *et al.,* 2012; Li *et al.,* 2007; Eita, 2012b; Soumya *et al.,* 2015; Soumya *et al.,* 2014]. Results strongly indicate PMMA polymer is a probable matrix for fabricating UV/NIR shielding transparent coatings. There are no reports on the application of silane modified ZnO nanohybrids/PMMA coatings on textiles that provide NIR control cooling effect.

In this work, assembly of silane treated nano ZnO hybrids encapsulated PMMA coatings onto the surface of the black cotton fabrics has been attempted to impart NIR reflectance quality. The colloidal sol prepared out of silane treated ZnO hybrid particulates in PMMA medium create nanometer thin multilayer coatings on the non-planar textile fabric surfaces via physico-chemical and electrostatic interactions. In the case of coatings designed with such *silane/ZnO/polymer* multiphase architectures, ample opportunity exists to incorporate any active functional molecules like proteins. Recently reported research articles clearly showed multilayered/multiphase topcoats could produce surface properties including UV protection, durability, hydrophobicity/hydrophilicity and antimicrobial activity [Jiang *et al.,* 2013; Chen *et al.,* 2015; Carosio *et al.,* 2015; Busila *et al.,* 2015]. Here, we demonstrate NIR reflective silane ZnO coatings on textiles for developing cool-clothes. NIR shielding properties of silane treated nano ZnO embedded PMMA polymer coatings on black cotton fabrics were systematically evaluated and

reported. In situ silane cross-linked nano ZnO hybrid particles were first synthesized *via* chemical precipitation. The mol% of silane was varied as 0, 1, 2, 5, and 20%. A stable silane modified ZnO/PMMA colloid was then prepared, and thin films of hybrid coatings on cotton fabrics were developed by simple dip-coating, *via* Layer-by-Layer (LbL) technique. The effect of silane on the nano ZnO particle size, surface charge characteristics, crystallinity and chemical bonding were studied. Bulk NIR reflectance and total solar reflectance (TSR=R*) in the wavelength range of 700-1600 nm was evaluated. The results are correlated with silane concentrations and coating layers. The coated fabric was also briefly examined for the antifungal properties.

5.2. EXPERIMENTAL SECTION

5.2.1. Materials and Reagents

Black as well as white colored cotton cloth pieces with size 6 cm × 6 cm were first cleaned ultrasonically and then with ethanol and distilled water before use. Zinc acetate dihydrate ($Zn(OAc)_2.2H_2O$, Merck Specialities Pvt. Ltd., India, purity ≥98%), Sodium hydroxide (NaOH, Merck, India, 97%), (3-aminopropyl)trimethoxysilane (APS, Sigma-Aldrich, India, purity >99%), Poly(methyl methacrylate) (PMMA, Sigma-Aldrich) with an average M_w 996,000 were used as supplied. The fungal pathogens used for the antifungal study were *Aspergillus niger* MTCC 2756 and *A. flavus* MTCC 183. The fungal strains were procured from Microbial Type Culture Collection (MTCC) and Gene Bank, Institute of Microbial Technology, Chandigarh, India. The fungal strains were maintained on PDA agar slants at 4 °C. Toluene, ethanol, and acetone were selected as solvents. Double distilled water was utilized for all the preparation.

5.2.2. Synthesis of (3-aminopropyl)trimethoxysilane Modified Nano ZnO Hybrids

Silane modified ZnO colloidal particulates were synthesized by co-precipitation technique as reported earlier [Costenaro *et al.,* 2013]. 0.1 M zinc acetate dihydrate aqueous homogeneous solution was first prepared. To this solution, different amounts of 3-aminopropyl-trimethoxy silane were added in order to reach Si/Zn molar ratios of 0, 1, 2, 5, and 20%, respectively. The solution of 1 M NaOH, prepared in distilled water at room temperature, was added drop wise with constant stirring to maintain the pH 10. At this pH condition, white precipitated gel was obtained and stirred mechanically for 4 h.

Later, the gel mass was centrifugally washed using distilled water at 3000 rpm and then washed once with ethanol to remove any excess organosilane and a large part of un-reacted residual acetates. The gel mass was finally dried at 60 °C for overnight in an electrically heated oven. The obtained (3-aminopropyl)trimethoxysilane modified nano ZnO hybrids was designated as x% APZO NHs, where x indicates the Si/Zn molar ratio used. The untreated phase pure ZnO nanoparticle (0% APZO NHs) was also prepared for studying the comparative performance and the effect of silane.

5.2.3. Fabrication of APZO NHs Embedded PMMA Nanocoatings on Cotton fabrics

APZO NHs embedded PMMA (APZO NHs/PMMA) coating solution was prepared by dispersing 0.1 wt% silane modified ZnO nanohybrids in 60 mL toluene. Similarly, 10 wt% PMMA was also dissolved separately in toluene medium. Both solutions were mixed, sonicated for 30 min, and further stirred magnetically overnight to ensure homogeneous mixing. A stable silane modified ZnO/PMMA colloidal sol was successfully obtained and further applied to the white and black colored cotton fabrics *via* dipping-withdrawing coating technique. The cotton fabric pieces of 6 × 6 cm were immersed in the coating solution. The fabric was soaked in the coating precursor sol for 2 min. to ensure the better pick-up of nano ZnO layers. After coating, the cloth was dried by hanging at room temperature and cured to obtain APZO NHs/PMMA functional coatings. The dip-coating treatments were repeated for 1 to 7 times and finally 20 times to obtain 20 layer coatings. Simultaneously, neat PMMA coatings and ZnO/PMMA coatings without any silane were also made for reference. For convenience, specific codes were given to the coated cotton fabric samples as follows: Bare white cotton (Bare WC), bare black cotton (Bare BC) and after neat PMMA coating treatments, PMMA/WC, PMMA/BC, the same with silane treated nano ZnO; APZO NHs/PMMA/WC and APZO NHs/PMMA/BC.

The samples with varying mol% APS concentration were represented as 0, 1, 2, 5, and 20% APZO NHs. Figure 5.1 schematically described the chemical interaction involved between the reactants; silane molecule, nano ZnO and PMMA polymer matrix on the cotton fabrics.

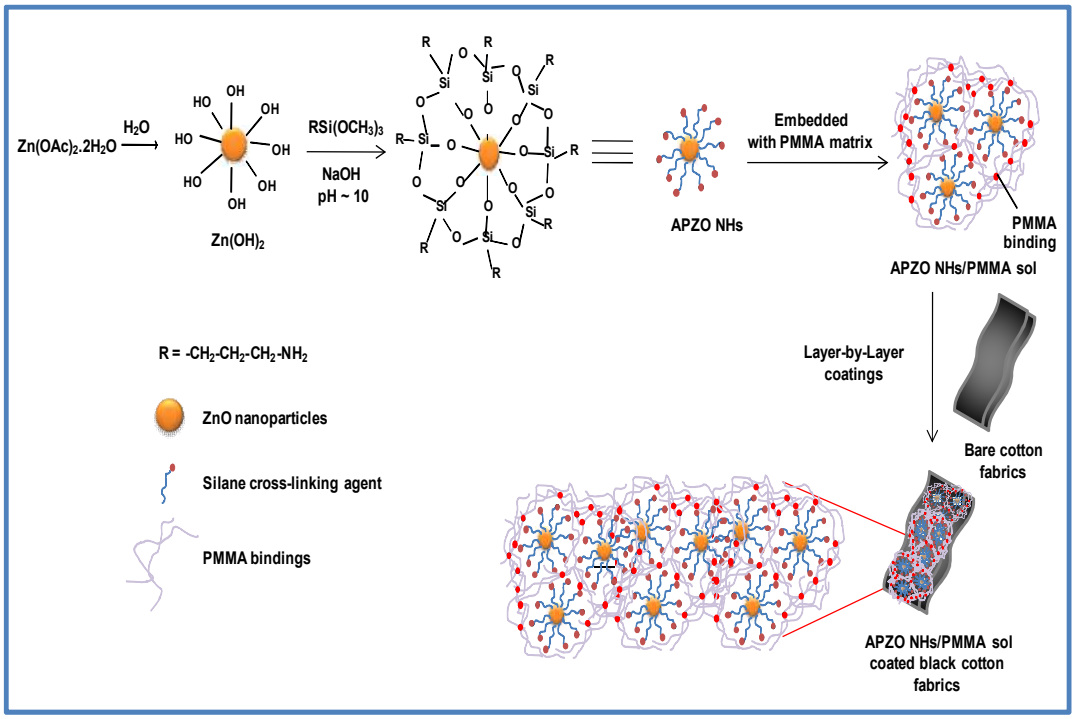

Figure 5.1: Procedure and chemical interaction involved between the reactants; silane capping molecule, nano ZnO and PMMA polymer matrix on the cotton fabrics.

5.2.4. Characterizations

In this Chapter, silane modified ZnO nanohybrids were characterized by XRD, FTIR, DLS, Zeta potential, TG, SEM, TEM, SAED, EDX, UV/Vis absorption, PL and UV/Vis/NIR spectroscopic analysis. The structural analysis of APZO NHs/PMMA coatings on cotton fabrics were carried out using XRD analysis. Functional group analysis of APZO NHs/PMMA coated cotton fabrics were obtained from ATR-FTIR spectroscopy. Surface morphology, EDX and mapping APZO NHs/PMMA coatings on cotton fabrics were measured from SEM-EDX. The surface roughness of APZO NHs/PMMA coated cotton fabrics was carried out by AFM. The optical properties of APZO NHs/PMMA LbL coatings on cotton fabrics were characterized by UV/Vis absorption and UV/Vis/NIR spectroscopic analysis. Anti-fungal activity of coated cotton fabrics was also evaluated.

The crystalline nature and phase purity of the nano APZO NHs were characterized by powder X-ray diffraction using X'Pert Pro, Philips X-ray diffractometer equipped with Cu K_α radiation (λ = 1.5406 A$^\circ$) in the 2θ range 10 to 70° with 0.02 scan increment. The dynamic light scattering (DLS) particle size distribution and zeta potential were

measured using Malvern Zetasizer Nano ZS (Worcestershire, UK). For these measurements, APZO NHs particulate colloids were prepared in aqueous media by dispersing 0.01 wt% APZO NHs and subsequently de-agglomerated through ultrasonication for 15 min. in an ultrasonicator (Ultrasonic Processor P2, Vibronics Pvt. Ltd., Bombay, India).

Surface functional groups in APZO nanohybrids were performed by IR Prestige-21, Shimadzu FTIR spectrophotometer from the scanning range of 4000-400 cm^{-1} using standard KBr (Sigma-Aldrich, 99%) pellet as the reference. In APZO NHs/PMMA treated cotton fabrics, the chemical interaction was recorded on a Bruker alpha ATR-FTIR spectrometer instrument used attenuated total reflectance (ATR) mode with a resolution of 4 cm^{-1} accumulating 24 scans. Thermogravimetric analysis (TGA) of the APZO NHs was conducted using TG 50 Shimadzu TGA in the air. A Mettler Toledo pH meter (Model μ-8603) was used for the pH measurements. The microstructure and morphological features of APZO NHs and APZO NHs/PMMA treated cotton fabrics were examined using ZEISS EVO 18 Special Edition scanning electron microscope operated at 20 kV. The chemical composition was ascertained using energy-dispersive X-ray (EDX) mapping. The TEM image analysis and selected area electron diffraction (SAED) of the APZO NHs were performed on FEI Tecnai 30G2S-TWIN transmission electron microscope operated at an accelerating voltage of 300 kV. The surface roughness behavior of bare and APZO NHs/PMMA coated cotton fabrics were obtained by AFM analysis (Bruker Multimode, Germany) in the tapping mode and was performed out at a scan size of 20 × 20 μm.

The optical properties of the APZO NHs and APZO NHs/ PMMA/cotton fabrics were monitored using Shimadzu UV/Vis spectrophotometer (UV 240 IPC) in the wavelength region 200 to 800 nm. The absorption coefficient (α) is evaluated by the equation, $\alpha = A/d_s$, where A is the measured absorbance and d_s is the thickness of the sample in UV/Vis cell (0.4 cm). The absorption coefficient is related to the energy band gap (E_g) by: $(\alpha h\nu)^2 = E_D(h\nu - E_g)$, where h the Planck's constant, ν the frequency of the incident photon, E_D is a constant and E_g is the direct band gap. If $(\alpha h\nu)^2$ is plotted versus $h\nu$ over the absorption wavelength range, the energy band gap (E_g) can be calculated by extrapolating the linear region of the curve to $\alpha = 0$. The band gap values were calculated from the absorbance spectra [as described in Chapter 2]. The photoluminescence spectra of the APZO NHs dispersed in water medium were acquired using a Cary Eclipse

fluorescence spectrophotometer (Varian India Pvt. Ltd.) equipped with a liquid sample holder accessory at an excitation wavelength of 330 nm.

The near-infrared diffuse reflectance (700-2500 nm) spectra of the bulk APZO NHs and APZO NHs/PMMA coated fabrics were analyzed by a Shimadzu UV/Vis/NIR spectrophotometer (UV-3600) with an integrating sphere attachment (ISR-3100). The instrument was calibrated using the reference PTFE. As reported in the literature, [Jose *et al.* 2014; Sangeetha *et al.,* 2012] the NIR solar reflectance (R^*) in the wavelength range from 700 to 2500 nm was calculated in accordance with the ASTM standard number E891-87. The NIR solar reflectance at wavelengths between 700 and 2500 nm that is reflected by a surface is the irradiance-weighted average of its spectral reflectance, $r(\lambda)$ in Wm^{-2}, can be determined as in the aforementioned Chapter.

The agar overlay method was used for the examination of anti-fungal properties of APZO NHs/PMMA coated cotton fabrics. Effect of fungal growth was examined using *Aspergillus niger* and *Aspergillus flavus* fungi species. In a typical experiment, the sterilized petri-plate containing APZO NHs/PMMA coated cotton fabrics was overlaid with the top potato dextrose agar (Hi-media, Mumbai, India) which contains the test fungal strains. The inhibitory effect was evaluated after 72 h incubation at 37 °C and the results were evaluated by the measurement of inhibition zone of around the APZO NHs/PMMA coated cotton fabrics.

5.3. RESULTS AND DISCUSSION

The main chemical constituent of a cotton fabric is cellulose, a macromolecular polymer, in which a long chain anhydro-beta-cellobiose building block is repeatedly present. The cellulose chains are mainly linked *via* hydrogen bonding. These hydrogen bonds occur between the hydroxyl groups of adjacent crystalline molecules of the cotton fiber [Chung *et al.,* 2004]. Hydroxyl groups in the cellobiose polymeric units are chemically reactive and organosilane molecules readily react with these hydroxyl groups. Silane coupling agents generally include of alkoxy and alkyl bridge cross-linked through organofunctionality. Hence, silane indeed plays a role of chemical adhesive promoter for the fixation of nano ZnO with the cellulosic cotton surface through NH_2-OH bonding [Xie *et al.,* 2010]. The organosilane is also a recognized surfactant/stabilizer to determine the growth of the ZnO particles that decide the ZnO colloidal stability. However, for the

firm binding of nano ZnO with cotton fabrics, one has to have the optimum amount of organic silane capping and appropriate surface charge characteristics in addition to the controlled particle size.

5.3.1. Effect of Silane Modification on the Bulk Properties of ZnO Nanohybrids

5.3.1.1. XRD Analysis of APZO NHs

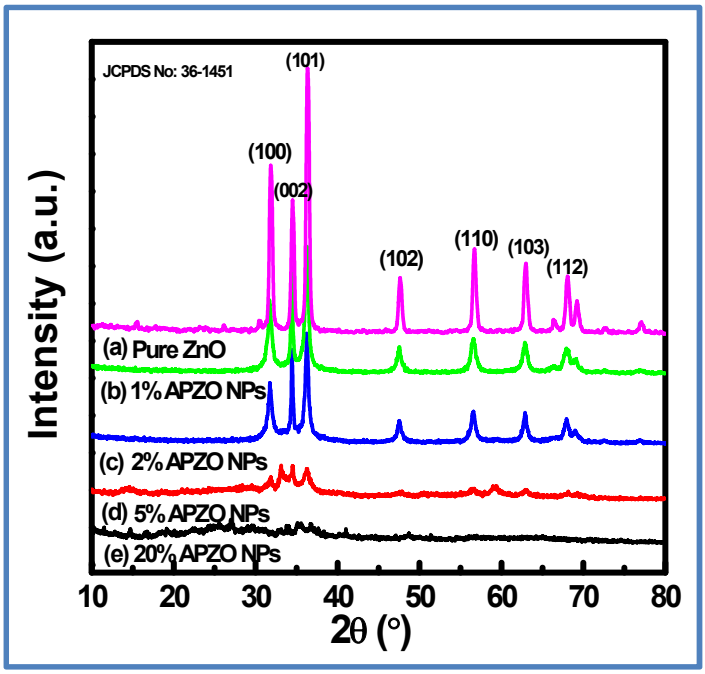

Figure 5.2: XRD analysis of APZO NHs with respect to silane modification: (a) 0, (b) 1, (c) 2, (d) 5, and (e) 20% APZO NHs.

The structural properties of ZnO, 1, 2, 5, and 20% APZO nanohybrids were estimated using the powder X-ray diffraction technique. As a general feature, the X-ray profiles of all samples [Figure 5.2] show diffraction lines at 31.8, 34.4, 36.6, 47.6 and 56.7° 2θ are consistent with the values reported in the database of ZnO JCPDS card (No: 36-1451) providing to the (100), (002), (101), (102), and (110) planes, respectively using Bragg's law of diffraction gives clear evidence for the formation of hexagonal wurtzite-type structure having space group of $P6_3mc$. Nevertheless, significant differences in terms of intensity and full width at half maximum (FWHM) of reflection peaks of the different mol% of APS capped ZnO samples can be observed. In uncapped ZnO NPs, all the diffraction peaks are rather sharp which indicates that the ZnO samples have the high

degree of crystallinity. In particular, the diffractograms of ZnO, 1% and 2% APZO samples show well-resolved reflections, and the diffractograms of the samples functionalized with high organic APS loading (5% APZO and 20% APZO) are characterized by a general broadening of the X-ray peaks. This effect can be interpreted that on increasing the amount of APS, the crystallinity is slightly reduced and/or particle size due to promoted by the presence of high loading of the silane groups introduced on the surface of ZnO NPs during synthesis. On higher concentration of APS clearly gives the amorphous nature of APZO and also its crystallinity were completely removed.

The average crystallite sizes of the different mol% of APZO NPs were evaluated by applying the Debye Scherer's formula (Equation 2.2). From the XRD data, the $< D >$ crystallite size of 0, 1, 2, and 5% APZO NPs were calculated to be 19.34, 17.06, 17.78, and 18.81 nm respectively.

5.3.1.2. Functional Group Analysis of APZO NHs

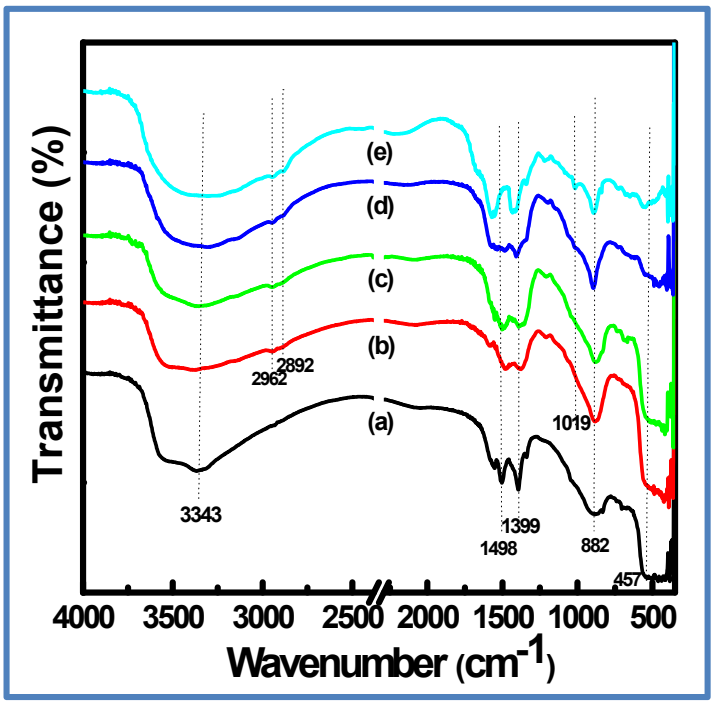

Figure 5.3: FTIR spectra of unmodified and different concentration of APZO NHs: (a) 0, (b) 1, (c) 2, (d) 5, and (e) 20% APZO NHs.

Figure 5.3 shows the FTIR spectra of ZnO hybrids prepared with 1 mol% of silane. In FTIR spectra, the broad peak existing between the wavelengths ~3262-3540

cm^{-1} represents the –OH stretching. The chemical adsorption of the water molecules generates the hydroxyl groups onto the ZnO particle surface through hydrogen bonding. The two broad bands in the wavelength region ~ 457-427 cm^{-1} clearly indicate the Zn-O bonding. Upon silane treatment, in the APZO NHs asymmetric and symmetric stretching modes of $–CH_2$ groups appeared at wavelength ~2962 and ~2892 cm^{-1}. A vibrational mode typical of ammoniumpropyl moieties is also observed in the wavelengths 1600-1400 cm^{-1}. The APZO hybrid particles show further vibrational bands at ~1149 and ~1019 cm^{-1}, which can be attributed to the vibrational modes of Si–O–Si groups formed by self-condensation of the organosilanes. The hybridization of silane with ZnO is further evident from the FTIR analysis carried out on the APZO NHs.

5.3.1.3. Particle Size Analysis

The DLS particle size distribution and zeta potential analysis results observed for the silane modified ZnO hybrid particles with its unmodified counterpart were illustrated in Figure 5.4 A and B.

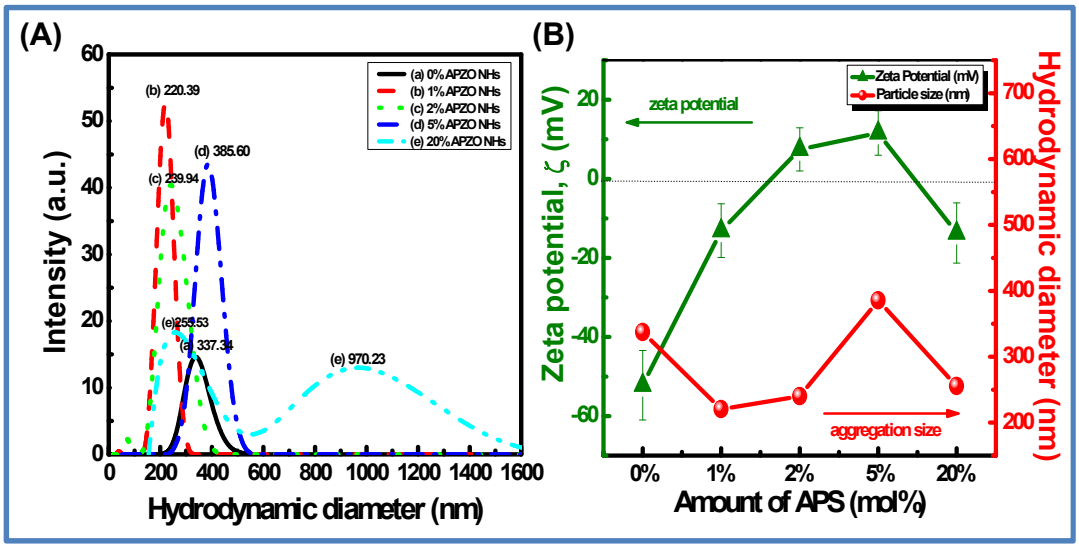

Figure 5.4: (A) DLS particle size distribution analysis of APZO NHs with respect to silane modification (a) 0, (b) 1, (c) 2, (d) 5, and (e) 20% APZO NHs; (B) illustration of DLS particle size distribution and zeta potential measurements with respect to the different mol% of APS in the APZO NHs.

The average hydrodynamic diameter (Z_{ave}) varies strongly with the surface-anchored amine functional groups present in organosilane. The Z_{ave} values determined for the unmodified ZnO, and silane treated hybrid ZnO are 337, 220, 239, and 385 nm for the

respective silane concentrations of 0, 1, 2, and 5 mol%. The corresponding size distribution curves are presented in the Figure 5.4A. The size distribution is very narrow when the ZnO nanoparticles are prepared by the in situ addition of silane. However, when an excess amount of silane was used, the particle size curve indicates bi-model size distribution. In this case, the particles fall in the range 255 and 970 nm, respectively. The broad size distribution clearly indicated that in the absence of silane, the precipitation technique produced only ZnO nano aggregates. Upon in situ silane addition, preferably with least amount of silane, more specifically at Si/Zn mol. ratio 1%, the size distribution is very narrow with an average particle size of 220 nm. The size controlled the growth of nano ZnO is attributed to the capping effect of the organosilane. Earlier studies on the synthesis of silane treated ZnO strongly confirm the capping effect of silane molecules to achieve size controlled growth of nano ZnO with tuned physicochemical properties [Costenaro *et al.,* 2013].

In one-pot synthesis, the strong chemical interaction of organic ligands in APS controls the condensation reaction with ZnO/$Zn(OH)_2$ species. This further limits the ZnO self-condensation processes that ultimately decrease the particle growth [Costenaro *et al.,* 2013]. At higher loadings, the excess silane possibly produced a thick silanol capping layer due to the chemical cross-linking of organo functional group with the ZnO surface hydroxyls. This increases the tendency of localized aggregation finally led to bi-model size distribution with wide particle size range. The larger diameter in the DLS data can also be the effect of outermost hydration layer of colloidal nanoparticles [Liu *et al.,* 2012b]. The zeta-potential (ζ) analysis clearly describes the electrostatic interactions as well as the influence of surface charges in the single phase ZnO and silane treated ZnO hybrid colloidal particles. ZnO exhibits the isoelectric point (IEP) at pH ranging between 8.7-10.3 [Marsalek, 2014]. The DLS particle size distribution and zeta potential analysis results observed for the silane modified ZnO hybrid particles with its unmodified counterpart were illustrated in Figure 5.4B also shows the zeta potential trend in nano ZnO prepared with various amounts of silane molecules measured at pH 10. Compared with unmodified nano ZnO, the average zeta potential of the silane treated APZO NHs varied from -52.2 to -13.1, 7.46, and 11.6 mV with 0, 1, 2, and 5 mol% addition of APS respectively. The change of zeta potential suggests that the ZnO hybridization occurred with silanes depending on its concentration. The positively charged surface of APZO NHs is, in fact, essential for the chemical coupling of silane modified ZnO with the

highly hydrophilic linear cellulose microfibrils. The DLS particle size distribution and zeta potential analysis results observed for the silane modified ZnO hybrid particles with its unmodified counterpart were illustrated in Figure 5.4B.

5.3.1.4. Morphological Features

The SEM images of APZO NHs with various molar ratios were shown in Figure 5.5. Upon increasing the concentration of APS, the morphology was also varied. The SEM images of without APS shows the rice-like particle of ~ 300 nm in length can be seen in Figure 5.5(a). By increasing the amount of APS, the morphology was slightly changed due to the surface capping with APS. Since the effect of capping strongly influences the particle size reduction at the same scale bar confirmed from 1% APZO NHs morphology. Here, we noticed that the same rice-like morphology was obtained as in the case of 0% APZO NHs [Figure 5.5(a)]. As the concentration of APS increases, the hybrid morphology gradually changes to nanospherical. The aggregation tendency was increased due to the amorphous nature of silane capping which was covalently bonded to the ZnO surface to form a hybrid [Figure 5.5(c)-(e)].

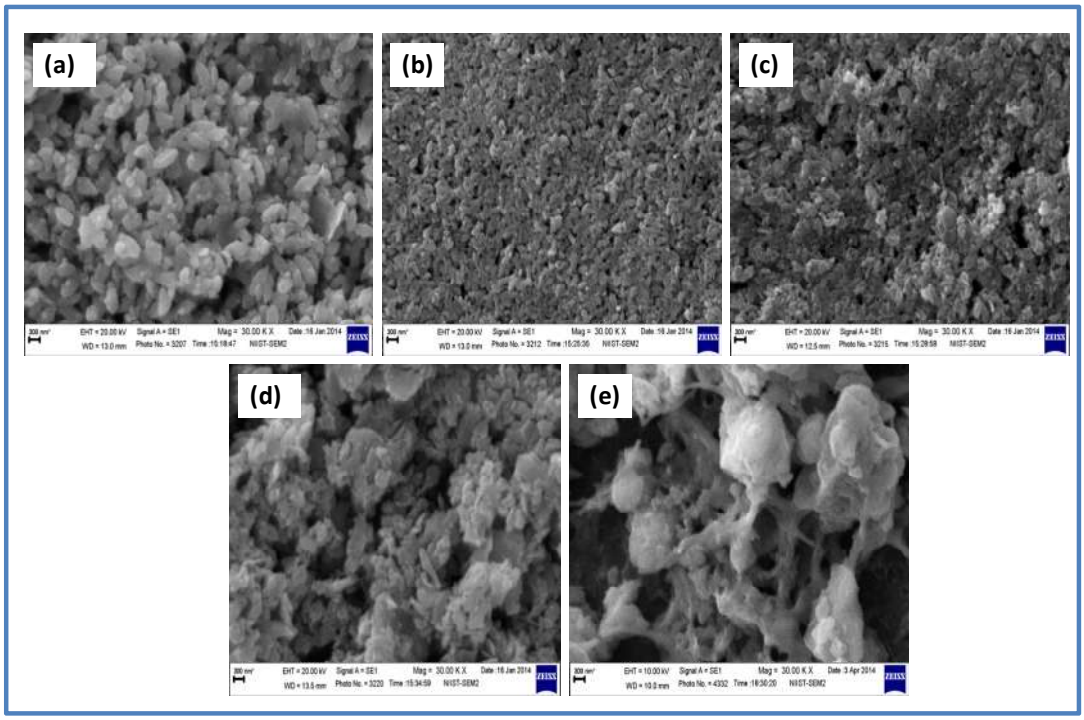

Figure 5.5: SEM images of (a) 0, (b) 1, (c) 2, (d) 5, and (e) 20 mol% APZO NHs. Scale bar 300 nm.

Figure 5.6A shows the TEM images of 0, 1, 2, 5 and 20% APZO NHs. The TEM images were observed to be same morphology as in SEM, which is further evidenced the actual morphology and size of synthesized samples. The 0% APZO NHs shows rice-like images in the scale bar 0.5µm [Figure 5.6A (a)]. The 1% APZO NHs clearly observed the surface coverage of APS with ZnO NPs [Figure 5.6A (b)]. The morphology of higher mol% of APS evidenced the morphological changes [Figure 5.6A (c)-(e)]. The inset of the figures shows corresponding selected area electron diffraction (SAED) pattern which can be indexed to the reflection of the monocrystalline wurtzite ZnO structure, and this is consistent with the XRD results. The chemical purity and elemental compositions of the APZO NHs were further detected by energy-dispersive X-ray (EDX) spectroscopy. In Figure 5.6B depicted the corresponding EDX spectra of ZnO samples. In Figure 5.6B, except 5.6B (a), reveals the presence Si which shows APS capped on the ZnO surface. It confirms that the APZO NHs was composed of the elements Zn, O, and Si.

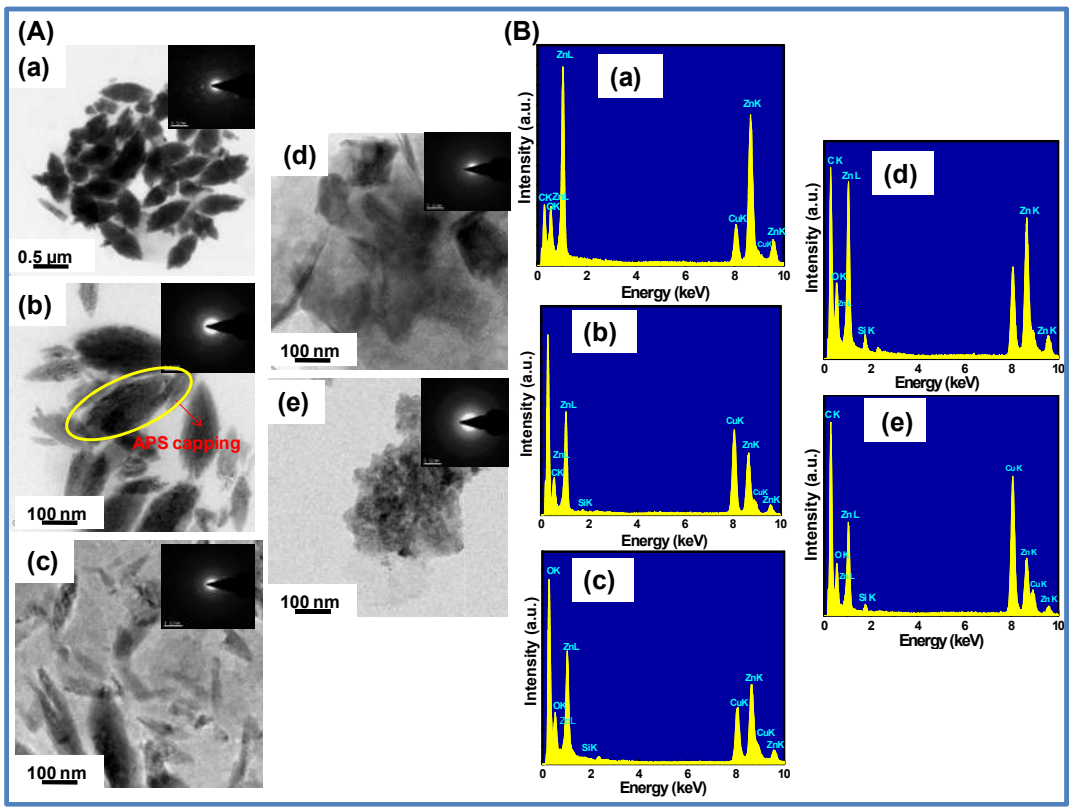

Figure 5.6: TEM images of (A) (a) 0, (b) 1, (c) 2, (d) 5, and (e) 20% APZO NHs. The EDX spectra of the corresponding TEM images are shown in (B) (a), (b), (c), (d), and (e). The inset of the figures shows corresponding selected area electron diffraction (SAED) pattern.

5.3.1.5. Thermal Properties of APZO NHs

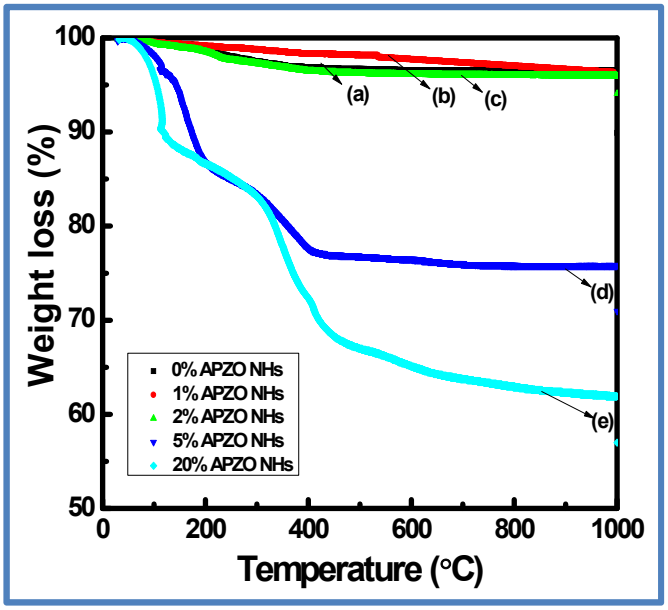

Figure 5.7: TG analysis of (a) 0, (b) 1, (c) 2, (d) 5 and (e) 20% APZO NHs.

TG thermogram profiles taken for ZnO and silane modified hybrids nanoparticles are presented in Figure 5.7. In pure ZnO, two stage weight loss, the first one at the temperature around 118 °C amounting to below 4 wt% was estimated which is due to the removal of adsorbed water, and the second one centered at 400 °C assigned to the thermal decomposition of acetates ions bound to the ZnO surface was seen. In organo-modified samples, about 7% weight loss was observed at temperatures below 120 ^{o}C confirming the less amounts of adsorbed water molecules thus indicating a reduced hydrophilic character of ZnO samples containing surface organic species. Besides the weight loss at 100 °C, the TGA profiles of organo-modified ZnO samples show an additional weight loss with a maximum at 310 °C which can be assigned to the decomposition of the ammoniumpropyl groups. In the case of APS functionalized ZnO, at 310 °C the weight loss was increased gradually with increasing mol% of silane loading, except 1 mol%, is due to the decomposition of organic coating. The effective capping on the surface of the ZnO with 1 mol% silane which can reduces the particle size of the ZnO, as a result, the decomposition was slightly decreased.

5.3.1.6. Optical Properties of APZO NHs

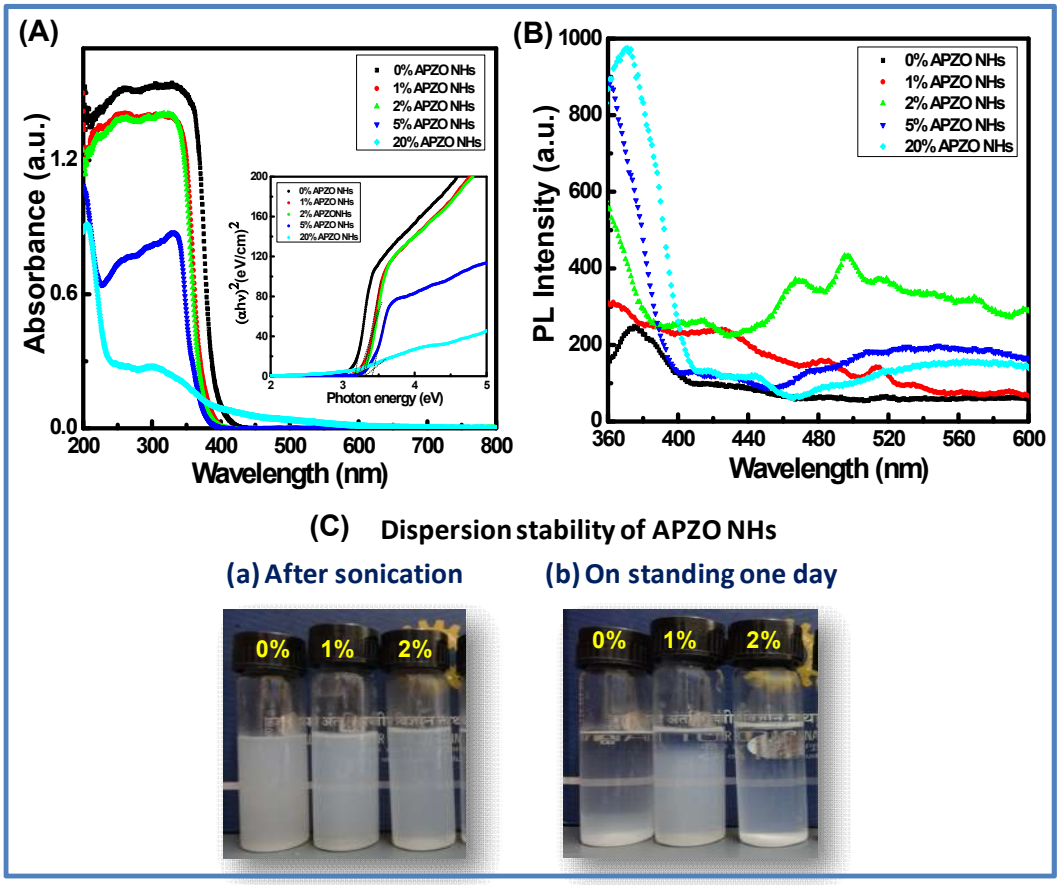

Figure 5.8: (A) Solid-state UV/Vis absorption spectra of APZO NHs (Inset shows evolution of the $(\alpha h\nu)^2$ *vs.* $h\nu$ curves of respective samples); (B) PL spectra of different mol% of APZO NHs; (C) Dispersion stability of 0.01 wt% APZO NHs with different mol% concentrations.

Solid-state UV/Vis absorbance spectra of all samples, measured using $BaSO_4$ as the reference, [Figure 5.8A] showed a wide band in the 200-800 nm range with absorption maxima at 362 nm for 0% APZO NHs. The absorption at 362 nm was assigned to the electronic transition from the valence band (mainly formed by orbitals of the oxide anions) to the conduction band (mainly formed by orbitals of the Zn^{2+} cations) of ZnO. The band gap for this transition was estimated to be 3.42 eV, slightly higher than the band gap typical of bulky ZnO samples (3.26 eV) and which was somehow more resolved for APZO NHs. The samples 1, 2, 5, and 20% APZO NHs shows absorption wavelength shows 343 (E_g=3.61 eV), 339 (E_g=3.66 eV), 334 (E_g=3.71 eV), and 316 (E_g= 3.92 eV) nm, respectively. By increasing the amount of organic moieties exposed on the

ZnO surface, a blue-shift of the absorption band at lower wavelengths (passing from 360 nm to 340 nm) was observed. The blue-shift behavior or broadening in the band gap is mainly due to the Moss-Burstein band filling effect. Based on the Moss-Burstein theory, for the samples 1, 2, 5, and 20% APZO NHs, the donor electrons occupied states at the bottom of the conduction band.

The influence of the APS capping and surface functionalization on the inherent optical properties of APZO NHs, room temperature PL spectroscopy was performed on both the silane treated and untreated ZnO nanoparticle dispersion in water medium [Figure 5.8B]. The presence of the APS induces a stable, reproducible bimodal enhancement of the UV and visible emission intensity. The UV emission peak at ~375 nm in the pure ZnO NPs exhibit an intensity increases with increase in mol% of APS. Compared to standard ZnO NPs, the APZO NHs shows the increase in the intensity of visible emission peak at ~510 nm. The enhancement of UV emission occurs because it is the higher-energy process and therefore energetically less stable. A surfactant molecule with a relatively high local negative charge passivated the green emission due to the oxygen ions, during micelle formation, occupying vacancies on the positively charged nano-ZnO surface. This is not expected to occur within our APS capping approach where the APZO NHs is being synthesized in the bulk state. As the APS surface coverage increases, the retention of the bimodal peak is anticipated. However, the relative intensities of UV and visible emission are expected to be influenced by the particle size distributions. The photographic images [Figure 5.8C] showed the colloidal stability of APZO NHs dispersed in water under ultrasonication for 15 min. and standing one day indicating that the 1% APZO NHs was colloidally stable in water medium.

5.3.1.7. NIR Reflectance and NIR Solar Reflectance Properties.

NIR reflectance depends on the mean particle size coupled with smaller crystallite size. The NIR reflectance spectra of pure ZnO NPs and APZO NHs are given in Figure 5.9A. Multiplying the (normalized) spectral irradiance of the Sun $i(\lambda)$ by the spectral reflectivity yields the NIR solar reflectance spectrum presented in Figure 5.9B. The NIR solar reflectance (R^*) of the 0, 1, 2, 5 and 20% APZO NHs are 86.45, 84.50, 89.26, 79.59 and 90.03%, respectively. Such the high NIR solar reflectance displayed by all the Zn/Si hybrids makes them as interesting candidates for use as cool white pigments.

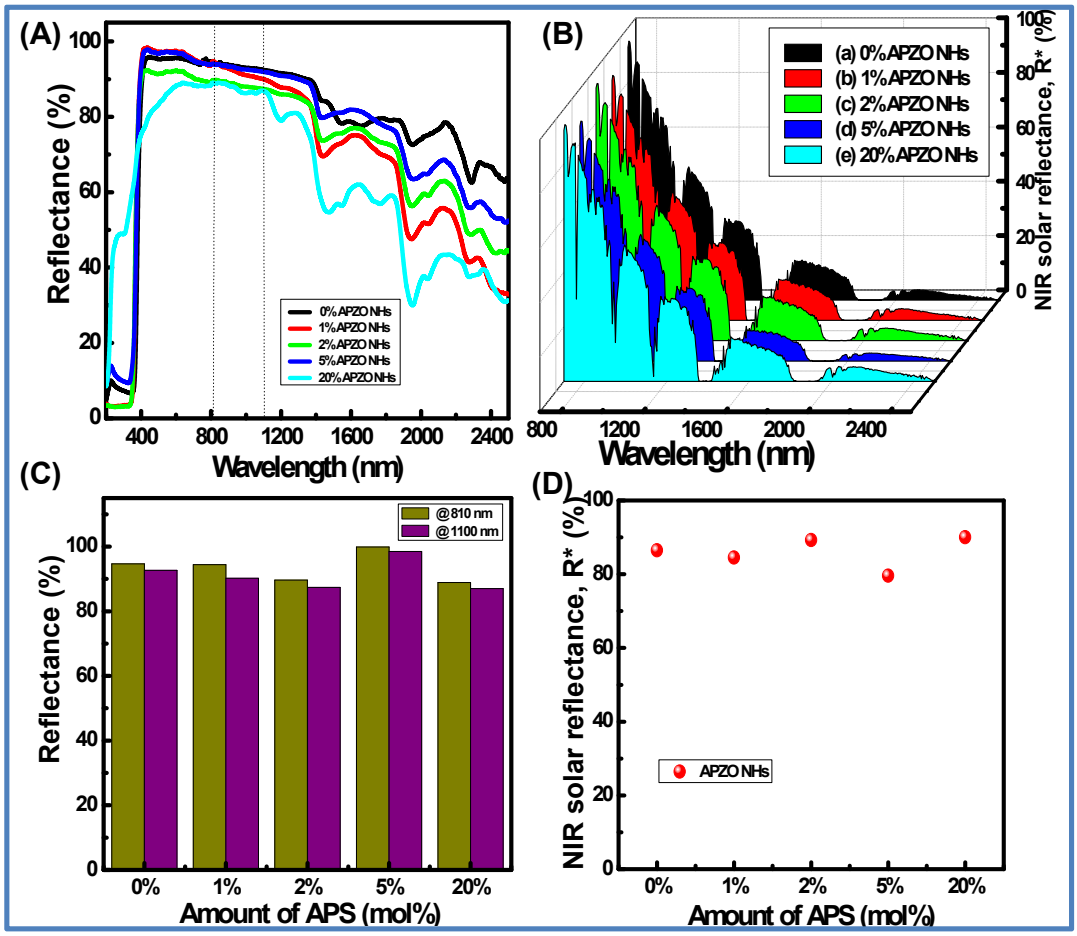

Figure 5.9: (A) NIR reflectance of different mol% of APZO NHs; (B) NIR solar reflectance spectra of corresponding APZO NHs; (C) reflectance *vs.* APS concentration @ 810 and 1100 nm; (D) NIR solar reflectance *vs.* the amount of APS in mol%.

5.3.2. APZO NHs Embedded PMMA Nanocomposite Coatings on Cotton fabrics

The APZO NHs, when dispersed in PMMA solution obtained by dissolving the polymer in toluene medium produced stable organic-inorganic hybrid/polymer colloid. As expected, the PMMA could not only physically fix the APZO NHs over the cotton surface, but also chemically interact with the cellulose through organo silane capping layers.

5.3.2.1. XRD Analysis of APZO NHs/PMMA Nanocomposite Coatings on Cotton fabrics

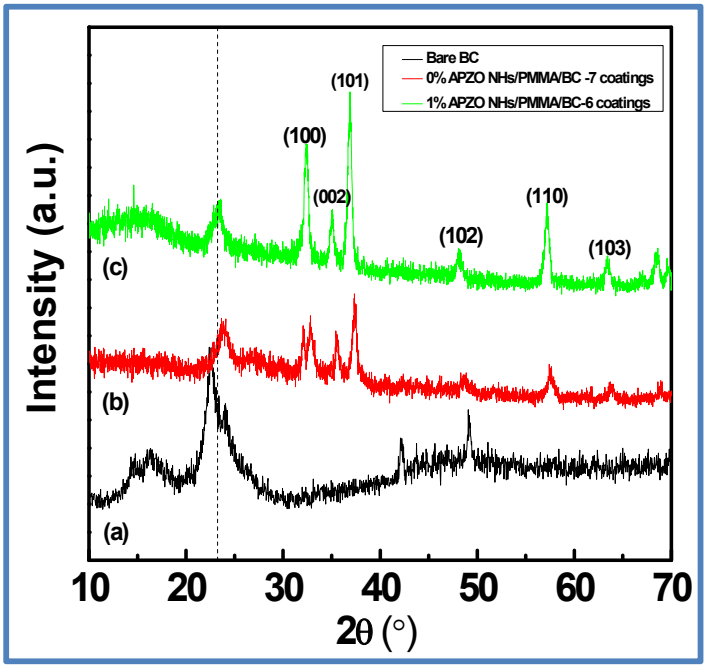

Figure 5.10: XRD pattern of (a) bare BC, (b) 0% APZO NHs/PMMA/BC-7 coatings, and (c) 1% APZO NHs/PMMA/BC-6 coatings.

Figure 5.10 presents the XRD analysis of the cotton fabrics treated with APZO NHs/PMMA colloidal coatings. The bare cotton gives the broad crystalline peak at 2θ values between 15-16° and a narrow peak at approximately 23° representing the monoclinic cellulose unit cell with planes (101), (10$\bar{1}$), and (002) respectively, which matches with cellulose I structure (JCPDS No. 03-0226) [Athauda *et al.,* 2013]. When the cotton fabric is coated with APZO NHs/PMMA, the XRD shows six reflection peaks appeared at 2θ values of 31.9°, 34.6°, 36.5°, 47.7°, 56.8°, and 63.1° correspond to the planes (100), (002), (101), (102), (110), and (103), which could be indexed to the hexagonal wurtzite structure of ZnO. The crystalline structure of nano ZnO is consistent with the standard JCPDS card No: 36-1451.

5.3.2.2. ATR-FTIR Spectra of APZO NHs/PMMA Coatings

ATR-FTIR spectra in Figure 5.11 further confirm the chemical interaction of APZO NHs/PMMA coatings with the cellulosic cotton fabrics. In uncoated cotton fabric,

the characteristic bands correspond to the hydroxyl contribution (OH stretching at ~3269 cm^{-1}) and C-H stretching (~ at 3000-2800 cm^{-1}) and the symmetric and asymmetric stretching mode of the cellulose functional group (-CH_2-) in the broad wavelength range 1000-1500 cm^{-1} are clearly observed. In silane modified ZnO embedded PMMA coated fabrics, the absorption bands at wavelengths 1154 and 1733 cm^{-1} clearly indicate the Si-O-Si and C=O symmetrical stretching vibrations strongly confirms the chemical hybridization of the APZO NHs/PMMA with the cotton surface [Chung, 2004].

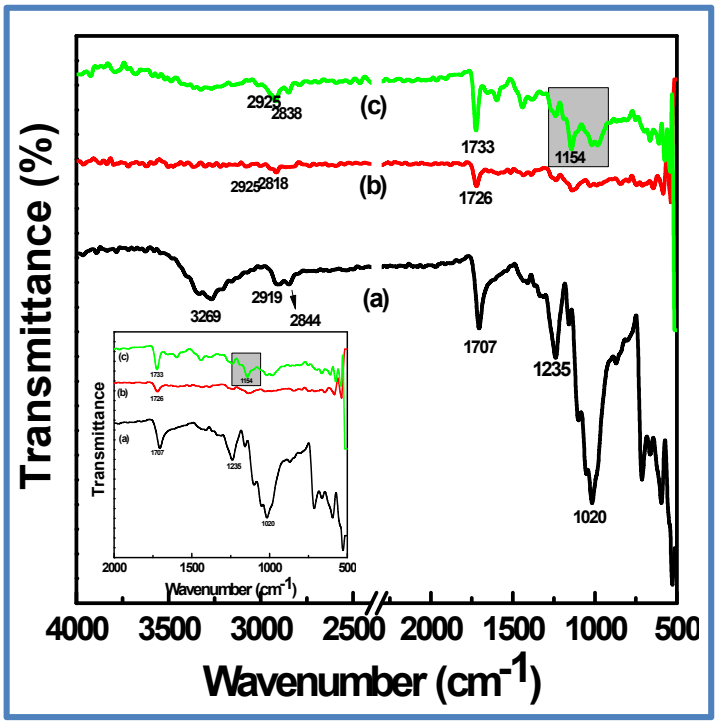

Figure 5.11: ATR-FTIR spectra of (a) bare BC, (b) 0% APZO NHs/PMMA/BC-7 coating, and (c) 1% APZO NHs/PMMA/BC-7 coating.

5.3.2.3. Microstructures of APZO NHs/PMMA Coatings

The SEM images in Figure 5.12 show the microstructures and the surface morphologies of the APZO NHs/PMMA coated and uncoated cotton fabrics. The SEM image corresponding to bare cotton is presented in Figure 5.12A (a)-(c) at different magnifications. The image reveals the web-like network of cellulose fibrils. These woven networks are composed of thick cellulose fibril bundles. Each fiber bundle has a thickness of about 50 microns in which individual fibril has a width of 5 μm. The fiber texture, its physical length, and the orientation are clear from the magnified images [Figure 5.12A (b), (c)]. Interwoven cotton fabrics have micrometer size voids between

the fiber bundles. The fibrous structural framework is also micro-porous. This porous material could be easily realized by the penetration of light energy. The air trapped in the micro-capillaries of cellulose fibers absorbs the heat energy when they are exposed to strong solar heat and build the surface temperature over cotton textiles. A mildly applied homogenous coating prepared out of any active nanoscale functional material can completely cover the porous cellulose fabrics and probably permit only the light to transfer but effectively avoid the energy absorption depending upon its optical properties. SEM images in Figure 5.12B (a)-(c) represent the black cotton applied with neat PMMA solution. It can be seen that the PMMA adhesion with the cellulosic fabric is firmly strong. The methylene bonded carbon functional group in PMMA polymer aid bridging with hydroxyl group and chemically adhere to the cotton fabric. At higher magnifications, the neat PMMA coatings appear porous. The pore size is in micrometer size. The evaporation of solvent molecules resulted in nearly homogeneous porous coatings. However, the SEM images explicitly show the PMMA film adhered on cellulose surface. The porous nature is seen only above this continuously covered film. Figure 5.12C (a)-(c) represents the microstructures of ZnO/PMMA coatings without any silane. In the absence of silane, the coatings have rough surface texture. When coatings are made with silane modified ZnO NHs/PMMA coatings (Figure 5.12D (a)-(c)), they become physically smooth, and in these soft coatings the hybrid particulates are deeply penetrated into the inter-fiber voids and dispersed along the continuous layers. The coated layers have highly uniform coverage of the cotton fabrics. In both cases, the magnified images apparently show the firm sticking of nano size ZnO particles, although some of them are micro-aggregates, on to the textile fibrils. One notable feature observed from these SEM images are the hierarchical porosity of the multilayered coatings. One can have the following advantages in this kind of nanohybrids embedded PMMA coatings. First of all, the porous feature of coatings effectively allows the nano ZnO to interact with the incident light directly. The PMMA polymer top coat makes the fabric hydrophobic in nature. Its porous multilayer architecture resembles the membrane like surface that allows the light and promotes the convection air-flow for passive cooling. In this work, it is seen that the silane treated ZnO nanohybrids encapsulated in PMMA matrix which is embedded in cotton fabrics finally resulted in hydrophobic, photoactive top coats. EDX spectroscopy analyzed the chemical composition of the coated surface of the fabrics. It confirmed that the hybrid coatings have elemental Zn, O and Si atoms. The

SEM microstructures strongly support the effective impregnation of the APZO NHs/PMMA colloidal sol through the microcapillaries of the cellulosic cotton fibers. Morphological analysis of white cotton fabrics 0% APZO NHs/PMMA/WC and 1% APZO NHs/PMMA/WC was shown in the Figure 5.13. The elemental mapping analysis of white cotton fabrics 0% APZO NHs/PMMA/WC and 1% APZO NHs/PMMA/WC was shown in the Figure 5.14.

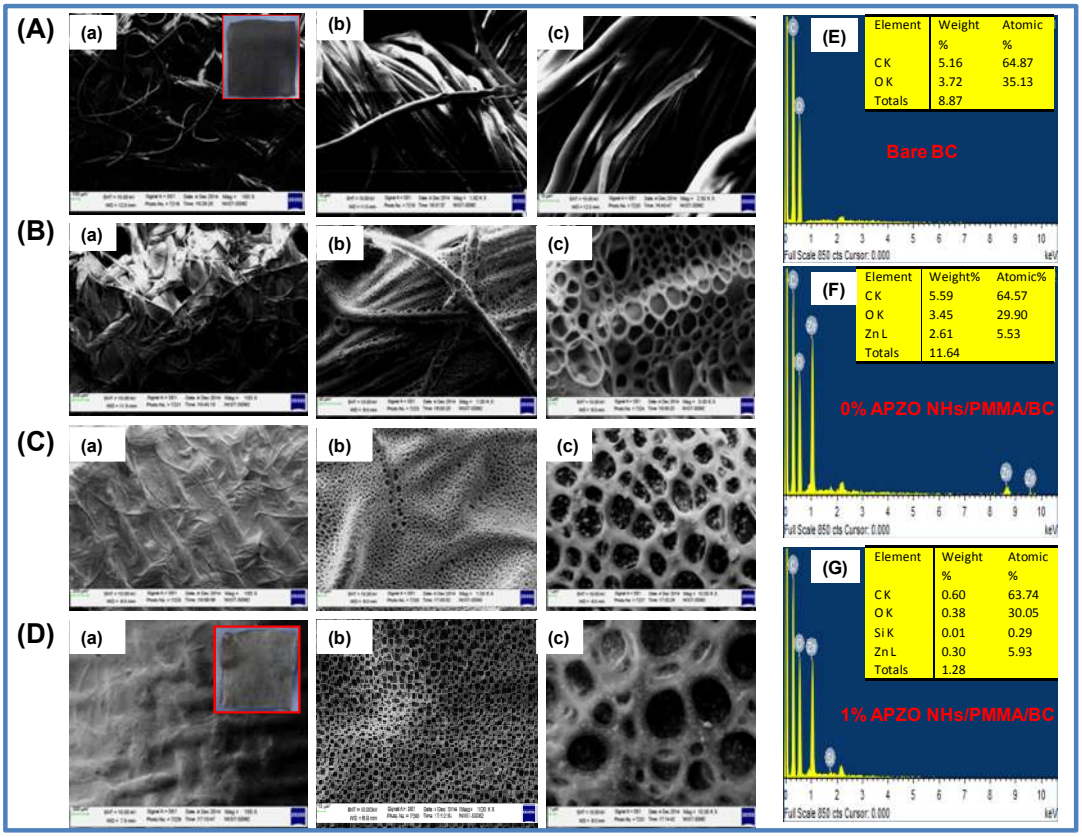

Figure 5.12: SEM images showed (A) bare BC, (B) PMMA/BC, (C) 0% APZO NHs/PMMA/BC-6 coatings, and (D) 1% APZO NHs/PMMA/BC-6 coatings. The different magnifications of the corresponding samples were also shown in (a)-(c). The higher magnifications of the corresponding samples with scale bar: A (a) 100 µm, (b) 10 µm, (c) 10 µm; B (a) 200 µm, (b) 20 µm, (c) 2 µm; C (a) 200 µm, (b) 10 µm, (c) 1 µm; D (a) 200 µm, (b) 10 µm, (c) 1 µm. The EDX patterns have reveals the elemental analysis of (E) bare BC, (F) 0% APZO NHs/PMMA/BC-6 coatings, and (G) 1% APZO NHs/PMMA/BC-6 coatings.

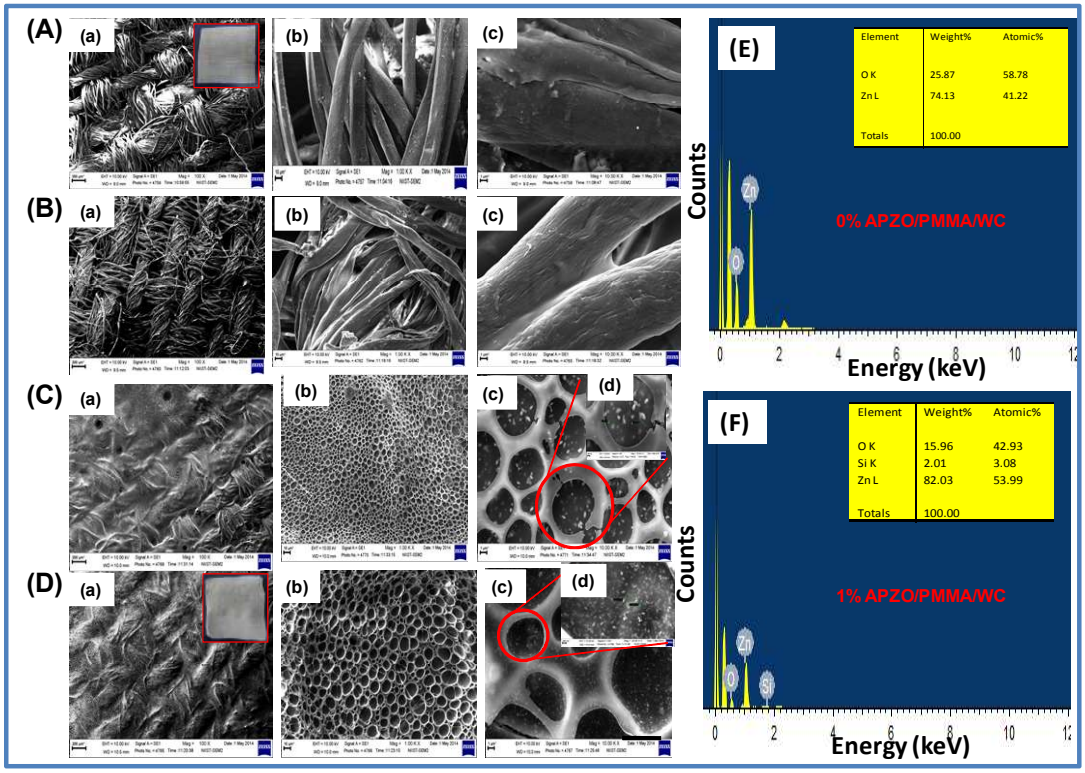

Figure 5.13: SEM images of (A) bare WC, (B) PMMA/WC, (C) 0% APZO NHs/PMMA/WC-6 coatings, and (D) 1% APZO NHs/PMMA/WC-6 coatings. The higher magnifications of the corresponding samples with scale bar: A (a) 200 µm, (b) 10 µm, (c) 1 µm; B (a) 200 µm, (b) 10 µm, (c) 1 µm; C (a) 200 µm, (b) 10 µm, (c) 1 µm, (d) 300 nm; D (a) 200 µm, (b) 10 µm, (c) 1 µm, (d) 300 nm. The EDX patterns and its corresponding elemental mapping have reveals the elemental analysis of (E) 0% APZO NHs/PMMA/WC-6 coatings, and (F) 1% APZO NHs/PMMA/WC-6 coatings.

An insight over the surface smoothness of APZO NHs/PMMA coatings on cotton fabrics can be seen from the AFM images were presented in Figure 5.15. In 1 mol% silane modified ZnO/PMMA coatings, the pore depth seems to decrease roughly 50%. The pore depth was about 2.7 µm in 0% silane treated ZnO/PMMA coatings. However, the pore depth was decreased to 1.4 µm in the presence of silane treated the coatings. The controlled rate of evaporation in chemically bridged APZO NHs/PMMA colloid is a plausible reason for the evolution of fine pores with restricted overall pore width and pore wall thickness that contribute the decreased roughness.

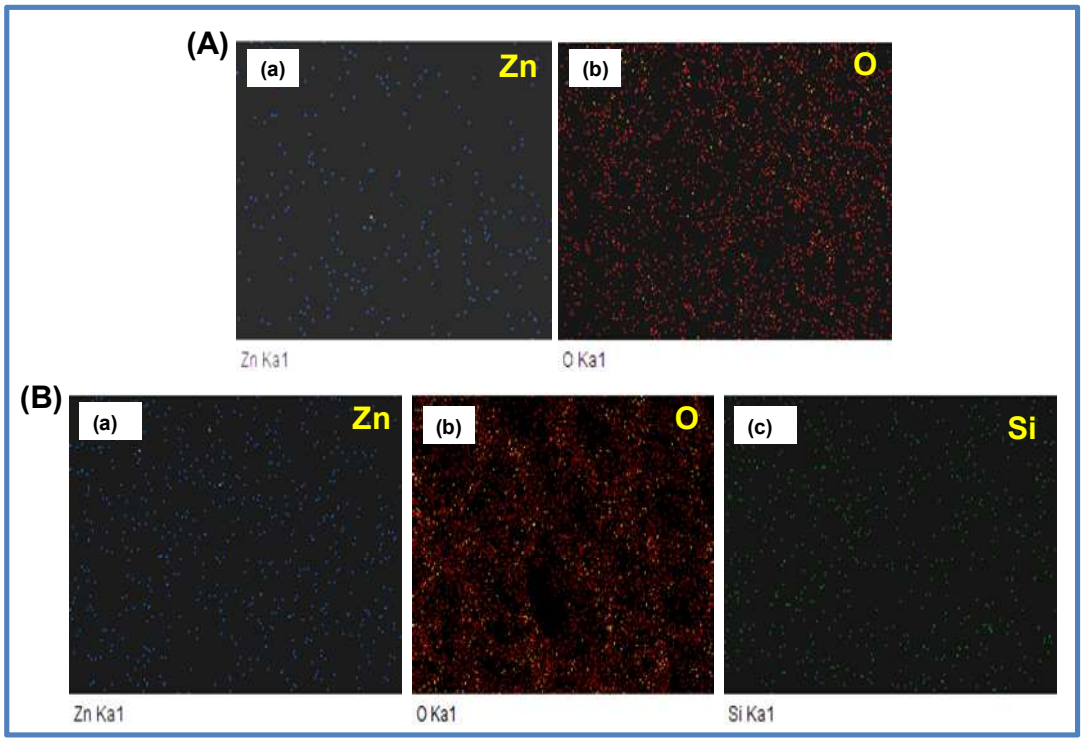

Figure 5.14: Elemental mapping have reveals the elemental analysis of (A) 0% APZO NHs/PMMA/WC-6 coatings (a) Zn and (b) O; (B) 1% APZO NHs/PMMA/WC-6 coatings (a) Zn, (b) O, and (c) Si.

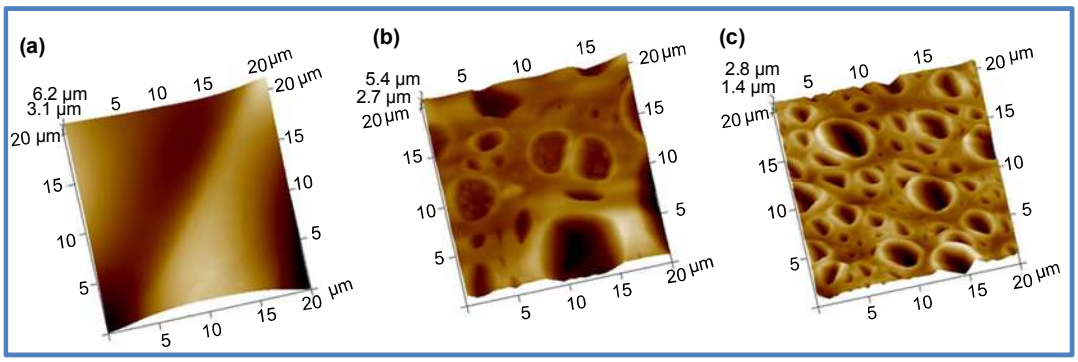

Figure 5.15: 3D AFM topographic images of (a) bare black cotton, (b) 0% APZO NHs/PMMA/BC-3 coatings, and (c) 1% APZO NHs/PMMA/BC-3 coatings.

5.3.2.4. Weight Gain of Coatings and Water Absorption Ability of Cotton fabrics

The amount of APZO NHs/PMMA coated on the cotton fabrics is to determine the weight gain of the cotton fabrics was shown in Figure 5.16(a). The percentage weight gain of the cotton fabrics was calculated by the equation:

$$wt_{coatings}\% = (wt_{final} - wt_{before})/wt_{before} \times 100 \quad (5.1)$$

where $wt_{coatings}\%$ is the weight gain of coatings, wt_{final} is the final weight of the fabrics (dried to zero moisture content) after coatings, wt_{before} is the weight of the fabrics (dried to zero moisture content) before coatings. The results confirmed that 1% APZO/PMMA coatings show less weight gain compared to its counterpart. The water absorption property of untreated cotton, coatings made with APZO NHs/PMMA sol was tested against simple ZnO/PMMA and the results are compared in Figure 5.16(b). The percentage water absorption was calculated according to the following equation;

$$w\% = (w_a - w_o)/w_o \times 100 \quad (5.2)$$

where $w\%$ is the water absorption ability of the fabrics, w_a is the mass of the fabric with absorbed water and w_o is the mass of the dried fabric samples. This test demonstrates the layers prepared with hybrid nanoparticles have comparatively better hydrophobicity. The degree of hydrophobic nature indirectly indicated the uniform coverage of hybrid films at the interface over cellulose capillaries and intervoid-cavities.

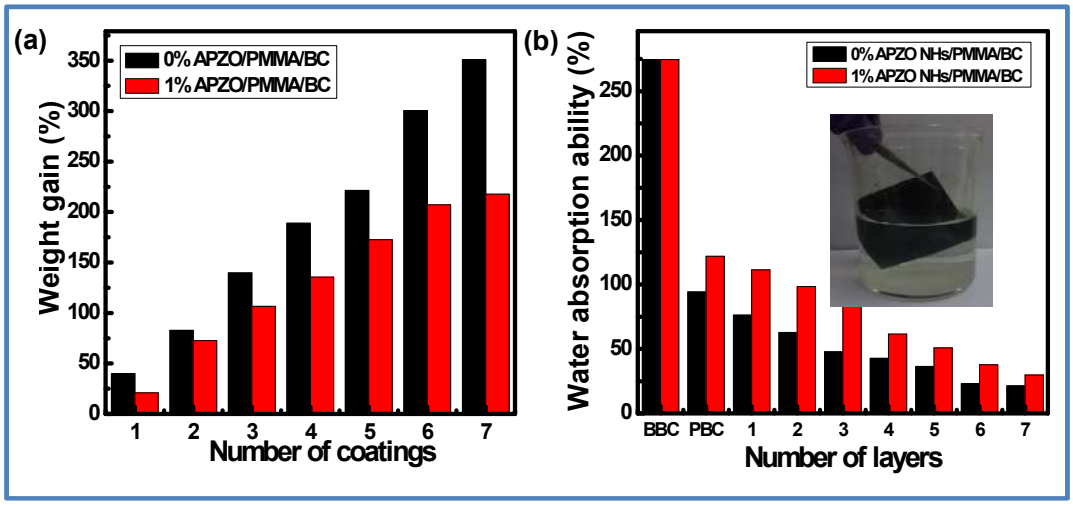

Figure 5.16: (a) Weight gain of cotton fabrics without moisture absorption after coatings, (b) Water absorption ability of 0% and 1% APZO NHs/PMMA/BC samples with respect to the number of layers. (BBC= bare black cotton, PBC= neat PMMA coated cotton). Inset of Figure (b) shows the photographic image of black cotton fabrics immersed in water.

5.3.2.5. UV Shielding Effect of Black Cotton Fabrics with APZO NHs/PMMA Coatings

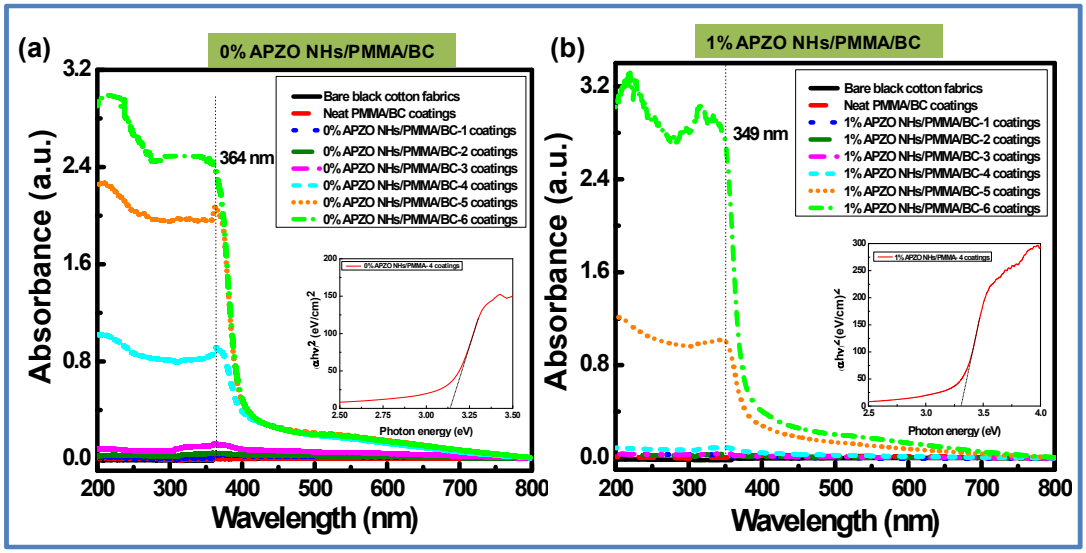

Figure 5.17: UV/Vis absorbance spectra with LbL coatings of (a) 0% APZO NHs/PMMA/BC and (b) 1% APZO NHs/PMMA/BC (Inset shows the optical absorption spectra for photon energy in terms of eV.).

UV/Vis absorbance spectra [Figure 5.17] of the APZO NHs/PMMA coated on cotton fabrics, *via* LbL technique, were measured in the wavelength region 200-800 nm using the bare cotton fabrics as the reference. The UV absorption analysis shows the bare cotton and the neat PMMA coatings are highly transparent to UV rays. The cotton textile applied with ZnO dispersed PMMA and silane modified nano ZnO hybrids embedded PMMA coatings exhibit absorption of UV radiation at wavelengths 364 and 349 nm, respectively as evidenced from the UV absorption spectra provided in Figure 5.17(a) and (b). A more UV absorption is seen above 5 layers of hybrid coatings onto the cotton fabrics. UV absorption by the multilayer hybrid coatings takes place at the same wavelength as that of the dispersion of nano ZnO indicating that the hybrid nanoparticles preserve their molecular state even after it is modified with silane organics and embedded in the PMMA polymer matrix. The blue-shift of the wavelength at 349 nm evidences the effective capping of APS. Inset in Figure 5.17 illustrates the bandgap of the 0% APZO NHs/PMMA/BC and 1% APZO NHs/PMMA/BC coatings which was computed as 3.13 and 3.32 eV, respectively. Apparently, it can be understood that the nano ZnO and APZO

NHs embedded PMMA coatings on cotton fabrics can efficiently block the UV and produce safe textiles.

5.3.2.6. NIR Reflectance and Total Solar Reflectance (R*) of Coated Cotton Fabrics

NIR reflectance of white as well as black color cotton fabrics treated with APZO NHs/PMMA sol coatings were shown in Figure 5.18 and Figure 5.19, respectively. Overall, the bare as well as light transparent PMMA coated black color cotton surface has shown only less than 30% NIR reflectance. At the same time, when compared to black color cotton fabrics, the white cotton has about 50% NIR reflectance by virtue of its bright surface, though the fabric texture is identical. In both cotton fabrics, the level of diffuse NIR reflectance is declined with increasing wavelength region 1500-2500 nm. When nano ZnO and silane modified nano ZnO hybrids embedded PMMA coatings were applied over the black fabric, the reflectance is increased from the low value of 30% to high value of 50%, close to that of white cotton fabrics, without affecting its black appearance. It is seen that coating layers strongly enhance NIR reflectance. Higher numbers of APZO NHs/PMMA coatings lead to better reflectance because of the increased concentration of ZnO nanoparticles embedded in the multilayer coatings. The 1% APZO NHs/PMMA/BC-3 layers coatings show ~53 and 50% NIR reflectance at high heat energy carrying IR wavelengths 810 and 1100 nm, respectively [Figure 5.19C]. The same samples show NIR solar reflectance, R* as 48, 49, and 52% for 3, 5, and 7 layers coatings respectively [Figure 5.19D]. The weak Rayleigh scattering or strong Mie scattering determines the optical properties of a material when solar light energy interacts with the matter, depending upon its crystalline arrangement. In cotton fabrics, the interaction with the light energy is weak due to its visible opaqueness where a strong Mie scattering can be possible. If the matter contains any nanoscale optically transparent elements, depending upon the nano-dimensions, the light can be absorbed or transmitted. Cotton fabric is composed of parallel-aligned microfibrils and SEM images indicate the cellulosic fibre diameter has less than one micron size. This micrometer range of the microfibrils is in fact inadequate for the effective reflection of the near IR waves in the critical region 800-1100 nm. Moreover, another important criteria for the light-matter interaction are the matching refractive index values of the matter. In the cotton fabric crystalline domains, the cellulose chains are connected by hydrogen bonds to form a highly ordered crystalline structure. The refractive index of cellulose is 1.618 along the

fiber and 1.544 in the transverse direction. This value was enhanced when APZO NHs embedded PMMA top coat was provided. It is a nanocomposite coating, and the high refractive index of active nano ZnO contributes to high reflection of near-IR energy. The high refractive index and loosely agglomerated nano aggregates with the particle diameter in the range 250-350 nm have a combined effect on the NIR reflectance of the APZO NHs/PMMA coatings.

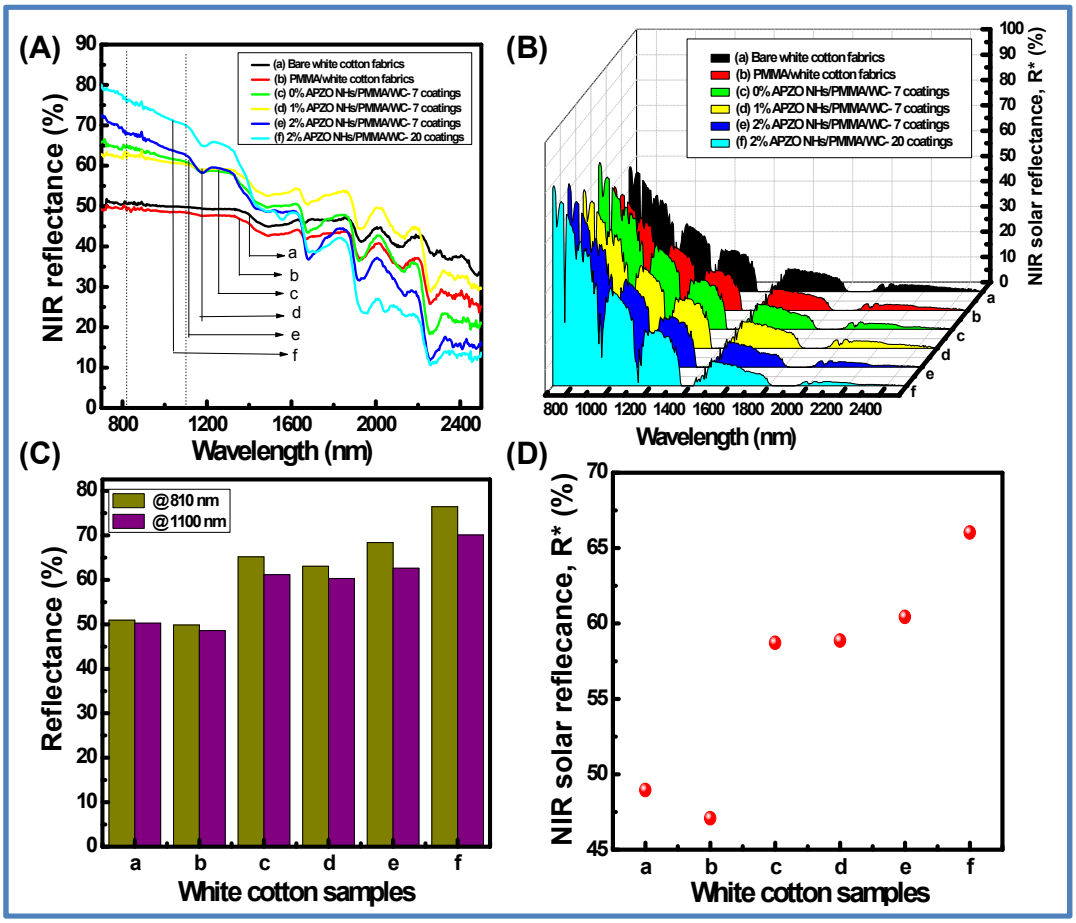

Figure 5.18: (A) NIR reflectance of APZO NHs/PMMA treated white cotton fabrics; (B) NIR solar reflectance of corresponding samples; (C) reflectance @ 810 and 1100 nm; (D) NIR solar reflectance *vs.* white cotton samples. (a) Bare white cotton fabrics, (b) PMMA/WC, (c) 0% APZO NHs/PMMA/WC-7 coatings, (d) 1% APZO NHs/PMMA/WC-7 coatings, (e) 2% APZO NHs/PMMA/WC-7 coatings, (f) 2% APZO NHs/PMMA/WC-20 coatings.

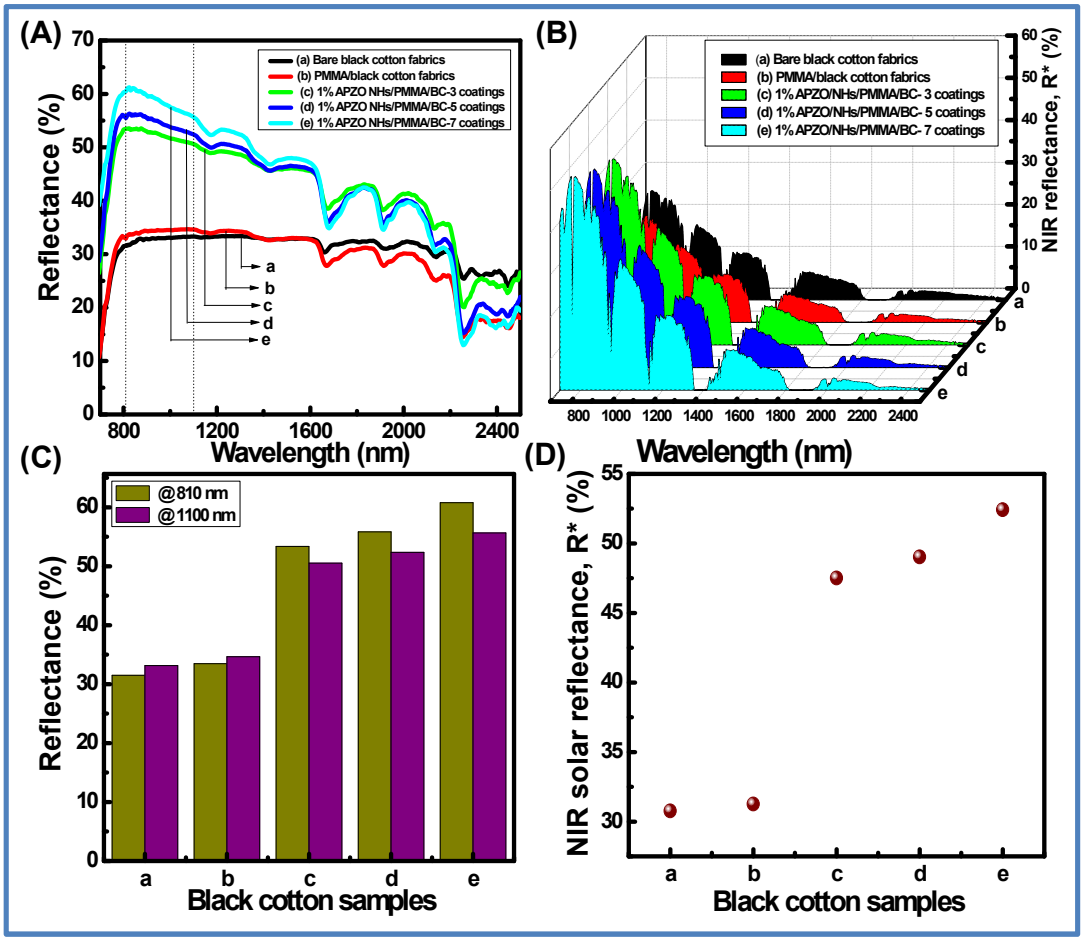

Figure 5.19: (A) NIR reflectance of APZO NHs/PMMA coated black cotton fabrics; (B) NIR solar reflectance of corresponding samples; (C) diffuse reflectance @ 810 and 1100 nm. (D) NIR solar reflectance *vs.* black cotton samples. (a) Bare BC, (b) PMMA/BC, (c) 1% APZO NHs/PMMA/BC-3 coatings, (d) 1% APZO NHs/PMMA/BC-5 coatings, (e) 1% APZO NHs/PMMA/BC-7 coatings.

Figure 5.20 depicts the comparative NIR reflectance and NIR solar reflectance performances of the white cotton fabrics in comparison with black color counterpart prepared with 1% APZO NHs/PMMA coatings having 7 layers. The white cotton fabrics showed 63 and 60% NIR reflectance. The corresponding values for black cotton fabrics being 60 and 55% at wavelengths of 810 and 1100 nm, respectively [Figure 5.20A]. The NIR solar reflectance (R*) of white, as well as black fabrics modified with 1% APZO NHs/PMMA/cotton-7 coatings, were evaluated as 58 and 52%, respectively. It can be concluded that irrespective of the surface of the cotton textiles, the APZO NHs embedded PMMA coatings can enhance the NIR solar reflectance [Figure 5.20B]. Photographic

images of uncoated and coated white and black cotton fabrics were also shown in Figure 5.20C. Showing good flexibility of the cotton textile 1% APZO NHs/PMMA/BC coated with 7 layers was shown in Figure 5.21.

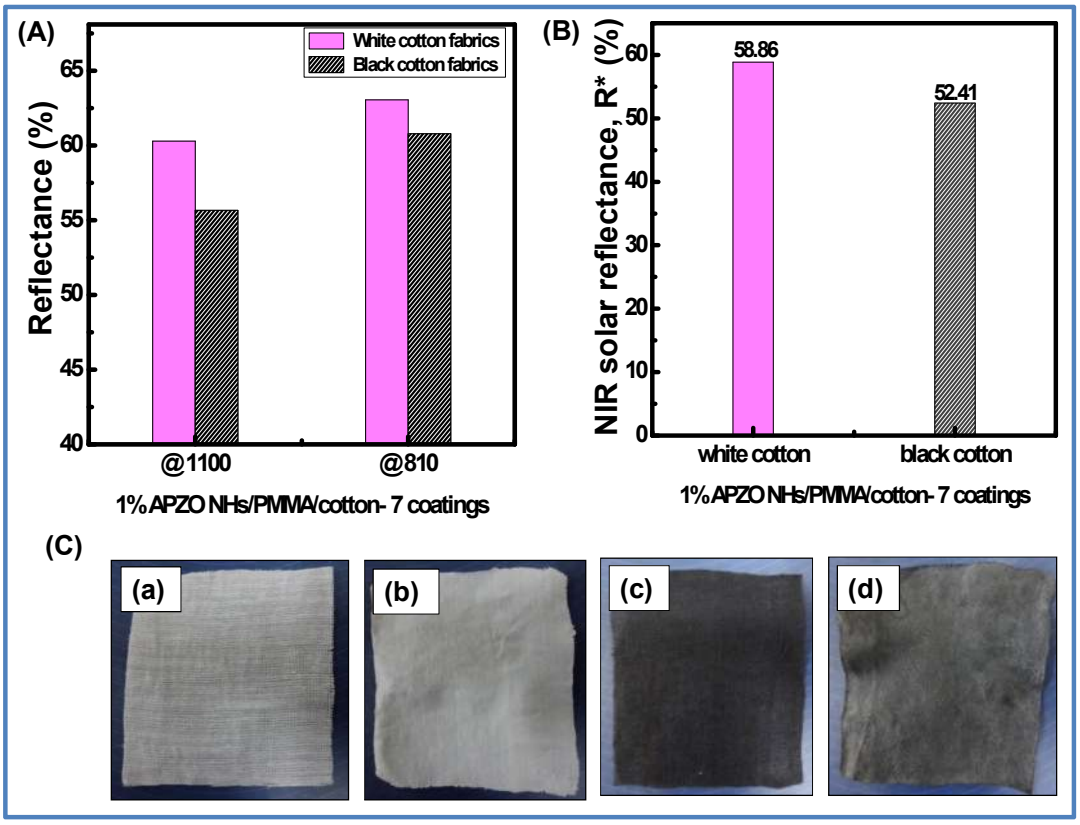

Figure 5.20: (A) NIR reflectance of 1% APZO NHs/PMMA coated black and also white cotton fabrics @ 810 and 1100 nm; (B) NIR solar reflectance of black and also white cotton fabrics treated with 1% APZO NHs/PMMA-7 coatings; (C) Photographic images of cotton fabrics. (a) Bare WC, (b) 1% APZO NHs/PMMA/WC-7 coatings, (c) bare BC, and (d) 1% APZO NHs/PMMA/BC-7 coatings.

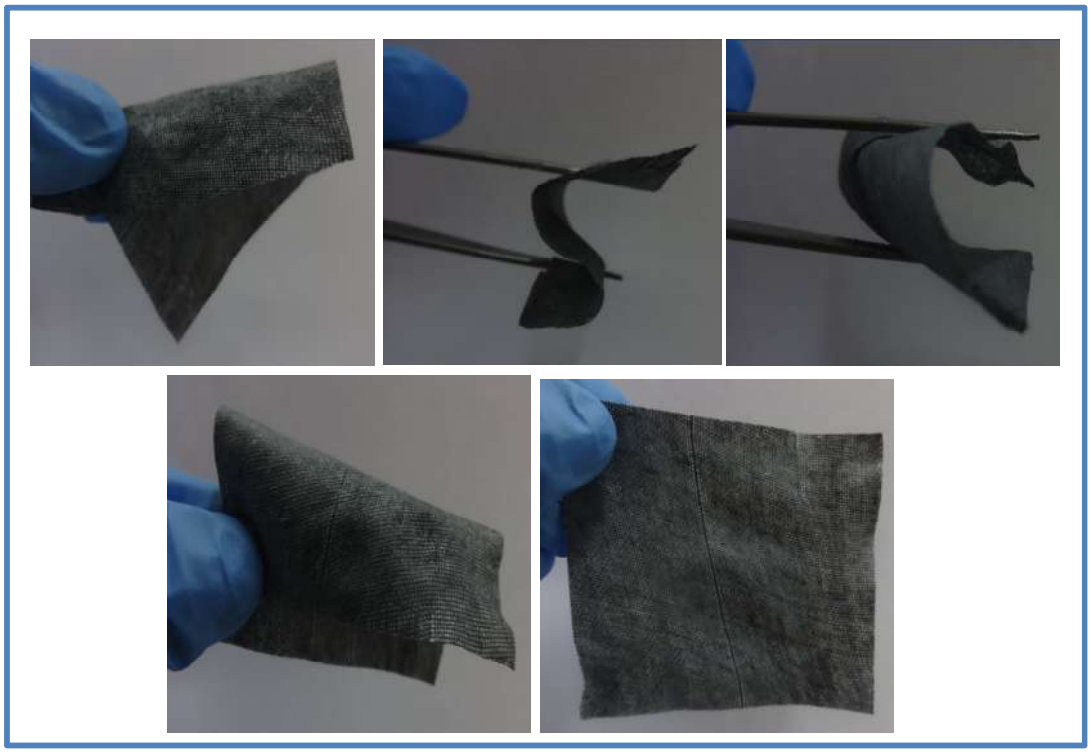

Figure 5.21: A photograph of the cotton textile 1% APZO NHs/PMMA/BC coated with 7 layers.

5.3.2.7. Evaluation of Antifungal Activity

Figure 5.22 shows the antifungal property of the cotton textiles coated with APZO NHs/PMMA colloid materials. Compared to the bare cotton fabrics, the APZO NHs dispersed PMMA matrix coated cotton textiles distinctly exhibit the better zone of inhibition to the test fungi species *Aspergillus niger* and *Aspergillus flavus*. Cotton fabrics are microporous, and their surfaces are hydrophilic. Under any humid environments, absorption of moisture favors the growth of fungi. The fungus is in general one of the responsible factors for allergic, asthma and cough. The silane modified ZnO hybrids embedded PMMA coatings not only introduce the hydrophobicity in cotton fabrics for the effective moisture repellence quality but also offer resistance against fungal growth, indicating the APZO NHs/PMMA modified cotton textiles perform as bio-safe cool textiles.

Plausible Antimicrobial Mechanism: Previous studies on the antibacterial behavior of ZnO NPs confirmed that the morphology and oxidative stress play important roles in the antibacterial activity [Sourabh *et al.,* 2014; Krishna *et al.,* 2011]. Due to semiconducting

nature of ZnO (band gap 3.2 eV), it acts as photocatalytic material. Superoxide anion production due to the photocatalytic reaction is one of the probable reasons for disturbing microbial process that kills the microorganisms including bacteria and fungi. The combined effects of hydrophobic nature and photo-active property of ZnO, the hybrid coatings showed excellent antifungal property [Navale *et al.,* 2015].

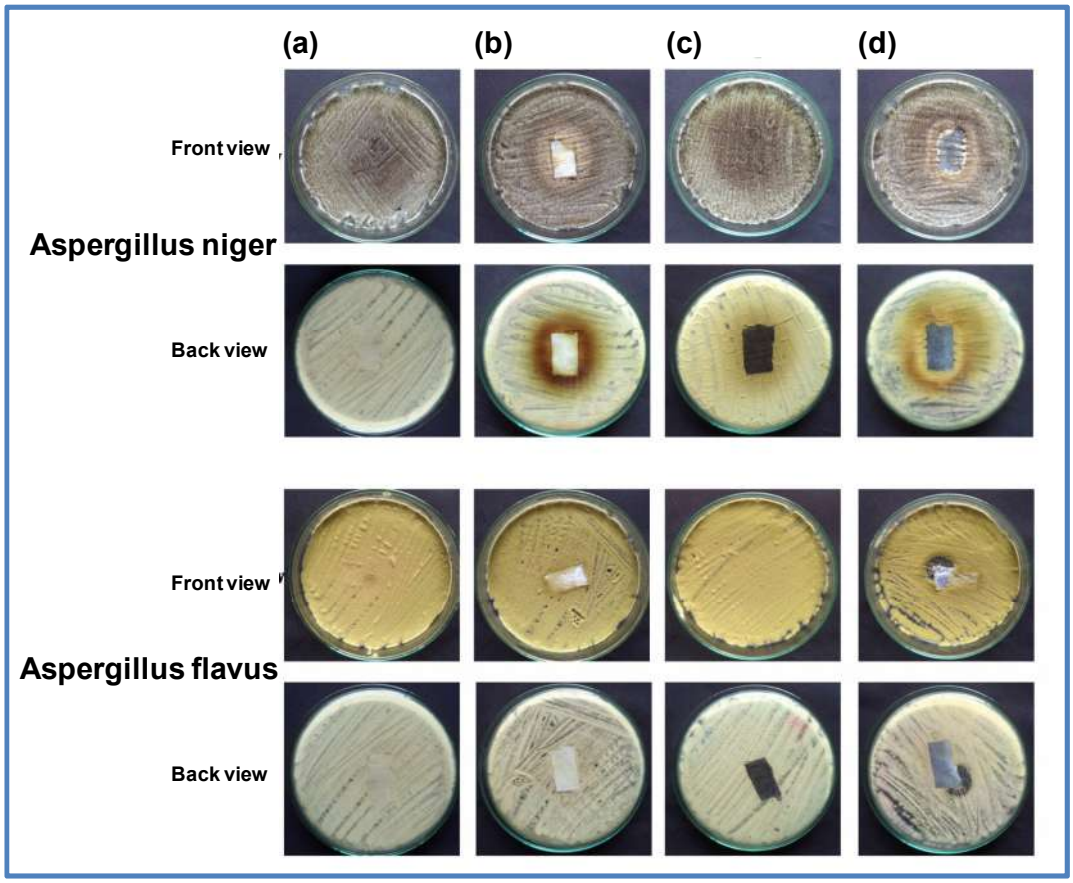

Figure 5.22: Antifungal activities of (a) bare white cotton fabrics, (b) 1% APZO NHs/PMMA coated white cotton fabrics, (c) bare black cotton fabrics, (d) 1% APZO NHs/PMMA coated black cotton fabrics.

5.4. CONCLUSIONS

In summary, a novel chemically reactive, multifunctional hybrids/polymer nanocoatings were designed with silane treated ZnO/PMMA which is validated on the black color cotton fabrics. The nanohybrid/polymer top-coats offer beneficial properties such as UV absorption, enhanced NIR reflectance, hydrophobicity and antifungal property. Co-precipitation synthesis of ZnO in the presence of *in situ* organosilanes resulted in nano ZnO hybrid with particle size in the range 220-350 nm. The formation of silanol functional groups on the surface of nano ZnO produced positively charged surfaces that chemically react with hydroxyl groups present in the cellulosic building blocks that promote firm physico-chemical adhesion of nano ZnO over the cellulosic fibrils through chemical cross-linking. A multilayer porous hybrid coatings consisting of APZO NHs/PMMA colloids and the hybrid sol is dip-coated on the cotton surface. The hybrid top coats enhanced the NIR reflectance of bare black cotton fabric from 30 to 63% when the coating layer was applied 7 times and inherent flexibility. The hybrid coating also makes the textile prone to water absorption and better resistance against fungal growth. Upon coated with silane treated ZnO embedded PMMA hybrids, the black cotton fabric finally attained NIR reflectance close to that of the white cotton textiles.

The investigations of this Chapter have been published.

Soumya, S.; Kumar, S. N., Mohamed, A. P., Ananthakumar, S., Silanated nano ZnO hybrid embedded PMMA polymer coatings on cotton fabrics for near-IR reflective, antifungal cool-textiles, *New Journal of Chemistry*, 40, **2016**, 7210-7221.

SUMMARY

ZnO is undoubtedly a versatile functional material where it has a proven record as a promising antibacterial/antifungal ingredients in paints and functional coatings. When it compared with the TiO_2, one of the other unique candidate materials extensively recommended for functional coatings. ZnO is, in fact, stand closely to TiO_2 in terms of the IR reflectance and UV shielding properties. For any practical use, mostly TiO_2 is preferred. However, the coating industries are serious to find alternate to TiO_2 because of its high price. In this context, ZnO can be one of the alternatives because, in the broad sense, ZnO can be easily synthesized in its nanocrystalline nature via simple precipitation technique in presence of normal surfactants. Even though ZnO is easily obtained in nano-form by simple chemical technique, it is essential to identify what grade of nano ZnO is more useful for any kind of functional coatings. Textiles and glass industries are expecting functional coatings that can have good transparency and multiple benefits ranging from hydrophobic to corrosion resistant. In this regard, factors like morphology, particle size, coating thickness, photoluminescence etc are important. In broad sense, this thesis work is carried to bring out the beneficial properties of ZnO when they are used as active fillers in any polymer substrates. Thrust is given on solar heat control top coats in which two components are usually required; a polymer matrix and an active ingredient. Nano ZnO as active filler, highly favored to improve the IR reflectance as well as UV shielding property of polymer matrix coatings. The present thesis work is revolving around this aspect to find out what kind of nano ZnO is important for having effective IR reflectance without compromising on UV shielding.

In summary, the present thesis deals with the ZnO embedded PMMA nanocomposite coatings and films for UV/IR shielding solar thermal control surfaces which find applications as cool-coatings on industrial products like polymers, glass panels, and textiles.

Chapter 1

The first chapter encompassed introduction about nanomaterials and its functional nanocomposites and coatings. A brief description about IR reflective nanomaterials is covered. A list of nanomaterials preferred for solar heat control coatings is also mentioned. Solar heat controlling mechanism and factors deciding the IR reflectance is explained with literature evidence. Since ZnO and PMMA are selected for this study, the salient features of these study materials are also described. A brief review of ZnO, its synthesis, properties, and applications were cited. Research problems and outline of the thesis was clearly defined at the end of the chapter.

Chapter 2

NIR reflectance property of ZnO dispersed PMMA polymer nanocomposite films is studied and presented in this working chapter. Nano ZnO particles were successfully synthesized *via* microwave and reflux techniques with various capping agents. ZnO morphologies, average physical size, and IR reflectance, UV shielding features of ZnO are ascertained through different characterization techniques. Nano ZnO embedded PMMA film shows enhanced reflectance compared to neat PMMA. Apart from PMMA/ZnO films, the PU/PMMA/ZnO nanocomposite film was also fabricated and examined for IR reflectance. More than 50% IR reflectance was seen even with 0.1 wt% addition of nano ZnO. The ZnO/polymer composite films can be explored as interface layers/films and membranes in glass and polymer type sandwich panels for the effective solar thermal controlled indoors of buildings.

Chapter 3

In this chapter, Al-doped ZnO nanoparticles was prepared and dispersed in PMMA matrix for fabricating multifunctional nanocomposite coatings. It was found that the Al doped coatings deliver excellent UV absorption in the most harmful region of UV radiation and enhanced the NIR reflectance. The UV active photodegradation of MB dye confirmed the self-cleaning activity of the coatings. Interestingly, AZO/PMMA coating showed significant surface temperature cut-off up to $8^{o}C$ even when the coating is made with 7 layers. The AZO/PMMA coating also showed anti-icing property.

Chapter 4

In this chapter, Sn and Ag doped ZnO quantum dots [ZQDs] were synthesized *via* microwave-reflux assisted sol-gel synthesis. The doped ZnO quantum dots were confirmed by XRD, DLS, Raman, UV, PL, and FTIR analysis. *In situ* polymerization was carried out for obtaining ZQDs embedded PMMA coatings. Doped ZQDs/PMMA coatings showed UV shielding and luminescence property. AFM and SEM analysis confirmed the surface homogeneity and coating thickness. Ag doped coating shows higher reflectance. The $LaPO_4$ modified Sn doped ZQDs/PMMA coatings enhanced the reflectance compared to undoped sample. A better photochromic and luminescence behavior was observed in *Spiropyran* added doped ZQDs/PMMA coatings.

Chapter 5

In this working chapter, use of IR reflective ZnO was explored to design cool-textiles. Chemically reactive, multifunctional ZnO hybrid/polymer nanocoatings were made with silane treated ZnO/PMMA which was further coated on black color cotton fabrics and subsequently validated for cool-textiles. The nanohybrid/polymer coatings offered beneficial properties such as UV absorption, enhanced NIR reflectance, hydrophobicity, and antifungal property.

REFERENCES

Abdel, S. A., Photochromism of dihydroindolizines part VI: synthesis and photochromic behavior of a novel type of IR-absorbing photochromic compounds based on highly conjugated dihydroindolizines, *Journal of Physical Organic Chemistry,* 19, **2006**, 402–414.

Abidi, N.; Cabrales, L.; Hequet, E., Functionalization of a cotton fabric surface with titania nanosols: applications for self-cleaning and UV-protection properties*, ACS Applied Materials & Interfaces,* 10, **2009**, 2141–2146.

Acosta, M. A. R.; Huerta, A. M. T.; Crespo, M. A. D.; Vela, A. F.; Rosales, H. J. D.; Adame J. A. A., Thermal, mechanical and UV-shielding properties of poly(methyl methacrylate)/cerium dioxide hybrid systems obtained by melt compounding, *Polymers,* **2015**, 7, 1638-1659.

Ahmad, M.; Zhu, J., ZnO based advanced functional nanostructures: synthesis, properties and applications, *Journal of Materials Chemistry*, 21, **2011**, 599–614.

Amerio, E.; Fabbri, P.; Malucelli, G.; Messori, M; Sangermano, M; Taurino, R., Scratch resistance of nano-silica reinforced acrylic coatings, *Progress in Organic Coatings,* 62, **2008**, 129–133.

Andersson, N.; Alberius, P.; Ortegren, J.; Lindgren, M.; Bergstrom, L., Photochromic mesostructured silica pigments dispersed in latex films, *Journal of Materials Chemistry*, 15, **2005**, 3507-3513.

Anumol, E. A.; Kundu, P.; Deshpande, P. A.; Madras, G.; Ravishankar, N., New insights into selective heterogeneous nucleation of metal nanoparticles on oxides by microwave-assisted reduction: rapid synthesis of high-activity supported catalysts, *ACS Nano,* 5, **2011**, 8049–8061.

Asok, A.; Gandhi M. N.; Kulkarni A. R., Enhanced visible photoluminescence in ZnO quantum dots by promotion of oxygen vacancy formation, *Nanoscale*, 4, **2012**, 4943–4946.

Athauda, T. J.; Hari, P.; Ozer, R. R., Tuning physical and optical properties of ZnO nanowire arrays grown on cotton fibers, *ACS Applied Materials & Interfaces*, 5, **2013**, 6237−6246.

Avendaño, E.; Azens, A.; Isidorsson, J.; Karmhag, R.; Niklasson, G. A.; Granqvist, C. G., Optimized nickel-oxide-based electrochromic thin films, *Solid State Ionics,* 165, **2003**, 169-173.

Bai, S.; Hu, J.; Li, D.; Luo, R.; Chen, A.; Liu, C. C., Quantum-sized ZnO nanoparticles: Synthesis, characterization and sensing properties for NO_2, *Journal of Materials Chemistry*, 21, **2011,** 12288-12294.

Balamurugan, S.; Dheebikha, K.; Raja, G. T. S., Nanocrystalline $Gd_2Ti_2O_7$ pyrochlore material for NIR reflective pigment application: Micro-structural and optical studies, journal of nanoscience and nanotechnology, 16, **2016**, 677–688.

Balanand, S.; Maria, M. J.; Rajan, T. P. D.; Mohamed, A. P.; Ananthakumar, S., Bulk processing of ZnO nanostructures via microwave assisted oxidation of mechanically seeded Zn dust for functional paints and coatings*, Chemical Engineering Journal,* 284, **2016**, 657–667.

Bartek, M.; Correia, J. H.; Wolffenbuttel, R. F., Silver-based reflective coatings for micromachined optical filters, *Journal of Micromechanics and Microengineering,* 9, **1999**, 162–165.

Bendiganavale, A. K.; Malshe, V. C., Infrared reflective inorganic pigments, *Recent Patents on Chemical Engineering*, 1, **2008**, 67-79.

Biswas, K.; Das, B.; Rao, C. N. R., Growth kinetics of ZnO nanorods: capping-dependent mechanism and other interesting features, *Journal of Physical Chemistry* C, 112, **2008**, 2404–2411.

Brady, R. F Jr.; Wake, L. V., Principles and formulations for organic coatings with tailored infrared properties, *Progress in Organic Coatings*, 20, **1992**, 1-25.

Briener, J. M.; Mark, J. E., Preparation, structure, growth mechanisms and properties of siloxane composites containing silica, titania or mixed silica–titania phases, *Polymer*, 39, **1998**, 5483-5493.

Brus, L. E., Electronic wavefunctions in semiconductor clusters, *Journal of Physical Chemistry*, 90, **1968**, 2555-2560.

Busila, M.; Musat, V.; Textor, T.; Mahltig, B., Synthesis and characterization of antimicrobial textile finishing based on Ag:ZnO nanoparticles/chitosan biocomposites, *RSC Advances*, 5, **2015**, 21562-21571.

Cano, L.; Gutierrez, J.; Tercjak, A., Rutile TiO_2 nanoparticles dispersed in a self-assembled polystyrene-block-polymethyl methacrylate diblock copolymer template, *Journal of Physical Chemistry C,* 117, **2013**, 1151–1156.

Cao, Z.; Zhang, Z.; Wang, F.; Wang, G., Synthesis and UV shielding properties of zinc oxide ultrafine particles modified with silica and trimethyl siloxane, *Colloids and Surfaces: A Physicochemical Engineering Aspects,* 340, **2009**, 161–167.

Carosio, F.; Fontaine, G.; Alongi, J.; Bourbigot, S., Starch-based layer-by-layer assembly: Efficient and sustainable approach to cotton fire protection, *ACS Applied Materials & Interfaces*, 7, **2015**, 12158−12167.

Chakraborty, H.; Sinha, A.; Mukherjee, N.; Ray, D.; Chattopadhyay, P. P., Indentation and scratch behavior of functionalized MWCNT–PMMA composites at the micro/nanoscale, *Polymer Composites*, 35, **2014**, 948–955.

Chakradhar, R. P. S.; Kumar, V. D.; Rao, J. L.; Basua, B. J., Fabrication of superhydrophobic surfaces based on ZnO–PDMS nanocomposite coatings and study of its wetting behavior, *Applied Surface Science,* 257, **2011**, 8569–8575.

Chang, C. -C.; Huang, F. -H.; Chang, H. -H.; Don, T. -M.; Chen, C. -C.; Cheng, L. -P., Preparation of water-resistant antifog hard coatings on plastic substrate, *Langmuir*, 28, **2012**, 17193-17201.

Chen, F.; Jiang, X.; Liu, R.; Yin, J., Well-defined PMMA brush on silica particles fabricated by surface-initiated photopolymerization (SIPP), *ACS Applied Materials & Interfaces,* 2, **2010**, 1031–1037.

Chen, S.; Li, X.; Li, Y.; Sun, J., Intumescent flame-retardant and self healing superhydrophobic coatings on cotton fabric, *ACS nano*, 9, **2015**, 4070–4076.

Cho, S.; Jung, S. H.; Lee, K. H., Morphology-controlled growth of ZnO nanostructures using microwave irradiation: from basic to complex structures, *Journal of Physical Chemistry C,* 112, **2008**, 12769–12776.

Choi, J.; Han, K.; Kim, J. H., Enhanced near infrared reflectance of $TiO_2/SiO_2/TiO_2$ multilayer structure using a base-catalyzed SiO_2 film, *Thin Solid Films,* 569, **2014**, 100–103.

Chung, C.; Lee, M.; Choe, E. K., Characterization of cotton fabric scouring by FT-IR ATR spectroscopy, *Carbohydrate Polymers,* 58, **2004**, 417–420.

Condo, P. D.; Kirkman, J. R.; Bright, C. I.; Stoss, W, Infrared reflecting films for solar control and other uses, US Patent No. 0316852 A1, **2010**.

Coser, E.; Moritz, V. F.; Krenzinger, A.; Ferreira, C. A., Development of paints with infrared radiation reflective properties, *Polímeros,* 25, **2015**, 305-310.

Costenaro, D.; Carniato, F.; Gatti, G.; Marchese, L.; Bisio, C., Preparation of luminescent ZnO nanoparticles modified with aminopropyltriethoxy silane for optoelectronic applications, *New Journal of Chemistry,* 37*,* **2013**, 2103−2109.

de Dood, M. J. A.; Kalkmann, J.; Strohhofer, C.; Michielsen, J.; Elsken, J. V., Hidden transition in the "unfreezable water" region of the PVP−water system, *Journal of Physical Chemistry B,* 107, **2003**, 5906.

Demir, M. M.; Memesa, M.; Castignolles, P.; Wegner, G., PMMA/Zinc oxide nanocomposites prepared by in-situ bulk polymerization, *Macromolecular Rapid Communications,* 27, **2006**, 763–770.

Demir, M. M.; Wegner, G., Challenges in the preparation of optical polymer composites with nanosized pigment particles: A review on recent efforts, *Macromolecular Materials and Engineering*, 297, **2012**, 838–863.

Djurisic, A. B.; Chen, X.; Leung Y. H.; Ng, A. M. C., ZnO nanostructures: growth, properties and applications, *Journal of Materials Chemistry*, 22, **2012**, 6526.

Droval, D.; Aranberri, I.; Bilbao, A.; German, L.; Verelst, M.; Dexpert-ghys, J., Antimicrobial activity of nanocomposites: poly(amide) 6 and low density polyethylene filled with zinc oxide, *e- Polymers,* 128, **2008**, 1-13.

Du, H.; Xu, G. Q.; Chin, W. S.; Huang, L.; Ji, W., Synthesis, characterization, and nonlinear optical properties of hybridized CdS-polystyrene nanocomposites, *Chemistry of Materials*, 14, **2002**, 4473–4479.

Du, X.; Dong, L.; Li, C.; Liang, Y.; Chen, Y., Diffuse reflectance infrared fourier transform and raman spectroscopic studies of MoO_3 dispersed on CeO_2 support, *Langmuir*, 15, **1999**, 1693.

Duan, W.; Xie, A.; Shen, Y.; Wang, X.; Wang, F.; Zhang, Y.; Li, J., Fabrication of superhydrophobic cotton fabrics with UV protection based on CeO_2 particles, *Industrial & Engineering Chemistry Research,* 50, **2011**, 4441–4445.

Eita, M.; Sayed, R. E.; Muhammed, M., Optical properties of thin films of zinc oxide quantum dots and polydimethylsiloxane: UV-blocking and the effect of cross-linking, *Journal of Colloid and Interface Science,* 387, **2012a**, 135–140.

Eita, M.; Wagberg, L.; Muhammed, M., Spin-assisted multilayers of poly(methyl methacrylate) and zinc oxide quantum dots for ultraviolet-blocking applications, *ACS Applied Materials & Interfaces,* 4, **2012b**, 2920–2925.

Espi, R. M.; Chandra, A.; Wegner, G., Crystal perfection in zinc oxide with occluded carboxyl-functionalized latex particles, *Crystal Growth & Design*, 7, **2007**, 1584–1589.

Fang, V.; Kenedy, J.; Futter, J.; Manning, J., A review of near infrared reflectance properties of metal oxide nanostructures, *GNS Science Report,* 39, **2013**, 23.

Fang, X.; Roushan, M.; Zhang, R.; Peng, J.; Zeng, H.; Li, J., Tuning and enhancing white light emission of II–VI based inorganic–organic hybrid semiconductors as single-phased phosphors, *Chemistry of Materials,* 24, **2012**, 1710–1717.

Fangqiang, F.; Zhengbin, X.; Qingying, L.; Zhong, L.; Huanqin, C., ZrO_2/PMMA nanocomposites: Preparation and its dispersion in polymer matrix, *Chinese Journal of Chemical Engineering*, 21, **2013**, 113-120.

Fateh, R.; Dillert, R.; Bahnemann, D., Self-cleaning properties, mechanical stability, and adhesion strength of transparent photocatalytic TiO_2−ZnO coatings on polycarbonate, *ACS Applied Materials & Interfaces,* 6, **2014**, 2270−2278.

Feng, Y.; Zhang, M.; Guo, M.; Wang, X., Studies on the PEG-assisted hydrothermal synthesis and growth mechanism of ZnO microrod and mesoporous microsphere arrays on the substrate, *Crystal Growth & Design,* 10, **2010**, 1500–1507.

Fu, H. P.; Hong, R. Y.; Zhang, Y. J.; Li, H. Z.; Xu, B.; Zheng, Y.; Wei, D. G., Preparation and properties investigation of PMMA/silica composites derived from silicic acid, *Polymers for Advanced Technologies*, 20, **2009**, 84–91.

Fu, Y. -S.; Du, X. -W.; Kulinich, S. A.; Qiu, J. -S.; Qin, W. -J.; Li, R.; Sun, J.; Liu, J., Stable aqueous dispersion of ZnO quantum dots with strong blue emission via simple solution route, *Journal of the American Chemical Society*, 129, **2007**, 16029-16033.

Gao, Y.; Gereige I.; Labban A. E.; Cha D.; Isimjan T. T.; Beaujuge, P. M., Highly transparent and UV-resistant superhydrophobic SiO_2-coated ZnO nanorod arrays, *ACS Applied Materials & Interfaces,* 6, **2014**, 2219−2223.

George, G.; Vishnu, V. S.; Reddy, M. L. P., The synthesis, characterization and optical properties of silicon and praseodymium doped Y_6MoO_{12} compounds: Environmentally benign inorganic pigments with high NIR reflectance, *Dyes and Pigments,* 88, **2011**, 109-115.

Georgekutty, R.; Seery, M. K.; Pillai, S. C., A highly efficient Ag-ZnO photocatalyst: Synthesis, properties, and mechanism, *Journal of Physical Chemistry C,* 112*,* **2008**, 13563–13570.

Gibelli, E. B.; Kai, J.; Teotonio, E. E. S.; Malta, O. L.; Felinto, M. C. F. C.; Brito, H. F., Photoluminescent PMMA polymer films doped with Eu^{3+} diketonate crown ether complex, *Journal of Photochemistry and Photobiology A: Chemistry,* 251, **2013**, 154–159.

Giusti, G.; Consonni, V.; Puyoo, E.; Bellet, D., High performance ZnO-SnO_2:F nanocomposite transparent electrodes for energy applications, *ACS Applied Materials & Interfaces,* 6, **2014**, 14096−14107.

Glenn, D.; Johnson, H.; Dannenberg, R.; Sieck, P. A.; Countrywood, J., Double silver low-emissivity and solar control coatings, US Patent No. 8512883 B2, **2013**.

Gorgolis, G.; Karamanis, D., Solar energy materials for glazing technologies, *Solar Energy Materials & Solar Cells,* 144, **2016**, 559–578.

Granqvist, C. G., Transparent conductors as solar energy materials: A panoramic review, *Solar Energy Materials & Solar Cells,* 91, **2007**, 1529–1598.

Granqvist, C. G., Window coatings for the future, *Thin Solid Films,* 193–194, **1990**, 730-741.

Guo, C.; Yin, S.; Yanb, M.; Sato, T., Facile synthesis of homogeneous Cs_xWO_3 nanorods with excellent low-emissivity and NIR shielding property by a water controlled-release process, *Journal of Materials Chemistry,* 21, **2011**, 5099-5105.

Guo, L.; Yang, S., Synthesis and characterization of poly(vinylpyrrolidone) modified zinc oxide nanoparticles, *Chemistry of Materials*, 12, **2000**, 2268-2274.

Gupta, K. K.; Nishkam, A.; Kasturiya, N., Camouflage in the non-visible region, *Journal of Industrial Textiles,* 31, **2001**, 27.

Hayashida, K.; Takatani, Y., Poly(methyl methacrylate)-grafted ZnO nanocomposites with variable dielectric constants by UV light irradiation, *Journal of Materials Chemistry C,* 4, **2016**, 3640-3645.

He, C.; Sasaki, T.; Shimizu, Y.; Koshizaki, N., Synthesis of ZnO nanoparticles using nanosecond pulsed laser ablation in aqueous media and their self-assembly towards spindle-like ZnO aggregates, *Applied Surface Science*, 254, **2008**, 2196-2202.

Hosseini, S. M.; Sarsari, I. A.; Kameli, P.; Salamati, H., Effect of Ag doping on structural, optical, and photocatalytic properties of ZnO nanoparticles, *Journal of Alloys and Compounds,* 640, **2015**, 408–415.

Hu, Z.; Oskam, G.; Searson, P. C., Influence of solvent on the growth of ZnO nanoparticles, *Journal of Colloid and Interface Science,* 263, **2003**, 454-460.

Huang, H. C.; Hsieh, T. E., Preparation and characterizations of highly transparent UV-curable ZnO-acrylic nanocomposites, *Ceramics International,* 36, **2010**, 1245-1251.

Huang, Q.; Rokowski, J. M.; Zhang, Y., Infrared reflective coating compositions, US Patent No. 0121886 A1, **2012**.

Hung, C. -H.; Whang, W. -T., Effect of surface stabilization of nanoparticles on luminescent characteristics in ZnO/poly(hydroxyethyl methacrylate) nanohybrid films, *Journal of Materials Chemistry,* 15, **2005**, 267–274.

Hwang, D. K.; Moon, J. H.; Shul, Y. G., Scratch resistant and transparent UV-protective coating on polycarbonate, *Journal of Sol-Gel Science and Technology,* 26, **2003**, 783–787.

Hwang, H.; Park, J. -H.; Kim, B. -G., Solar heat blocking coating solution and solar heat blocking coated glass using the same, US Patent No. 0059148A1, **2013**.

Jang, R. Y., Camouflage fabric having near infrared ray reflectance adjusting characteristics, US Patent No. 0154482 A1, **2014**.

Janotti, A.; Walle, C. G. V., Fundamentals of zinc oxide as a semiconductor, *Reports on Progress in Physics,* 72, **2009**, 126501.

Jeevanandam, P.; Mulukutla, R. S.; Phillips, M.; Chaudhuri, S.; Erickson, L. E.; Klabunde, K. J., Near infrared reflectance properties of metal oxide nanoparticles, *Journal of Physical Chemistry C*, 111, **2007**, 1912-1918.

Jiang, C.; Cheng, M.; Liu, H.; Shao, L.; Zeng, X.; Zhang, Y.; Shi, F., Fabricating transparent multilayers with UV and Near-IR double-blocking properties through layer-by-layer assembly, *Industrial & Engineering Chemistry Research,* 52, **2013**, 13393−13400.

Johnson, J. A.; Heidenreich, J. J.; Mantz, R. A.; Baker, P. M.; Donley, M. S., A multiple-scattering model analysis of zinc oxide pigment for spacecraft thermal control coatings, *Progress in Organic Coatings*, 47, **2003**, 432-442.

Jose, S.; Prakash, A.; Laha, S.; Natarajan, S.; Reddy M. L. P., Green colored nano-pigments derived from Y_2BaCuO_5: NIR reflective coatings, *Dyes and Pigments*, 107, **2014**, 118-126.

Jose, S.; Reddy, M. L. P., Lanthanum-strontium copper silicates as intense blue inorganic pigments with high near-infrared reflectance, *Dyes and Pigments,* 98, **2013**, 540-546.

Jose, S; Jayaprakash, A; Laha, S; Natarajan, S; Nishanth, K. G.; Reddy, M. L. P., *Dyes and Pigments*, 124, **2016**, 120-129.

Jung, S. C., Photocatalytic activities and specific surface area of TiO_2 films prepared by CVD and sol-gel method, *Korean Journal of Chemical Engineering.,* 25, **2008**, 364-367.

Kafizas, A.; Parry, S. A.; Chadwick, A. V.; Carmaltd, C. J., Parkin, I. P., An EXAFS study on the photo-assisted growth of silver nanoparticles on titanium dioxide thin-films and the identification of their photochromic states, *Physical Chemistry Chemical Physics,* 15, **2013**, 8254-8263.

Kang, L.; Gao, Y.; Luo, H., A novel solution process for the synthesis of VO_2 thin films with excellent thermochromic properties, *ACS Applied Materials & Interfaces*, 10, **2009**, 2211-2218.

Kang, Y. C.; Park, S. B., Preparation of zinc oxide-dispersed silver particles by spray pyrolysis of colloidal solution, *Materials Letters*, 40, **1999**, 129–133.

Kango, S.; Kalia, S.; Celli, A.; Njuguna, J.; Habibi, Y.; Kumar, R., Surface modification of inorganic nanoparticles for development of organic-inorganic nanocomposites-A review, *Progress in Polymer Science,* 38, **2013**, 1232–1261.

Kanu, S. S.; Binions, R., Thin films for solar control applications, *Proceedings of the Royal Society A,* 466, **2010**, 19–44.

Keefe, O., Thermal infrared reflective pigments for coatings, US Patent No. 7455904 B2, **2008**.

Khanna, P. K.; Singh, N., Light emitting CdS quantum dots in PMMA: Synthesis and optical studies, *Journal of Luminescence*, 127, **2007**, 474–482.

Kiomarsipour, N.; Razavi, R. S.; Ghani, K.; Improvement of spacecraft white thermal control coatings using the new synthesized Zn-MCM-41 pigment, *Dyes and Pigments*, 96, **2013a**, 403-406.

Kiomarsipour, N.; Razavi, R. S.; Ghani, K.; Kioumarsipour, M., Evaluation of shape and size effects on optical properties of ZnO pigment, *Applied Surface Science,* 270, **2013b**, 33–38.

Kiomarsipourn, N.; Razavi, R. S., Hydrothermal synthesis of ZnO nanopigments with high UV absorption and vis/NIR reflectance, *Ceramics International*, 40, **2014**, 11261–11268.

Kitano, M.; Funatsu, K.; Matsuoka, M.; Ueshima, M.; Anpo, M., Preparation of nitrogen-substituted TiO_2 thin film photocatalysts by the radio frequency magnetron sputtering deposition method and their photocatalytic reactivity under visible light irradiation, *Journal of Physical Chemistry B*, 110, **2006**, 25266-25272.

Kittler, W. C.; Argoitia, A.; Coombs, P. G.; Markantes, C. T., Non-toxic flakes for authentication of pharmaceutical articles, US Patent No. 7550197 B2, **2009**.

Kluth, O.; Schope, G.; Hupkes, J.; Agashe, C.; Muller, J.; Rech, B., Modified thornton model for magnetron sputtered zinc oxide: film structure and etching behavior, *Thin Solid Films,* 442, **2003**, 80-85.

Kortum, G., Reflectance spectroscopy: Principles, methods and applications, *Springer-Verlag*: New York, **1969**.

Kos, T.; Anzlovar, A.; Pahovnik, D.; Žagar, E.; Orel, Z. C.; Zigon, M., Zinc-containing block copolymer as a precursor for the in situ formation of nano ZnO and PMMA/ZnO nanocomposites, *Macromolecules,* 46, **2013**, 6942−6948.

Kotecha, M.; Veeman, W.; Rohe, B.; Tausch, M., NMR investigations of silane-coated nano-sized ZnO particles, *Microporous and Mesoporous Materials*, 95, **2006**, 66–75.

Krishna, R. R.; Ranjit, T. K.; Adhar, C. M., Size-dependent bacterial growth inhibition and mechanism of antibacterial activity of zinc oxide nanoparticles, *Langmuir,* 27, **2011**, 4020-4028.

Kulyk, S.; Kapustianyk, V.; Tsybulskyy, V.; Krupka, O.; Sahraoui, B., Optical properties of ZnO/PMMA nanocomposite films, *Journal of Alloys and Compounds*, 502, **2010**, 24-27.

Kumar, R.; Anandan, S.; Hembram, K.; Rao, T. N., Efficient ZnO-based visible-light-driven photocatalyst for antibacterial applications, *ACS Applied Materials & Interfaces,* 6, **2014**, 13138−13148.

Kumar, S.; Verma, N. K.; Singla, M. L., Study on reflectivity and photostability of Al-doped TiO_2 nanoparticles and their reflectors, *Journal of Materials Research,* 3, **2013**, 521-528.

Kuriakose, S.; Choudhary, V; Satpatib, B.; Mohapatra, S., Facile synthesis of Ag-ZnO hybrid nanospindles for highly efficient photocatalytic degradation of methyl orange, *Physical Chemistry Chemical Physics,* 16, **2014**, 17560-17568.

Lakshmeesha, T. R.; Sateesh, M. K.; Prasad, B. D.; Sharma, S. C.; Kavyashree, D.; Chandrasekhar, M.; Nagabhushana, H., Reactivity of crystalline ZnO superstructures against fungi and bacterial pathogens: Synthesized using nerium oleander leaf extract, *Crystal Growth & Design*, 14, **2014**, 4068−4079.

Levinson, R.; Akbari, H.; Berdahl, P.; Wood, K.; Skilton, W., Petersheim, J., A novel technique for the production of cool colored concrete tile and asphalt shingle roofing products, *Solar Energy Materials & Solar Cells*, 94, **2010**, 946-54.

Levinson, R.; Berdahl, P.; Akbari, H., Solar spectral optical properties of pigments-part I: model for deriving scattering and absorption coefficients from transmittance and reflectance measurements, *Solar Energy Materials & Solar Cells*, 89, **2005a**, 319–349.

Levinson, R.; Berdahl, P.; Akbari, H., Solar spectral optical properties of pigments-Part II: survey of common colorants, *Solar Energy Materials & Solar Cells,* 89, **2005b**, 351–389.

Levinson, R.; Berdahl, P.; Akbari, H.; Miller, W.; Joedicke, I.; Reilly, J.; Suzuki, Y.; Vondran, M., Methods of creating solar-reflective non white surfaces and their application to residential roofing materials*, Solar Energy Materials & Solar Cells*, 91, **2007**, 304−314.

Li, S.; Lin, M. M.; Toprak, M. S.; Kim, D. K.; Muhammed, M., Nanocomposites of polymer and inorganic nanoparticles for optical and magnetic applications, *Nano Reviews,* 1, **2010**, 5214.

Li, S.; Toprak, M. S.; Jo, Y. S.; Dobson, J.; Kim, D. K.; Muhammed, M., Bulk synthesis of transparent and homogeneous polymeric hybrid materials with ZnO quantum dots and PMMA, *Advanced Materials*, 19, **2007**, 4347–4352.

Li, Y. -Q.; Mei, S. -G.; Byon, Y. -J.; Wang, J. -L.; Zhang G. -L., Highly solar radiation reflective Cr_2O_3−$3TiO_2$ orange nanopigment prepared by a polymer pyrolysis method*, ACS Sustainable Chemistry & Engineering,* 2, **2014**, 318−321.

Li, Y.; Liu, J.; Liang, J.; Yu, X.; Li, D., Tunable solar-heat shielding property of transparent films based on mesoporous Sb-doped SnO_2 microspheres*, ACS Applied Materials & Interfaces,* 7, **2015**, 6574−6583.

Libbra, A.; Tarozzi, L.; Muscio, A.; Corticelli, M. A., Spectral response data for development of cool coloured tile coverings, *Optics & Laser Technology*, 43, **2011**, 394–400.

Lide, D. R. (Ed.), CRC Handbook of Chemistry and Physics, 73rd Edition, *CRC Press*, New York, **1992**.

Liu, H. T.; Zeng, X. F.; Zhao, H.; Chen, J. F., Highly transparent and multifunctional polymer nanohybrid film with superhigh ZnO content synthesized by a bulk polymerization method, *Industrial & Engineering Chemistry Research*, 51, **2012a**, 6753–675.

Liu, J.; Lu, Y.; Liu, J.; Yang, X.; Yu, X., Investigation of near infrared reflectance by tuning the shape of SnO_2 nanoparticles, *Journal of Alloys and Compound*, 496, **2010**, 261–264.

Liu, J.; Yang, X.; Wang, K.; He, X.; Wang, Q.; Huang, J.; Liu, Y., Aggregation control of quantum dots through ion-mediated hydrogen bonding shielding, *ACS Nano,* 6, **2012b**, 4973–4983.

Liu, X.; Ge, L.; Li, W.; Wang, X.; Li, F., Layered double hydroxide functionalized textile for effective oil/water separation and selective oil adsorption*, ACS Applied Materials & Interfaces*, 7, **2015**, 791−800.

Lupan, O.; Chow, L.; Ono, L. K.; Cuenya, B. R.; Chai, G.; Khallaf, H.; Park, S.; Schulte, A., Synthesis and characterization of Ag- or Sb-doped ZnO nanorods by a facile hydrothermal route, *Journal of Physical Chemistry C,* 114 ,**2010**, 12401–12408.

Mahlitig, B.; Bottcher, H.; Rauch, K.; Dieckmann, U.; Nitsche, R.; Fritz, T., Optimized UV protecting coatings by combination of organic and inorganic UV absorbers, *Thin Solid Films*, 485, **2005**, 108-114.

Mahmood, K.; Park, S. B.; Sung, H. J., Enhanced photoluminescence, raman spectra and field-emission behavior of indium-doped ZnO nanostructures, *Journal of Material Chemistry C*, 1, **2013**, 3138-3149.

Manna, J.; Goswami, S.; Shilpa, N.; Sahu, N.; Rana, R. K., Biomimetic method to assemble nanostructured Ag@ZnO on cotton fabrics: application as self-cleaning flexible materials with visible-light photocatalysis and antibacterial activities*, ACS Applied Materials & Interfaces*, 7, **2015**, 8076−8082.

Marsalek, R., Particle size and zeta potential of ZnO*, APCBEE Procedia,* 9, **2014**, 13-17.

Mastai, Y; Diamant, Y.; Aruna, S. T.; Zaban, A., TiO_2 nanocrystalline pigmented polyethylene foils for radiative cooling applications: synthesis and characterization, *Langmuir,* 17, **2001**, 7118–7123.

Matsuyama, K.; Mishima, K.; Kato, T.; Irie, K.; Mishima, K., Transparent polymeric hybrid film of ZnO nanoparticle quantum dots and PMMA with high luminescence and tunable emission color, *Journal of Colloid and Interface Science*, 367, **2012**, 171–177.

Mauro, A. D.; Cantarella, M.; Nicotra, G.; Pellegrino, G.; Gulino, A.; Brundo, M. V.; Privitera V.; Impellizzeri, G., Novel synthesis of ZnO/PMMA nanocomposites for photocatalytic applications, *Scientific Reports*, 7, **2017**, 40895.

Mehrizi, M. K.; Mortazavi, S. M.; Mallakpour, S.; Bidoki, S. M., The effect of nano and micro-TiO_2 particles on reflective behavior of printed cotton/nylon fabrics in vis/NIR Regions, *Color Research & Application*, 37, **2012**, 199–205.

Meng, X.; Zhang, Z.; Luo, N.; Cao, S.; Yang, M., Transparent poly(methyl methacrylate)/TiO_2 nanocomposites for UV-shielding applications, *Polymer Science Series A*, 53, **2011**, 977–983.

Mennig, M.; Fries, K.; Lindenstruth, M.; Schmidt, H., Development of fast switching photochromic coatings on transparent plastics and glass, *Thin Solid Films,* 351, **1999**, 230-234.

Meulenkamp, E. A., Synthesis and growth of ZnO nanoparticles, *Journal of Physical Chemistry B*, 102, **1998**, 5566-5572.

Miao, D.; Li, A.; Jiang, S.; Shang, S., Fabrication of Ag and AZO/Ag/AZO ceramic films on cotton fabrics for solar control*, Ceramics International,* 41*,* **2015**, 6312–6317.

Minhao, W.; Katsumi, Y.; Ryotaro, T., Transparent polymer nanocomposites containing nanoparticles and method of making same, US Patent No. 233090 A1, **2009**.

Minkin, V. I., Photo-, thermo-, solvato-, and electrochromic spiroheterocyclic compounds, *Chemical Reviews,* 104, **2004**, 2751–2776.

Moezzi, A.; McDonagh, A. M.; Cortie, M. B., Zinc oxide particles: Synthesis, properties and applications, *Chemical Engineering Journal*, 185, **2012**, 1-22.

Mohelnikova, J., Infrared reflective coatings for window glazing, *Solid State Phenomena*, 144, **2009**, 226-231.

Mu, S.; Wu, D.; Qi, S.; Wu, Z., Preparation of polyimide/zinc oxide nanocomposite films via an ion-exchange technique and their photoluminescence properties, *Journal of Nanomaterials*, 2011, **2011**, 10.

Naoi, K.; Ohko, Y.; Tatsuma, T., TiO_2 films loaded with silver nanoparticles: Control of multicolor photochromic behavior, *Journal of the American Chemical Society,* 126, **2004**, 3664–3668.

Navale, G. R.; Thripuranthaka, M.; Late, D. J.; Shinde, S. S., Antimicrobial activity of ZnO nanoparticles against pathogenic bacteria and fungi, *JSM Nanotechnology & Nanomedicine*, 3, **2015**, 1033.

Nussbaumer, R. J.; Caseri, W. R.; Smith, P.; Tervoort, T., Polymer-TiO_2 nanocomposites: A route towards visually transparent broadband UV filters and high refractive index materials, *Macromolecular Materials and Eng*ineering, 288, **2003**, 44–49.

Ogata, T.; Yagi, R.; Nakamura, N.; Kuwahara, Y.; Kurihara, S. Modulation of polymer refractive indices with diamond, nanoparticles for metal-free multilayer film mirrors, *ACS Applied Materials & Interfaces*, 4, **2012**, 3769−3772.

Ohko, Y.; Tatsuma, T.; Fujii, T.; Naoi, K.; Niwa, C.; Kubota, Y.; Fujishima, A., Multicolour photochromism of TiO_2 films loaded with silver nanoparticles, *Nature Materials,* 2, **2003**, 29-31.

Omer, A. M. Energy, environment and sustainable development, *Renewable & Sustainable Energy Reviews,* 12, **2008**, 2265-2300.

Özgür, Ü.; Alivov, Ya. I.; Liu, C.; Teke, A.; Reshchikov, M. A.; Doğan, S.; Avrutin, V.; Cho, S.-J.; Morkoç, H. A comprehensive review of ZnO materials and devices, *Journal of Applied Physics*, 98*,* **2005**, 041301.

Pandey, A.; Prasad, A.; Moscatello, J. P.; Yap, Y. K., Stable electron field emission from PMMA−CNT matrices, *ACS Nano,* 4, **2010**, 6760–6766.

Panigrahy, B.; Aslam, M.; Mirsa, D. S.; Bahadur, D., Polymer-mediated shape-selective synthesis of ZnO nanostructures using a single-step aqueous approach, *Crystal Engineering Communications*, 11, **2009**, 1920-1925.

Pardo, R.; Zayat M.; Levy, D., Photochromic organic–inorganic hybrid materials, *Chemical Society Reviews,* 40, **2011**, 672–687.

Park, D.; Choi, J.; Park, T.; Jung, S.; Yeo, J. W.; Seo, J., External light-shielding layer, filter for display device including the external light-shielding layer and display device including the filter, US Patent No. 7755263 B2, **2010**.

Parlak, O.; Demir, M. M., Toward transparent nanocomposites based on polystyrene matrix and PMMA-grafted CeO_2 nanoparticles, *ACS Applied Materials & Interfaces,* 3, **2011**, 4306–4314.

Perelshtein, I.; Applerot, G.; Perkas, N.; Sigl, E. W.; Hasmann, A.; Guebitz G. M.; Gedanken, A., Antibacterial properties of an in situ generated and simultaneously deposited nanocrystalline ZnO on fabrics, *ACS Applied Materials & Interfaces*, 2, **2009**, 361–366.

Petkova, P.; Francesko, A.; Fernandes, M. M.; Mendoza, E.; Perelshtein, I.; Gedanken A.; Tzanov, T., Sonochemical coating of textiles with hybrid ZnO/chitosan antimicrobial nanoparticles*, ACS Applied Materials & Interfaces*, 6, **2014**, 1164−1172.

Pueyo, C. L.; Berg, M. W. E.; Toni, A. D.; Goes, T.; Polarz, S., Nucleation and growth of ZnO in organic solvents - an in situ study, *Journal of American Chemical Society*, 130, **2008**, 16601-16610.

Qiu, J.; Guo, M.; Wang, X., Electrodeposition of hierarchical ZnO nanorod-nanosheet structures and their applications in dye-sensitized solar cells, *ACS Applied Materials & Interfaces,* 3, **2011**, 2358–2367.

Radzimska, A. K.; Jesionowski, T., Zinc oxide-from synthesis to application: A review, *Materials,* 7, **2014**, 2833-2881.

Raghupathi, R. K.; Koodali, T. R.; Manna, C. A., Size-dependent bacterial growth inhibition and mechanism of antibacterial activity of zinc oxide nanoparticles, *Langmuir*, 27, **2011**, 4020–4028.

Raj, A. K. V., Rao, P. P, Sameera, S.; Divya, S., Pigments based on terbium-doped yttrium cerate with high NIR reflectance for cool roof and surface coating applications, *Dyes and Pigments*, 122, **2015**, 116-125.

Ranade, A., Synthesis and characterization of transparent oxide coatings with enhanced near infrared reflectance, Doctor of Philosophy, *Northwestern University*, **2011**.

Raula, M.; Rashid, M. H.; Paira, T. K.; Dinda, E.; Mandal, T. K., Ascorbate-assisted growth of hierarchical ZnO nanostructures: sphere, spindle, and flower and their catalytic properties, *Langmuir*, 26, **2010**, 8769–8782.

Rezaei, S. D.; Shannigrahi, S.; Ramakrishna, S., A review of conventional, advanced, and smart glazing technologies and materials for improving indoor environment, *Solar Energy Materials & Solar Cells*, 159, **2017**, 26–51.

Rong, M. Z.; Zhang, M. Q.; Zheng, Y. X.; Zeng, H. M.; Friedrich, K., Improvement of tensile properties of nano-SiO_2/PP composites in relation to percolation mechanism, *Polymer*, 42, **2001**, 3301-3304.

Sameera, S.; Rao, P. P; Divya, S.; Raj, A. K. V., Brilliant IR reflecting yellow colorants in rare earth double molybdate substituted $BiVO_4$ solid solutions for energy saving applications, *ACS Sustainable Chemistry & Engineering*, 3, **2015**, 1227−1233.

Sangeetha, S.; Basha, R.; Sreeram, K. J., Sangilimuthu, S. N., Balachandran U. N., Functional pigments from chromium(III) oxide nanoparticles, *Dyes and Pigments*, 94, **2012**, 548-552.

Sangermano, M.; Messori, M., Scratch resistance enhancement of polymer coatings, *Macromolecular Materials & Engineering*, 295, **2010**, 603–612.

Senger R. T.; Bajaj, K. K., Optical properties of confined polaronic excitons in spherical ionic quantum dots, *Physical Reviews B,* 68, **2003**, 045313.

Serpone, N.; Lawless, D.; Khairutdinov, R., Size effects on the photophysical properties of colloidal anatase TiO_2 particles: size quantization versus direct transitions in this indirect semiconductor, *Journal of Physical Chemistry*, 99, **1995**, 16646-16654.

Serrano, J.; Manjón, F. J.; Romero, A. H.; Ivanov, A.; Lauck, R.; Cardona, M.; Krisch, M., The phonon dispersion of wurtzite-ZnO revisited, *Physica Status Solidi,* 244, **2007**, 1478–1482.

Shah, A. H.; Manikandan, E.; Ahmed, B. M.; Ganesan, V., Enhanced bioactivity of Ag/ZnO Nanorods-A comparative antibacterial study, *Journal of Nanomedicine & Nanotechnology*, 4, **2013**, 168.

Shahroosvand, H.; Ghorbani-asl, M. Solution-based synthetic strategies for Eu doped ZnO nanoparticle with enhanced red photoluminescence, *Journal of Luminescence*, 144, **2013**, 223-229.

Shan, F. K.; Yu, Y. S. Band gap energy of pure and Al-doped ZnO thin films, *Journal of the European Ceramic Society*, 24, **2004**, 1869-1872.

Shi, H. -Q.; Li, W. -N.; Sun, L. -W.; Liu, Y.; Xiao H. -M.; Fu, S. -Y., Synthesis of silane surface modified ZnO quantum dots with ultrastable, strong and tunable luminescence, *Chemical Communications*, 47, **2011**, 11921–11923.

Shi, J.; Karlsson, H. L.; Johansson, K.; Gogvadze, V.; Xiao, L.; Li, J.; Burks, T.; Bennett, A. G.; Uheida, A.; Muhammed, M.; Mathur, S.; Morgenstern, R.; Kagan, V. E.; Fadeel, B., Microsomal glutathione transferase 1 protects against toxicity induced by silica nanoparticles but not by zinc oxide nanoparticles*, ACS Nano,* 6, **2012**, 1925–1938.

Shi, X.; Pan, L.; Chen, S.; Xiao, Y.; Liu, Q.; Yuan, L.; Sun, J.; Cai, L., Zn(II)-PEG 300 globules as soft template for the synthesis of hexagonal ZnO micronuts by the hydrothermal reaction method, *Langmuir*, 25, **2009**, 5940–5948.

Shiao, M. L.; Hong, K. C.; Kalkanoglu H. M.; Jacobs, G. F., Solar heat reflective roofing granules, solar heat reflective shingles, and process for producing same, US Patent No. 8361597 B2, **2013**.

Shiao, M. L.; Kalkanoglu, H. M.; Hong, K. C., Colored roofing granules with increased solar heat-reflective shingles, and process for producing same, US Patent No. 0072114A1, **2005**.

Shim, J. W.; Kim, J. W.; Han, S. H.; Chang, I. S.; Kim, H. K.; Kang, H. H.; Lee, O. S.; Suh, K. D., Zinc oxide/polymethylmethacrylate polymerization and their morphological study. *Colloids and Surfaces A: Physicochemical and Engineering Aspects,* 207, **2002**, 105–111.

Sirelkhatim, A.; Mahmud, S.; Seeni, A.; Kaus, N. H. M.; Ann, L. C.; Bakhori, S. K. M.; Hasan, H.; Mohamad, D., Review on zinc oxide nanoparticles: Antibacterial activity and toxicity mechanism, *Nano-Micro Letters*, 7, **2015**, 219–242.

Smith, G. B., Materials and systems for efficient lighting and delivery of daylight, *Solar Energy Materials & Solar Cells*, 84, **2004**, 395–409.

Smith, G. B.; Deller, C. A.; Swift, P. D.; Gentle, A.; Garrett P. D.; Fisher, W. K., Nanoparticle-doped polymer foils for use in solar control glazing, *Journal of Nanoparticle Research,* 4, **2002**, 157–165.

Smith, G. B.; Gentle, A.; Swift, P.; Earp, A.; Mronga, N., Coloured paints based on coated flakes of metal as the pigment, for enhanced solar reflectance and cooler interiors: description and theory, *Solar Energy Materials & Solar Cells,* 79, **2003**, 163-177.

Soumya, S.; Kumar, S. N.; Mohamed A. P.; Ananthakumar, S., Silanated nano ZnO hybrid embedded PMMA polymer coatings on cotton fabrics for near-IR reflective, antifungal cool-textiles, *New Journal of Chemistry,* 40, **2016**, 7210–7221.

Soumya, S.; Mohamed, A. P.; Mohan K.; Ananthakumar, S., Enhanced near-infrared reflectance and functional characteristics of Al-doped ZnO nano-pigments embedded PMMA coatings, *Solar Energy Materials & Solar Cells,* 143, **2015**, 335–346.

Soumya, S.; Mohamed, A. P.; Paul, L.; Mohan, K.; Ananthakumar, S., Near IR reflectance characteristics of PMMA/ZnO nanocomposites for solar thermal control interface films*, Solar Energy Materials & Solar Cells*, 125, **2014**, 102–112.

Sourabh, D.; Rizwan, W; Farheen, K.; Yogendra, K. M.; Javed M.; Abdulaziz, A. A., Reactive oxygen species mediated bacterial biofilm inhibition via zinc oxide nanoparticles and their statistical determination, *PLoS One,* 9, **2014**, 111289.

Spanhel, L.; Anderson, M. A., Semiconductor clusters in the sol-gel process: quantized aggregation, gelation, and crystal growth in concentrated zinc oxide colloids, *Journal of the American Chemical Society,* 113, **1991**, 2826-2833.

Sriramulu, D.; Reed, E. L.; Annamalai, M.; Venkatesan, T. V.; Valiyaveettil, S., Synthesis and characterization of superhydrophobic, self-cleaning NIR-reflective silica nanoparticles, *Scientific Reports,* 6, **2016**, 35993.

Stefan, S., Smith, G. B., Dilute LaB_6 nanoparticles in polymer as optimized clear solar control glazing, *Applied Physics Letters*, 82, **2003**, 4346–4348.

Stieberova, B.; Zilka, M.; Ticha, M.; Freiberg, F.; González, P. C.; McKechnie, J.; Lester, E., Application of ZnO nanoparticles in a self-cleaning coating on a metal panel: An assessment of environmental benefits, *ACS Sustainable Chemistry & Engineering*, 5, **2017**, 2493–2500.

Subramanian, M.; Vijayalakshmi, S.; Venkataraj S.; Jayavel, R., Effect of cobalt doping on the structural and optical properties of TiO_2 films prepared by sol–gel process, *Thin Solid Films,* 516, **2008**, 3776-3782.

Sun, D.; Miyatake, N.; Sue, H. J., Transparent PMMA/ZnO nanocomposite films based on colloidal ZnO quantum dots, *Nanotechnology*, 18, **2007**, 215606.

Sun, L. W.; Shi, H. Q.; Li, W. N.; Xiao, H. M.; Fu, S. Y.; Cao, X. Z.; Li, Z. X., Lanthanum-doped ZnO quantum dots with greatly enhanced fluorescent quantum yield, *Journal of Materials Chemistry,* 22, **2012**, 8221-8227.

Sun, X. M.; Chen, X.; Deng, Z. X.; Li, Y. D., A CTAB-assisted hydrothermal orientation growth of ZnO nanorods, *Material Chemistry and Physics*, 78, **2002**, 99-104.

Sun, Z.; Zhao, B.; Lombardi, J. R., ZnO nanoparticle size-dependent excitation of surface Raman signal from adsorbed molecules: Observation of a charge-transfer resonance, *Applied Physics Letters,* 91, **2007**, 221106.

Takahashi, K.; Yoshikawa, A.; Sandhu, A., Wide bandgap semiconductors: Fundamental properties and modern photonic and electronic devices, *Springer*, **2007**.

Textor, T.; Schroter, F.; Schollmeyer, E., Thin coatings with photo-catalytic activity based on inorganic-organic hybrid polymers modified with anatase nanoparticles, *Macromolecular Symposia*, 254, **2007**, 196–202.

Thara, T. R. A.; Rao, P. P.; Divya, S.; Raj A. K. V.; Sreena, T. S., Enhanced near infrared reflectance with brilliant yellow hues in scheelite type solid solutions, $(LiLaZn)_{1/3}MoO_4{-}BiVO_4$ for energy saving products, *ACS Sustainable Chemistry & Engineering*, 5, **2017**, 5118–5126.

Tong, Y.; Fu, J.; Chen, Z., Synthesis, characterization, and NIR reflectance of highly dispersed $NiTiO_3$ and $NiTiO_3/TiO_2$ composite pigments, *Journal of Nanomaterials,* 2016, **2016**, 1-6.

Tu, Y.; Zhou, L.; Jin, Y. Z.; Gao, C.; Ye, Z. Z.; Yang, Y. F.; Wang, Q. L., Transparent and flexible thin films of ZnO-polystyrene nanocomposite for UV-shielding applications, *Journal of Materials Chemistry*, 20, **2010**, 1594–1599.

Verma, A.; Khan, F.; Kumar, D.; Kar, M.; Chakravarty, B. C.; Singh, S. N.; Husain, M., Sol–gel derived aluminum doped zinc oxide for application as anti-reflection coating in terrestrial silicon solar cells, *Thin Solid Films*, 518, **2010**, 2649-2653.

Verscharen, P. C. M.; Daponte, T. L. F.; Kieser, M.; Edler, G., Composite material for energy screen, PCT International Application 9626070, **1996**.

Viasnoff, E., Thin films including nanoparticles with solar reflectance properties for building materials, US Patent No. 8623499 B2, **2014**.

Viasnoff, E.; Shiao, L., Thin films with high near-infrared reflectivity deposited on building materials, US Patent No. 8277943 B2, **2012**.

Vishnu, V. S.; Reddy, M. L. P., Near-infrared reflecting inorganic pigments based on molybdenum and praseodymium doped yttrium cerate: synthesis, characterization and optical properties, *Solar Energy Materials & Solar Cells,* 95, **2011**, 2685-2692.

Viswanatha, R.; Sarma, D. D., Study of the growth of capped ZnO nanocrystals: A route to rational synthesis, *Chemistry-A European Journal*, 12, **2006**, 180-186.

Wang, R. H.; Wang, X. W.; Xin, J. H., Advanced visible-light-driven self-cleaning cotton by $Au/TiO_2/SiO_2$ photocatalysts, *ACS Applied Materials & Interfaces,* 1, **2010a**, 82–85.

Wang, R. H.; Xin J. H.; Tao, X. M., UV-blocking property of dumbbell-shaped ZnO crystallites on cotton fabrics, *Inorganic Chemistry,* 44, **2005**, 3926−3930.

Wang, W.; Liu, J.; Yu, X.; Yang, G., Transparent poly(methyl methacrylate)/ZnO nanocomposites based on KH570 surface modified ZnO quantum dots., *Journal of Nanoscience and Nanotechnololgy,* 10, **2010b**, 5196-201.

Wang, X.; Zhou S.; Wu, L., Facile encapsulation of SiO_2 on ZnO quantum dots and its application in waterborne UV-shielding polymer coatings*, Journal of Materials Chemistry C,* 1, **2013a**, 7547-7553.

Wang, Y.; Xue, J.; Wang, Q.; Chen, Q.; Ding, J., Verification of icephobic/anti-icing properties of a superhydrophobic surface, *ACS Applied Materials & Interfaces,* 5, **2013b**, 3370−3381.

Wang, Z. L., Zinc oxide nanostructures: Growth, properties and applications, *Journal of Physics: Condensed Matter,* 16, **2004**, 829–858.

Wen, M.; Wang, L.; Zhang, M.; Jiang, L.; Zheng, Y., Antifogging and icing-delay properties of composite micro- and nanostructured surfaces, *ACS Applied Materials & Interfaces*, 6, **2014**, 3963−3968.

Wendel, R. -D., Camouflage pattern with extended infrared reflectance separation, US Patent No. 8932965 B1, **2015**.

Wong, A.; Daoud, A. -W.; Liang, H.; Szeto, Y. S., Application of rutile and anatase onto cotton fabric and their effect on the NIR reflection/surface temperature of the fabric*, Solar Energy Materials & Solar Cells,* 134, **2015**, 425–437.

Wu, J. M.; Chen, Y. R., Ultraviolet-light-assisted formation of ZnO nanowires in ambient air: comparison of photoresponsive and photocatalytic activities in zinc hydroxide, *Journal of Physical Chemistry C*, 115, **2011**, 2235–2243.

Wu, J. M.; Chen, Y. R.; Kao, W. T., Ultrafine ZnO nanoparticles/nanowires synthesized on a flexible and transparent substrate: formation, water molecules, and surface defect effects, *ACS Applied Materials & Interfaces*, 6, **2014**, 487−494.

Wu, L.; Baghdachi, J., Functional polymer coatings: Principles, methods and applications, *John Wiley & Sons*, New Jersey, **2015**.

Wu, L.; Zhang, J.; Lia B.; Wanga, A., Mimic nature, beyond nature: Facile synthesis of durable superhydrophobic textiles using organosilanes, *Journal of Materials Chemistry B*, 1, **2013**, 4756–4763.

Wu, X.; Lee, J.; Varshney, V.; Wohlwend, J. L.; Roy A. K.; Luo, T. X., Thermal conductivity of wurtzite zinc-oxide from first-principles lattice dynamics - a comparative study with gallium nitride, *Scientific Reports*, 6, **2016**, 22504.

Wu, Y. L.; Tok, A. I. Y.; Boey, F. Y. C.; Zeng, X. T.; Zhang, X. H., Surface modification of ZnO nanocrystals, *Applied Surface Science,* 253, **2007**, 5473–5479.

Xie, Y.; Hill, C. A. S.; Xiao, Z.; Militz, H.; Mai, C., Silane coupling agents used for natural fiber/polymer composites: A review, *Composites: Part A,* 41*,* **2010**, 806–819.

Xing, Z.; Tay, S. -W.; Liu, Y.; Hong, L., Solar heat reflective coating consisting of hierarchically assembled polystyrene nanoparticles, *Surface & Coatings Technology,* 265, **2015**, 99–105.

Xiong, D.; Liu, G. Diblock-copolymer-coated water- and oil-repellent cotton fabrics, *Langmuir*, 28, **2012**, 6911−6918.

Xiong, H. M., Photoluminescent ZnO nanoparticles modified by polymers, *Journal of Materials Chemistry*, 20, **2010**, 4251–4262.

Xiong, H. M.; Shchukin, D. G.; Mohwald, H.; Xu, Y.; Xia, Y.Y., Sonochemical synthesis of highly luminescent zinc oxide nanoparticles doped with magnesium(II), *Angewandte Chemie*, 121, **2009**, 2765 –2769.

Xu, S.; Wang, Z. L., One-dimensional ZnO nanostructures: Solution growth and functional properties, *Nano Research*, 4, **2011**, 1013–1098.

Yang, C.; Wang, F.; Li, W.; Ou, J.; Li, C.; Amirfazli, A., Anti-icing properties of superhydrophobic ZnO/PDMS composite coating, *Applied Physics A,* 1, **2016**, 122.

Yang, Y.; Ren, L.; Zhang, C.; Huang, S.; Liu, T., Facile fabrication of functionalized graphene sheets (FGS)/ZnO nanocomposites with photocatalytic property, *ACS Applied Materials & Interfaces,* 3, **2011**, 2779-2785.

Yoffe, A., Semiconductor quantum dots and related systems: Electronic, optical, luminescence and related properties of low dimensional systems, *Advances in Physics*, 50, **2001**, 1-208.

Yong, S. L.; Jiao, P. Y.; Xiao, J. D.; Yang, Y.; Shao, Y. F., Preparation and optical properties of novel transparent Al-doped-ZnO/epoxy nanocomposites, *Journal of Physical Chemistry C*, 113, **2009**, 9406–9411.

Yoon, B.; Lee, J.; Park, I. S.; Jeon, S.; Lee, J.; Kim, J. M., Recent functional material based approaches to prevent and detect counterfeiting, *Journal of Materials Chemistry C*, 1, **2013**, 2388-2403.

Yu, M.; Wang, Z.; Liu, H.; Xie, S.; Wu, J.; Jiang, H.; Zhang, J.; Li, L.; Li, J., Laundering durability of photocatalyzed self-cleaning cotton fabric with TiO_2 nanoparticles covalently immobilized, *ACS Applied Materials & Interfaces,* 5, **2013**, 3697−3703.

Yuan, Q. L.; Yong, K.; Hong, M. X.; Shi, G. M.; Guang, L. Z.; Shao, Y. F., Preparation and characterization of transparent Al doped ZnO/epoxy composite as thermal-insulating coating, *Composites Part B: Engineering*, 42, **2011**, 2176-2180.

Zhang, H.; Yang, D.; Ji, Y.; Ma, X.; Xu, J.; Que, D., Low temperature synthesis of flowerlike ZnO nanostructures by cetyltrimethylammonium bromide-assisted hydrothermal process, *Journal of Physical Chemistry B,* 108, **2004**, 3955-3958.

Zhang, L.; Yin, L.; Wang, C.; Lun, N.; Qi, Y., Sol-gel growth of hexagonal faceted ZnO prism quantum dots with polar surfaces for enhanced photocatalytic activity, *ACS Applied Materials & Interfaces*, 2, **2010a**, 1769–1773.

Zhang, L.; Yin, L.; Wang, C.; Lun, N.; Qi, Y.; Xiang, D., Origin of visible photoluminescence of ZnO quantum dots: Defect-dependent and size-dependent, *Journal of Physical Chemistry C,* 114*,* **2010b**, 9651–9658.

Zhang, Y.; Wang, X.; Liu, Y.; Song, S.; Liu, D., Highly transparent bulk PMMA/ZnO nanocomposites with bright visible luminescence and efficient UV-shielding capability, *Journal of Materials Chemistry*, 22, **2012**, 11971–11977.

Zhang, Y.; Zhuang, S.; Xu, X.; Hu, J., Transparent and UV-shielding ZnO@PMMA nanocomposite films, *Optical Materials*, 36, **2013**, 169–172.

Zhao, X. K.; Fendler, J. H., Size quantization in semiconductor particulate films, *Journal of Physical Chemistry*, 95, **1991**, 3716-3723.

Zhao, Y.; Kong, X. R.; Zeng, X. F.; Pu, Y.; Fu, J. W.; Tao, X.; Chen, J. F., Preparation of ITO nanoparticles and their composite films with infrared property, *Journal of Beijing University of Chemical Technology,* 36, **2009**, 4.

Zhou, H.; Wang, H.; Zheng, K.; Gu, Z.; Wu, Z.; Tian, X., Aluminum-doped zinc oxide nanoparticles with tunable near-infrared absorption/reflectance by a simple solvothermal process, *RSC Advances*, 4, **2014**, 42758-42763.

Zou, J.; Zhang, P.; Liu, C.; Peng, Y., Highly dispersed (Cr, Sb)-co-doped rutile pigments of cool color with high near-infrared reflectance, *Dyes and Pigments*, 109, **2014,** 113-119.

LIST OF PUBLICATIONS

List of Publications in SCI Journal

1. **S. Soumya**, A. Peer Mohamed, Lucy Paul, Kiran Mohan, S. Ananthakumar, *Near IR Reflectance characteristics of PMMA/ZnO nanocomposites for solar thermal control interface films*, Solar Energy Materials and Solar Cells, 125, **2014**, 102-112.

2. **S. Soumya**, A. Peer Mohamed, Kiran Mohan, S. Ananthakumar, *Enhanced near-infrared reflectance and functional characteristics of Al-doped ZnO nano-pigments embedded PMMA coatings*, Solar Energy Materials and Solar Cells, 143, **2015**, 335-346.

3. **S. Soumya**, S. Nishanth Kumar, A. Peer Mohamed, S. Ananthakumar, *Silanated nano ZnO hybrid embedded PMMA polymer coatings on cotton fabrics for near-IR reflective, antifungal cool-textiles,* New Journal of Chemistry, 40, **2016**, 7210.

4. **S. Soumya**, V. N. Sheemol, A. Peer Mohamed and S. Ananthakumar, *Sn and Ag doped ZnO quantum dots with PMMA by in situ polymerization for UV/NIR protective, photochromic multifunctional hybrid coatings,* (Communicated, **2017**).

List of International/National Conference Proceedings

1. **S. Soumya,** S. S. Sujith, A. Peer mohamed and S. Ananthakumar, *ZnO:$LaPO_4$(1:1) Colloidal Coatings for NIR Reflective, Anti-freezing Glass Surfaces*. International Conference on Science, Technology and Applications of Rare Earths 'ICSTAR 2015' held at Thiruvananthapuram during April 23rd-25th 2015 (**Poster presentation**).

2. **S. Soumya** and S. Ananthakumar, *Nano ZnO/PMMA Hybrid Engineered Black and White Cotton Fabrics for Near –IR Reflective Textiles Interfaces.* Nano Mission's National Level meet, [NANO-INDIA-2015], Jan 29-30th, 2015, SASTRA University, Thanjavur, Tamil Nadu (**Poster presentation**).

3. **S. Soumya**, A. Peer mohamed, Kiran Mohan and S. Ananthakumar, *Near IR reflectance and Solar Heat Shielding Capacity of PMMA polymer Coatings Composed of Al-doped ZnO Nanopigment dispersoids for Cool-Windows Application*. A National Seminar of Young Scientist of Hydrogen Energy and Other Renewable Energy Sources 'HEAM Scientist 2014' (Best Paper Presentation Award), on 17-18th Nov 2014, University Campus, Kariavattom, Trivandrum (**Best Poster presentation**).

4. **S. Soumya**, Lucy Paul, Kiran Mohan, A. Peer Mohamed and Ananthakumar S. *Optically Transparent Intense Red Luminescence ZnO/PMMA Thin films.* National seminar: Materials; Process and Applications of Novel Technologies [NMAT], 7th Nov, 2013, Department of Physics, HHMSPB NSS College, Thiruvananthapuram (**Oral presentation**).

5. **S. Soumya** and S. Ananthakumar*, Morphologically tuned nano ZnO through wet chemical technique and its NIR reflectance characteristics for solar thermal control surfaces*.National Seminar on 'Emerging Trends in Chemical Sciences (ETCS-2013)" in connection with the Platinum Jubilee Celebrations held on 29-31 May 2013, Department of Chemistry, University of Kerala, Kariavattom, Trivandrum (**Poster presentation**).

6. **S. Soumya** and S. Ananthakumar, *A cumulative analysis on the optical properties of morphologically varied nano ZnO synthesized @ different pH conditions and bases additions*, National Seminar on Frontiers in Chemistry (NSFC-2012), in connection with Platinum Jubilee Celebration held on 25-27 April 2012. Department of Chemistry, University of Kerala, Kariavattom, Trivandrum (**Poster presentation**).